High-Current Inductors for High-Power Automotive DC-DC Converters

Brendan Lyons, B.E.

A thesis presented to the National University of Ireland for the degree of **Doctor of Philosophy**

November, 2008

Supervised by Dr. John G. Hayes and Dr. Michael G. Egan,
Department of Electrical and Electronic Engineering,
University College Cork,
Ireland.

Abstract

This thesis is focused on the investigation of magnetic materials for high-power dc-dc converters in hybrid and fuel cell vehicles and the development of an optimized high-power inductor for a multi-phase converter.

The thesis introduces the power system architectures for hybrid and fuel cell vehicles. The requirements for power electronic converters are established and the dc-dc converter topologies of interest are introduced. A compact and efficient inductor is critical to reduce the overall cost, weight and volume of the dc-dc converter and optimize vehicle driving range and traction power.

Firstly, materials suitable for a gapped CC-core inductor are analyzed and investigated. A novel inductor-design algorithm is developed and automated in order to compare and contrast the various magnetic materials over a range of frequencies and ripple ratios. The algorithm is developed for foil-wound inductors with gapped CC-cores in the low (10 kHz) to medium (30 kHz) frequency range and investigates the materials in a natural-convection-cooled environment.

The practical effects of frequency, ripple, air-gap fringing, and thermal configuration are investigated next for the iron-based amorphous metal and 6.5 % silicon steel materials. A 2.5 kW converter is built to verify the optimum material selection and thermal configuration over the frequency range and ripple ratios of interest. Inductor size can increase in both of these laminated materials due to increased airgap fringing losses. Distributing the airgap is demonstrated to reduce the inductor losses and size but has practical limitations for iron-based amorphous metal cores. The effects of the manufacturing process are shown to

degrade the iron-based amorphous metal multi-cut core loss. The experimental results also suggest that gap loss is not a significant consideration in these experiments. The predicted losses by the equation develped by Reuben Lee and cited by Colonel McLyman are significantly higher than the experimental results suggest. Iron-based amorphous metal has better preformance than 6.5 % silicon steel when a single cut core and natural-convection-cooling are used.

Conduction cooling, rather than natural convection, can result in the highest power density inductor. The cooling for these laminated materials is very dependent on the direction of the lamination and the component mounting. Experimental results are produced showing the effects of lamination direction on the cooling path. A significant temperature reduction is demonstrated for conduction cooling versus natural-convection cooling. Iron-based amorphous metal and 6.5% silicon steel are competitive materials when conduction cooled.

A novel inductor design algorithm is developed for foil-wound inductors with gapped CC-cores for conduction cooling of core and copper. Again, conduction cooling, rather than natural convection, is shown to reduce the size and weight of the inductor. The weight of the 6.5 % silicon steel inductor is reduced by around a factor of ten compared to natural-convection cooling due to the high thermal conductivity of the material. The conduction cooling algorithm is used to develop high-power custom inductors for use in a high power multi-phase boost converter.

Finally, a high power digitally-controlled multi-phase boost converter system is designed and constructed to test the high-power inductors. The performance of the inductors is compared to the predictions used in the design process and very good correlation is achieved.

The thesis results have been documented at IEEE APEC, PESC and IAS conferences in 2007 and at the IEEE EPE conference in 2008.

Acknowledgements

I wish to express my sincere thanks to the many individuals in Germany, California and Ireland who contributed to my work throughout the past four years.

Firstly, I want to thank my academic advisers at University College Cork for their support, advice, guidance and friendship. The enthusiasm, expertise, patience, and invaluable suggestions of Dr. John Hayes and Dr. Michael Egan contributed considerably to our work. I wish to thank Prof. Charles Sullivan for examining my thesis.

The technical and financial support of General Motors is greatly appreciated. I wish to thank Stephen Raiser in Mainz Kastel, Germany for his invaluable support and enthusiasm during our work. Additionally, I wish to thank George Woody in California for his motivation and financial support.

I wish to thank the students and staff of Power Electronic Research Laboratories and U.C.C. for their enthusiasm, friendship and banter. Among the many contributors are Marek Rylko, James Griffiths, Kevin Hartnett, Dr. Ray Foley, Dr. Richard Morrison, Dr. Dara O'Sullivan, Daithi Power, John Slowey, Jason Hannon, Alex Kyriakopoulos, Tomas Meade, David Cashman, Naveen Boggarapu, Gerry McCarthy, Sharon Babbington, Tim Power and Michael O'Shea.

The support of my family and friends has been ever so important to the success of my work. I want to thank Seamus, David, Jennifer, Philomena, Helen and young Abigail for their invaluable support and interest in my work. I want

to thank my wonderful girlfriend, Anita Reiss, for her love, support and patience during our cross-country adventures.

Finally, my sincere gratitude goes to my parents, Jim and Margaret, for their love, support, patience, encouragement, and understanding during the past 26 years.

Table of Contents

Abstract i

Acknowledgements iii

Table of Contents v

List of Tables ix

List of Figures xii

1 Introduction 1
- 1.1 Overview . . . 1
- 1.2 Thesis Objectives . . . 2
- 1.3 Thesis Structure . . . 4
- 1.4 General Background . . . 5
  - 1.4.1 Hybrid Vehicle Architecture . . . 7
  - 1.4.2 Fuel Cell Vehicle Architecture . . . 12
  - 1.4.3 DC-DC Converter Topologies for Hybrid and Fuel Cell Vehicles . . . 15
  - 1.4.4 Magnetic Materials for DC-DC Converters . . . 21

2 Magnetic Material Comparisons for High-Current Inductors in Low-Medium Frequency DC-DC Converters 24
- 2.1 Introduction . . . 25
- 2.2 Magnetic Material Characteristics . . . 26
- 2.3 Inductor Design Algorithm and Flowchart . . . 29
- 2.4 Area Product Analysis for Magnetic Materials . . . 44
  - 2.4.1 Constant Inductance, Variable Frequency Analysis . . . 44
  - 2.4.2 Constant Frequency, Variable Ripple Analysis . . . 49

2.5 Summary 54

3 Experimental Investigation of Iron-based Amorphous Metal and 6.5 % Silicon Steel 55
3.1 Introduction 56
3.2 Air-Cooled Experimental Analysis 57
3.2.1 Constant Inductance, Variable Frequency 58
3.2.2 Constant Frequency, Variable Ripple 62
3.2.3 Constant Frequency, Variable Load 66
3.3 Distributed Gap Effect 72
3.4 The Shielding Effect 80
3.5 Thermal Configuration 81
3.6 Experimental Anomalies 87
3.6.1 Constant Inductance, Variable Frequency Revised Tests . . 87
3.6.2 Constant Frequency, Variable Ripple Revised Tests 90
3.7 Revised Area Product Analysis for Magnetic Materials 91
3.7.1 Constant Inductance, Variable Frequency Analysis 92
3.7.2 Constant Frequency, Variable Ripple Analysis 95
3.7.3 Constant Ripple, Variable Frequency Analysis 100
3.8 Summary 105

4 Conduction Cooling Design Algorithm for High-Power Inductors 107
4.1 Introduction 108
4.2 Conduction Cooling Inductor Design Algorithm and Flowchart . . 110
4.3 Constant Inductance, Variable Frequency Analysis 121
4.4 High-Power Custom Inductor Design 122
4.4.1 Design 1 124
4.4.2 Design 2 125
4.5 Summary 127

5 High-Power Boost Inductor Analysis and Design 129
5.1 Toyota Prius THSII Boost Inductor 129
5.1.1 THSII Boost Inductor Characteristics 130
5.1.2 THSII Boost Inductor Analysis 131
5.2 Automotive Boost Inductor 135
5.2.1 Automotive Boost Inductor Characteristics 136
5.2.2 Automotive Boost Inductor Analysis 137
5.3 Boost Inductor Design 139

5.3.1 Design 1 . . . 139
5.3.2 Design 2 . . . 147
5.4 Helical Windings . . . 152
5.4.1 Design 1 with Helical Windings . . . 152
5.4.2 Design 2 with Helical Windings . . . 155
5.5 Experimental Results . . . 155
5.6 Summary . . . 158

6 3-Phase High-Power Interleaved Boost Converter 160
6.1 Introduction . . . 160
6.2 97.2 kW Boost Converter System and Specifications . . . 161
6.3 Boost Converter Power Stage . . . 162
6.3.1 Input and Output Capacitance . . . 162
6.3.2 Semiconductors . . . 163
6.3.3 Gate Drive . . . 163
6.3.4 High-Power Boost Inductor . . . 165
6.4 System Control . . . 168
6.4.1 Control Structure . . . 168
6.4.2 Analog-Digital Conversion (ADC) and Timing Requirements 170
6.4.3 Control Interface Board . . . 172
6.5 Experimental Results . . . 173
6.5.1 Thermal Results . . . 173
6.5.2 System Efficiency . . . 176
6.6 Summary . . . 176

7 Conclusions and Future Work 177
7.1 Thesis Summary . . . 177
7.2 Future work . . . 182

Bibliography 185

A Converter Active and Passive Component Stresses 195
A.0.1 Boost Converter Voltage Transfer Function . . . 195
A.0.2 Inductor and Input Capacitor Current Stresses . . . 197
A.0.3 Switch and Diode Current Stresses . . . 198
A.0.4 Output Capacitor Current Stress . . . 199

B Fourier Analysis of a Triangular Waveform **201**
B.0.5 Fourier Background 201
B.0.6 Harmonic Currents for 40 kW Inductor Design Point . . . 207
B.0.7 Expansion of Dowell's Equations 208
B.0.8 AC Loss Analysis for Design 1 211
B.0.9 AC Loss Analysis for Design 2 211

C Experimental Analysis **213**
C.0.10 B-H loops and inductor current and voltage waveforms for Section 3.2.3 213
C.0.11 Experimental Tables for Chapter 3 213

D High-Power Boost Converter Analysis **228**
D.1 Gate Drive 228
D.2 Control Structure and Software 230
D.2.1 Software Control Algorithm 232
D.3 Control Interface Board 237

List of Tables

1.1 Toyota Prius half-bridge dc-dc converter currents. 17
1.2 FCV multi-phase dc-dc converter currents. 19

2.1 Magnetic material characteristics. 28
2.2 Inductor area product vs. frequency for constant inductance (1 kW). 46
2.3 Inductor area product vs. frequency for constant inductance (10 kW). 48
2.4 Inductor area product vs. frequency for constant inductance (40 kW). 49
2.5 Inductor area product vs. ripple for constant frequency (1 kW). . 51
2.6 Inductor area product vs. ripple for constant frequency (10 kW). . 53
2.7 Inductor area product vs. ripple for constant frequency (40 kW). . 53

3.1 Custom inductor characteristics. 59
3.2 Table of losses and temperature rise for constant inductance. . . . 60
3.3 Core temperatures rise vs. gap length for constant frequency (30 kHz). 64
3.4 Silicon steel loss components vs. gap length for constant frequency (30 kHz). 65
3.5 Reduced temperatures due to distributed airgap. 79
3.6 Silicon steel core and copper temperatures for different winding configurations. 80
3.7 Conduction vs. convection cooling experimental results. 87
3.8 Custom inductor characteristics. 88
3.9 Table of losses and temperature rise for constant inductance. . . . 89

3.10 Inductor loss components vs. gap length for constant frequency (30 kHz). 92
3.11 Inductor area product vs. frequency for constant inductance (1 kW). 94
3.12 Inductor area product vs. frequency for constant inductance (10kW). 95
3.13 Inductor area product vs. frequency for constant inductance (40kW). 96
3.14 Inductor area product vs. ripple for constant frequency (1 kW). . 98
3.15 Inductor area product vs. ripple for constant frequency (10 kW). . 99
3.16 Inductor area product vs. ripple for constant frequency (40 kW). . 99
3.17 Inductor area product vs. frequency for 30 % ripple (1 kW). . . . 100
3.18 Inductor area product vs. frequency for 70 % ripple (1 kW). . . . 101
3.19 Inductor area product vs. frequency for 30 % ripple (10 kW). . . 103
3.20 Inductor area product vs. frequency for 70 % ripple (10 kW). . . 103
3.21 Inductor area product vs. frequency for 30 % ripple (40 kW). . . 104
3.22 Inductor area product vs. frequency for 70 % ripple (40 kW). . . 104

4.1 Design 1 boost inductor characteristics. 124
4.2 Summary of designed inductors. 125
4.3 Design 2 boost inductor characteristics. 126

5.1 Prius THSII boost inductor characteristics. 131
5.2 Automotive boost inductor characteristics. 137
5.3 Copper loss versus distance from gap and foil thickness. 142
5.4 Copper hotspot versus distance from gap and foil thickness (FEA Analysis). 144
5.5 Copper loss versus distance from gap and foil thickness. 148
5.6 Copper hotspot versus distance from gap and foil thickness (FEA Analysis). 151
5.7 Summary of analyzed and designed inductors. 156
5.8 Summary of core and copper temperatures for Designs 1 and 2. . 157

6.1 IGBT modules losses and junction temperatures 163

6.2 Inductor temperatures and weights. 166
6.3 Inductor temperatures and weights. 176

7.1 Summary of analyzed and designed inductors. 180
7.2 Inductor temperatures and weights. 181

B.1 Harmonic currents in Design 1. 208
B.2 AC Loss calculations for Design 1. 211
B.3 AC Loss calculations for Design 2. 212

C.1 Experimental results for Fig. 3.4. 218
C.2 Experimental results for Fig. 3.5. 219
C.3 Experimental results for Fig. 3.6. 220
C.4 Experimental results for Fig. 3.8. 221
C.5 Experimental results for Fig. 3.25. 222
C.6 Experimental results for Section 3.4 illustrating the shielding effect of the winding. 223
C.7 Experimental results for Fig. 3.26. 224
C.8 Experimental results for Fig. 3.31. 225
C.9 Experimental results for Fig. 3.32. 226
C.10 Experimental results for Fig. 3.33. 227

List of Figures

1.1 Increase in global temperature versus time. 5
1.2 Increase in oil prices versus time. 6
1.3 Series hybrid vehicle architecture. 7
1.4 Parallel hybrid vehicle architecture. 8
1.5 Series/Parallel hybrid vehicle architecture (THS in Prius). 9
1.6 The Toyota Hybrid System II for the '03 Toyota Prius. 11
1.7 Higher voltage operation of Lexus RX400h and Highlander SUVs. 12
1.8 Polymer Electrolyte Membrane Fuel Cell (PEMFC). 13
1.9 Typical fuel cell vehicle system architecture. 15
1.10 Circuit diagram of a bidirectional half-bridge converter. 16
1.11 Circuit diagram of a unidirectional multi-phase converter. 18
1.12 Circuit diagram of a two-phase coupled-inductor dc-dc converter. 19
1.13 Circuit diagram of a cascade converter. 20
1.14 Circuit diagram of a Z-source inverter. 21
1.15 Hitachi material comparison method for a fixed frequency (10 kHz). 22
1.16 Ferrite material comparison method for a fixed power density. . . 23
1.17 JFE Steel material comparison method of power loss vs. saturation flux density. 23

2.1 Eddy currents induced in the core due to airgap fringing flux. . . 29
2.2 Area product flow chart. 32
2.3 Drawing of core dimensions. 36

2.4 Inductor area product vs. frequency for constant inductance (1 kW). 46
2.5 Inductor area product vs. frequency for constant inductance (10 kW). 47
2.6 Inductor area product vs. frequency for constant inductance (40 kW). 48
2.7 Inductor area product vs. ripple for constant frequency (1 kW). . 51
2.8 Inductor area product vs. ripple for constant frequency (10 kW). . 52
2.9 Inductor area product vs. ripple for constant frequency (40 kW). . 53

3.1 Drawing of core dimensions. 58
3.2 6.5 % Si Steel (left) and iron-based amorphous (right) cores. . . . 59
3.3 2.5 kW, 125-250 V hard switched dc-dc converter setup. 59
3.4 Inductor temperature rise for constant inductance. 61
3.5 Temperatures for three sample cores at $f = 30$ kHz, $l_g = 1$mm. . . 62
3.6 Core temperature rise vs. gap length for constant frequency (30 kHz). 64
3.7 Silicon steel loss components vs. gap length for constant frequency (30 kHz). 65
3.8 Core temperature rise for varying load current. 67
3.9 Fe-based amorphous metal B-H analysis for varying gap length. . 68
3.10 Silicon steel B-H analysis for varying gap length. 68
3.11 Fe-based amorphous metal B-H analysis for varying load current. 69
3.12 Silicon steel B-H analysis for varying load current. 70
3.13 Inductance versus load current for 2605SA1 and 10JNHF600 (LCR meter). 71
3.14 λ-I loop for 2605SA1 at 30 kHz, 0 mm gap. 72
3.15 Inductor waveforms for 2605SA1 at 30 kHz, 0 mm gap. 73
3.16 λ-I for 2605SA1 at 20 kHz, 0 mm gap. 73
3.17 Inductor waveforms for 2605SA1 at 20 kHz, 0 mm gap. 74
3.18 λ-I loop for 2605SA1 at 10 kHz, 0 mm gap. 74
3.19 Inductor waveforms for 2605SA1 at 10 kHz, 0 mm gap. 75
3.20 λ-I loop for 2605SA1 at 30 kHz, 1 mm gap. 75
3.21 Inductor waveforms for 2605SA1 at 30 kHz, 1 mm gap. 76

3.22 FEA of single inductor airgap (1 x 3 mm). 77
3.23 FEA of distributed inductor airgap (3 x 1 mm). 77
3.24 FEA of copper loss of distributed inductor airgap. 78
3.25 Reduced temperatures due to distributed airgaps. 79
3.26 Fe-amorphous metal vs 6.5 % silicon steel at input current of 180 A. 82
3.27 Magnetic core segments. 83
3.28 Horizontal mounting of Fe-base amorphous metal (left), vertical mounting of 6.5 % silicon steel (right). 84
3.29 Aluminium thermal jig. 84
3.30 FEA of horizontal mounting of 6.5 % silicon steel core (0.2 T, 20 kHz). 85
3.31 Conduction cooling experimental results. 86
3.32 Inductor temperature rise for constant inductance. 90
3.33 Core temperature rise vs. gap length for constant frequency (30 kHz). 91
3.34 Inductor area product vs. frequency for constant inductance (1 kW). 94
3.35 Inductor area product vs. frequency for constant inductance (10kW). 95
3.36 Inductor area product vs. frequency for constant inductance (40kW). 96
3.37 Inductor area product vs. ripple for constant frequency (1 kW). . 97
3.38 Inductor area product vs. ripple for constant frequency (10 kW). . 98
3.39 Inductor area product vs. ripple for constant frequency (40 kW). . 99
3.40 Inductor area product vs. frequency for 30 % ripple (1 kW). . . . 101
3.41 Inductor area product vs. frequency for 70 % ripple (1 kW). . . . 102
3.42 Inductor area product vs. frequency for 30 % ripple (10 kW). . . 102
3.43 Inductor area product vs. frequency for 70 % ripple (10 kW). . . 103
3.44 Inductor area product vs. frequency for 30 % ripple (40 kW). . . 104
3.45 Inductor area product vs. frequency for 70 % ripple (40 kW). . . 105

4.1 Inductor core and copper thermal structure. 108
4.2 Drawing of Metglas core. 109
4.3 Conduction cooling inductor flow chart. 113

4.4 Inductor core and winding dimensions. 117
4.5 Inductor cooling 2-D model (above) and its equivalent 1-D model (below). 119
4.6 Winding cooling 2-D model and its 1-D equivalent. 120
4.7 Inductor weight vs. frequency for constant inductance (40 kW). . 123
4.8 Drawing of Metglas core: Design 2. 126

5.1 Electrical schematic of the Prius THSII boost converter 130
5.2 Picture of TMC Prius THSII boost inductor. 132
5.3 Picture of TMC Prius THSII boost inductor (topview). 132
5.4 Picture of Prius THSII boost inductor with ceramic spacers. . . . 133
5.5 Drawing of Prius THSII inductor core and windings (not to scale). 133
5.6 AC loss simulation of Prius THSII inductor. 134
5.7 Thermal simulation of Prius THSII inductor. 135
5.8 Electrical schematic of 3-phase high power interleaved boost converter 136
5.9 Automotive boost inductor. 138
5.10 Drawing of automotive boost inductor core and windings. 138
5.11 Thermal simulation of the core used in Design 1. 141
5.12 Properties of CMC foil. 141
5.13 AC copper loss versus distance from gap and foil thickness (FEA Analysis). 142
5.14 Total copper loss versus distance from gap and foil thickness. . . . 143
5.15 Copper hotspot versus distance from gap and foil thickness (FEA Analysis). 144
5.16 FEA of Al winding located 1.5 mm from the airgap. 146
5.17 Thermal simulation of Al winding located 1.5 mm from the airgap. 146
5.18 Thermal simulation of the core used in Design 2 (FEA Analysis). 148
5.19 FEA of 0.3 mm foil winding located 3 mm back from airgap. . . . 149

5.20 AC copper loss versus distance from gap and foil thickness (FEA Analysis). 149
5.21 Total copper loss versus distance from gap and foil thickness. . . . 150
5.22 Copper hotspot of 0.5 mm foil located 2 mm away from the airgap (FEA Analysis). 151
5.23 Copper hotspot versus distance from gap and foil thickness (FEA Analysis). 152
5.24 AC loss of helical winding on Design 1. 154
5.25 Thermal simulation of helical winding on Design 1. 154
5.26 Fe-amorphous metal vs 6.5 % silicon steel (Design 1). 157
5.27 Fe-amorphous metal vs 6.5 % silicon steel (Design 2). 158

6.1 3-phase interleaved boost converter. 162
6.2 SKYPER 32 PRO with adapter board on top of SEMiX module. . 164
6.3 Picture of inductor tray for Design 1. 166
6.4 Thermal simulation of potted inductor. 167
6.5 1.9 kg, Design 1 (left) vs. 3.62 kg, automotive inductor (right). . . 168
6.6 Overview of control structure. 169
6.7 Detailed control structure. 170
6.8 PWM sampling in the middle of each PWM on state. 171
6.9 Control timing requirements. 171
6.10 Picture of control interface board. 172
6.11 3-phase 97.2 kW interleaved boost converter. 173
6.12 The boost converter input and output voltage waveforms. 174
6.13 Phase 1 and phase 2 pole voltage and inductor current waveforms. 174
6.14 Inductor experimental thermal results. 175

7.1 Design 1, foil wound inductor and earlier automotive inductor. . . 181
7.2 Core size reduction using a hybrid core. 183
7.3 Potential 3-phase integrated silicon steel inductor (3D). 184

7.4 Potential 3-phase integrated silicon steel inductor. 184

A.1 Boost converter circuit waveforms. 196
A.2 Capacitor triangular current waveform. 197

B.1 Normalized triangular waveform for Fourier analysis. 204

C.1 λ-I loop for 10JNHF600 at 10 kHz, 0 mm gap. 215
C.2 Inductor waveforms for 10JNHF600 at 10 kHz, 0 mm gap. 215
C.3 λ-I loop for 10JNHF600 at 20 kHz, 0 mm gap. 216
C.4 Inductor waveforms for 10JNHF600 at 20 kHz, 0 mm gap. 216
C.5 λ-I for 10JNHF600 at 20 kHz, 1 mm gap. 217
C.6 Inductor waveforms for 10JNHF600 at 20 kHz, 1 mm gap. 217

D.1 SKYPER 32 PRO with adapter board on top of SEMiX module. . 229
D.2 Tracking of inductor current. 231
D.3 Boost converter statemachine. 232
D.4 PWM sampling in the middle of each PWM on state. 237
D.5 Electrical schematic of phase 1 current sense network. 239
D.6 Electrical schematic of phase 2 current sense network. 240
D.7 Electrical schematic of phase 3 current sense network. 241
D.8 Electrical schematic of voltage sense network. 242
D.9 Electrical schematic of control interface components. 243

Chapter 1

Introduction

This chapter introduces the research project and outlines the structure of the thesis.

1.1 Overview

The development of extra-low-emission vehicles is a great challenge for the automotive industry and has become a significant technology driver for power electronics. Measurements clearly show power savings of up to 24 % for inner city driving by the recuperation of braking energy [1]. Pure electric vehicles suffer from a limited cruising range because of the low energy density of batteries in comparison to conventional fuels [2]. More attractive approachs are hybrid and fuel cell vehicles (FCV) using an electrical energy storage system for recuperation of braking energy.

Dc-dc converters play a key role in the power system architectures for hybrid vehicle and next-generation fuel cell vehicle propulsion and are a critical component between the electrical energy storage unit or fuel cell and the propulsion power bus. Typically, the dc-dc converter manages power flow between the onboard power sources during periods of high-power demand, such as high torque

conditions, vehicle acceleration or loading from auxiliary subsystems. Several hybrid and fuel cell vehicle architectures are discussed in [3]. Powerful and highly efficient dc-dc converters are key components of hybrid and fuel cell vehicles and several key topologies have previously been presented [1, 2, 4, 5, 6, 7, 8]. The dc-dc converter high power and low-voltage operation (normally less than 600 V_{dc}) result in currents of the order of hundreds of amps. These large currents not only increase the electric and thermal stresses in the converter but also reduce the converter efficiency. The wide input voltage range increases the current and voltage stresses on the converter even further since such stresses change with the input/output voltage ratio. In depth magnetic material analysis and component design ensures an efficient, compact inductor and is critical in reducing the overall dc-dc converter size, cost and losses.

Several design options in the dc-dc converter have an effect on the size of the required inductor, e.g. the number of stages and continuous versus discontinuous conduction [1, 4, 6]. The choice of core dimensional ratios can also significantly reduce the size of the inductor [9] and further size reduction can be achieved by using improved cooling methods [10]. There are currently many magnetic materials available to the magnetic designer, e.g. ferrite, laminated materials and powdered gapless cores [11, 12, 13, 14, 15, 16, 17, 18]. The correct choice of magnetic material is necessary to ensure a minimum size and cost-effective inductor [19].

1.2 Thesis Objectives

The first objective of the thesis is to investigate the magnetic materials of interest to dc-dc converters in the low (10 kHz) to medium (30 kHz) frequency range. The materials of interest are primarily iron-based amorphous metal, 6.5 % silicon steel,

nanocrystalline and low frequency ferrite. The thesis develops a novel inductor design algorithm that factors in several design considerations: winding skin and layer effects; airgap fringing, distance from airgap to minimize copper fringing loss; core loss; gap loss; natural convection cooling; creepage and safety clearance. The thesis further investigates the practical effects of operating frequency, ripple ratio, airgap and material laminations on the overall inductor size and power losses.

The second objective of this thesis is to investigate methods of optimizing inductor power density. It is demonstrated that conduction cooling, rather than convection, can result in the highest density inductor. A novel conduction cooling inductor design algorithm is presented for foil-wound inductors with gapped CC-cores in the low to medium frequency range. The algorithm is used to develop high-power custom inductors and the mass of the inductor is optimized in the design algorithm.

The third objective of the thesis is to develop two high-power custom inductors for the high-power automotive application. Finite element analysis is used to further optimize the inductor designs output from the conduction cooling inductor design algorithm. Emphasis is also placed on the high-volume manufacturing requirements of the inductor. Finally, a digitally-controlled, high-power multi-phase converter system is designed and constructed to test the optimized inductors. The prototype inductors form part of a high-power multi-phase converter for use in a fuel cell vehicle.

1.3 Thesis Structure

The organization of the thesis is as follows. The background to the modern interest in hybrid and fuel cell vehicles is discussed in the second part of this introductory chapter and the basic power system architectures for hybrid and fuel cell vehicles are presented. The requirements for power electronics converters to optimize the interface between the electrical sources and their loads are established. The general dc-dc converter topologies are outlined and the magnetic materials of interest to the dc-dc converter topologies are introduced.

Chapter 2 investigates iron-based amorphous metal, 6.5 % silicon steel, nanocrystanlline and low frequency ferrite. A novel inductor design algorithm is developed and automated in order to compare and contrast the magnetic materials over a range of frequencies and ripple ratios. Chapter 3 details the practical effects of frequency, ripple, air-gap fringing, and thermal configuration for iron-based amorphous metal and 6.5 % silicon steel. Chapter 4 develops a conduction cooling inductor design algorithm and presents two high-power custom inductor designs.

Chapter 5 presents finite element simulations for the two high-power custom inductors and comparisons are made with high-power inductors currently used in the automotive industry. Inductor winding options are also investigated. Chapter 6 presents the design, construction and experimental results of a high-power multi-phase converter that is used as a test bed for the inductors optimized in Chapter 5. The summary, conclusions, and suggestions for future work are contained in Chapter 7.

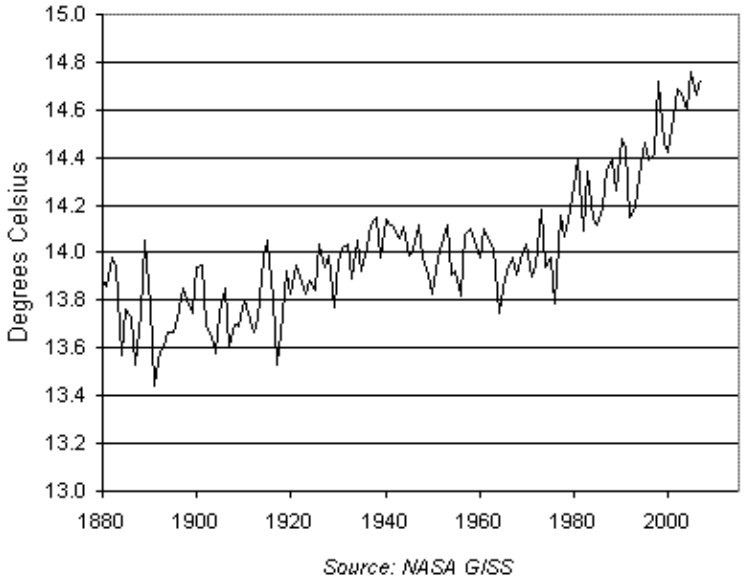

Figure 1.1: Increase in global temperature versus time.

1.4 General Background

There is a growing scientific consensus that increasing levels of greenhouse gas emissions are changing the climate of the earth resulting in a rise of global temperature [20]. Fig. 1.1 shows the increase in global temperature since the late 19th century [21]. It is clear that temperatures around the world are continuing their upward climb with the global average in 2007 the second warmest year on record, only 0.03 °C behind the 2005 maximum. Since oil-fired transport is a very major contributor to global greenhouse gas emissions research work in the area of alternative power train technologies for automotive applications is continuing in order to reduce these emissions and their effects on the environment. Some of these technologies are electric, hybrid, and fuel cell vehicles.

The diminishing supply of oil and gas, and the increasing instability in the security of their supply, have also led to research and development activity in the area of alternative-energy vehicles, which do not rely on fossil fuels to power

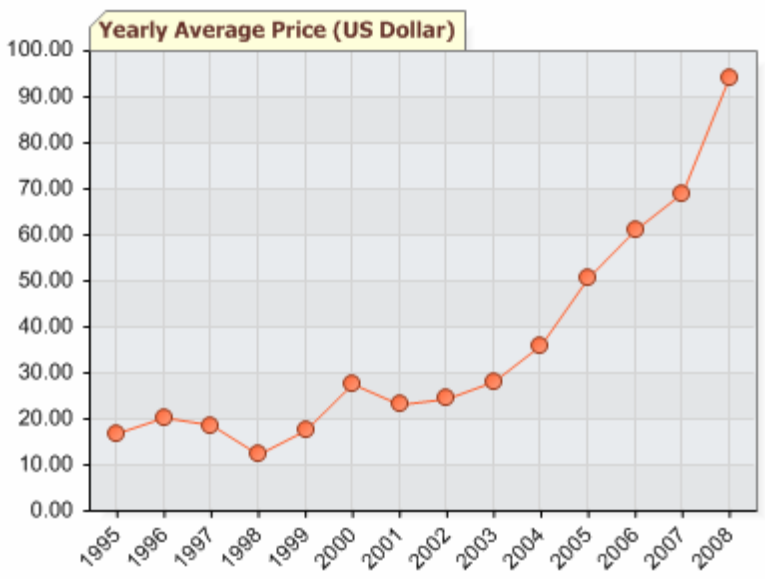

Figure 1.2: Increase in oil prices versus time.

them. The development of alternative and more efficient transport is essential in the face of constant increases in oil demands and consequently oil prices. Fig. 1.2 illustrates the increase in the cost of oil over the last decade [22].

Air pollution can be reduced significantly through the use of alternative fuels, increased fuel economy, and improved power unit and after-treatment technology [3]. Hybrid vehicles offer significant advantages over the internal combustion engine (ICE) such as: greatest potential for improved fuel efficiency and performance; reduced carbon dioxide emissions by using smaller internal combustion engines; eradication of idle fuel consumption during stops and decelerations; more efficient operation of the ICE; the recovery of vehicle kinetic energy by regenerative braking and, finally, engine size reduction with same vehicle performance through advanced power management systems.

Fuel cell vehicles have the advantages of high-power density and electrical efficiency and almost zero emissions if the hydrogen fuel is obtained using a renewable energy source. In addition, these vehicles have potential for increased

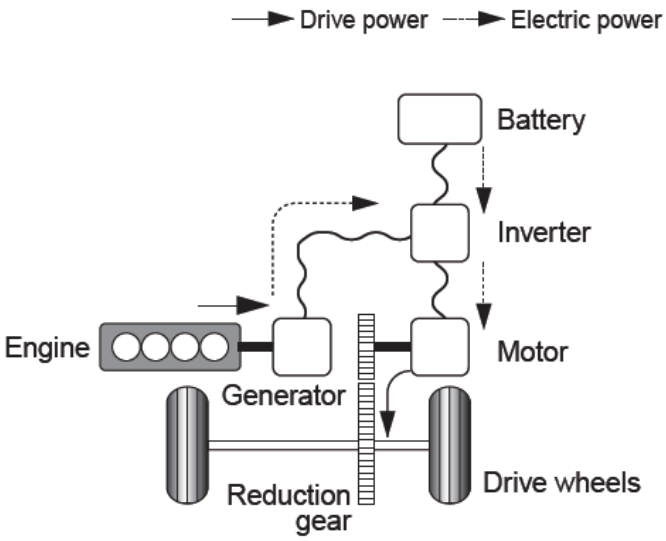

Figure 1.3: Series hybrid vehicle architecture.

reliability due to the reduction in moving parts and for reduced noise levels.

1.4.1 Hybrid Vehicle Architecture

Series, parallel and series/parallel hybrid systems are the three major types of architectures used in hybrid vehicles currently on the market [23]. A typical series-hybrid propulsion system architecture is shown in Fig. 1.3. The engine drives a generator, and an electric motor uses this generated electricity to drive the wheels. This is called a series-hybrid system because the engine power and the motor power are in series. The series-hybrid system can efficiently charge the battery and generate and supply electrical power to the electric traction motor. This system has two electrical machines, an electric motor and a generator. The series-hybrid system is used in the Toyota Coaster Hybrid [23] and is proposed by General Motors (GM) for the Clevy Volt.

A typical parallel-hybrid propulsion system architecture is shown in Fig. 1.4. In a parallel-hybrid system, both the engine and the electric motor drive the

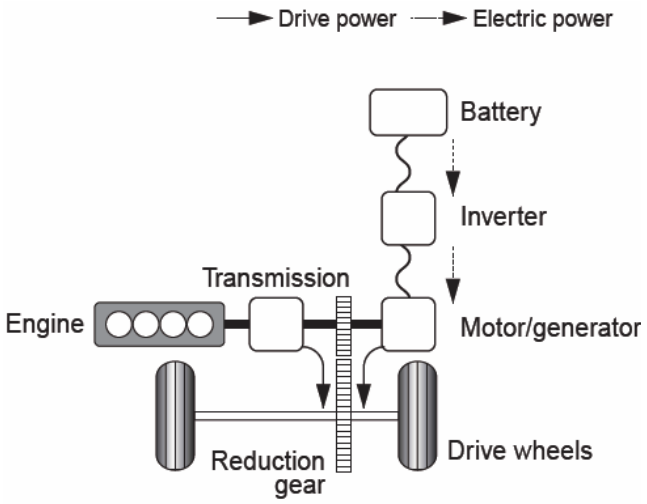

Figure 1.4: Parallel hybrid vehicle architecture.

wheels, and the power from these two sources can be utilized according to the driving conditions. This is called a parallel-hybrid system because the power flows to the wheels in parallel from the two mechanical sources. The electric motor is switched to act as a generator and charge the batteries, and the electricity from the batteries is used to drive the wheels. The parallel-hybrid system cannot drive the wheels from the electric motor while simultaneously charging the battery since this system has only one motor.

A series/parallel hybrid propulsion system architecture is shown in Fig. 1.5 and is similar to the Toyota Hybrid System (THS) in the Toyota Prius [23]. This system combines the series hybrid system with the parallel hybrid system in order to maximize the benefits of both systems. This system maximizes the vehicle overall efficiency by generating electricity under operating conditions in which the efficiency of the engine is high and by using the electric motor to run the vehicle under operating conditions in which the engine efficiency is low. It has two motors, and depending on the driving conditions, uses only the electric motor or the driving power from both the electric motor and the engine, in order

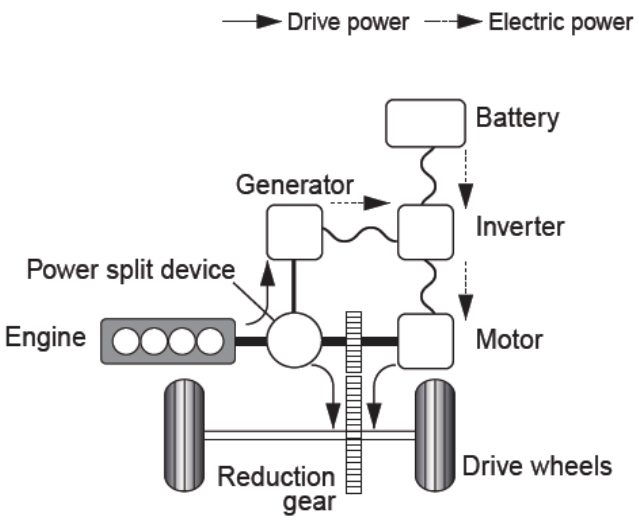

Figure 1.5: Series/Parallel hybrid vehicle architecture (THS in Prius).

to achieve the highest efficiency level. Furthermore, when necessary, the system drives the wheels while simultaneously generating electricity for the battery using a generator.

The Toyota Prius has a highly efficient 1.5 liter engine, a power-split device, a continuously-variable drive train, a permanent magnet generator, a 33 kW permanent magnet propulsion motor, two IGBT inverters and a 274 V, Ni-MH battery pack [23]. The system has five main operating modes.

1. The electric motor powers the vehicle under light load.

2. A combination of the engine and the electric motor powers the vehicle during normal driving conditions.

3. The electric motor receives additional power from the 274 V battery pack during a full acceleration.

4. The electric motor acts as a generator to recharge the batteries during deceleration or braking.

5. The batteries are regulated to maintain a constant charge.

Power from the engine is used to drive the generator when battery charging is required. This eliminates the need for an external charger or power connection. The power split device in the transmission sends engine power either directly to the wheels or to the generator. The power split device uses a planetary gear to constantly vary the amount of power supplied from the engine to either the wheels or generator. The engine speed, generator output and the speed of the electric motor are electronically controlled by the transmission. The system is designed to keep the engine running within its most efficient rpm range. At increased driving loads, if the engine's speed decreases, the control system shuts off the engine. The total driving power is then supplied by the electric motor. The engine is restarted and adds additional power until the extra power is no longer needed. At that point, the electric motor stops and the engine resumes its light load operation in its optimum speed range.

Fig. 1.6 illustrates the Toyota Hybrid System II (THS II) for the '03 Toyota Prius [24]. THS II is an advanced series/parallel hybrid propulsion system. The battery, the motor and the generator are all redesigned enabling higher efficiency and power of the system. A power control unit with a redesigned inverter and an additional dc-dc boost converter are also developed. The system consists of two power sources, i.e a 50 kW permanent magnet ac synchronous motor achieving 1.5 times more output power than the THS and a high-efficiency petrol engine. A reduction in the battery internal resistance and an improved cooling structure has enabled a 35 % increase in input/output density. The battery does not require external charging as the battery is discharged or receives charging energy from the motor and the generator.

The power control unit is a new technology that supports the THS II system. The dc-dc boost converter raises the voltage of the motor and the generator to a

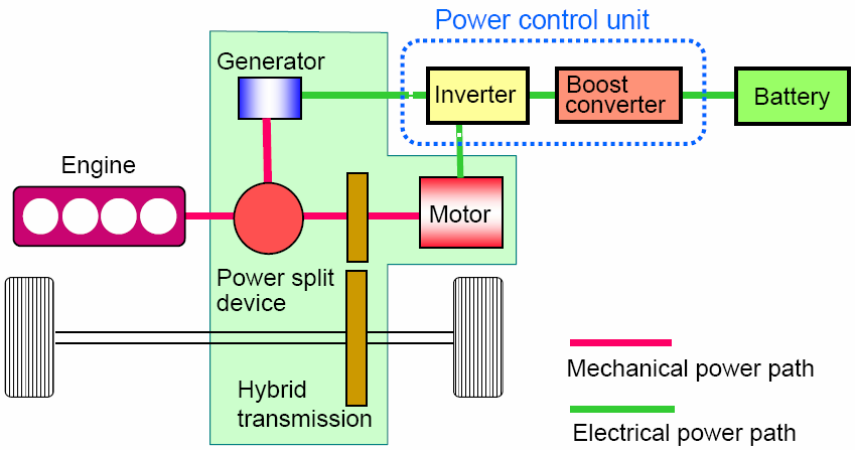

Figure 1.6: The Toyota Hybrid System II for the '03 Toyota Prius.

maximum of 500 V in THS II compared to 274 V in THS. As a result, electrical power can be supplied to the motor using a smaller current resulting in higher inverter efficiency. A reduction in the size of the inverter is also achieved with smaller current. Similarly, further enhancements in the THS II for the Lexus RX400h and Highlander SUVs [25] have increased the operating voltage of the motor and the generator to 650 V. Fig. 1.7 compares the Toyota Hybrid System II for the Toyota Prius versus Lexus RX400h and Highlander SUVs [25]. This improvement enables the motor to produce high output power with low power loss. The size of the motor is also increased by a factor of 2.4 from 50 kW in the Toyota Prius to 120 kW in Lexus RX400h and Highlander SUVs.

Interestingly, as the trend for higher voltage systems continues, Toyota Motor Corporation (TMC) has invested in the capability of IGBT development in-house [24]. It is clear that dc-dc boost converters have a key role in supporting hybrid electric vehicle propulsion.

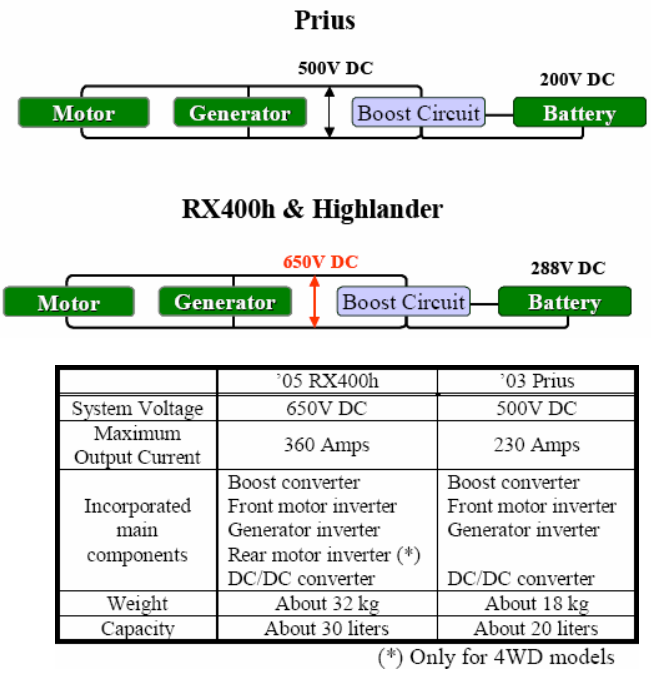

	'05 RX400h	'03 Prius
System Voltage	650V DC	500V DC
Maximum Output Current	360 Amps	230 Amps
Incorporated main components	Boost converter Front motor inverter Generator inverter Rear motor inverter (*) DC/DC converter	Boost converter Front motor inverter Generator inverter DC/DC converter
Weight	About 32 kg	About 18 kg
Capacity	About 30 liters	About 20 liters

(*) Only for 4WD models

Figure 1.7: Higher voltage operation of Lexus RX400h and Highlander SUVs.

1.4.2 Fuel Cell Vehicle Architecture

A hydrogen fuel cell system designed for vehicular propulsion applications must have fast response, high-power density, rapid start-up and volume and weight similar to the present day ICE based vehicles. Good fuel economy, low cost, long life-time, rapid acceleration and safety considerations with respect to fuel handling are also essential if fuel cell systems are to become an alternative option for next generation vehicles. The fuel cell as a source of energy has several advantages. The fuel cell itself operates noiselessly and has no moving parts to suffer mechanical wear. Furthermore, electricity generation in the hydrogen fuel cell causes no exhaust gas, and its efficiency, especially in the part-load area, is higher than that of an ICE [26]. A significant disadvantage of the hydrogen fuel cell is that hydrogen produced today is more expensive and less efficient than conventional fuels. The feasibility of hydrogen as the fuel of the future

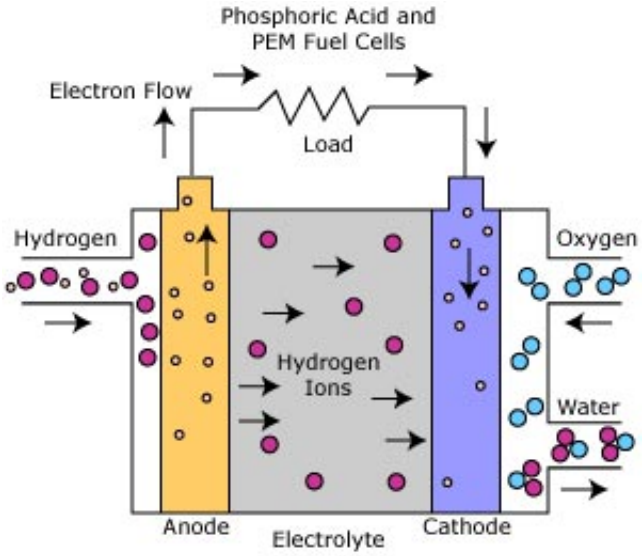

Figure 1.8: Polymer Electrolyte Membrane Fuel Cell (PEMFC).

also depends on the development of a hydrogen distribution infrastructure and a significant reduction in the costs involved in obtaining hydrogen from renewable sources of energy.

Various types of fuel cells are currently under development. The most common classification of fuel cells is by the type of the electrolyte used [27, 28, 29, 30]. The PEMFC (Polymer Electrolyte Membrane Fuel Cell) is regarded as the most suitable for use in vehicular applications because of its low operating temperature, higher power density, specific power, longevity and efficiency. It also has a relatively high durability as well as the ability to rapidly adjust to changes in power demand. One problem in the PEMFC is that the carbon monoxide (CO) concentration in fuel should be reduced to less than 10 ppm, because even small amounts of CO in fuels cause deterioration of the cell performance. Another problem is that they typically require expensive precious-metal catalysts. PEMFC use a solid polymer membrane (a thin plastic film, typically platinum) as the electrolyte. Fig. 1.8 illustrates a PEMFC structure. This polymer is permeable to

protons when it is saturated with water, but it does not conduct electrons. The fuel for the PEMFC is hydrogen and the charge carrier is the hydrogen ion (proton). At the anode, the hydrogen molecule is split into hydrogen ions (protons) and electrons. The hydrogen ions permeate across the electrolyte to the cathode while the electrons flow through an external circuit and produce electric power. Oxygen, usually in the form of air, is supplied to the cathode and combines with the electrons and the hydrogen ions to produce water. The anode, cathode and overall reactions are as follows:

$$2H_2 \Rightarrow 4H^+ + 4e^- \tag{1.1}$$

$$O_2 + 4H^+ + 4e^- = 2H_2O \tag{1.2}$$

$$2H_2 + O_2 = 2H_2O \tag{1.3}$$

During operation of the hydrogen fuel cell, the electrodes normally have a voltage differential of between 0.6 and 1.1 V. For this reason several cells must be stacked in series to provide a useful voltage for the vehicle.

A typical fuel cell vehicle system architecture is shown in Fig. 1.9. Inside the fuel cell stack, the hydrogen and oxygen are combined to produce electricity and heat. The output voltage of the fuel cell stack is typically stepped up with a dc-dc boost converter to obtain the required voltage for the inverter, as the fuel cell is a relatively high-output-impedance source with significant voltage variations when loaded. Reduced inverter size is also achieved with the higher system voltage. The inverter is used to convert the dc voltage to variable voltage and variable frequency to power the propulsion motor. Energy storage, such as a battery or an ultra-capacitor, is generally connected across the fuel cell system to provide supplemental power and for starting the system.

A fuel cell vehicle with a battery and a dc-dc converter enables the use of the inherently high energy density of the fuel cell and the high power density of the

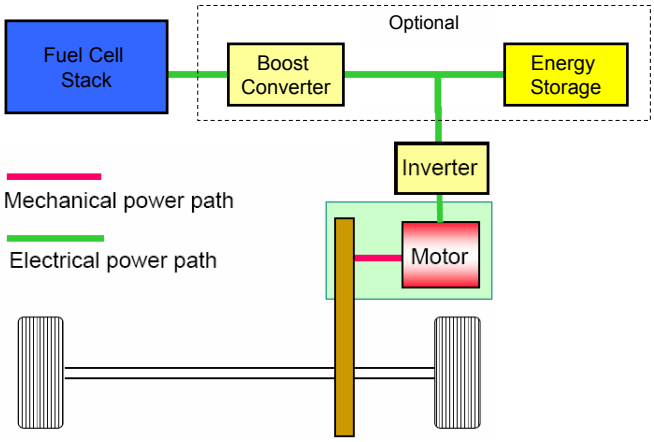

Figure 1.9: Typical fuel cell vehicle system architecture.

battery. During low power demand, such as cruising, the fuel cell provides the driving power and charges the batteries if required. When power demand is high, such as during an acceleration, batteries will provide the required peak power. The use of the battery allows rapid start-up of the fuel cell and protects it against cell reversal during this operation. Improvement in peak power, the capability of regenerative energy storage, and overall improved vehicle response is achieved with the battery. The cost of the battery pack and the dc-dc converter are the disadvantages of this system.

Several variations of the fuel cell vehicle architecture in Fig. 1.9 are discussed in [31], such as the operation of the fuel cell vehicle without a dc-dc converter and with, or without, a battery/ultra-capacitor.

1.4.3 DC-DC Converter Topologies for Hybrid and Fuel Cell Vehicles

There are several non-isolated dc-dc converter topologies that can be used in a hybrid or a fuel cell vehicle. Hard-switched, low (10 kHz) to medium (30 kHz)

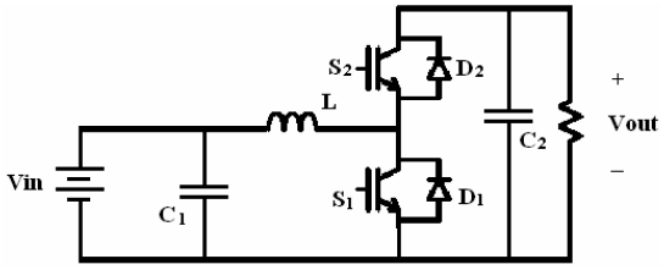

Figure 1.10: Circuit diagram of a bidirectional half-bridge converter.

frequency dc-dc converters result in the lowest component count compared to soft-switched, high frequency (> 100 kHz) converters due to the extra components required to achieve soft-switching operation [32, 33]. Low cost and volume due to the reduced component count makes the hard-switched dc-dc converter a competitive solution for high volume automotive production. The frequency is limited by audible noise at low frequencies and switching losses at higher frequencies. Several non-isolated hard-switched dc-dc converter topologies are considered next.

(A) Half-Bridge Converter

Fig. 1.10 illustrates the bidirectional half-bridge converter [4, 5, 25] similar to the converter in the Toyota Prius. The converter manages power flow between the voltage source and the high-voltage propulsion bus. The converter can boost in one direction and buck in the opposite direction. This limits the input voltage as the input voltage has to be less than the high voltage propulsion bus at all times. In the Toyota Prius, the propulsion power is provided by the engine during normal operating conditions. However, during periods of high power demand, such as high torque conditions, vehicle acceleration or loading from auxiliary subsystems, the converter operates in a boost-mode by stepping-up the battery voltage and providing additional power to the propulsion bus. Conversely, under

Current	A	Current	A
I_{in}	104	I_o	42
$I_{L,rms}$	105	$I_{L,pk-pk}$	28
$I_{sw,rms}$	81	$I_{sw,avg}$	63
$I_{d,rms}$	66	$I_{d,avg}$	42
$I_{sw,pk}$	119	$I_{d,pk}$	119

Table 1.1: Toyota Prius half-bridge dc-dc converter currents.

light propulsion loads, the converter operates in buck-mode, stepping down the high voltage from the propulsion bus and recharging the battery bank.

The Toyota Prius half-bridge converter has the following circuit parameters: input voltage, $V_{in} = 201\ V$, output voltage, $V_{out} = 500$ V, input power, $P_{in} = 21$ kW, inductance, $L = 425\ \mu$H, frequency, $f = 10$ kHz, input capacitance, $C_1 = 282\ \mu$F, and output capacitance, $C_2 = 1130\ \mu$F. The input current, I_{in}, output current, I_o, inductor rms current, $I_{L,rms}$, inductor peak-to-peak current, $I_{L,pk-pk}$, switch rms current, $I_{sw,rms}$, switch average current, $I_{sw,avg}$, switch peak current, $I_{sw,pk}$, diode rms current, $I_{d,rms}$, diode average current, $I_{d,avg}$, and diode peak current, $I_{d,peak}$, are calculated using the equations in Appendix A and are tabulated in Table 1.1 for ideal components.

(B) Multi-phase Converter

Fig. 1.11 illustrates the unidirectional version of the high power multi-phase converter presented in [1, 2, 4]. This converter is similar to the high power converter designed in Chapter 6 of this thesis for a fuel cell vehicle. The converter can only boost in one direction and is used to step the fuel cell voltage up to the required voltage for charging the battery and powering the inverter. The multi-phase converter has several key advantages. The advantage of scalability allows multiple phases to operate at a corresponding fraction of the total converter power. This facilitates component optimization based on a desired criterion such as size,

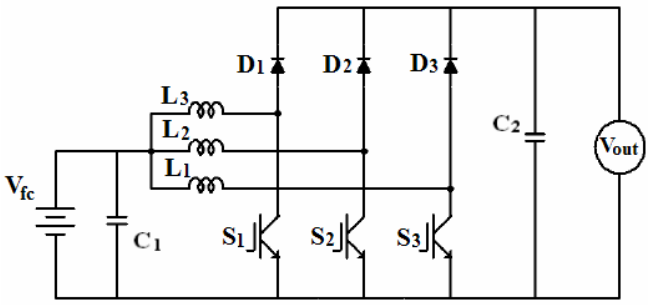

Figure 1.11: Circuit diagram of a unidirectional multi-phase converter.

cost, or other specifications. Converter phases operate independently with closely balanced current and voltage sharing, allowing phase interleaving. Phase interleaving causes portions of inductor phase currents to overlap as a function of duty cycle resulting in reduced ripple current in the capacitors. Higher efficiency at light load is also realized by disabling a number of phases under low power conditions. The unidirectional multi-phase converter also requires fewer components compared to its bidirectional counterpart.

The multi-phase converter designed in Chapter 6 has the following specifications: input voltage, $V_{in} = 180\ V$, output voltage, $V_{out} = 360$ V, total input current, $I_{in} = 540$ A, inductance per phase, $L = 45\ \mu$H, frequency, $f = 16$ kHz, input capacitance, $C_1 = 300\ \mu$F, and output capacitance, $C_2 = 900\ \mu$F. The total input current and the input current per phase, I_{in}, the total output current and the output current per phase, I_o, the inductor rms current, $I_{L,rms}$, the inductor peak-to-peak current, $I_{L,pk-pk}$, the switch rms current, $I_{sw,rms}$, the switch average current, $I_{sw,avg}$, the switch peak current, $I_{sw,pk}$, the diode rms current, $I_{d,rms}$, the diode average current, $I_{d,avg}$, and the diode peak current, $I_{d,peak}$, are all calculated using the equations in Appendix A and are tabulated in Table 1.2.

Current	A	Current	A
I_{in} per phase / total	180 / 540	I_o per phase / total	90 / 270
$I_{L,rms}$	184	$I_{L,pk-pk}$	125
$I_{sw,rms}$	130	$I_{sw,avg}$	90
$I_{d,rms}$	90	$I_{d,avg}$	130
$I_{sw,pk}$	243	$I_{d,pk}$	243

Table 1.2: FCV multi-phase dc-dc converter currents.

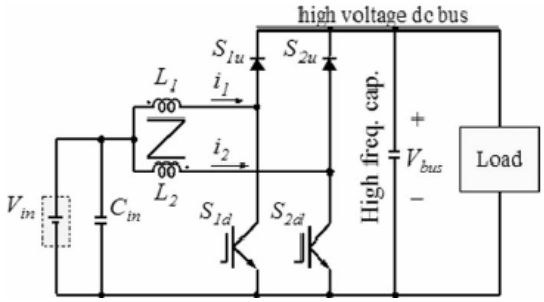

Figure 1.12: Circuit diagram of a two-phase coupled-inductor dc-dc converter.

(C) Multi-phase Coupled-Inductor Converter

Fig. 1.12 is a schematic diagram of a two-phase coupled-inductor dc-dc converter [8, 34, 35, 36]. Compared to single-phase converters, the multi-phase interleaved converter has more components. The optimum number of phases is determined by the power level, losses, cost, etc. The multi-phase interleaving structure has more inductors than the single-phase converter, which clearly increases the complexity of the converter. Integrated magnetic components allow a decrease in the core number and the complexity of the converter [35]. The two individual inductors of the two interleaved stages can be integrated together on a single pair of E-E or E-I cores enabling core loss reduction and a decrease in the component count. Typically, this converter is designed in discontinuous conduction mode (DCM) and has proved suitable for voltage regulator modules (VRMs) with low voltages, high currents, and fast transient responses [34, 35]. Further publications

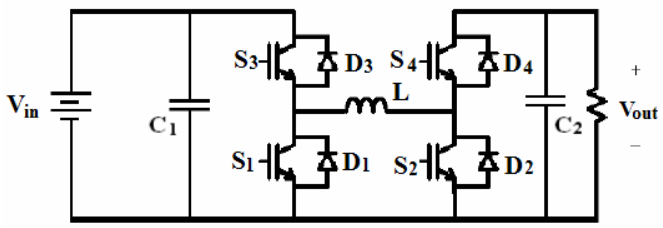

Figure 1.13: Circuit diagram of a cascade converter.

show that the coupled-inductor converter can also be considered as a potential candidate for high power converters [8, 36].

(D) Cascade Converter

Fig. 1.13 illustrates the cascade converter [37]. The significant advantage of the cascade converter is that it can buck and boost the voltage in both directions. This means that the input voltage (typically a battery) can be higher than the high voltage propulsion bus at any period of operation. This results in greater flexibility for the input voltage source design but at the expense of an increased component count and a more detailed control structure compared to its bidirectional counterpart.

(E) Z-Source Inverter

Fig. 1.14 presents the Z-source inverter [38, 39]. Currently, two types of inverters are used in hybrid and fuel cell vehicle traction drives: the traditional pulse width modulation (PWM) inverter and the dc-dc boosted PWM inverter. For FCVs, the fuel cell voltage to the inverter decreases with an increase in power drawn from the fuel cell. Therefore, the obtainable output voltage of the traditional PWM inverter is low at high power resulting in an over-sized inverter and motor. The dc-dc boosted PWM inverter does not have this problem but the extra dc-dc

stage increases the cost and complexity of the circuit, and reduces the overall system efficiency. The Z-source inverter provides single stage power conversion, higher efficiency and a reduced system component count [38, 39].

1.4.4 Magnetic Materials for DC-DC Converters

A major design aspect in a high power boost converter is the design and selection of the boost inductor. The major concern here is the size and weight of such a high power inductor that is perhaps the single heaviest component in the entire converter. In-depth magnetic material analysis and design ensures an efficient and compact inductor which is critical to reduce the overall dc-dc converter size, cost and power loss.

There are currently many magnetic materials available to the designer such as iron-based amorphous metal, 6.5% silicon steel, nanocrystalline, ferrite, etc [11, 12, 13, 14, 15, 16, 17, 18]. The correct choice of magnetic material is necessary to ensure a minimum size and cost-effective inductor [19]. Current methods for selecting core materials limit the designer to specific design points. Fig. 1.15 shows how magnetic materials are compared for a fixed frequency of 10 kHz [14] and Fig. 1.16 illustrates how ferrite materials are compared for a fixed power

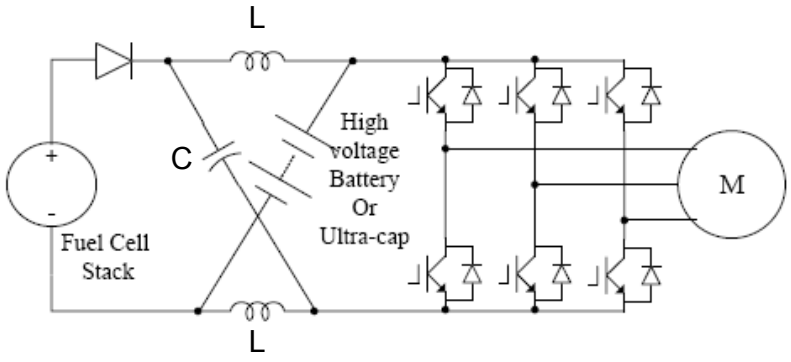

Figure 1.14: Circuit diagram of a Z-source inverter.

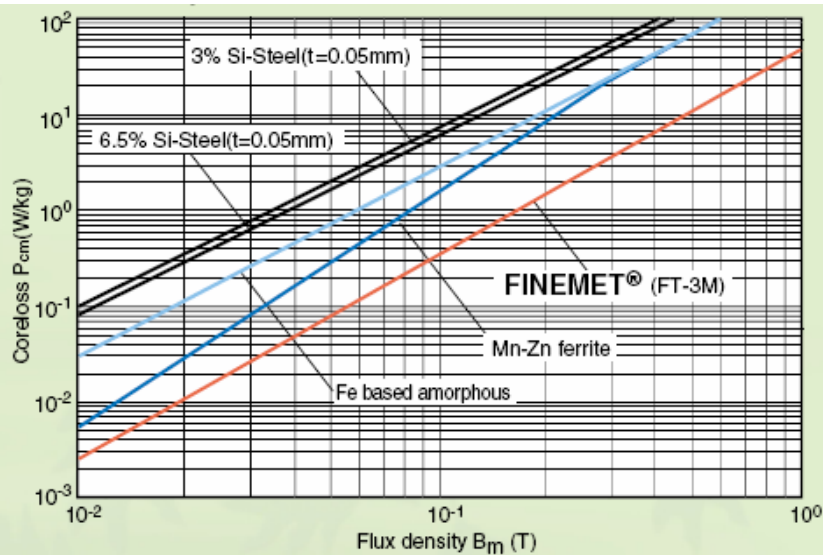

Figure 1.15: Hitachi material comparison method for a fixed frequency (10 kHz).

density of 500 mW/cm^3 [15]. Typically, the worst case inductor design point is analysed and the core loss at the derived induction is calculated as illustrated in Fig. 1.15. With ferrite materials the power throughput of the inductor is calculated and a ferrite material is then selected off the guide chart as shown in Fig. 1.16. Fig. 1.17 shows how the different materials are compared for power loss versus saturation flux density. Here, the ideal material has the lowest power loss and highest saturation flux density. However, this is a high-level material selection method as variations of power loss with frequency, and saturation flux density with temperature etc, are not considered. A novel method of comparing magnetic materials over a wide range of frequencies, ripple ratios and power levels is now described in Chapter 2 for a boost converter topology.

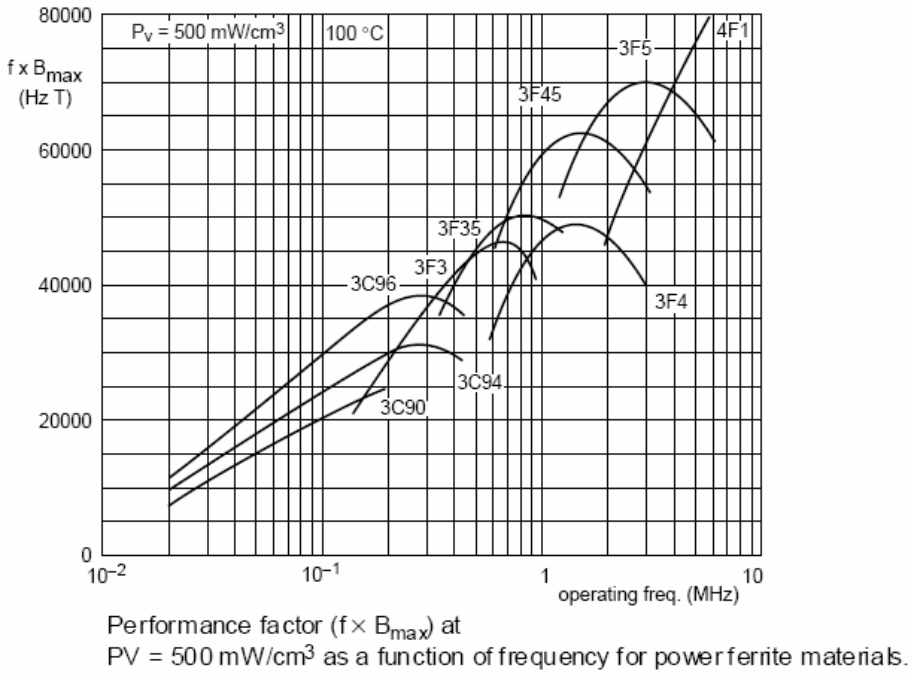

Figure 1.16: Ferrite material comparison method for a fixed power density.

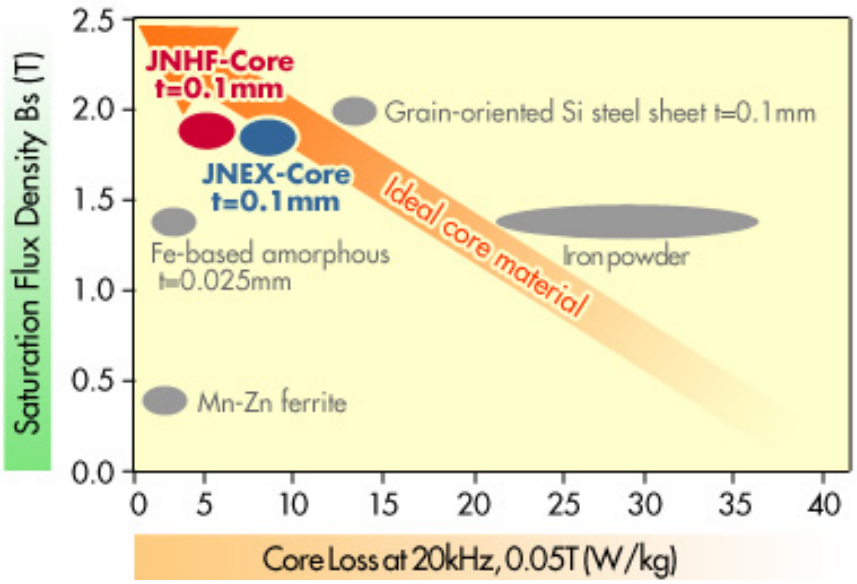

Figure 1.17: JFE Steel material comparison method of power loss vs. saturation flux density.

Chapter 2

Magnetic Material Comparisons for High-Current Inductors in Low-Medium Frequency DC-DC Converters

In this chapter, iron-based amorphous metal, 6.5 % silicon steel, nanocrystaline, and low-frequency ferrite materials are analysed and investigated for use in a gapped CC-core inductor. A novel inductor-design algorithm is developed and automated in order to compare and contrast the various magnetic materials over a range of frequencies and ripple ratios. The algorithm is developed for foil-wound inductors with gapped CC-cores in the low (10 kHz) to medium (30 kHz) frequency range. The algorithm considers the following factors: winding skin and layer effects; distance from airgap to minimize copper fringing loss; core loss and gap loss; creepage and clearance. As expected, inductor size for a given inductance decreases with increased frequency. Inductor size, however, can increase in the laminated materials due to increased air gap core loss effects.

2.1 Introduction

The low component count, high full-load efficiency, and simplicity of hard-switched dc-dc converters in the low-to-medium frequency range lead to a low-cost and low weight/volume solution for high-power dc-dc converters. There is a continuous demand for high-power-density magnetic designs in hard-switched dc-dc converters in the automotive, aerospace and stationary power generation industries. It is widely known that a compact and efficient magnetic design is critical to ensure that the overall weight and volume of hard-switched dc-dc converters is reduced [7]. As discussed in [5, 6] several design options have an effect on the size of the inductor, e.g. the number of stages and continuous versus discontinuous conduction. Choices of core dimensional ratios can also significantly reduce the size of the inductor [9] and further size reduction can be achieved by using improved cooling methods [10]. There are currently many magnetic materials available to the magnetic designer: Iron-based amorphous metal, 6.5 % silicon steel, nanocrystalline, ferrite, molypermalloy powder (MPP), high-flux, Kool Mu, iron powder, etc. [11, 12, 13, 14, 15, 16, 17, 18]. The correct choice of magnetic material is necessary to ensure high efficiency, minimum size and cost-effective inductor [19].

This chapter considers the selection of magnetic material for gapped CC-cores in the low (10 kHz) to medium (30 kHz) frequency range, and the effects of ripple ratio and air gap on the size of the inductor. The magnetic material characteristics are discussed in Section 2.2. The inductor-design algorithm presented in [40] is outlined in detail in Section 2.3. Theoretical results are presented and the effects of frequency and ripple ratio on the inductor size and losses are investigated in Section 3.7.

2.2 Magnetic Material Characteristics

The nominal specifications for the magnetic materials of interest in the low to medium frequency range for gapped CC cores are shown in Table 2.1 [11, 12, 13, 14, 15, 16, 17, 18]. In a joint publication with M. Rylko [41], serveral gap-less materials are compared and it is shown that gap-less materials can be competitive at frequencies greater than 20 kHz. However, the focus of this study is on gapped materials due to the limited core shapes of the gapless materials in high volume production. Toroidal cores are optimum for the gapless materials and help control stray fields and electromagnetic interference (EMI). There is also a considerable change in permeability with varying dc bias for the gapless materials. Gapless materials are additionally not recommended to be operated while in close or direct contact with electrically conductive surfaces, such as the metal surfaces of most common heat sinks. Flux lines stray near the surface of the core between distributed magnetic regions generating eddy currents in neighboring electrically conductive bodies [42]. Laminated cores do not exhibit this behavior and therefore are a good candidate for conductive cooling via an attached heat sink.

The 6.5% silicon steel material, 10JNHF600 from JFE, has the highest saturation flux density and thermal conductivity of 1.88 T and 18.6 W/mK, respectively [16]. The nominal operating temperature of 150 °C is similar to iron-based amorphous metal and is limited by the lamination epoxy, not by the material. It also has near-zero magnetostriction resulting in low audible noise. However, the silicon steel lamination has a greater thickness than that of iron-based amorphous metal and the nanocrystalline materials. This results in the silicon steel material having the highest nominal core loss of all the materials.

The iron-based amorphous metal material, 2605SA1 from Metglas, appears to

be a good compromise between saturation flux density, core loss and continuous operating temperature with a saturation flux density, B_{sat}, of 1.56 T, core loss of 43 W/kg (0.2 T, 20 kHz) and a continuous operating temperature of 150 °C [13]. The nominal iron-based amorphous metal material values for magnetostriction of 27 ppm and the thermal conductivity of 10 W/mK are not as good as for the 6.5% silicon steel material and limit the use of this material in the audible range ($<$ 16 kHz - 20 kHz).

The nanocrystalline material, Finemet FT-3H from Hitachi Metals [14], and the ferrite material, 3C92 from Ferroxcube [15], are low core-loss materials. These materials have lower saturation flux densities of 1.23 T and 0.4 T respectively and lower operating temperatures of 120 °C than both the 6.5% silicon steel and the iron-based amorphous materials. The nanocrystalline material likely has the best overall characteristics, but presently is significantly more expensive than the other materials. The cost of the nanocrystalline material increases further due to the manufacturing process required to cut the material.

The significant advantage of the ferrite 3C92 material is its high resistivity. Unlike the other materials, due to its bulk composition and high resistivity, ferrite does not suffer from additional eddy-current based core losses due to fringing of the air gap. These core losses vary with the size of the air gap and are caused by that magnetic flux which frings around the gap and re-enters the core in a direction of high loss as illustrated in Fig 2.1. As the air gap increases some of the fringing flux strikes the core perpendicular to the laminations and sets up eddy currents causing additional loss [11]. This means that for large ripple ratios, leading to an increase in gap size, the ferrite material core gap loss will not increase as it does for the other materials. This consideration is investigated in Section 3.7. Aging is not generally a factor in the selection of these materials.

Magnetic Material	Iron-based Amorphous	6.5% Silicon Steel	Nano-crystalline	Ferrite
Manufacturer	Metglas	JFE	Hitachi Metals	Ferroxcube
Material	2605SA1	10JNHF600	Finemet FT-3H	3C92
Bsat (T)	1.56	1.88	1.23	0.4
Rel. Permeability μr (0.1T, 10 kHz)	10,000	2000	$\approx$ 50000	1500
Curie Temp. (°C) (°C)	395	700	570	280
Continuous Operating Temp. (°C)	150*	150*	120*	120
Thermal Conductivity (W/mK)	10 #	18.6 #	$\approx$ 10	3.5-5
Specific Heat Capacity (J/°Ckg)	540	536	$\approx$ 540	700-800
Density (g/cm3)	7.19	7.53	7.3	4.8
Electrical Resistivity ($\mu\Omega$/m)	1.37	0.82	1.2	5x10^{6}
Lamination Thickness (mm)	0.025	0.1	0.018	Bulk
Core fill Factor	0.83	0.90	0.82	Bulk
Magnetostriction (ppm)	27	0.1	0	0.6
Core loss constant index: k	2.71	3.8	4.8x10^{-4}	16.3
Core loss frequency index: m	1.49	1.49	2.10	1.32
Core loss flux density index: n	1.94	1.63	1.79	3.28
Core Loss @ 0.2 T, 20 kHz (W/kg)	43	90	4	8
Relative Costs	$	$$	$$$$$	$

* Limited by lamination epoxy, # along lamination direction

Table 2.1: Magnetic material characteristics.

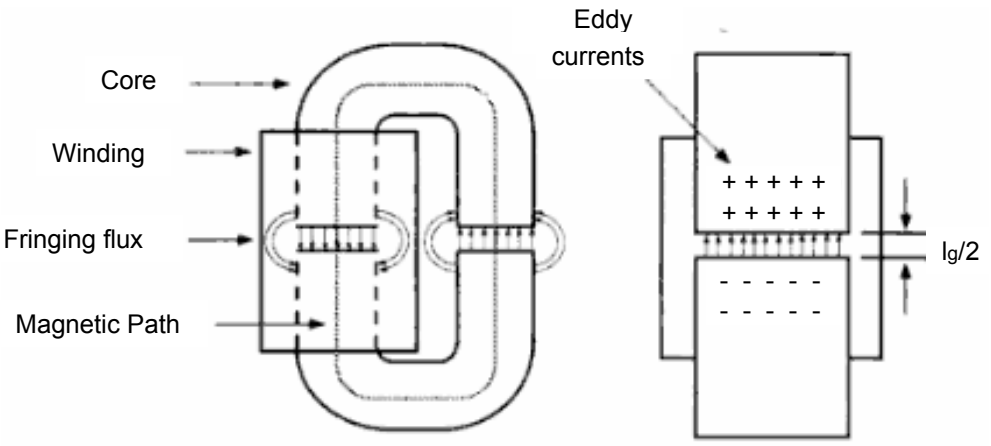

Figure 2.1: Eddy currents induced in the core due to airgap fringing flux.

2.3 Inductor Design Algorithm and Flowchart

Inductor design flowcharts typically involve the selection of a core size in an iterative design procedure [11, 12, 43, 44]. In this section, a novel inductor-design algorithm is presented for comparison of the various materials over a wide range of frequency and ripple. In order to focus the task and simplify the algorithm, the following assumptions are made:

(i) free-air cooling;

(ii) foil winding;

(iii) gapped CC core set;

(iv) a boost converter topology;

(v) a linear B-H curve.

The free-air cooling case is simplest to analyze and provides a very good insight into material selection.

Typically, a high-ripple converter design may lead the designer to either a foil or litz winding configuration due to the high eddy-current losses associated with a high-ripple converter. A low-ripple converter design may lead the designer to an edge-wound winding or to a simple spiral winding structure. In order to compare various magnetic materials and to simplify the analysis, this algorithm considers foil windings only. Helical and foil windings are later compared in Chapter 5.

For simplicity, the algorithm considers gapped CC cores only. The algorithm can be modified to consider EE gapped core sets and the various ungapped options [41].

The algorithm factors in the following design considerations:

(i) winding skin and layer effects;

(ii) distance from airgap to reduce copper fringing loss;

(iii) core loss;

(iv) gap loss;

(v) creepage and clearance.

As noted above, a significant loss component for the three laminated materials can be gap loss. As the air gap increases, fringing effects also increase with some flux striking the core perpendicular to the laminations resulting in an eddy current loss [11, 45]. This loss component is termed the gap loss. The nominal gap loss equation provided in [11] is used in this algorithm and is later investigated in Chapter 3.

The algorithm takes the relevant electrical, magnetic and thermal inputs and generates an area-product based on the greater value of the area-product calculated using the maximum flux density and that calculated using specific power.

The algorithm then generates a core size based on ranges of typical core ratios. Once core area is determined, the number of turns is calculated. The airgap length for energy storage is then calculated and adjusted for fringing flux. The winding is then moved a minimum distance away from the airgap to minimize copper fringing loss. A clearance is also provided between the core and the winding due to high voltage creepage. The ac copper loss effects are calculated using Dowell's method and the window length is adjusted to maintain the required current density. The core, gap, and copper losses of the inductor are then calculated. The core ratios are adjusted iteratively to ensure that the core-loss-to-core-plus-gap loss ratio, the core-plus-gap-loss-to-copper-loss ratio and the temperature rise of the inductor are not exceeded.

Fig. 2.2 shows the flow chart for a foil-winding configuration in a convection-cooling environment. The boxes in the area product flow chart are lettered to explain the design procedure. The various boxes are described as follows.

(A) In this section, the nominal electrical specifications for a boost converter are input: low-voltage input, V_I, high-voltage output, V_O, output power, P_O, efficiency, η, switching frequency, f, and the ratio of the peak-to-peak inductor current to the dc current, r.

(B) Using the electrical specifications for a boost converter input in (A), the following electrical outputs are determined: dc input current, I_I, peak-to-peak inductor current, ΔI_{pk-pk}, duty ratio, d, dc output current, I_O, boost inductance, L, inductor peak current, I_{pk}, and inductor rms current I_{rms}.

$$I_I = \frac{P_O}{\eta \cdot V_I} \ , \qquad \Delta I_{pk-pk} = r I_I \ , \qquad I_O = \frac{P_O}{V_O} \tag{2.1}$$

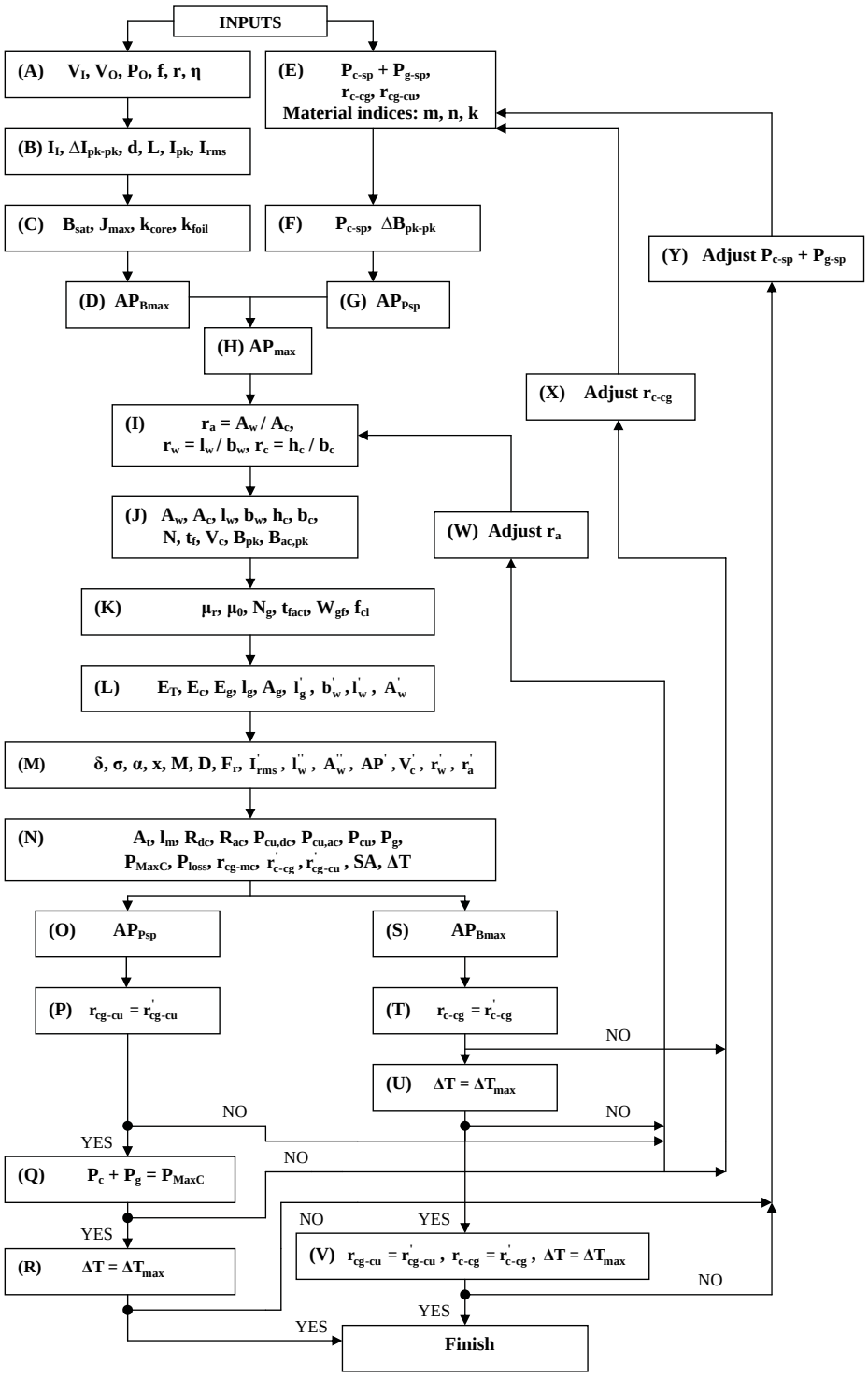

Figure 2.2: Area product flow chart.

$$d = 1 - \frac{V_I}{V_O}\,, \qquad L = \frac{V_I d}{f \Delta I_{pk-pk}} \tag{2.2}$$

$$I_{pk} = I_I + \frac{\Delta I_{pk-pk}}{2}\,, \qquad I_{rms} = \sqrt{I_I^2 + \left(\frac{\Delta I_{pk-pk}}{\sqrt{12}}\right)^2} \tag{2.3}$$

(C) The maximum flux density, B_{max}, foil current density, J_{max}, foil fill factor, k_{foil}, and core fill factor, k_{core}, are set. B_{max} is a derated value of the saturation flux density, B_{sat}, of the material (typically 80%). Note that k_{foil} only considers the foil copper insulation thickness relative to the foil thickness. The area required for winding voltage isolation from the core and winding distance from the core due to fringing are considered later in the procedure (K), at which point the standard window fill factor can be calculated.

(D) The area product, when limited by saturation flux density, termed AP_{Bmax}, is the product of the physical core area, A_c, calculated using B_{max} and the window area, A_w.

$$NA_c = \frac{LI_{pk}}{B_{max} k_{core}}\,, \qquad \frac{A_w}{N} = \frac{I_{rms}}{J_{max} k_{foil}} \tag{2.4}$$

$$AP_{B\,\max} = A_w A_c = \frac{LI_{pk} I_{rms}}{B_{max} J_{max} k_{foil} k_{core}} \tag{2.5}$$

(E) Next, the specific power loss in the core, P_{c-sp}+P_{g-sp}, is initially input, and is so termed because this input has two components: standard core loss and gap loss. Standard core loss, P_{c-sp}, is composed of hysteresis, eddy current and miscellaneous losses and is calculated per unit volume. Typically gap loss is estimated as a lumped figure but here, a figure for specific gap loss,

P_{g-sp}, is generated per unit volume. Two important specific power loss ratios are also defined. Firstly, we define the ratio of core loss to core-plus-gap loss, r_{c-cg}, in terms of the specific core loss, P_{c-sp}, and the specific gap loss, P_{g-sp}.

$$r_{c-cg} = \frac{P_{c-sp}}{P_{c-sp} + P_{g-sp}} \tag{2.6}$$

This ratio is dependent on the length of the air-gap which is unknown at this point. An iterative step later in the algorithm will adjust this ratio to ensure the core plus gap losses are not exceeded.

Secondly, we define the ratio of core-plus-gap loss to copper loss, r_{cg-cu}, in terms of the core loss, P_c, the gap loss, P_g, and the copper loss, P_{cu}. This ratio is nominally set at 1:1 for this study, although it is suggested in [45] that making core, gap, and copper losses equal can result in optimum efficiency for an inductor with significant gap losses.

$$r_{cg-cu} = \frac{P_c + P_g}{P_{cu}} \tag{2.7}$$

(F) The magnetic outputs of core specific-power loss, P_{c-sp}, and peak-to-peak magnetic flux swing, ΔB_{pk-pk}, are calculated based on the inputs in (E).

The equation for core-specific power loss, P_{c-sp}, describing hysteresis and eddy current losses is

$$P_{c-sp} = k\, f^m \left(\frac{\Delta B_{pk-pk}}{2} \right)^n \tag{2.8}$$

where k, m and n are the core specific-power loss indices and are illustrated in Table 2.1 for the materials of interest. Note that this equation does not consider the gap losses discussed earlier which are also induced in the core.

$$P_{c-sp} = r_{c-cg}\left(P_{c-sp} + P_{g-sp}\right) \tag{2.9}$$

$$\Delta B_{pk-pk} = 2\left(\frac{P_{c-sp}}{k}\right)^{\frac{1}{n}}\left(\frac{1}{f}\right)^{\frac{m}{n}} \tag{2.10}$$

(G) The area product when limited by specific power, AP_{Psp}, is the product of the physical core area, A_c, and the window area, A_w, and is determined using (C), (D), (E) and (F).

$$NA_c = \frac{V_I d}{f\Delta B_{pk-pk} k_{core}} \tag{2.11}$$

$$AP_{Psp} = A_w A_c = \frac{I_{rms} d V_I}{k_{core} k_{foil} J_{\max} f \Delta B_{pk-pk}} \tag{2.12}$$

(H) The maximum area product, AP_{max}, is now selected based on the greater of the area product defined by maximum flux density, AP_{Bmax}, given by (D), and the area product defined by maximum specific power, AP_{Psp}, given by (G).

(I) In this stage, the initial core aspect ratios are input and set. The area ratio is r_a, and is defined as the ratio of the window area, A_w, to the core area, A_c, and can range from 1 to 3 for standard core sizes [12, 13, 14, 15, 16]. An initial value is set but iteration later in the algorithm modifies this ratio to ensure the earlier design requirements in (E) are met. The window ratio is r_w, and is defined as the ratio of the initial length of the window, l_w, to the initial breadth of the window, b_w. This ratio is also set and typically ranges from 1.5 to 5 [9]. The same iterative step determines the final values of l_w and b_w. The core ratio is r_c, and is defined as the ratio of the actual

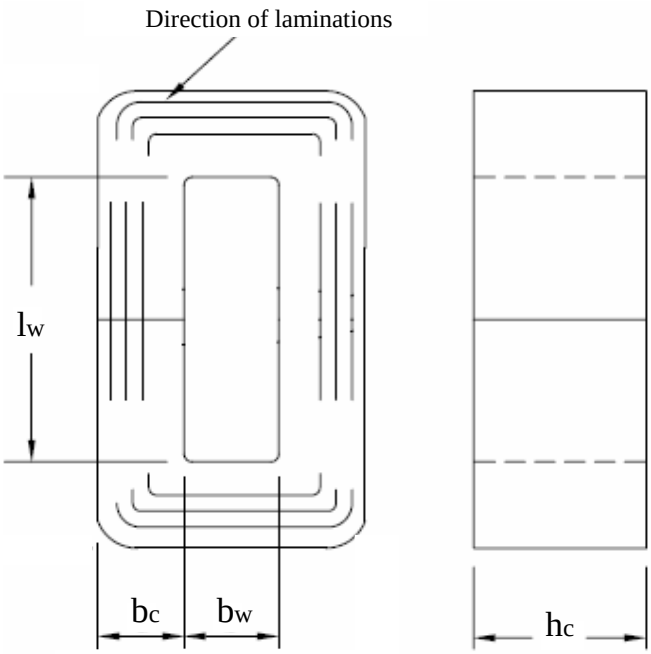

Figure 2.3: Drawing of core dimensions.

height of the core, h_c, to the breadth of the core, b_c. This ratio is set at this point and can range from 1 to 2.5 [12, 13, 14, 15, 16]. Fig. 2.3 illustrates the core dimensions.

$$r_a = \frac{A_w}{A_c}\,, \qquad r_w = \frac{l_w}{b_w}\,, \qquad r_c = \frac{h_c}{b_c} \tag{2.13}$$

(J) The initial core physical dimensions of window area, A_w, core area, A_c, window length, l_w, window breadth, b_w, core height, h_c, core breadth, b_c, number of turns, N, foil thickness, t_f, and initial core physical volume, V_c, are now calculated.

$$A_w = \sqrt{r_a A P_{max}}\,, \qquad A_c = \frac{A_w}{r_a} \tag{2.14}$$

$$l_w = \sqrt{r_w A_w}\ , \qquad b_w = \frac{A_w}{l_w} \tag{2.15}$$

$$h_c = \sqrt{r_c A_c}\ , \qquad b_c = \frac{A_c}{h_c} \tag{2.16}$$

$$N = \frac{k_{foil} J_{\max} A_w}{I_{rms}}\ , \qquad t_f = \frac{b_w k_{foil}}{N} \tag{2.17}$$

$$V_c = \left(2 b_c h_c l_w + 2 b_c h_c b_w + \pi b_c^2 h_c\right) \tag{2.18}$$

The peak flux density, B_{pk}, and the peak ac flux swing, $B_{ac,pk}$, are also calculated.

$$B_{pk} = \frac{L I_{pk}}{N A_c k_{core}}\ , \qquad B_{ac,pk} = \frac{L \Delta I_{pk-pk}}{2 N A_c k_{core}} \tag{2.19}$$

(K) The material relative permeability, μ_r, permeability of free space, μ_0, number of gaps per leg, N_g, actual specified foil thickness, $t_{f(act)}$, winding gap factor, W_{gf}, and foil clearance, f_{cl}, are now input. The actual foil thickness may increase or decrease the window length depending on the selected foil; a 0.5 mm thick foil is typically used in this study. The purpose of the winding gap factor is to push the foil away from the gap in order to reduce copper loss due to airgap fringing [46], and is defined as the number of airgap lengths that the foil is moved back from the airgap and so increases the breadth of the window. In this study, the factor is typically set at 2 and is investigated further in Sections 5.3.1 and 5.3.2. The foil clearance is to ensure that there is no creepage and so increases the length of the window. It is typically set at 4 mm in this study.

(L) The total energy stored in the inductor, E_T, the energy stored in the core, E_c, and the total airgap energy, E_g can now be calculated, in addition to estimating the airgap length required.

$$E_T = \frac{LI_{pk}^2}{2} \ , \qquad E_c = \frac{B_{pk}^2 V_c k_{core}}{2\mu_r \mu_0} \tag{2.20}$$

$$E_g = E_T - E_c \ , \qquad l_g = \frac{2E_g \mu_0}{A_c B_{pk}^2 N_g} \tag{2.21}$$

The airgap length is next adjusted to allow for fringing in the airgap. The fringing flux factor, F_f, accounts for the energy stored in the airgap due to fringing flux and is calculated using the equation in [11]. The initial airgap length, l_g, calculated above is revised to a corrected airgap length, $l_g^{'}$.

$$A_g = h_c b_c \ , \qquad l_g^{'} = l_g F_f = l_g (1 + \frac{l_g}{\sqrt{A_g}} \log \frac{2(l_w + l_g)}{l_g}) \tag{2.22}$$

The window breadth is similarly revised, $b_w^{'}$, from the earlier calculation to factor in the displacement of the foil away from the airgaps and the increase or decrease in foil thickness.

$$b_w^{'} = b_w + 2\, W_{gf}\, l_g^{'} - N \left(t_f - t_{f(act)} \right) \tag{2.23}$$

Finally, the window length is revised to $l_w^{'}$, as is the window area to $A_w^{'}$. The window length is increased to allow for clearance from the foil to the core at both ends of the foil and to decrease or increase the foil width in the window to correct for the adjustment to the foil thickness, above and maintain the required current density.

$$l_w^{'} = \left(\frac{t_f}{t_{f(act)}}\right) l_w + 2f_{cl} \ , \qquad A_w^{'} = l_w^{'} b_w^{'} \tag{2.24}$$

(M) In this stage Dowell's method is used to adjust the foil and core dimensions based on skin and layer effects. The ac copper losses due to the airgap are not considered in Dowell's method. In this design algorithm the ac copper losses due to the airgap are reduced by moving the winding away from the airgap.

Using the skin depth, δ, and the copper resistivity, σ, the ac copper loss effects are calculated [12, 47, 48]. Firstly, the skin depth, δ, is calculated based on the copper resistivity, σ, the permability, μ_0, and the switching frequency, *f*.

The porosity factor, α, is used in these modified Dowell equations because the length of the foil does not occupy the full length of the window [12]. Variables *x*, *M*, *D*, and F_r are then calculated.

$$\delta = \sqrt{\frac{\sigma}{f\pi\mu_0}} \ , \qquad \alpha = \frac{l_w^{'} - 2f_{cl}}{l_w^{'}} \ , \qquad x = \left(\frac{t_{fact}}{\delta}\right)\sqrt{\alpha} \tag{2.25}$$

$$M = x\left(\frac{e^{2x} - e^{-2x} + 2\sin(2x)}{e^{2x} + e^{-2x} - 2\cos(2x)}\right) \ , \quad D = 2x\left(\frac{e^{x} - e^{-x} - 2\sin(x)}{e^{x} + e^{-x} + 2\cos(x)}\right)$$

$$F_r = M + \frac{\left(\frac{N}{2} - 1\right) D}{3} \tag{2.26}$$

The inductor rms current, I_{rms}, is adjusted to a revised value, $I_{rms}^{'}$, to factor in the effects of skin and layers and allows a recalculation of the foil width to $l_w^{''}$ to meet the desired current density.

$$I_{rms}^{'} = \sqrt{I_I^2 + F_r \left(\frac{\Delta I_{pk-pk}}{\sqrt{12}} \right)^2} \ , \qquad l_w^{''} = \left(\frac{t_f I_{rms}^{'}}{t_{fact} I_{rms}} \right) l_w + 2 f_{cl} \tag{2.27}$$

Final values are now calculated for the revised window area, $A_w^{''}$, area product, $AP^{'}$, and core volume, $V_c^{'}$.

$$A_w^{''} = l_w^{''} b_w^{'} \ , \qquad AP^{'} = A_w^{''} A_c \tag{2.28}$$

$$V_c^{'} = \left(2 b_c h_c l_w^{''} + 2 b_c h_c b_w^{'} + \pi b_c^2 h_c \right) \tag{2.29}$$

The final window ratio, $r_w^{'}$, and core ratio, $r_a^{'}$, are also calculated.

$$r_w^{'} = \frac{l_w^{''}}{b_w^{'}} \ , \qquad r_a^{'} = \frac{A_w^{''}}{A_c} \tag{2.30}$$

(N) In this stage the various loss components, the loss ratios and the temperature rise of the inductor are calculated. Firstly, the dc resistance, R_{dc}, ac resistance, R_{ac}, dc copper loss, $P_{cu,dc}$, ac copper loss, $P_{cu,ac}$, and the revised total copper loss, P_{cu}, are calculated. The area of a single turn, A_t, and the mean turn length, l_m, are required for these calculations.

$$A_t = t_{f(act)} \left(l_w^{''} - 2 f_{cl} \right) \tag{2.31}$$

$$l_m = 2 \left(h_c + b_c + 4 W_{gf} l_g^{'} + \frac{N \, t_{fact}}{k_{foil}} \right) \tag{2.32}$$

$$R_{dc} = \frac{N \sigma l_m}{A_t} \ , \qquad R_{ac} = R_{dc} F_r \tag{2.33}$$

$$P_{cu,dc} = R_{dc} I_I^2 \ , \qquad P_{cu,ac} = R_{ac} \left(\frac{\Delta I_{pk-pk}}{\sqrt{12}} \right)^2 \tag{2.34}$$

$$P_{cu} = P_{cu,dc} + P_{cu,ac} \tag{2.35}$$

The gap loss, P_g, is now calculated in watts. This study uses the equation provided in [11], see also [45, 49].

$$P_g = k_i h_c N_g l_g^{'} f B_{ac,pk}^2 \qquad [W] \tag{2.36}$$

where k_i is a constant for laminated gapped CC cores (typically 0.0776 for a single-coil CC core and 0.0388 for a two-coil CC core), $l_g^{'}$ is the length of the airgap in cm, and h_c is the width of the lamination in cm. This estimation of gap loss will be revisited in Chapter 3.

The core loss, P_c, is now calculated, as is the maximum allowed core loss, P_{MaxC}. The maximum core loss is calculated from the initial value for the specific power loss allowed in the core, P_{c-sp}+P_{g-sp}, and the revised core volume, $V_c^{'}$. The total inductor power loss, P_{loss}, is also calculated.

$$P_c = k f^m B_{ac,pk}^n V_c k_{core} \ , \qquad P_{MaxC} = \left(P_{c-sp} + P_{g-sp} \right) V_c^{'} k_{core} \tag{2.37}$$

$$P_{loss} = P_c + P_g + P_{cu} \tag{2.38}$$

A new power loss ratio is now defined. We define the ratio of core-plus-gap loss to maximum-core loss, r_{cg-mc}, in terms of the core plus gap losses, $P_c + P_g$, and the maximum core loss, P_{MaxC}.

$$r_{cg-mc} = \frac{P_c + P_g}{P_{MaxC}} \tag{2.39}$$

The revised loss ratios of core-loss-to-core-plus-gap-loss, r'_{c-cg}, and of core-plus-gap-loss-to-copper-loss, r'_{cg-cu}, are also calculated.

$$r'_{c-cg} = \frac{P_c}{P_c + P_g}\,, \qquad r'_{cg-cu} = \frac{P_c + P_g}{P_{cu}} \tag{2.40}$$

The surface area, SA, available for cooling is calculated.

$$SA = 2\left(l''_w + 2b_c\right)\left(h_c + b'_w\right) + 2\left(b'_w + h_c\right)\left(b'_w + \left(b'_w + 2b_c\right)\right)$$

$$+2\left(l''_w + 2b_c\right)\left(b'_w + \left(b'_w + 2b_c\right)\right) \tag{2.41}$$

The temperature rise in the inductor, ΔT, can now be calculated for natural-convection cooling [12], where α_t is a constant and dependent on the core material. Typical values of 0.909 for the laminated materials [12] and 0.833 for ferrite [15] are used for α_t in this study.

$$\Delta T = \left(\frac{P_{loss}}{SA}\right)^{\alpha_t} \tag{2.42}$$

where the power loss, P_{loss}, is defined in mW and the surface area, SA, is defined in cm^2.

(O) The final inductor area product, AP', is selected if the inductor is limited by specific power, AP_{Psp}.

(P) In this stage, the designer has to ensure that the ratio of core-plus-gap loss to copper loss, r_{cg-cu} in (E) is equal to the revised value, r'_{cg-cu}, in (N). This

is done by adjusting the area ratio, r_a, increasing or decreasing the window size, as in iterative stage (W). This ensures a balance of core and copper losses.

(Q) The increase in core loss due to the air gap is now considered. If the core-plus-gap loss, $P_c + P_g$, is greater than the maximum core loss, P_{MaxC}, in (N) then the core loss, P_c, must be reduced by adjusting the ratio of core loss to core-plus-gap loss, r_{c-cg}, as in iterative stage (X).

(R) The temperature rise, ΔT, of the inductor is considered next. For an inductor limited by specific power, the temperature rise is dependent on the specific-power loss in the core, $P_{c-sp} + P_{g-sp}$. Adjusting this value in (E) and repeating the algorithm until the temperature rise equals the maximum temperature rise, $\Delta T = \Delta T_{max}$, will complete the design, as in iterative stage (Y).

(S) The final inductor area product, AP', is selected if the inductor is limited by saturation flux density, AP_{Bmax}.

(T) As the inductor is limited by saturation flux density, the core-plus-gap loss, $P_c + P_g$, will be less than the total copper loss, P_{cu}, for a given temperature rise, ΔT. To maximize the core-plus-gap loss, $P_c + P_g$, (i.e. distribute the total inductor losses) adjust the ratio of core loss to core-plus-gap loss, r_{c-cg}, as in iterative stage (X), until r_{c-cg} in (E) equals the revised value, r'_{c-cg}, in (N).

(U) The temperature rise is now considered. If the temperature rise, ΔT, is greater than the maximum temperature rise, ΔT_{max}, the area of the window must be increased. Adjust the area ratio, r_a, as in iterative stage (W), until $\Delta T = \Delta T_{max}$.

(V) As the inductor is limited by saturation flux density, the designer has to ensure that the ratio of core-plus-gap loss to copper loss, r_{cg-cu}, in (E), is equal to the revised value, r'_{cg-cu}, in (N) by adjusting the specific-power loss in the core, $P_{c-sp} + P_{g-sp}$, in (E), as in iterative stage (Y). By using the solver in Microsoft Office Excel a minimum AP_{Bmax} is calculated by adjusting $P_{c-sp} + P_{g-sp}$ in (E) with the following constraints: $r_{c-cg} = r'_{c-cg}$, ΔT=ΔT_{max}, and $r_{cg-cu} = r'_{cg-cu}$.

The above procedure is fully automated in Microsoft Office Excel using the goal seek function, macros and the solver. Excel is used due to its wide industrial availability.

2.4 Area Product Analysis for Magnetic Materials

In this section we investigate the variation of inductor sizes with (a) frequency for a constant inductance value, and (b) with ripple current for a constant frequency.

2.4.1 Constant Inductance, Variable Frequency Analysis

The above design procedure is used to analyse inductor designs for 1, 10 and 40 kW converters with inductances of 2 mH, 200 μH and 50 μH respectively. The four magnetic materials described in Table 2.1 are analysed for the same converter specifications with input voltage, V_I = 200 V and output voltage, V_O = 400 V. The switching frequency, *f*, is swept from 10 to 30 kHz in steps of 5 kHz. The inductance values of 2 mH, 200 μH and 50 μH are selected to ensure the ripple ratio, *r*, decreases from a maximum of 1 at 10 kHz to a minimum of

0.333 at 30 kHz.

The inductor specifications are: current density, $J_{max} = 6$ A/mm^2, foil fill factor, $k_{foil} = 0.75$, core fill factor, k_{core}, is selected from Table 2.1, maximum flux density, B_{max}, is de-rated by 80 % of the saturation flux density, B_{sat}, core ratio, $r_c = 2.2$, winding gap factor, $W_{gf} = 2$, number of gaps, $N_g = 2$, actual foil thickness, $t_{f(act)} = 0.5$ mm and foil cleareance, $f_{cl} = 2$ mm. The ambient temperature is set at $T_{amb} = 70$ °C. The maximum temperature rise, ΔT_{max}, allowed for each material is dependent on the continuous operating temperature of the material shown in Table 2.1, e.g. $\Delta T_{max} = 80$ °C for iron-based amorphous material (150 °C minus 70 °C), $\Delta T_{max} = 50$ °C for nanocrystalline, and $\Delta T_{max} = 30$ °C for ferrite.

Fig. 2.4 plots the area product vs. frequency for the 1 kW power level and the above inputs. The results are also illustrated in Table 2.2 where the results in bold illustrate when the inductor is limited by saturation flux density. The area-product decreases with increasing frequency for a given material temperature rise. As the frequency is increased the peak-to-peak ripple current, ΔI_{pk-pk}, and the peak-to-peak magnetic flux swing, ΔB_{pk-pk} are reduced. The loss in the core material is reduced as the core loss index for flux swing, n, in equation 2.8 is more dominant than the core loss index for frequency, m, as illustrated in Table 2.1. For a given temperature rise (dependent on total power loss) the inductor size decreases with increasing frequency in the low to medium frequency range.

Clearly, for the conditions given, the ferrite inductor is significantly larger than the other materials because all four materials are close to being limited by saturation flux density. For this curve set, the silicon steel is limited by saturation flux density between 25 kHz and 30 kHz and by specific power between 10 and 25 kHz. Thus, silicon steel is the smallest of the four at 25 and 30 kHz, while the amorphous metal and nanocrystalline are smaller at the lower frequencies due to

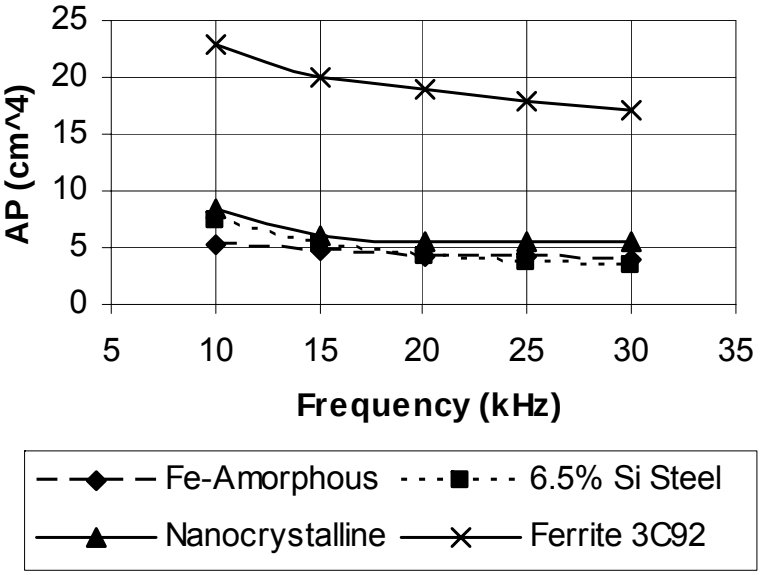

Figure 2.4: Inductor area product vs. frequency for constant inductance (1 kW).

r	**f (kHz)**	**Fe-Amorphous AP (cm^4)**	**6.5 % Si Steel AP (cm^4)**	**Nanocrystalline AP (cm^4)**	**3C92 AP (cm^4)**
1.0	10	**5**	7	**8**	**23**
0.667	15	**5**	5	**6**	**20**
0.5	20	**4**	4	**6**	**19**
0.4	25	**4**	**4**	**5**	**18**
0.333	30	**4**	**3**	**5**	**17**

Table 2.2: Inductor area product vs. frequency for constant inductance (1 kW).

the silicon steel becoming loss limited. The ferrite material is the largest inductor over the analysed frequency range. The low saturation flux density and the low allowed temperature rise results in the largest inductor. The inductor losses in the saturation limited designs are dominated by copper loss. The window is decreased to increase the copper loss (less copper) and this shrinks the overall inductor size.

Fig. 2.5 plots the area product vs. frequency for the 10 kW power level. The results are also illustrated in Table 2.3 where the results in bold illustrate when the

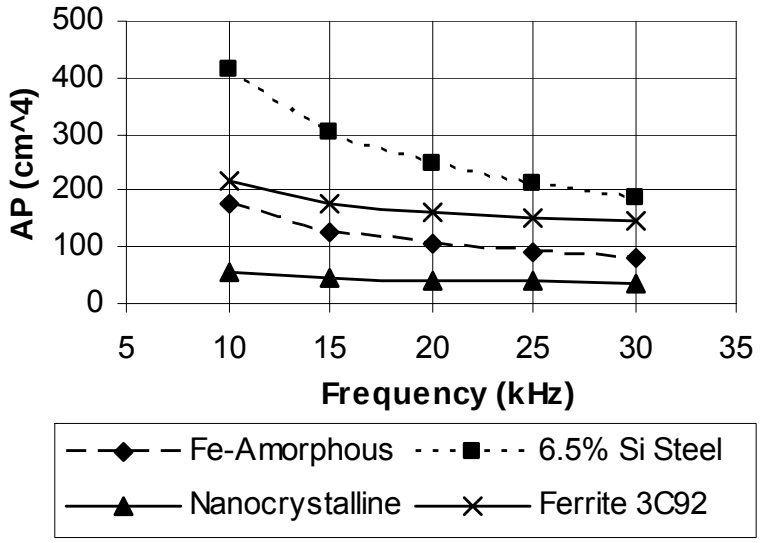

Figure 2.5: Inductor area product vs. frequency for constant inductance (10 kW).

inductor is limited by saturation flux density. Clearly, given the same constraints as in the 1 kW converter, as the power level increases, the higher loss materials such as the amorphous metal and silicon steel become specific-power limited resulting in a significant size increase. The ferrite and nanocrystalline materials remain saturation limited. The losses in these inductors are again dominated by copper losses, as the core materials are low loss materials. The silicon steel material is a high loss material resulting in a larger core for a given temperature rise. However, it is worth noting that silicon steel has the highest thermal conductivity. If a conductive cooling path is provided for the core, the performance of the silicon steel core will improve due to the higher thermal conductivity. This is investigated further in Section 3.5.

Fig. 2.6 plots the area product vs. frequency for the 40 kW power level. The results are also illustrated in Table 2.4 where the results in bold illustrate when the inductor is limited by saturation flux density. Here, the higher loss materials such as the amorphous metal and silicon steel are again limited by specific-power

r	f (kHz)	Fe-Amorphous AP (cm^4)	6.5 % Si Steel AP (cm^4)	Nanocrystalline AP (cm^4)	3C92 AP (cm^4)
1.0	10	175	415	**54**	**218**
0.667	15	128	303	**45**	**179**
0.5	20	104	246	**41**	**162**
0.4	25	90	210	**39**	**152**
0.333	30	81	185	**37**	**145**

Table 2.3: Inductor area product vs. frequency for constant inductance (10 kW).

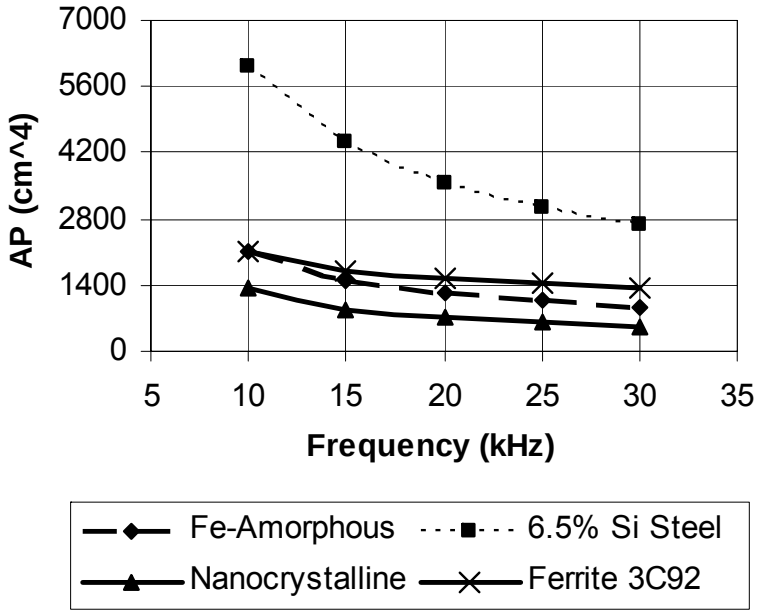

Figure 2.6: Inductor area product vs. frequency for constant inductance (40 kW).

where as the ferrite and nanocrystalline materials remain saturation limited. For the given converter constraints, the saturation limited ferrite inductor starts to become competitive with the specific-power limited iron-based amorphous metal inductor. The high ripple ratio and ac flux swing at low frequencies cause large core losses in the 6.5 % silicon steel material.

r	f (kHz)	Fe-Amorphous AP (cm^4)	6.5 % Si Steel AP (cm^4)	Nanocrystalline AP (cm^4)	3C92 AP (cm^4)
1.0	10	2087	6039	**1131**	**2132**
0.667	15	1507	4409	**887**	**1713**
0.5	20	1233	3565	**700**	**1525**
0.4	25	1065	3033	**604**	**1417**
0.333	30	950	2662	**520**	**1348**

Table 2.4: Inductor area product vs. frequency for constant inductance (40 kW).

2.4.2 Constant Frequency, Variable Ripple Analysis

In this section, the peak-to-peak ripple ratio is varied from very low, 0.125, to very high, 2. The boost converter and inductor specifications are as in the previous section, except that the frequency is set at 20 kHz. Fig. 2.7 shows the plot of area product vs. frequency for the 1 kW power level. In this plot, the inductance decreases from a high of 8 mH at a ripple ratio of 0.125 to 500 μH at a ripple ratio of 2.

When the inductor is limited by saturation flux density the area product decreases with increasing ripple ratio and constant frequency. As the inductance decreases with increase in ripple ratio, the peak current does not increase at the same rate of decrease of the inductance. This is due to the inductor dc current component of the peak current given by:

$$I_{pk} = I_{dc} + \frac{\Delta I_{pk-pk}}{2} \tag{2.43}$$

Therefore, the peak flux density, B_{pk}, decreases for an increasing ripple ratio, a given core size, and number of turns as given by:

$$B_{pk} = \frac{LI_{pk}}{NA_c k_{core}} \tag{2.44}$$

Thus, as B_{pk} decreases, the area product decreases.

When the inductors with laminated cores are limited by specific power, the inductor sizes increases with ripple due to the increase in gap losses with increase in gap lengths. As the ripple ratio increases the value of inductance decreases for a constant core size, i.e. a constant number of turns, N, flux swing, ΔB, core fill factor, k_{core}, and core cross-sectional area, A_c, as given by:

$$\Delta B_{p-p} = \frac{L\Delta I_{p-p}}{NA_c k_{core}} \tag{2.45}$$

As the ripple increases the length of the air gap also increases as follows:

$$l_g = A_g \left(\frac{\mu_0 N^2}{L} - \frac{l_m}{\mu_r A_c k_{core}} \right) \tag{2.46}$$

The gap core loss, due to airgap fringing is then given by:

$$P_g = k_i h_c l_g f \left(\frac{\Delta B_{p-p}}{2} \right)^2 \tag{2.47}$$

where k_i is a constant for laminated gapped CC cores (typically 0.0776 for a single-coil CC core and 0.0388 for a two-coil CC core), l_g is the length of the airgap in cm, and h_c is the width of the lamination in cm.

For a given temperature rise, the size of the inductor increases for an increase in power loss. This increase in power loss is due to the increase in ripple ratio and associated increase in gap length. Hence, a smaller value of inductance does not mean a smaller size inductor if the inductor is limited by specific power.

Fig. 2.7 plots the area product vs. ripple for the 1 kW power level and the above inputs. The results are also illustrated in Table 2.5 where the results in bold illustrate when the inductor is limited by saturation flux density. In Fig. 2.7 all the materials are initially limited by saturation flux density and the area products decrease. As the laminated materials become limited by specific power the area products starts to increase.

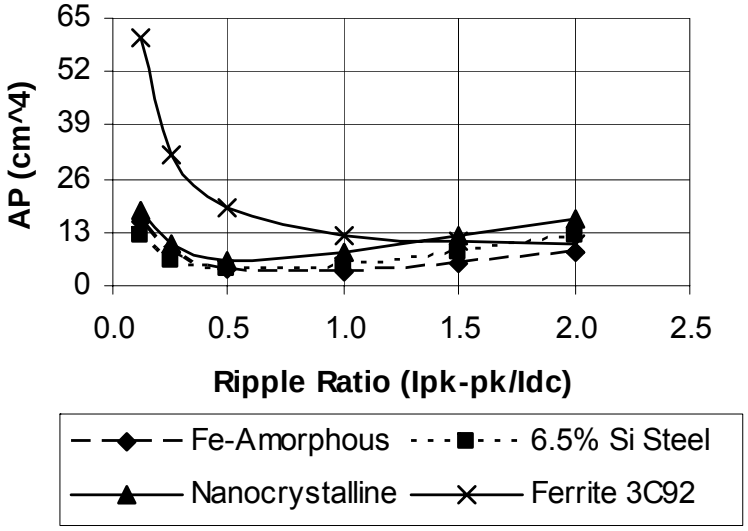

Figure 2.7: Inductor area product vs. ripple for constant frequency (1 kW).

r	**f (kHz)**	**Fe-Amorphous AP (cm^4)**	**6.5 % Si Steel AP (cm^4)**	**Nanocrystalline AP (cm^4)**	**3C92 AP (cm^4)**
0.125	20	**37**	**12**	**18**	**60**
0.25	20	**21**	**6**	**10**	**32**
0.5	20	**4**	**4**	**6**	**19**
1.0	20	3	5	8	**12**
1.5	20	5	8	12	**11**
2.0	20	8	12	16	**10**

Table 2.5: Inductor area product vs. ripple for constant frequency (1 kW).

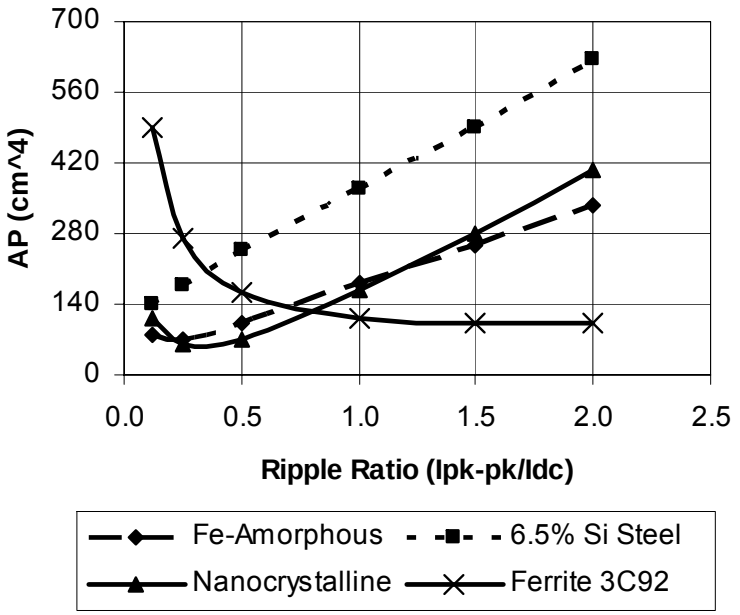

Figure 2.8: Inductor area product vs. ripple for constant frequency (10 kW).

Similar trends are seen for the 10 kW and 40 kW designs shown in Fig. 2.8 and Fig. 2.9 respectively, where the effects of gap loss become dominant at relatively low ripple ratios. At a ripple ratio of about 1.5, the ferrite material becomes limited by its specific power as illustrated in Fig. 2.9. Clearly, for the higher ripple, the ferrite can become competitive with the laminated materials operating at lower ripples. The ferrite material, because of its high resistivity, does not suffer from additional gap loss due to the fringing flux around the airgap. The high ripple ratio of 2 would also suit a soft switching topology such as a synchronous boost converter [50]. High-frequency (100 kHz) and high-ripple analysis is discussed in [41]. The effect of the gap loss is investigated further in Chapter 3.

r	f (kHz)	Fe-Amorphous AP (cm^4)	6.5 % Si Steel AP (cm^4)	Nanocrystalline AP (cm^4)	3C92 AP (cm^4)
0.125	20	**79**	138	**112**	**489**
0.25	20	70	176	**63**	**270**
0.5	20	104	246	71	**162**
1.0	20	180	369	167	**112**
1.5	20	257	491	282	**101**
2.0	20	338	625	404	**101**

Table 2.6: Inductor area product vs. ripple for constant frequency (10 kW).

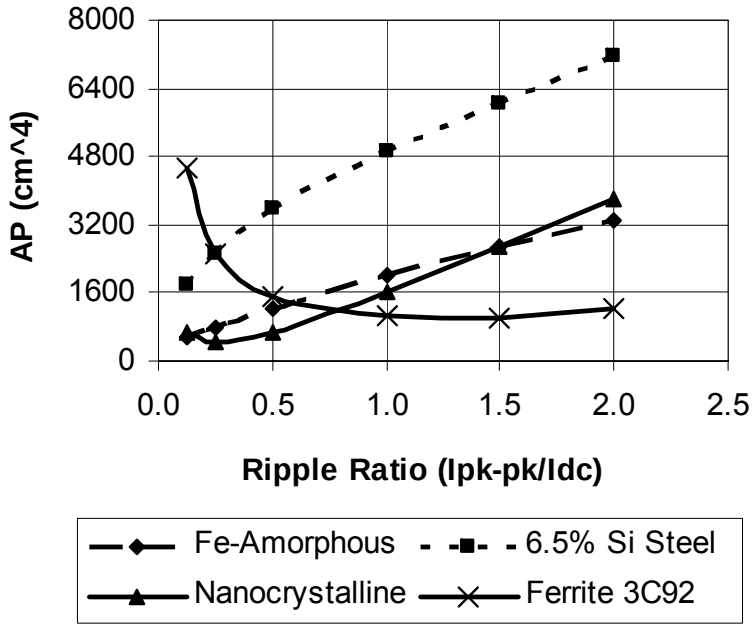

Figure 2.9: Inductor area product vs. ripple for constant frequency (40 kW).

r	f (kHz)	Fe-Amorphous AP (cm^4)	6.5 % Si Steel AP (cm^4)	Nanocrystalline AP (cm^4)	3C92 AP (cm^4)
0.125	20	**557**	1780	**691**	**4535**
0.25	20	777	2526	**473**	**2517**
0.5	20	1233	3565	691	**1525**
1.0	20	2019	4912	1624	**1085**
1.5	20	2686	6015	2702	**1025**
2.0	20	3317	7148	3823	1254

Table 2.7: Inductor area product vs. ripple for constant frequency (40 kW).

2.5 Summary

The correct choice of magnetic material can significantly reduce the size of the inductor in the low to medium frequency range. In this chapter, a novel area-product EXCEL-based program is developed for comparison of various materials over a wide range of frequency and ripple. The program factors in gap loss and foil layer effects, and generates a custom core for the various converter inputs. The algorithm is fully automated.

Theoretical results are shown for various design points. As expected, inductor size and loss decreases for increased frequency. However, inductor size and loss can increase in the laminated materials due to increased air-gap core loss effects. The ferrite material becomes competitive at high ripple ratios and can be considered in high-ripple converters. Experimental validation is presented in the next chapter.

Chapter 3

Experimental Investigation of Iron-based Amorphous Metal and 6.5 % Silicon Steel

Iron-based amorphous metal and 6.5 % silicon steel are competitive materials for high-power-density inductors in the low-to-medium-frequency range. In this chapter, the practical effects of frequency, ripple, air-gap fringing, and thermal configuration are experimentally investigated for these materials. Earlier work suggest that inductor size can increase in both of these laminated materials due to increased air-gap fringing losses. Experimental testing does not show airgap core losses to be as high as predicted by [11, 49] Distributing the air gap is demonstrated to reduce the inductor losses and size but has a practical limitation for iron-based amorphous metal cores due to core loss degradation with additional cuts. It is also demonstrated that a thermal configuration ensuring heat flow in the direction of the material lamination results in optimum cooling for conduction cooled inductors. A 2.5 kW converter is built to verify the optimum material selection and thermal configuration over the ranges of frequency and ripple. Experimental, analytical and simulation results are presented.

3.1 Introduction

Iron-based amorphous metal, 6.5 % silicon steel, nanocrystalline, and low-frequency ferrite have been investigated in [19, 40], and a novel area-product algorithm is derived to compare and contrast the various materials. Iron-based amorphous metal and 6.5 % silicon steel are cost and volume competitive for high-current, low-to-medium-frequency dc-dc converters. Table 2.1 in the previous Chapter contains the nominal specifications of interest to this chapter for iron-based amorphous metal of type 2605SA1 supplied by Metglas [13], and 6.5 % silicon steel of type 10JNHF600 supplied by JFE [16]. Note that for the purposes of this testing, the material upper temperatures are limited by the lamination epoxies. The materials, especially the silicon steel, can go higher in temperature if higher temperature lamination epoxies are used, eg. 180 °C.

This chapter investigates the experimental performances of iron-based amorphous metal and 6.5 % silicon steel for gapped CC-cores in the low (10 kHz) to medium (30 kHz) frequency range.

These laminated materials can have additional eddy-current core loss due to the airgap fringing flux [11, 49]. This airgap fringing core loss and the more well-known airgap copper loss can be reduced by distributing the airgap. Experimental results are presented demonstrating the beneficial effects of introducing distributed gaps into the core legs. However, there are practical limitations for iron-based amorphous metal cores due to observed degradation in the core loss of the material.

The experimental results also suggest that gap loss is not a significant consideration in these experiments. The losses predicted by the equation in [11, 49] are significantly higher at the low-to-medium frequencies of interest here (10 kHz to 30 kHz) than the experimental results would suggest. Based on these results, we

will neglect gap loss as a design factor in Chapter 4.

Conduction cooling, rather than convection, can result in the highest density inductor. The cooling for these laminated materials is very dependent on the direction of the lamination and the component mounting. Experimental results are produced showing the effects of lamination direction on the cooling path. A significant temperature reduction is observed compared to the natural convection cooling experimental results for the same test conditions.

The practical effects of frequency, ripple ratio, and air gap on the inductor size and losses are investigated in Section 3.2. The effect of distributing the inductor air gap is discussed in Section 3.3. Core thermal conductivity, lamination direction and inductor mounting techniques are investigated in Section 3.4. The gap loss and the effects of the manufacturing process on the iron-based amorphous metal core loss are investigated further in Section 3.5. Full experimental results for this Chapter are tabulated in Appendix C.

Note, the experimental testing in this Chapter is to characterize and analyze the magnetic materials rather than testing an optimized inductor.

3.2 Air-Cooled Experimental Analysis

In this section we investigate the experimental variation of inductor size with (a) varying frequency for a constant inductance value, (b) varying ripple for a constant frequency, and (c) varying load current for a constant frequency and ripple.

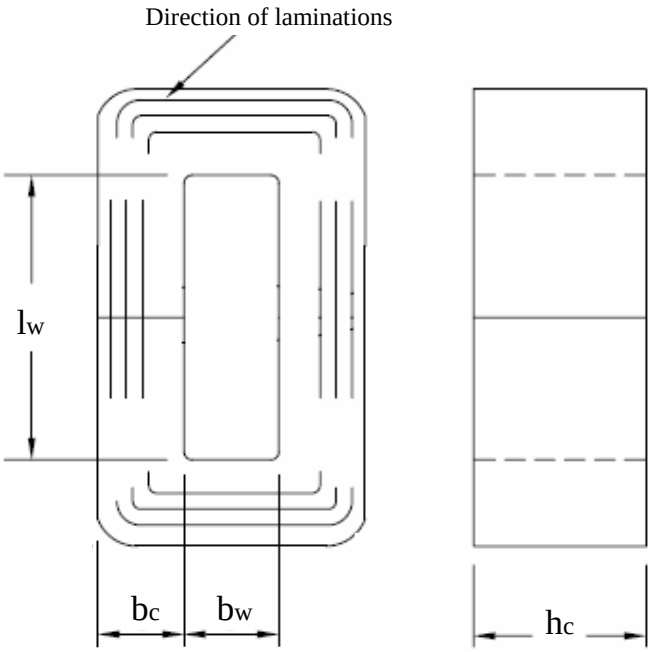

Figure 3.1: Drawing of core dimensions.

3.2.1 Constant Inductance, Variable Frequency

For the first test, two almost-identical custom inductors are designed to have an inductance of 125 μH. The iron-based amorphous metal and the 6.5 % silicon steel inductors are tested in a hard-switched boost converter. The input power is 2.5 kW and the input voltage of 125 V is boosted up to 250 V at the output. The window area, core area and mean-magnetic-path length are 720 mm^2, 500 mm^2 and 212 mm, respectively. A 0.3 mm thick foil winding with 11 turns on each core leg is used. The windings are connected in series giving a total of 22 turns. An aluminum-oxide thermal spacer (20 W/mK, 180 °C) with a length of 1 mm is inserted in each core leg. Natural convection cooling is used and the system is run until the inductor reaches a steady state temperature. Table 3.1 and Fig. 3.1 illustrate the inductor characteristics. Fig. 3.2 and Fig. 3.3 show the magnetic cores and the converter setup, respectively.

Figure 3.2: 6.5 % Si Steel (left) and iron-based amorphous (right) cores.

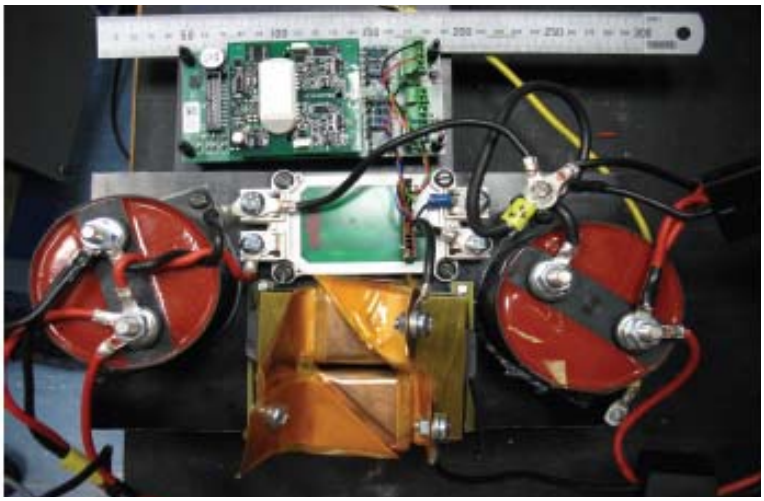

Figure 3.3: 2.5 kW, 125-250 V hard switched dc-dc converter setup.

L (μH)	**N**	$\mathbf{l}_g$**/leg** (mm)	$\mathbf{b}_c$ (mm)	$\mathbf{h}_c$ (mm)	$\mathbf{b}_w$ (mm)	$\mathbf{l}_w$ (mm)	$\mathbf{A}_c$ (cm^2)	$\mathbf{A}_w$ (cm^2)	**AP** (cm^4)	$\mathbf{M}_{idr}$ (kg)
125	22	1.00	25	20	20	37	5	7.4	37	0.838

Table 3.1: Custom inductor characteristics.

Material	**f** (kHz)	$\mathbf{P}_{core}$ (W)	$\mathbf{P}_{g}$ (W)	$\mathbf{P}_{cu}$ (W)	$\mathbf{P}_{tot}$ (W)	ΔT_{th} (°C)	ΔT_{expt} (°C)
2605SA1	15	18	12	4	34	75	113
2605SA1	20	16	9	4	29	64	100
2605SA1	25	14	7	4	25	57	89
2605SA1	30	13	6	4	23	52	80
10JNHF600	15	42	15	4	61	122	114
10JNHF600	20	40	11	4	55	112	102
10JNHF600	25	39	9	4	52	106	94
10JNHF600	30	38	7.5	4	49.5	100	87

Table 3.2: Table of losses and temperature rise for constant inductance.

Fig. 3.4 shows the core temperature rise above ambient for the iron-based amorphous metal and the 6.5 % silicon steel as the frequency is increased from 15 kHz to 30 kHz in steps of 5 kHz. Fig. 3.4 and Table 3.2 show that the theoretical power losses and the measured and theoretical temperature rises of the cores decrease with increasing frequency. Full experimental results for Fig. 3.4 are tabulated in Appendix C, Table C.1. The theoretical predictions are generated by the algorithm developed in [40]. As the frequency is increased the peak-to-peak current is reducing the flux swing, and the hysteresis loss in the core. The experimental results suggest that the iron-based amorphous metal and the silicon steel materials have comparable performance over the frequency range of interest for a natural convection cooling environment. The nominal core loss values supplied by the manufacturers suggest that silicon steel should run hotter due to its higher core loss.

There is a large deviation between the measured and theoretical core loss for the iron-based amorphous metal. Three core samples of each material were tested and the experimental results are comparable for all three core sample sets. Fig. 3.5 shows the temperatures for a single test point, (30 kHz, 1 mm gap per leg), for the 3 core samples. The experimental results are presented in Appendix C, Table C.2. It is seen that the experimental results for both materials are within

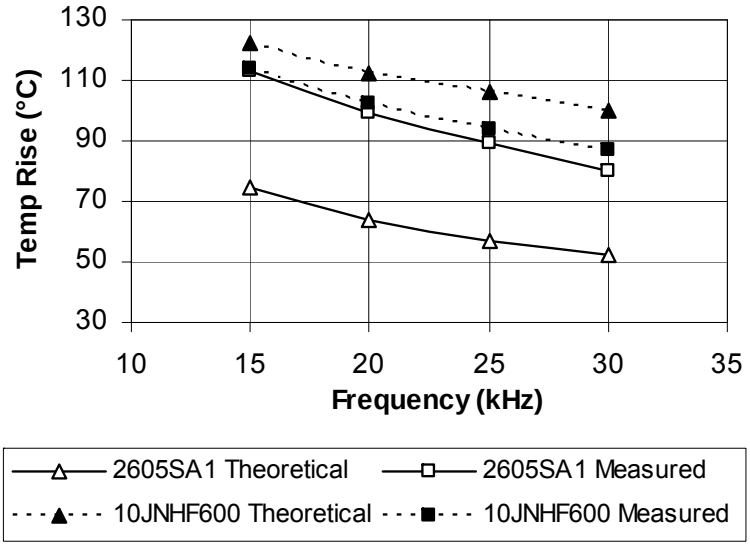

Figure 3.4: Inductor temperature rise for constant inductance.

several degrees Celsius of each other. A possible reason for the divergence between the theoretical and experimental results is provided in [51] where the effects of the manufacturing process are shown to degrade the iron-based amorphous metal core loss by 68 %. These cores have three cuts per leg possibly resulting in increased core loss. This is investigated further in Section 3.6 where a similar, single cut iron-based amorphous metal core is tested with the same frequency, f, and flux swing, ΔB_{pk-pk}.

The theoretical temperature rise of the silicon steel inductor is also over estimated compared to the experimental results by approximately 10 %. This experimental error is acceptable given the variation of core loss across core samples and the variation of the core loss indices used by the designer.

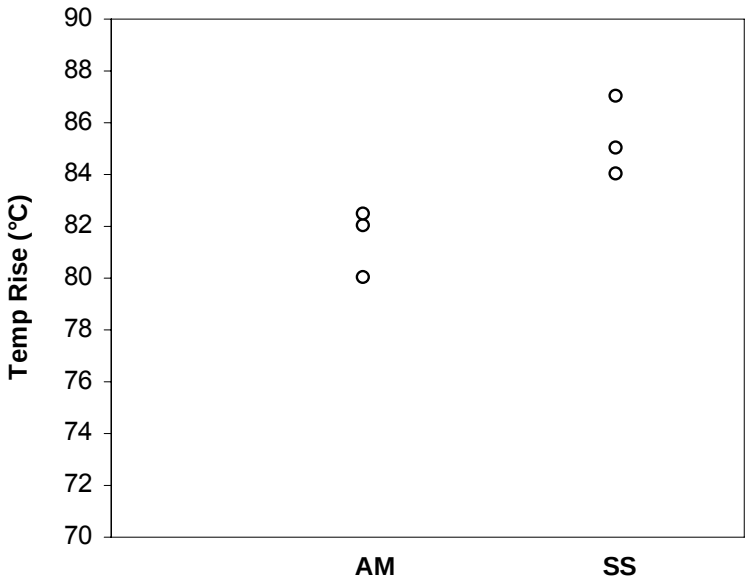

Figure 3.5: Temperatures for three sample cores at $f = 30$ kHz, $l_g = 1$mm.

3.2.2 Constant Frequency, Variable Ripple

For the second test the inductor ripple ratio is increased from low to high while the frequency is kept constant at 30 kHz. The inductance decreases as the ripple ratio is increased and the ac flux swing remains constant. For the same inductor cores with 22 turns, the length of the air gap is increased to change the ripple ratio. Table 3.3 and Fig. 3.6 show the rise in core temperatures in a natural-convection-cooled environment. Full experimental results are presented in Appendix C, Table C.3.

At large airgaps the theoretical temperature rise of the silicon steel inductor is significantly over estimated compared to the experimental results. Table 3.4 and Fig. 3.7 show the theoretical loss components for the silicon steel inductor as the gap length is increased. Here, due to the larger airgaps, finite element simulations are carried out to predict the ac copper loss due to the fringing flux. Note that the algorithm in [40] does not quantify the copper fringing loss, but

rather seeks to render it less significant by pushing the winding a certain distance away from the airgap.

Per the finite element analysis, the copper foil losses due to the fringing flux increase as the gap increases, from less than 3 W at 1 mm to more than 16 W at 3 mm. The ac copper losses increase mainly due to the large increase in the peak-to-peak inductor current, ΔI_{pk-pk}, from 11.2 A at 0.3 mm to 37.2 A at 3 mm. In Table 3.4, the ac resistance remains constant (R_{ac} = 93 mΩ) as the length of the airgap increases from 2 mm to 3 mm. However, the ac copper losses, $P_{cu,ac}$, increase from 8.9 W to 16.2 W due to the increase in the peak-to-peak inductor current, ΔI_{pk-pk}, from 27.6 A to 37.2 A. This effect is also illustrated in Fig. 7 in [52], where the ac resistance actually decreases as the ratio of the length of the airgap to the length of the window increases. This is due to a more even current distribution in the winding as the length of the airgap relative to the length of the window increases for large airgaps.

Table 3.4 also shows that the theoretical core gap loss, P_g, increases from 1.8 W to 18.1 W as the airgap length is increased from 0.3 mm to 3 mm. The design algorithm in [40] uses the equation in [11, 49] to calculate the gap loss. It is likely that this estimation of gap loss is inaccurate as this equation was developed from core data analyzed at 60 Hz. The accuracy of this equation is stated to be within $\pm$ 25 % at 60 Hz based on the analysis of the reported test data. The deviations were stated as being wider at 400 Hz [49]. The measured temperature rise of the inductor at 30 kHz does not increase at the theoretical rate calculated using the gap loss equation in [11, 49]. It is more likely that the increase in the measured inductor temperature is due to the increase in the copper foil losses caused by the fringing flux. Even though the airgap is increased from 1 mm to 3 mm, the measured temperature rise for the silicon steel inductor is only 14°C. The gap loss equation is investigated further in Section 3.6 where results are

l_g (mm)	$\Delta T_{AM,theoretical}$ (°C)	$\Delta T_{SS,theoretical}$ (°C)	$\Delta T_{AM,expt}$ (°C)	$\Delta T_{SS,expt}$ (°C)
0.300	44	94	77	105
0.625	51	100	71	79
1.000	56	105	80	87
2.000	81	129	88	89
3.000	107	153	98	101

Table 3.3: Core temperatures rise vs. gap length for constant frequency (30 kHz).

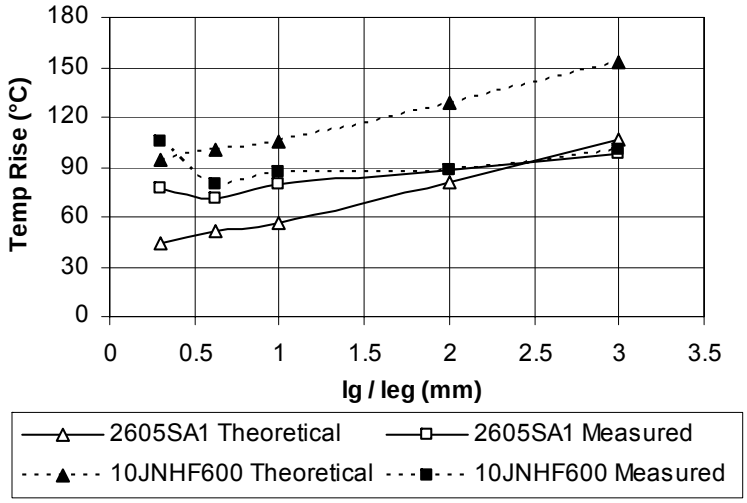

Figure 3.6: Core temperature rise vs. gap length for constant frequency (30 kHz).

obtained suggesting that gap loss can be neglected in this investigation.

At large airgaps the theoretical values here correlate better for the iron-based amorphous metal than previously seen in Fig. 3.4 with a 1 mm gap per leg. It can be shown that if the gap loss was neglected then the theoretical temperature rise of the iron-based amorphous metal would be significantly lower than the measured temperature rise. The high temperature rise of the iron-based amorphous metal core in Fig. 3.6 is due to the increased core losses caused by the manufacturing process of the multi-cut core and not the core gap losses as suggested by equation (1) in [49]. This is discussed further in Section 3.6 where the gap loss equation is not used and a single-cut core is tested under the same experimental

$\mathbf{l}_g$ (mm)	$\Delta\mathbf{I}_{pk-pk}$ (A)	$\mathbf{I}_{rms}$ (A)	$\mathbf{R}_{ac}$ (mΩ)	$\mathbf{P}_{cu,ac}$ (W)	$\mathbf{P}_{cu,dc}$ (W)	$\mathbf{P}_c$ (W)	$\mathbf{P}_g$ (W)	$\mathbf{P}_{tot}$ (W)
0.300	11.2	4.0	66.4	1.04	3.2	38	2.25	44.49
0.625	14.4	5.1	83.3	2.16	3.2	38	4.75	48.11
1.000	16.4	5.8	75.0	2.52	3.2	38	7.6	51.32
2.000	27.6	9.8	93.5	8.9	3.2	38	15	65.2
3.000	37.2	13.2	93.7	16.21	3.2	38	23	80.51

Table 3.4: Silicon steel loss components vs. gap length for constant frequency (30 kHz).

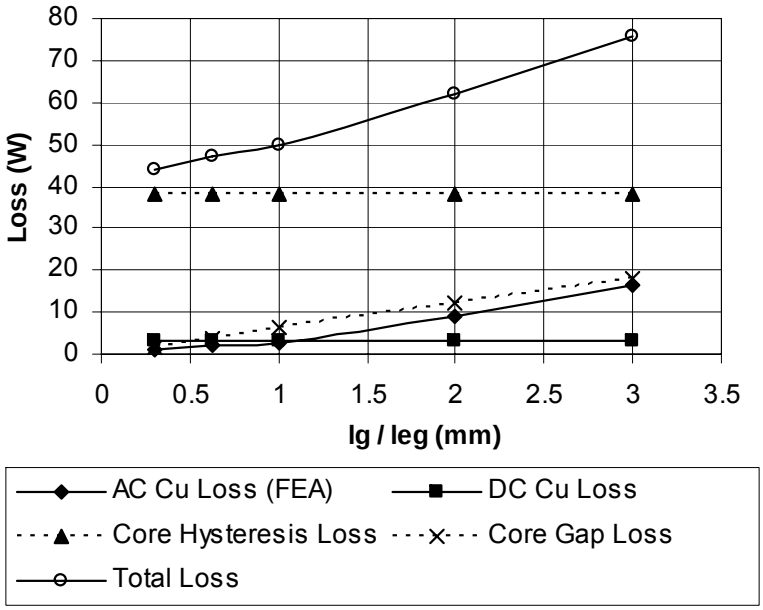

Figure 3.7: Silicon steel loss components vs. gap length for constant frequency (30 kHz).

conditions.

Fig. 3.6 also shows that for a small airgap (low ripple ratios) the silicon steel and the iron-based amorphous materials have a relatively high loss. This is likely due to dc bias current effects as shown by the inflection of the curves for both the iron-based amorphous metal and the 6.5 % silicon steel at an airgap length of 0.3 mm [53, 54, 55]. The average relative permeability, μ_r, for this set of experimental tests is calculated at 345.7 and 308.1 for the iron-based amorphous metal and the 6.5 % silicon steel respectively. The relative permeability, μ_r, for each test is illustrated in Table C.3. For both materials, the cores overheated when there was no airgap in the core legs and the relative permeability dropped significantly. This zero gap effect is investigated further in Fig. 3.8 for varying load current.

3.2.3 Constant Frequency, Variable Load

For the third test set, the effect of varying the load current is analyzed with, and without, an airgap. The frequency is kept constant at 30 kHz and the load current is reduced from 100 % (10 A) to 50 % (5 A). The same boost ratio as above is maintained keeping the peak-to-peak ripple current constant. Airgaps of 1 mm and 0 mm per leg are tested for both core materials. Experimental measurements are presented in Appendix C, Table C.4.

Fig. 3.8 shows that the effect of varying the load current on the core temperature is minimal when an airgap length of 1 mm per leg is maintained. The slight increase in temperature as the load current is increased is likely due to the distribution of heat from the copper to the core rather than increased core losses. Even though the 0 mm airgap scenario is not realistic as most inductors are designed with airgaps, it is necessary to investigate in this case as an central

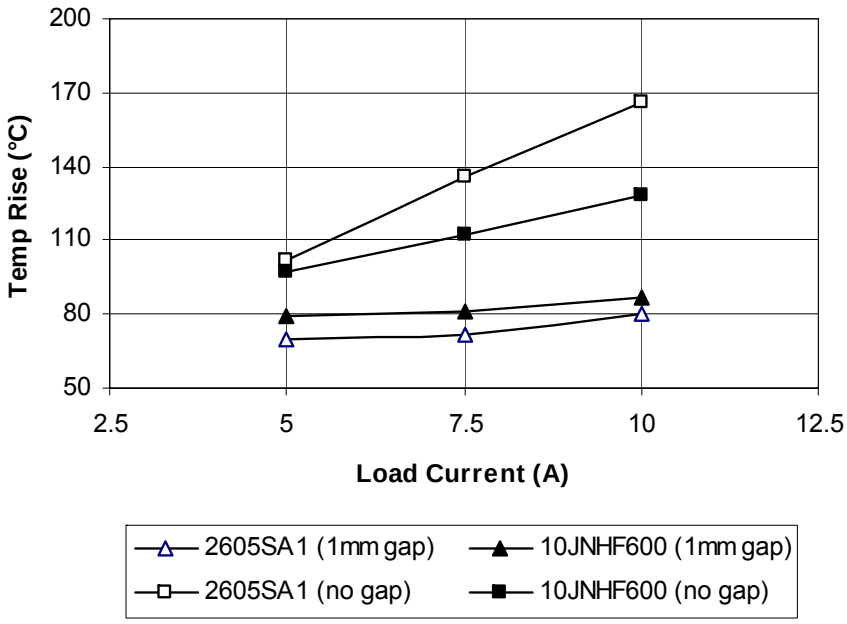

Figure 3.8: Core temperature rise for varying load current.

objective of this work is to operate high on the magnetization curve.

Fig. 3.9 and Fig. 3.10 plot the magnetization curves of the materials at 25 °C and the magnetic circuit load lines along the minimum magnetic path length of the inductors. The intersection of load line and magnetization curve represents the operating point of the material. The core losses increase as the magnetic circuit load lines are pushed further up the magnetization curve [53, 54, 55]. The specified saturation flux density of the iron-based amorphous metal is 1.56 T. Information is not available showing the variation of the magnetization curves with temperature. The results of Fig. 3.6 suggest that both materials are performing well thermally at 0.3 mm. The load lines suggest that the iron-based amorphous metal core loss is as predicted up until about 1.2 T, the plot intersection at 0.3 mm, while the 6.5 % silicon steel is operating as predicted up until about 1 T.

Fig. 3.11 and Fig. 3.12 show that both materials are still operating above about 1.4 T even at 50 % load or 5 A and both materials are overheating at 50 %

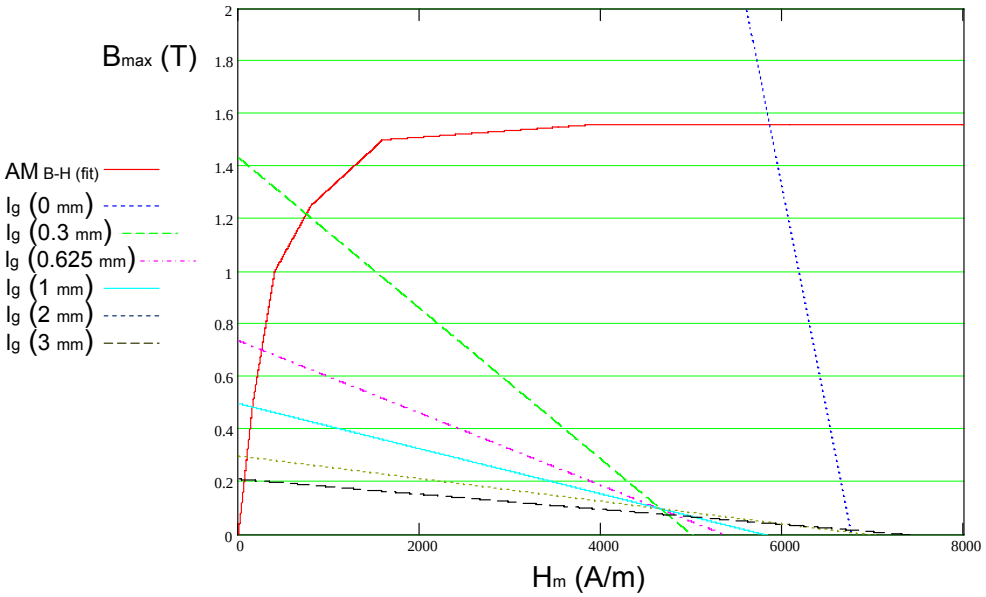

Figure 3.9: Fe-based amorphous metal B-H analysis for varying gap length.

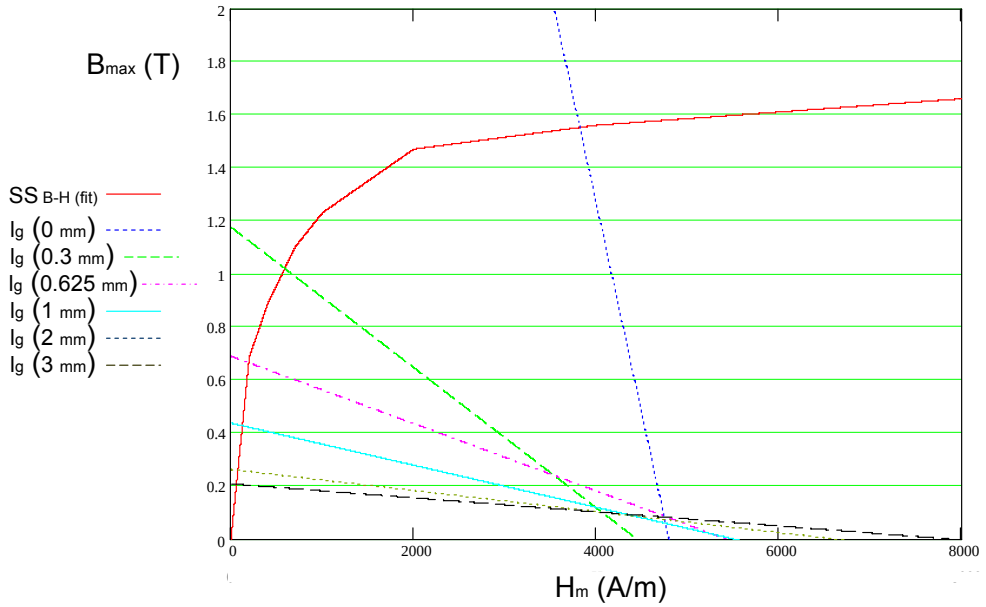

Figure 3.10: Silicon steel B-H analysis for varying gap length.

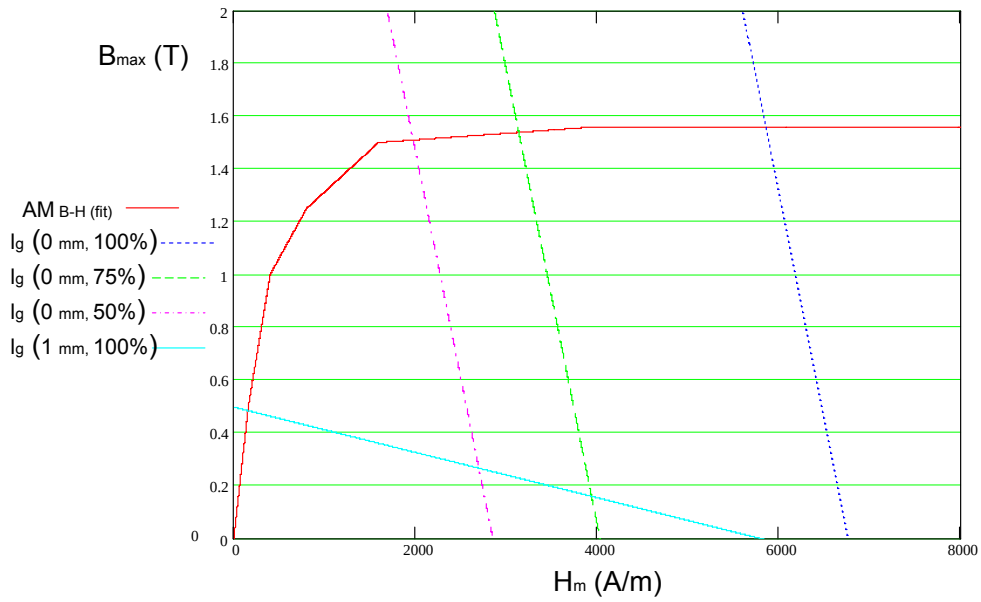

Figure 3.11: Fe-based amorphous metal B-H analysis for varying load current.

load. This suggests that at some flux density levels below 1.4 T, both materials begin to deviate from their published core losses as they go over the knee. Iron-based amorphous metal can easily saturate as it goes over the knee. The 6.5 % silicon steel has a higher nominal saturation flux density of 1.88 T and the results show it is not likely to saturate. However, because of the softer magnetization curve as it goes over the knee, the 6.5 % silicon steel losses are likely to increase at some level between 1 T and 1.4 T. As apples and apples comparisons are not available comparing the various materials, we will apply a general derating of 75 % (iron-based amorphous metal - 1.125 T, 6.5 % silicon steel - 1.36 T) for the various materials. Further investigation is required to establish correct deratings for the various materials.

As illustrated in Table C.4, the relative permeability, μ_r, drops significantly as the load current is increased. At 0 mm airgap, the relative permeability, μ_r, of the iron-based amorphous metal drops from 211.7 at 50 % load current to

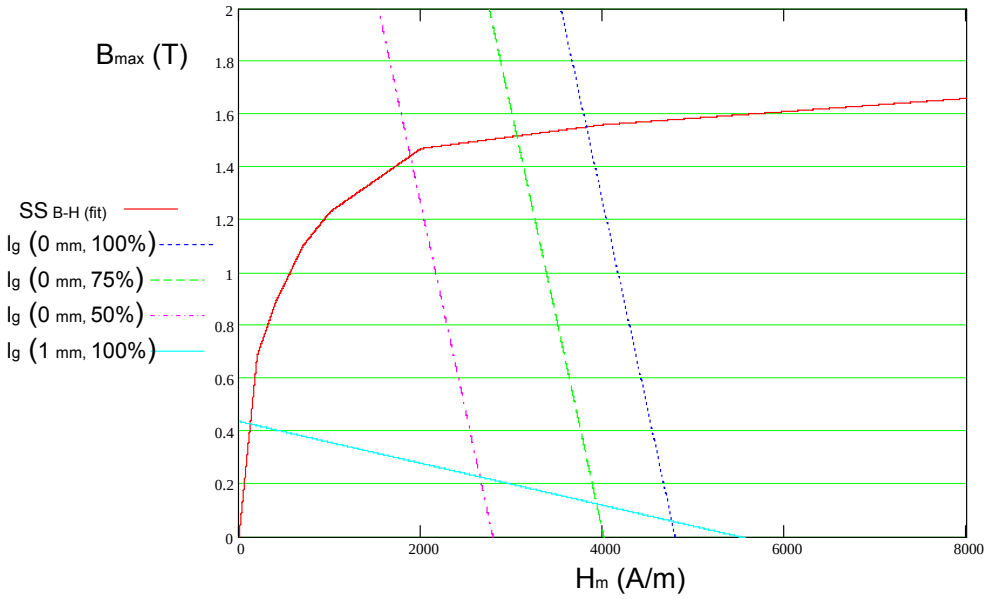

Figure 3.12: Silicon steel B-H analysis for varying load current.

76.1 at 100 % load current. The relative permeability, μ_r, of the 6.5 % silicon steel drops from 205.2 at 50 % load current to 141 at 100 % load current. The relative permeability, μ_r, of the iron-based amorphous metal, calculated from the magnetic circuit load lines, drops from 433 at 50 % load current to 102 at 100 % load current. The relative permeability, μ_r, of the 6.5 % silicon steel, calculated from the magnetic circuit load lines, drops from 445 at 50 % load current to 195 at 100 % load current. The experimental relative permeability is significantly lower than the predicted relative permeability and is likely due to temperature variations and high-frequency effects. This needs further investigation.

Fig. 3.13 shows the effect of dc bias current on the inductances for airgaps of 0 and 1 mm per leg. The frequency is kept constant at 10 kHz and the dc bias current is increased from 0 to 20 A in steps of 2 A. The inductances are recorded using a HP 4284A precision LCR meter. As the dc current is increased the inductances remains constant at an airgap length of 1 mm per leg. However,

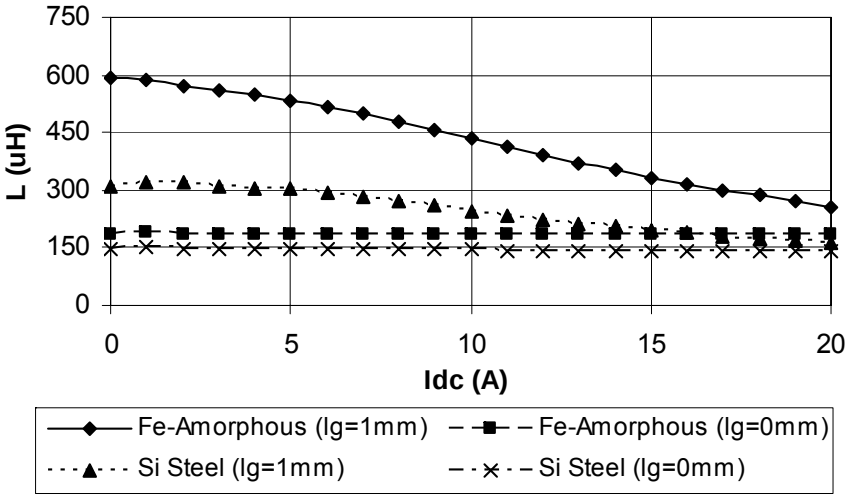

Figure 3.13: Inductance versus load current for 2605SA1 and 10JNHF600 (LCR meter).

the inductances drop significantly when a 0 mm airgap is used, illustrating core saturation.

For the next test set, the frequency is decreased from 30 kHz to 10 kHz in steps of 10 kHz and the λ-I loops and inductor current and voltage waveforms are recorded for gaps of 0 mm and 1 mm per leg. The dc current in the inductor is 20 A. It is clear from the temperature rises recorded and shown in Fig 3.8 that the core loss increases for a given flux swing as the cores are pushed up the magnetization curve toward saturation. At 30 kHz, as shown in Fig. 3.14 and Fig. 3.15 respectively, it appears that the iron-based amorphous metal core is just about going into saturation. There is a slight curve at the top of the λ-I loop and the inductor current is just beginning to lose its triangular characteristic on the down ward slope. As the frequency is decreased to 20 kHz and 10 kHz the inductor core goes further into saturation as shown by the λ-I loops and inductor current waveforms in Fig. 3.16 to Fig. 3.19. As the frequency is decreased the pk-pk current increases and the core is pushed into saturation. Fig. 3.20 and

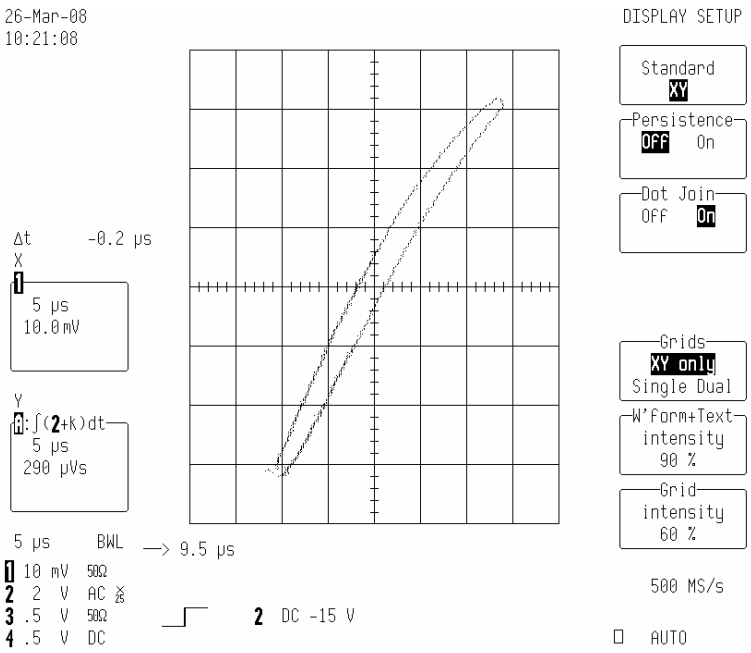

Figure 3.14: λ-I loop for 2605SA1 at 30 kHz, 0 mm gap.

Fig. 3.21 show that at 1 mm airgap the inductor does not saturate. The λ-I loop and core loss is reduced compared to Fig. 3.15 with a 0 mm gap and the inductor current waveform does not show any deformation. Further λ-I loops and inductor current and voltage waveforms are presented in Appendix C for the 6.5 % silicon steel material. The trends are similar but not as pronounced due to the higher saturation flux density of the silicon steel material.

3.3 Distributed Gap Effect

A method of reducing airgap fringing flux is to distribute the air gap into several smaller air gaps. Fig. 3.22 shows a finite element simulation for a single gapped inductor core. The fringing flux is significantly reduced by distributing a single large airgap into several smaller airgaps as illustrated in Fig. 3.23. Fig. 3.24 shows

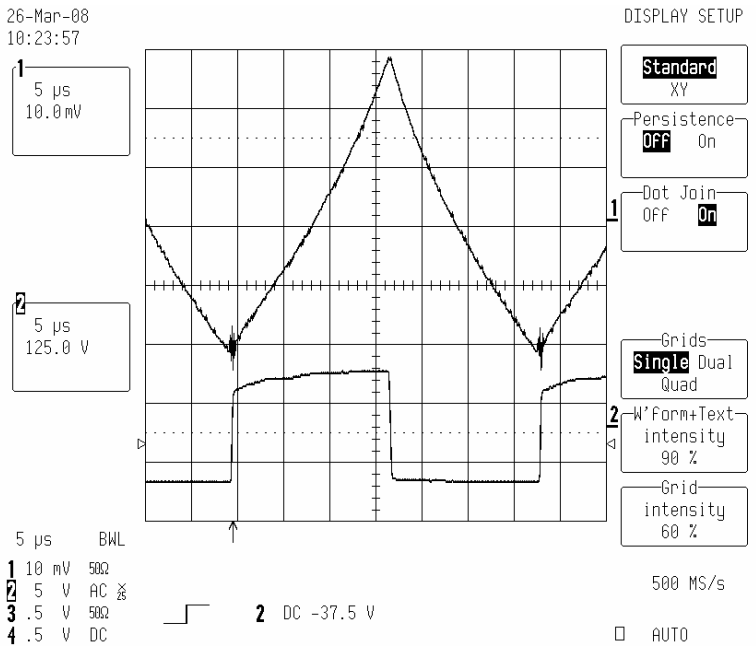

Figure 3.15: Inductor waveforms for 2605SA1 at 30 kHz, 0 mm gap.

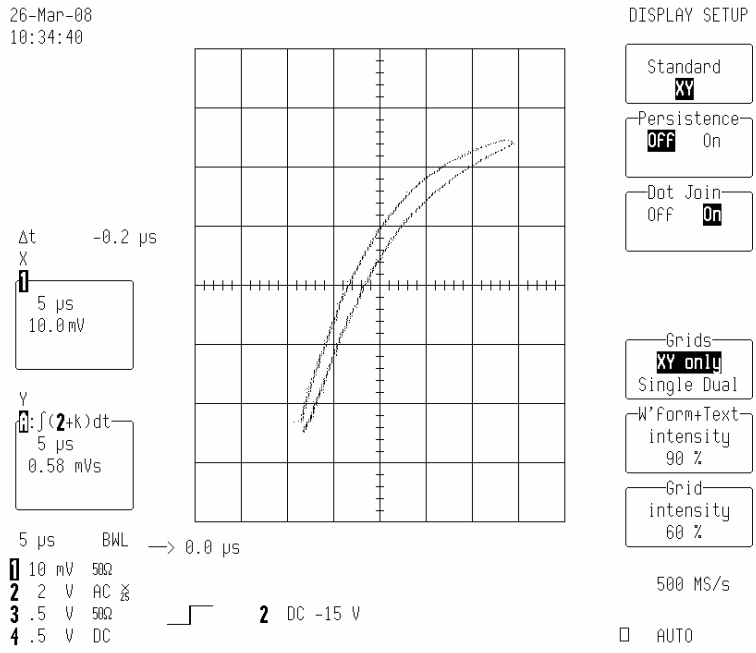

Figure 3.16: λ-I for 2605SA1 at 20 kHz, 0 mm gap.

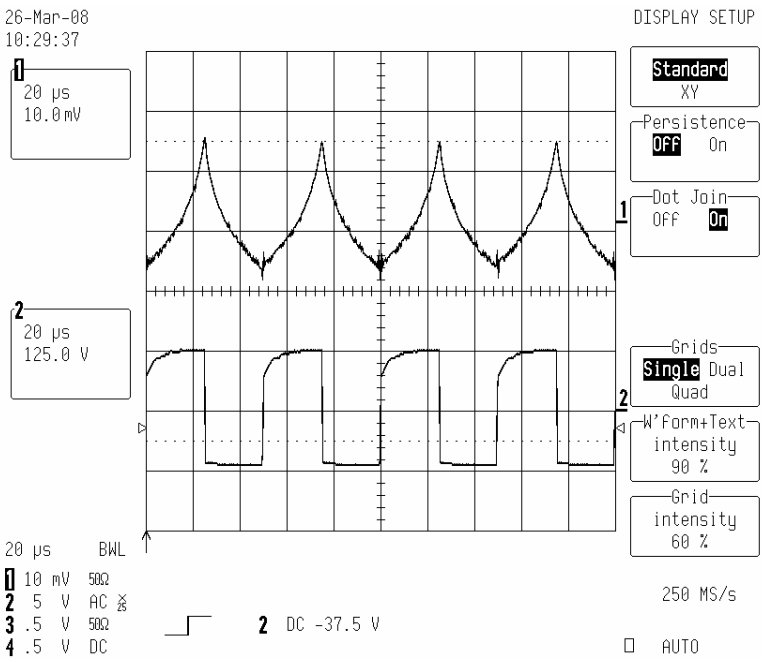

Figure 3.17: Inductor waveforms for 2605SA1 at 20 kHz, 0 mm gap.

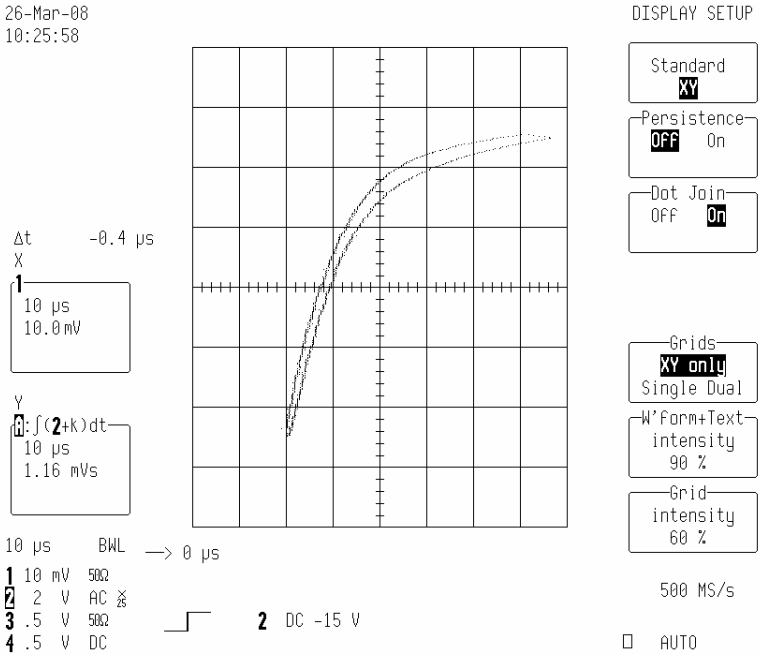

Figure 3.18: λ-I loop for 2605SA1 at 10 kHz, 0 mm gap.

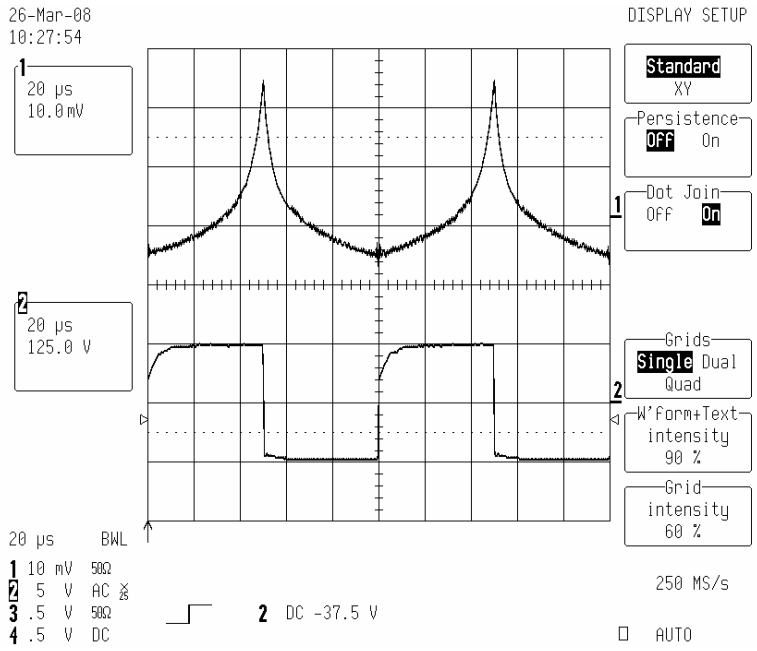

Figure 3.19: Inductor waveforms for 2605SA1 at 10 kHz, 0 mm gap.

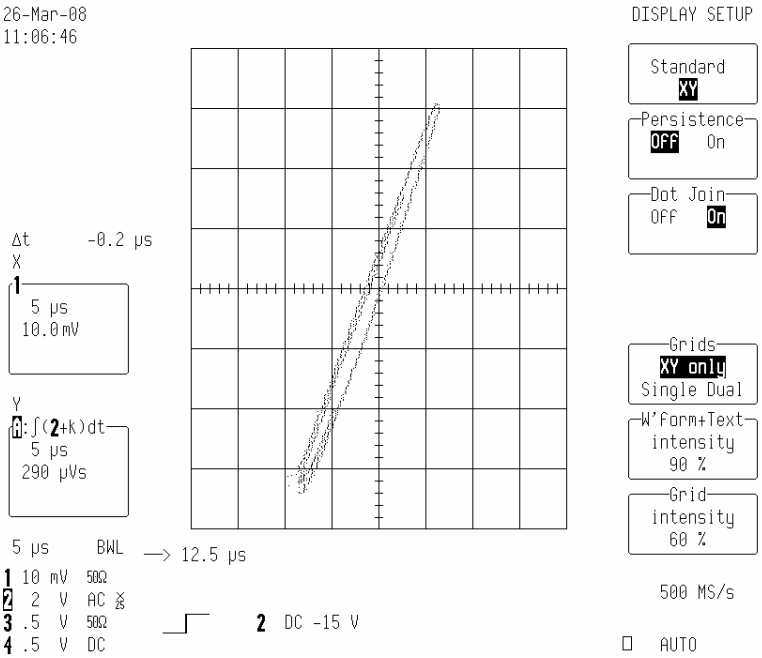

Figure 3.20: λ-I loop for 2605SA1 at 30 kHz, 1 mm gap.

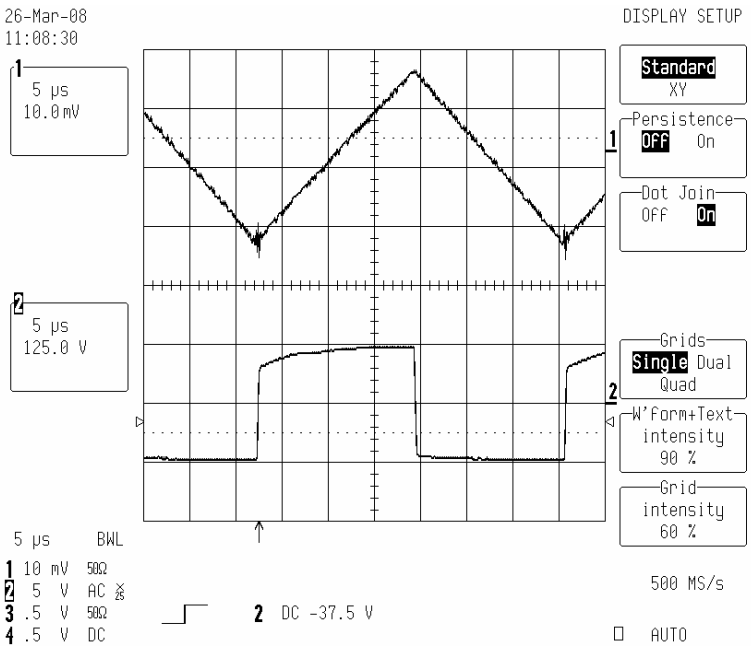

Figure 3.21: Inductor waveforms for 2605SA1 at 30 kHz, 1 mm gap.

finite element simulation results for the copper windings as a single 3 mm airgap is split into 2 gaps of 1.5 mm and 3 gaps of 1 mm respectively. The same inductor core size as above is used. As expected, the losses in the copper are decreased by distributing the airgap from approximately 16 W with a single 3 mm gap to approximately 4.5 W with three gaps of length 1 mm.

For the next experimental test, the effects of the distributed gap are investigated. These results are produced in Appendix C, Table C.5. The total gap length per leg is 2.625 mm and the frequency is kept constant at 30 kHz. The effects of splitting this single gap into two and three smaller gaps are separately tested. For the first test, a single gap of 2.625 mm is located in the centre of the leg for both the iron-based amorphous and the silicon steel cores. For the second test, there are two gaps in each leg with lengths of 1.625 mm and 1 mm respectively. The gaps are located at an equal distance from the core end sections

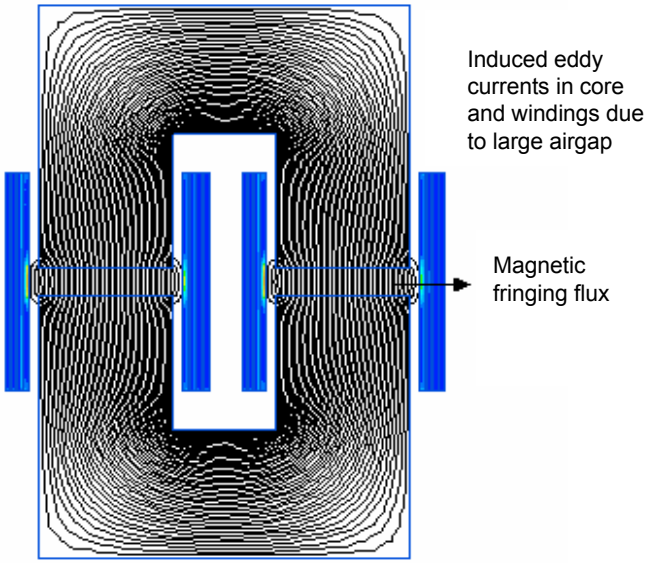

Figure 3.22: FEA of single inductor airgap (1 x 3 mm).

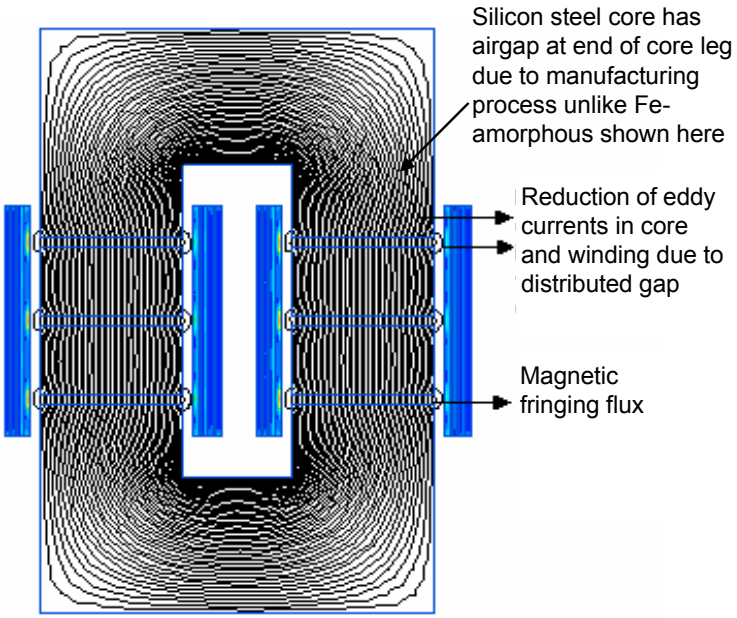

Figure 3.23: FEA of distributed inductor airgap (3 x 1 mm).

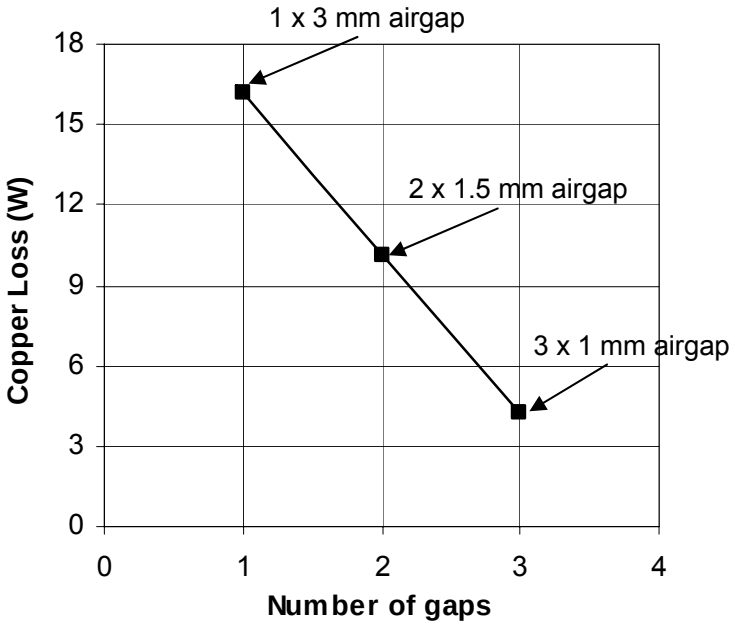

Figure 3.24: FEA of copper loss of distributed inductor airgap.

for both materials. For the third test there are three gaps in each leg with lengths of 1 mm, 1 mm, and 0.625 mm respectively. The gaps are located equally along the core leg for the iron-based amorphous core as shown in Fig. 3.23. However, the silicon steel core, because of its manufacturing process, has a 0.625 mm gap at one end of the core leg. This affects the experimental results and is discussed below.

Fig. 3.25 and Table 3.5 show how the experimental temperatures of the cores and the copper windings decrease with the number of gaps. As expected, the core and copper temperatures drop, e.g. 18 °C for the amorphous metal copper windings. The core for the silicon steel only drops 7 °C. This is because of the gap located at the end of the core leg. This is good for the copper winding as the winding is located further away from the airgap. However, there are increased core losses in the end section of the inductor core if the airgap is located at the end of the core leg. As the copper winding is not located directly around the

Material	**f (kHz)**	**l_g (mm)**	ΔT_{core} (°C)	ΔT_{cu} (°C)
2605SA1	30	1 x 3 mm	91	80
2605SA1	30	1 x 1.625 mm, 1 x 1 mm	81	70
2605SA1	30	2 x 1 mm, 1 x 0.625 mm	76	63
10JNHF600	30	1 x 3 mm	90	78
10JNHF600	30	1 x 1.625 mm, 1 x 1 mm	84	70
10JNHF600	30	2 x 1 mm, 1 x 0.625 mm	83	60

Table 3.5: Reduced temperatures due to distributed airgap.

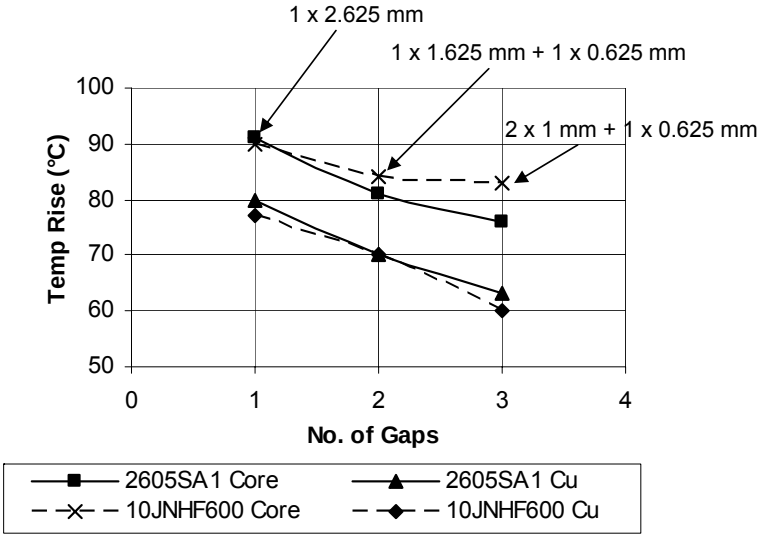

Figure 3.25: Reduced temperatures due to distributed airgaps.

airgap the increased fringing flux induces eddy currents in both the core leg and the core end section. The iron-based amorphous core did not have a gap located at the end of the core leg and this shows better performance when there are three airgaps in the core legs compared to the silicon steel core. This highlights the importance of the selection of the position of the gaps in the core legs. Note also, the gap loss equation in [11, 45, 49] does not consider the effect of distributing the airgap and that the gap loss calculated using this equation is a function of the total airgap length per leg.

$\mathbf{l_g}$/**leg** (mm)	**L** (μH)	**Winding type**	$\Delta T_{SS,core}$ (°C)	$\Delta T_{SS,cu}$ (°C)
2.625	53.61	N = 1 x 22 turns	90	70
2.625	53.08	N = 2 x 11 turns	84	65

Table 3.6: Silicon steel core and copper temperatures for different winding configurations.

3.4 The Shielding Effect

In the next test the 6.5 % silicon steel inductor temperature is compared with one single winding of 22 turns located around a single core leg versus two windings of 11 turns each located on both core legs. A single 2.625 mm airgap per leg is used and the frequency is kept constant at 30 kHz. Table 3.6 illustrates the shielding effect of the two windings compared to the single winding. The full experimental results are produced in Appendix C, Table C.6. There is a minor increase in the core and copper temperatures when a single winding is used. The copper and core temperature are 5 °C and 6 °C higher respectively for the inductor with the single winding versus the inductor with two windings. The eddy currents induced in the windings produce magnetic fields that repel the fringing flux around the airgap. This results in lower losses in the inductor with two windings versus a single winding configuration.

Further evidence in [45, 51, 56, 57] illustrate increased gap losses when the length of the airgap is increased. In Fig. 6 in [51] the gap losses increase as the length of the airgap is increased for both the iron-based amorphous metal and the 6.5 % silicon steel. The windings in these tests are located around the end sections of the cores and not around the airgaps. Similarly, in Table 1 in [45] the gap losses increase as the length of the airgap is increased for a single winding inductor. In [57] the core losses of the AMCU Series amorphous cut cores increase from around 8 W at 0.5 mm to approximately 15 W at 1.2 mm for a magnetic

induction of 0.1 T at 20 kHz. In [56] the gap losses are calculated in the design procedure using the gap loss equation in [45].

3.5 Thermal Configuration

The variation of inductor core temperature rise with thermal conductivity and lamination direction is now investigated. This interest in thermal configuration was spurred by experimental results recorded in device testing in Mainz Kastel, Germany.

Two inductors, designed with iron-based amorphous metal and 6.5 % silicon steel respectively, were tested in a single phase boost converter with the following specifications: frequency, $f = 16$ kHz, input voltage, $V_{in} = 180$ V, output voltage, $V_o = 360$ V, input current, $I_{in} = 180$ A, and inductance, $L = 45$ μH. A 0.5 mm thick foil winding with 11 turns on each core leg was used. The windings were connected in series giving a total of 22 turns. Thermal spacers with a total length of 4 mm were distributed in each core leg. These inductors were designed using the design algorithm developed in Chpater 4, Section 4.2 and the inductors are mounted horizontally as illustrated in Fig. 4.1. Fig. 3.26 shows the core and copper temperature rises above the cold plate for the two inductors. The results are presented in Appendix C, Table C.7. The 6.5 % silicon steel core is 49 °C higher than the iron-based amorphous metal core. This was an unexpected result and instigated this investigation into the effects of the lamination direction on the thermal path.

In Fig. 3.26, the core loss heat flows from the core to the heatsink in the direction of the lamination for the iron-based amorphous metal core and against the lamination for the 6.5 % silicon steel core. The heat generated due to the core power loss has to flow through the core to the cold plate as the inductor

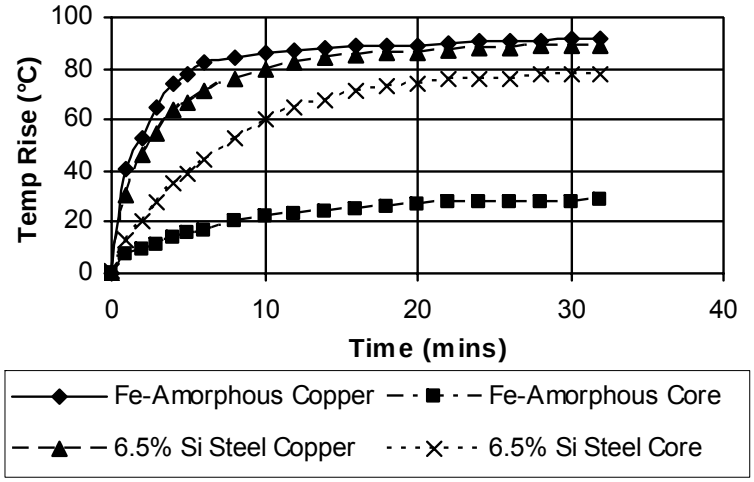

Figure 3.26: Fe-amorphous metal vs 6.5 % silicon steel at input current of 180 A.

cores and copper are isolated from each other. The silicon steel core sees a significant thermal resistance against the lamination. Thus, the effects of lamination direction on temperature rise are now investigated.

The temperature rise, ΔT, of a material is directly proportional to the power loss, P, and the thermal path, h. It is inversely proportional to the thermal conductivity, λ, and the surface area, A [58].

$$\Delta T = \frac{Ph}{\lambda A} \tag{3.1}$$

As shown above, the lamination direction has a significant impact on the thermal conductivity and subsequent heating of the inductor core. Fig. 3.27 shows core segments for 6.5 % silicon steel and iron-based amorphous metal. The 6.5 % silicon steel material is developed using a stamping process. The specified thermal conductivity of the material is 18.6 W/mK along the lamination [16] as shown in Fig. 3.27. However, the thermal conductivity against the lamination is much less (approx. 1 W/mK). The iron-based amorphous metal is developed using a winding process. The specified thermal conductivity of this material is

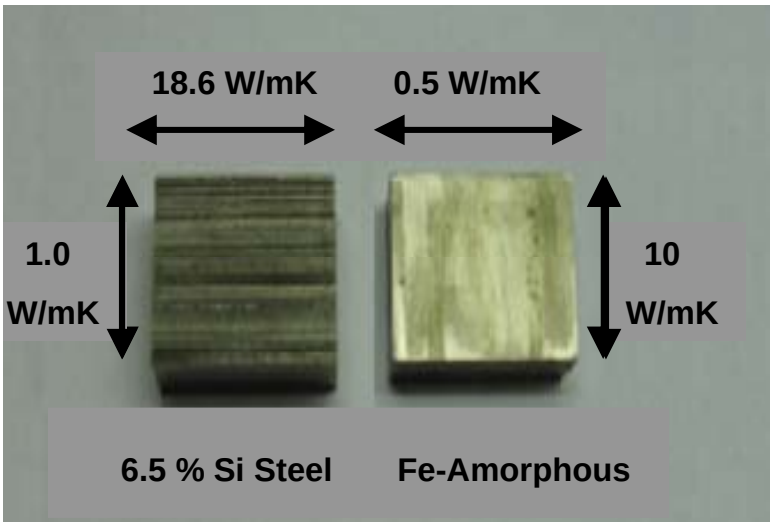

Figure 3.27: Magnetic core segments.

10 W/mK along the lamination. It is only 0.5 W/mK against the lamination [13]. The lamination direction is a critical parameter regarding inductor mounting as it affects both the thermal conductivity and the length of thermal path. The iron-based amorphous metal must be mounted horizontally to ensure the thermal conductivity along the lamination is used as illustrated in Fig. 3.28. Horizontal mounting also reduces the length of thermal path for regular inductor cores. The 6.5 % silicon steel material should be mounted vertically to ensure thermal conduction along the lamination direction unless another cooling path is provided for the core. The vertically mounted method increases the length of thermal path for most inductor cores as shown in Fig.3.28.

For the finite element simulations and the experimental thermal comparisons, an aluminium thermal bracket is designed as shown in Fig. 3.29. The thermal bracket ensures that the surface area, A, and thermal path, h, in (3.1) are equal for both materials. The other two parameters of (3.1) are dependent on the core material. The inductor cores are mounted horizontally but the thermal bracket provides an alternative path for the silicon steel core loss.

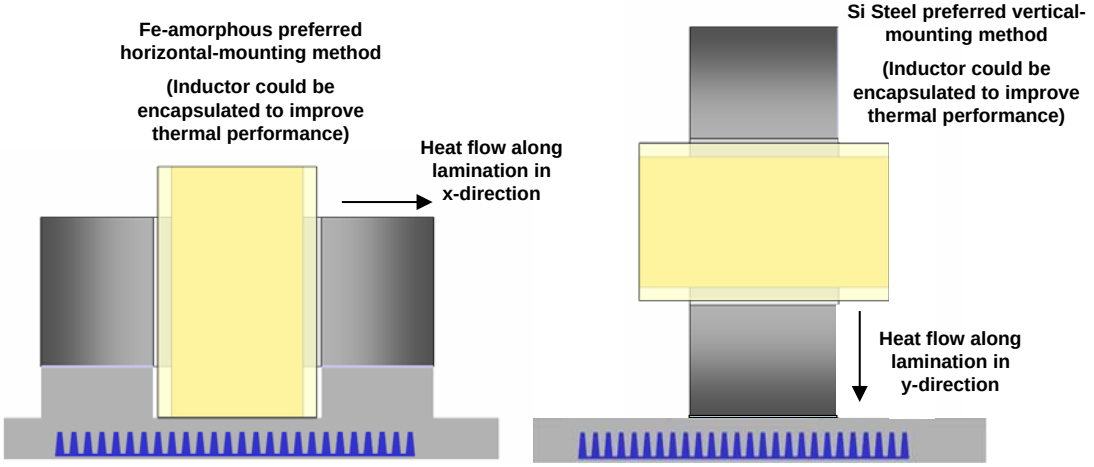

Figure 3.28: Horizontal mounting of Fe-base amorphous metal (left), vertical mounting of 6.5 % silicon steel (right).

Figure 3.29: Aluminium thermal jig.

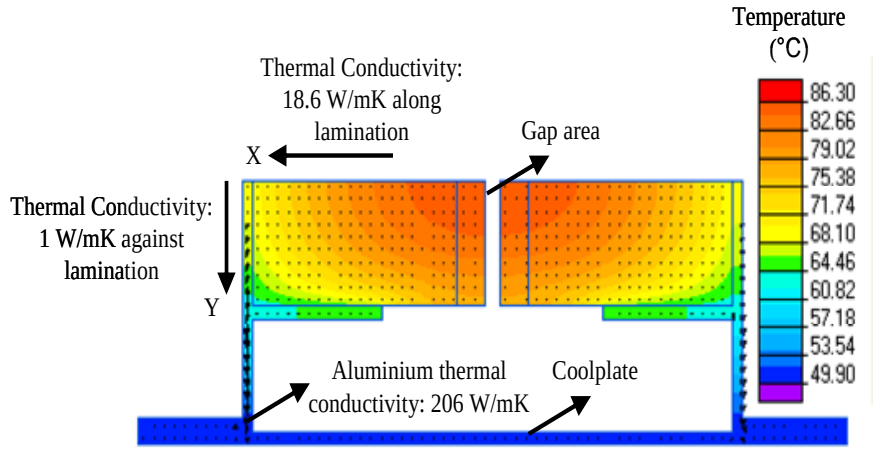

Figure 3.30: FEA of horizontal mounting of 6.5 % silicon steel core (0.2 T, 20 kHz).

Fig. 3.30 shows a FEA simulation for the 6.5 % silicon steel material. The copper winding is not shown. The copper winding is isolated from the inductor core using a Teflon bobbin. The thermal conductivity of Teflon (0.02 W/mK) [59] ensures that the heat distribution to the core from the copper is low. The aluminium bracket has a thermal conductivity of 206 W/mK [12], and extracts the heat out of the inductor core both along and against the lamination direction.

For the final set of tests, the thermal jig shown in Fig. 3.29 is used. The total gap length per leg of 2.625 mm is chosen as both core materials demonstrate similar losses at this design point (see Fig. 3.6). Three thermal conditions are tested and the experimental results are shown in Fig. 3.31. Full experimental results are presented in Appendix C, Table C.8. Firstly, heat is pulled from both the cores optimally in the x-y directions as illustrated in Fig. 3.30. The silicon steel has the lowest temperature rise of 16 °C due to its higher thermal conductivity. In the second test, heat is pulled out along the x direction only and a Teflon barrier is used to block heat flow in the y direction. There is only a minor

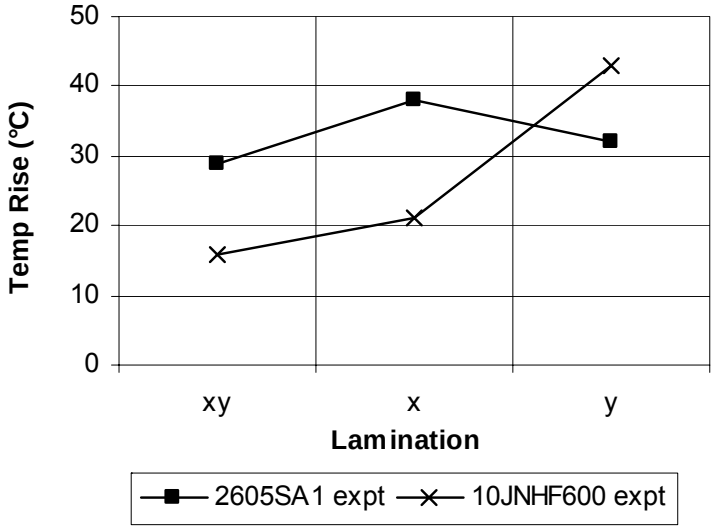

Figure 3.31: Conduction cooling experimental results.

increase in temperature from 16 °C to 21 °C for the silicon steel core as the heat is still been pulled out along the lamination. However, there is a larger increase in temperature from 29 °C to 38 °C for the iron-based amorphous core because the heat flow is against the lamination using the poorer thermal conductivity.

In the final test, heat is pulled out in the y direction only and a Teflon barrier is used to block heat flow in the x direction. This test is almost optimum for the amorphous metal but is against the lamination for silicon steel resulting in a significant temperature increase of 25 °C due to the poorer thermal conductivity.

There is an approximate 10 % experimental error in the above experiments due to the thickness of the teflon barrier ($R = \frac{\rho l}{A}$ where $\rho = \frac{1}{\lambda}$).

Fig. 3.31 suggests that conduction cooling, rather than natural convection, can result in the highest power density inductor when compared to Fig. 3.6. The comparative results for a single test point are presented in Table 3.7. The silicon steel inductor has a temperature rise of 16 °C for conduction cooling compared to a temperature rise of 95 °C for natural convection cooling. A reduction of

Material	l_g/leg (mm)	f (kHz)	$\Delta T_{core,conduction,xy}$ (°C)	$\Delta T_{core,convection}$ (°C)
Fe-based Amorphous	2.625	30	29	94
6.5 % Si Steel	2.625	30	16	95

Table 3.7: Conduction vs. convection cooling experimental results.

six fold suggests that a significantly smaller inductor design can be achieved for conduction cooling.

3.6 Experimental Anomalies

Sections 3.2.1 and 3.2.2 are now investigated further due to the experimental anomalies that arose with the iron-based amorphous metal multi-cut core and the gap loss equation from [11, 45]. In the following analysis the gap loss equation is neglected as the experimental temperature rise of the inductor at 30 kHz does not increase at the theoretical rate calculated using the gap loss equation. As shown earlier in Section 3.2.2, it is more likely that the increase in the measured inductor temperature is due to the increase in the copper foil losses caused by the fringing flux. In the following analysis finite element simulations on the foil windings are carried out to quantify the increase in copper foil losses due to the length of the airgap.

3.6.1 Constant Inductance, Variable Frequency Revised Tests

Earlier Fig. 3.4 showed the core temperature rise above ambient for the iron-based amorphous metal and the 6.5 % silicon steel as the frequency is increased from 15 kHz to 30 kHz in steps of 5 kHz. The experimental results suggest that the iron-based amorphous metal and the silicon steel materials have comparable

L (μH)	**N**	$\mathbf{l}_g$**/leg** (mm)	$\mathbf{b}_c$ (mm)	$\mathbf{h}_c$ (mm)	$\mathbf{b}_w$ (mm)	$\mathbf{l}_w$ (mm)	$\mathbf{M}_{core}$ (kg)
125	22	1.00	25	20	20	37	0.592
53	16	1.00	25	15	18	30	0.481

Table 3.8: Custom inductor characteristics.

performance over the frequency range of interest for a natural convection cooling environment. However, the nominal core loss values supplied by the manufacturers suggest that silicon steel should run hotter due to its higher core loss than the iron-based amorphous metal. The theoretical predictions are generated by the algorithm developed in [40] and there is a large deviation between the measured and theoretical core loss for the iron-based amorphous metal. A possible reason for the divergence between the theoretical and experimental results is provided in [51] where the effects of the manufacturing process are shown to degrade the iron-based amorphous metal core loss by 68 %. These cores have three cuts per leg possibly resulting in increased core loss.

In the next test, a single-cut iron-based amorphous metal core is tested with the same frequency, f, and flux swing, ΔB_{pk-pk}, as in Section 3.2.1. The single cut core is almost identical to the multi-cut core used in Section 3.2.1. The inductor characteristics are compared in Table 3.8. The inductance, L, of the single cut iron-based amorphous metal inductor is 53 μH and the number of turns, N, is 16. The input voltage, V_{in}, of the converter is reduced to 64 V to keep the same flux swing, ΔB_{pk-pk}, as the iron-based amorphous metal inductor tested in Section 3.2.1. A 0.6 mm thick foil winding with 8 turns on each core leg is used. The windings are connected in series giving a total of 16 turns. A thermal spacer with a length of 1 mm is inserted in each core leg. The input current, I_{in}, is 20 A and the input voltage, V_{in}, of 64 V is boosted up to 128 V on the output.

Fig. 3.32 shows the core temperature rise above ambient for the iron-based

Material	**f** (kHz)	$\mathbf{P}_{core}$ (W)	$\mathbf{P}_{cu,ac}$ (W)	$\mathbf{P}_{cu,dc}$ (W)	$\mathbf{P}_{tot}$ (W)	ΔT_{th} (°C)	ΔT_{expt} (°C)
2605SA1	15	12.5	8.5	1.7	22.7	56	64
2605SA1	20	11	6.3	1.7	19	47	55
2605SA1	25	10	5	1.7	16.7	42	50
2605SA1	30	9	3.64	1.7	14.34	39	45
10JNHF600	15	42	4.9	3.2	50.1	106	114
10JNHF600	20	40	4	3.2	47.2	101	102
10JNHF600	25	39	3.3	3.2	45.5	97	94
10JNHF600	30	38	2.5	3.2	43.7	93	87

Table 3.9: Table of losses and temperature rise for constant inductance.

amorphous metal and the 6.5 % silicon steel as the frequency is increased from 15 kHz to 30 kHz in steps of 5 kHz. Fig. 3.32 and Table 3.9 show that the theoretical power losses and the measured and theoretical temperature rises of the cores decrease with increasing frequency. Full experimental results for Fig. 3.32 are tabulated in Appendix C, Table C.9. Here, the measured temperature rise of the iron-based amorphous metal is significantly lower than that measured in Fig 3.4. The measured temperature of the iron-based amorphous metal at 15 kHz has decreased from 113 °C in Fig. 3.4 to 64 °C in Fig. 3.32. This illustrates the increase in core loss due to the manufacturing process of the multi-cut core.

The iron-based amorphous metal inductor also operates significantly cooler than the 6.5 % silicon steel inductor over the analyzed frequency range when natural-convection-cooling is used. This is expected as the nominal core loss values supplied by the manufacturers suggest that silicon steel should run hotter due to its higher core loss.

There is good correlation between the theoretical and experimental results for both the iron-based amorphous metal and 6.5 % silicon steel inductors. The ac copper losses are calculated using finite element analysis and the gap loss equation from [11, 45] is neglected.

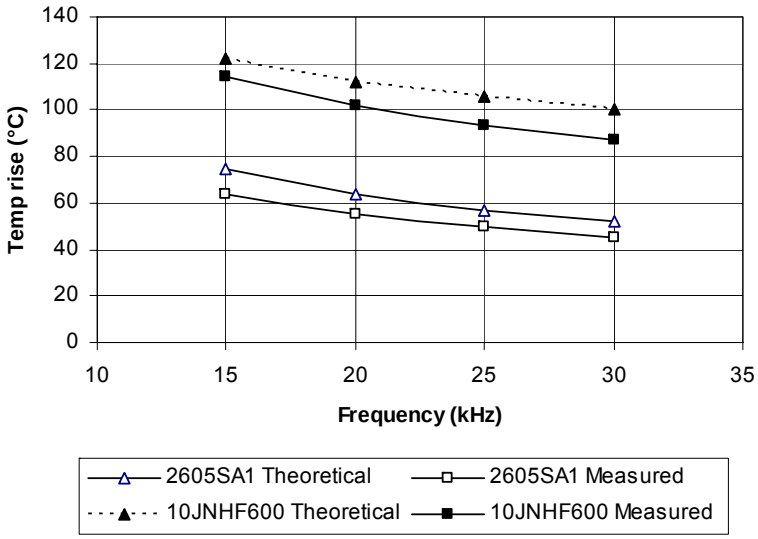

Figure 3.32: Inductor temperature rise for constant inductance.

3.6.2 Constant Frequency, Variable Ripple Revised Tests

Fig. 3.6 shows that at large airgaps the theoretical temperature rise of the silicon steel inductor is significantly over-estimated compared to the experimental results. This is largely due to the inaccurate theoretical predication for gap loss. The accuracy of the equation in [45] is stated to be within $\pm$ 25 % at 60 Hz based on the analysis of the reported test data. The deviations were stated as being wider at 400 Hz [49]. The measured temperature rise of the inductor in Section 3.2.2 at 30 kHz does not increase at the theoretical rate calculated when the gap loss equation in [11, 49] is considered.

In the next test the inductor ripple ratio is increased from low to high while the frequency is kept constant at 30 kHz. The inductance decreases as the ripple ratio is increased and the ac flux swing remains constant. As above, the single-cut iron-based amorphous metal inductor is used and the temperature rise is measured. Table 3.10 and Fig. 3.33 show the rise in core temperatures in a natural-convection-cooled environment. Full experimental results are presented

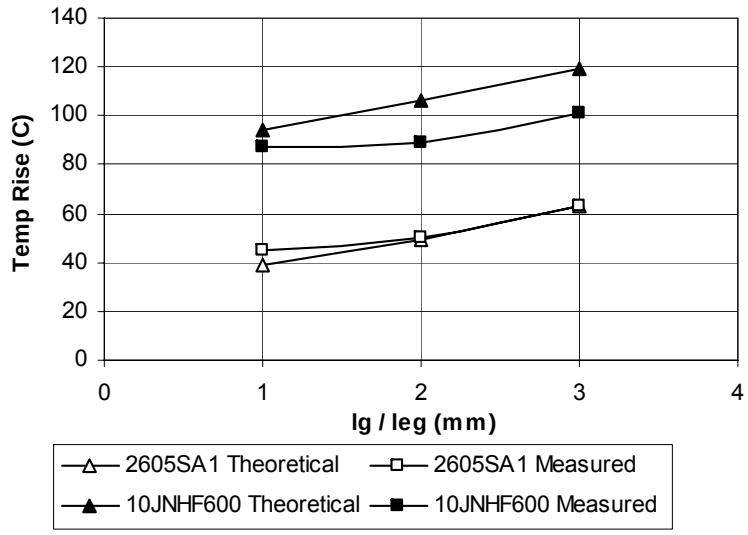

Figure 3.33: Core temperature rise vs. gap length for constant frequency (30 kHz).

in Appendix C, Table C.10. There is a significant improvement in the correlation between the theoretical and measured temperatures. The ac copper losses are calculated using finite element analysis and the gap loss equation in [11, 49] is now neglected. Again, the measured temperature rise of the iron-based amorphous metal is significantly lower than that measured in Fig. 3.6. The single-cut iron-based amorphous metal inductor has better performance than the 6.5 % silicon steel inductor over the range of analyzed ripple ratios.

3.7 Revised Area Product Analysis for Magnetic Materials

In this section the learnings from the experimental analysis in Chapter 3 is used to revise the area product analysis in Chapter 2. The design algorithm used in this section is similar to the design algorithm used in Chapter 2, except that the

Material	$\mathbf{l}_g$ (mm)	$\mathbf{P}_c$ (W)	$\mathbf{P}_{cu,ac}$ (W)	$\mathbf{P}_{cu,dc}$ (W)	$\mathbf{P}_{tot}$ (W)	ΔT_{th} (°C)	ΔT_{expt} (°C)
2605SA1	1.0	9	3.64	1.7	14.34	39	45
2605SA1	2.0	9	8	1.7	18.7	49	50
2605SA1	3.0	9	14	1.7	24.7	63	63
10JNHF600	1.0	38	2.52	3.2	43.72	94	87
10JNHF600	2.0	38	8.9	3.2	50.1	106	89
10JNHF600	3.0	38	16.21	3.2	57.41	119	101

Table 3.10: Inductor loss components vs. gap length for constant frequency (30 kHz).

core gap loss, P_g, is neglected and the maximum flux density, B_{max}, is de-rated by 75 % of the saturation flux density instead of 80 %. The modified design algorithm is used to investigate the variation of inductor sizes with (a) frequency for a constant inductance value, (b) ripple current for a constant frequency, and (c) with frequency for a constant ripple.

3.7.1 Constant Inductance, Variable Frequency Analysis

The design algorithm in Chapter 2 is used to analyse inductor designs for 1, 10 and 40 kW converters with inductances of 2 mH, 200 μH and 50 μH respectively. The four magnetic materials described in Table 2.1 are analysed for the same converter specifications with input voltage, V_I = 200 V and output voltage, V_O = 400 V. The switching frequency, f, is swept from 10 to 30 kHz in steps of 5 kHz. The inductance values of 2 mH, 200 μH and 50 μH are selected to ensure the ripple ratio, r, decreases from a maximum of 1 at 10 kHz to a minimum of 0.333 at 30 kHz.

The inductor specifications are: current density, J_{max} = 6 A/mm^2, foil fill factor, k_{foil} = 0.75, core fill factor, k_{core}, is selected from Table 2.1, maximum flux density, B_{max}, is de-rated by 75 % of the saturation flux density, B_{sat}, core ratio, r_c = 2.2, winding gap factor, W_{gf} = 2, number of gaps, N_g = 2, actual

foil thickness, $t_{f(act)}$ = 0.5 mm and foil cleareance, f_{cl} = 2 mm. The ambient temperature is set at T_{amb} = 70 °C. The maximum temperature rise, ΔT_{max}, allowed for each material is dependent on the continuous operating temperature of the material shown in Table 2.1, e.g. ΔT_{max} = 80 °C for iron-based amorphous material (150 °C minus 70 °C), ΔT_{max} = 50 °C for nanocrystalline, and ΔT_{max} = 30 °C for ferrite.

Fig. 3.34 plots the area product vs. frequency for the 1 kW power level and the above inputs. The results are also illustrated in Table 3.11 where the results in bold illustrate when the inductor is limited by saturation flux density. As in Chapter 2, the area-product decreases with increasing frequency for a given material temperature rise. The sizes of the inductors in Fig. 3.34 are similar to the sizes of the inductors in Fig. 2.4 as the inductors at this design point are mostly limited by saturation flux density and not specific power. The inductors in Fig. 3.34 are slightly larger due to the lower saturation flux density derating factor of 75 % compared to 80 % in Fig. 2.4.

Clearly, for the conditions given, the ferrite inductor is significantly larger than the other materials because all four materials are close to being limited by saturation flux density. For this curve set, the silicon steel is the smallest of the four inductors due to its high saturation flux density. The ferrite material is the largest inductor over the analysed frequency range. The low saturation flux density and the low allowed temperature rise results in the largest inductor. The inductor losses in the saturation limited designs are dominated by copper loss. The window is decreased to increase the copper loss (less copper) and this shrinks the overall inductor size.

Fig. 3.35 and Fig. 3.36 show that as the power levels increase the laminated inductor sizes decrease when compared to similar design points in Fig. 2.5 and Fig. 2.6 respectively. The results for Fig. 3.35 and Fig. 3.36 are also illustrated

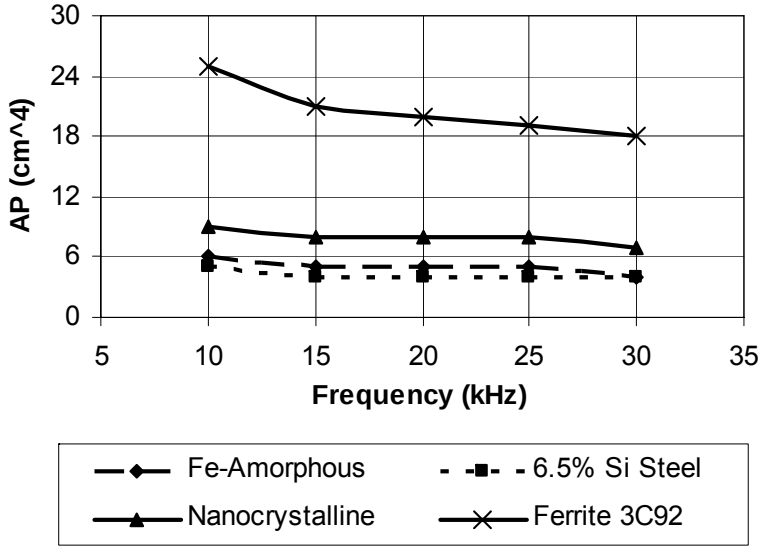

Figure 3.34: Inductor area product vs. frequency for constant inductance (1 kW).

r	**f (kHz)**	**Fe-Amorphous AP (cm^4)**	**6.5 % Si Steel AP (cm^4)**	**Nanocrystalline AP (cm^4)**	**3C92 AP (cm^4)**
1.0	10	**6**	**5**	9	**25**
0.667	15	**5**	**5**	**8**	**21**
0.5	20	**5**	**4**	**8**	**20**
0.4	25	**5**	**4**	**8**	**19**
0.333	30	**4**	**4**	**7**	**18**

Table 3.11: Inductor area product vs. frequency for constant inductance (1 kW).

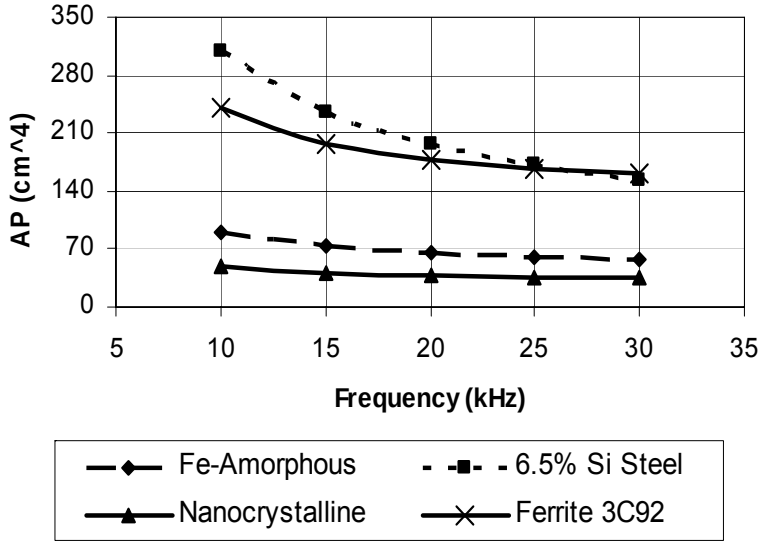

Figure 3.35: Inductor area product vs. frequency for constant inductance (10kW).

r	**f (kHz)**	**Fe-Amorphous AP (cm^4)**	**6.5 % Si Steel AP (cm^4)**	**Nanocrystalline AP (cm^4)**	**3C92 AP (cm^4)**
1.0	10	89	310	**48**	**240**
0.667	15	75	235	**41**	**197**
0.5	20	66	196	**38**	**177**
0.4	25	61	171	**36**	**167**
0.333	30	57	153	**35**	**160**

Table 3.12: Inductor area product vs. frequency for constant inductance (10kW).

in Table 3.12 and Table 3.13 respectively. As the gap loss is neglected the sizes of the laminated inductors decrease when compared to Fig. 2.5 and Fig. 2.6. However, the ferrite inductor sizes are larger due to the lower saturation flux density derating factor of 75 % compared to 80 % in Fig. 2.5 and Fig. 2.6.

3.7.2 Constant Frequency, Variable Ripple Analysis

In this section, the peak-to-peak ripple ratio is varied from very low, 0.125, to very high, 2. The boost converter and inductor specifications are as in the previous

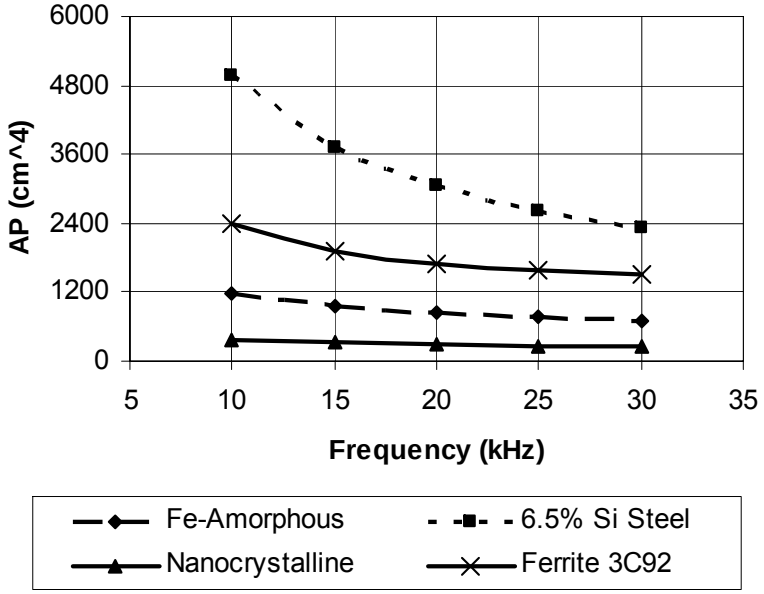

Figure 3.36: Inductor area product vs. frequency for constant inductance (40kW).

r	**f (kHz)**	**Fe-Amorphous AP (cm^4)**	**6.5 % Si Steel AP (cm^4)**	**Nanocrystalline AP (cm^4)**	**3C92 AP (cm^4)**
1.0	10	1184	4974	**377**	**2381**
0.667	15	965	3714	**313**	**1911**
0.5	20	845	3052	**286**	**1695**
0.4	25	766	2630	**272**	**1569**
0.333	30	707	2331	**264**	**1497**

Table 3.13: Inductor area product vs. frequency for constant inductance (40kW).

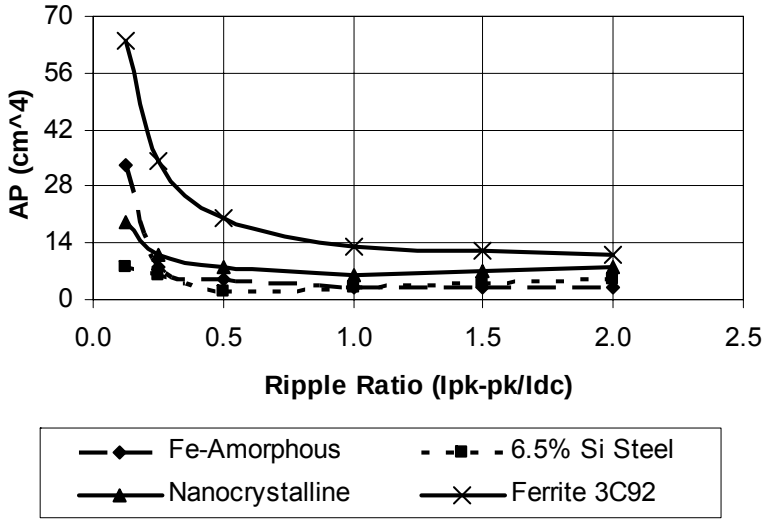

Figure 3.37: Inductor area product vs. ripple for constant frequency (1 kW).

section, except that the frequency is set at 20 kHz.

Fig. 3.37 plots the area product vs. ripple for the 1 kW power level and the above inputs. The results are also illustrated in Table 3.14 where the results in bold illustrate when the inductor is limited by saturation flux density. In this plot, the inductance decreases from a high of 8 mH at a ripple ratio of 0.125 to 500 μH at a ripple ratio of 2. In Fig. 3.37 all the materials are initially limited by saturation flux density and the area products decrease. As the laminated materials become limited by specific power the area products increase due to the increase in ac copper losses. The area products do not increase at the same rate of increase as the area products shown in Fig. 2.7 where the increase in inductor sizes are mostly driven by the core gap loss and not the ac copper losses. The inductor sizes in Fig. 3.37 are also smaller when compared to the inductor sizes in Fig. 2.7 due to the neglected gap loss.

Similar trends are seen for the 10 kW and 40 kW designs shown in Fig. 3.38 and Fig. 3.39 respectively. Again, the area products do not increase at the same

r	f (kHz)	Fe-Amorphous AP (cm^4)	6.5 % Si Steel AP (cm^4)	Nanocrystalline AP (cm^4)	3C92 AP (cm^4)
0.125	20	**33**	**8**	**19**	**64**
0.25	20	**8**	**5**	**11**	**34**
0.5	20	**5**	**2**	**8**	**20**
1.0	20	**4**	3	6	**13**
1.5	20	**4**	4	7	**12**
2.0	20	**4**	5	8	**11**

Table 3.14: Inductor area product vs. ripple for constant frequency (1 kW).

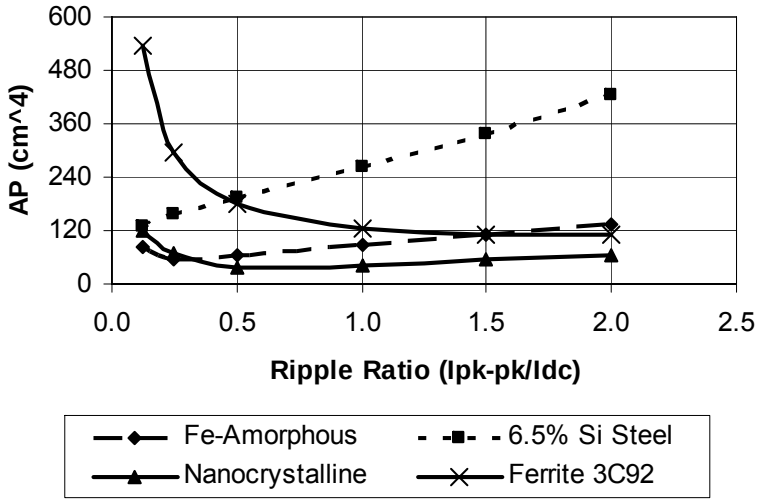

Figure 3.38: Inductor area product vs. ripple for constant frequency (10 kW).

rate of increase as the area products shown in Fig. 2.8 and Fig. 2.9 respectively. The increase in inductor sizes is due to the increase in ac copper losses and not the gap loss. The inductor sizes in Fig. 3.38 and Fig. 3.39 are also smaller when compared to the inductor sizes in Fig. 2.8 and Fig. 2.9 respectively. This is due to the neglected gap loss.

r	f (kHz)	Fe-Amorphous AP (cm^4)	6.5 % Si Steel AP (cm^4)	Nanocrystalline AP (cm^4)	3C92 AP (cm^4)
0.125	20	**84**	130	**119**	**537**
0.25	20	56	156	**67**	**297**
0.5	20	66	196	39	**178**
1.0	20	87	265	43	**123**
1.5	20	110	338	54	**111**
2.0	20	136	423	65	**111**

Table 3.15: Inductor area product vs. ripple for constant frequency (10 kW).

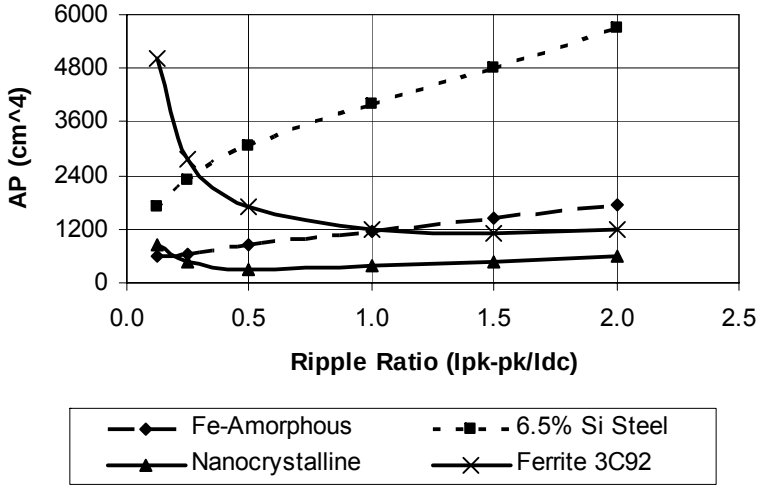

Figure 3.39: Inductor area product vs. ripple for constant frequency (40 kW).

r	f (kHz)	Fe-Amorphous AP (cm^4)	6.5 % Si Steel AP (cm^4)	Nanocrystalline AP (cm^4)	3C92 AP (cm^4)
0.125	20	**583**	1691	**872**	**5014**
0.25	20	631	2293	**486**	**2787**
0.5	20	845	3052	**300**	**1695**
1.0	20	1165	3994	367	**1201**
1.5	20	1450	4813	477	**1126**
2.0	20	1751	5709	595	1208

Table 3.16: Inductor area product vs. ripple for constant frequency (40 kW).

L (mH)	**f (kHz)**	**Fe-Amorphous AP (cm^4)**	**6.5 % Si Steel AP (cm^4)**	**Nanocrystalline AP (cm^4)**	**3C92 AP (cm^4)**
6.67	10	**13**	**12**	**18**	**58**
4.44	15	**9**	**8**	**12**	**39**
3.33	20	**7**	**6**	**9**	**30**
2.67	25	**6**	**5**	**9**	**24**
2.22	30	**5**	**4**	**8**	**20**

Table 3.17: Inductor area product vs. frequency for 30 % ripple (1 kW).

3.7.3 Constant Ripple, Variable Frequency Analysis

In this section, the frequency, f, is increased from 10 to 30 kHz in steps of 5 kHz and the ripple ratio, r, is kept constant. Two ripple ratios of 0.3 and 0.7 are tested at 1, 10 and 40 kW for the inputs in the above sections.

Fig. 3.40 plots the area product vs. frequency for the 1 kW power level and the above inputs at a ripple ratio of 0.3. The results are also illustrated in Table 3.17 where the results in bold illustrate when the inductor is limited by saturation flux density. In Fig. 3.40 all the materials are limited by saturation flux density and the area products decrease with increasing frequency. The inductance, L, decreases as the frequency increases for a constant ripple ratio. As the inductance decreases the area product, $\mathrm{AP}_{B\,\max}$, decreases.

$$L = \frac{V_I d}{f \Delta I_{pk-pk}} \tag{3.2}$$

$$AP_{B\,\max} = A_w A_c = \frac{L I_{pk} I_{rms}}{B_{max} J_{max} k_{foil} k_{core}} \tag{3.3}$$

Fig. 3.41 plots the area product vs. frequency for the 1 kW power level and a ripple ratio, r, of 0.7. The results are also illustrated in Table 3.18. Again, as the frequency is increased the area products decrease. The area products decrease further as the ripple ratio increases from 0.3 to 0.7. As the nanocrystalline material becomes limited by specific power the area products also decrease as the

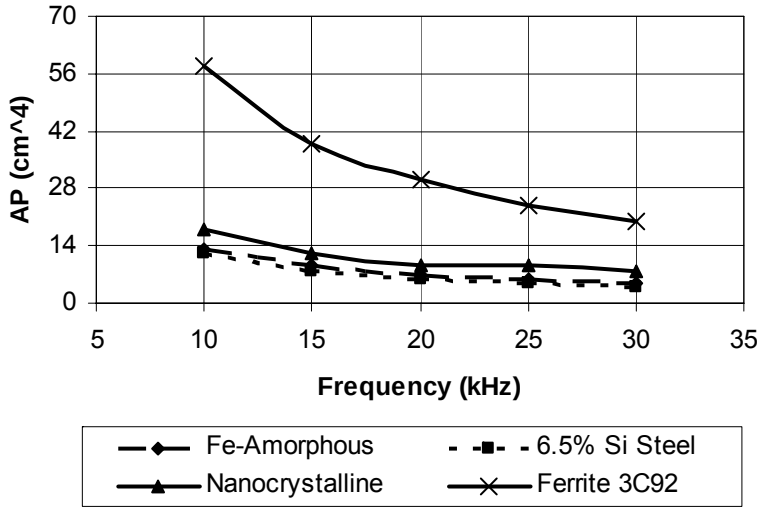

Figure 3.40: Inductor area product vs. frequency for 30 % ripple (1 kW).

L (mH)	**f (kHz)**	**Fe-Amorphous AP (cm^4)**	**6.5 % Si Steel AP (cm^4)**	**Nanocrystalline AP (cm^4)**	**3C92 AP (cm^4)**
2.86	10	**7**	**6**	**9**	**31**
1.9	15	**5**	**4**	**6**	**21**
1.43	20	**4**	**4**	5	**16**
1.14	25	**3**	**4**	4	**13**
0.95	30	**3**	**4**	4	**11**

Table 3.18: Inductor area product vs. frequency for 70 % ripple (1 kW).

frequency increases.

$$AP_{Psp} = A_w A_c = \frac{I_{rms} dV_I}{k_{core} k_{foil} J_{\max} f \Delta B_{pk-pk}} \tag{3.4}$$

Similar trends are seen in Fig. 3.42, Fig. 3.43, Fig. 3.44 and Fig. 3.45 as the power levels are increased to 10 and 40kW respectively.

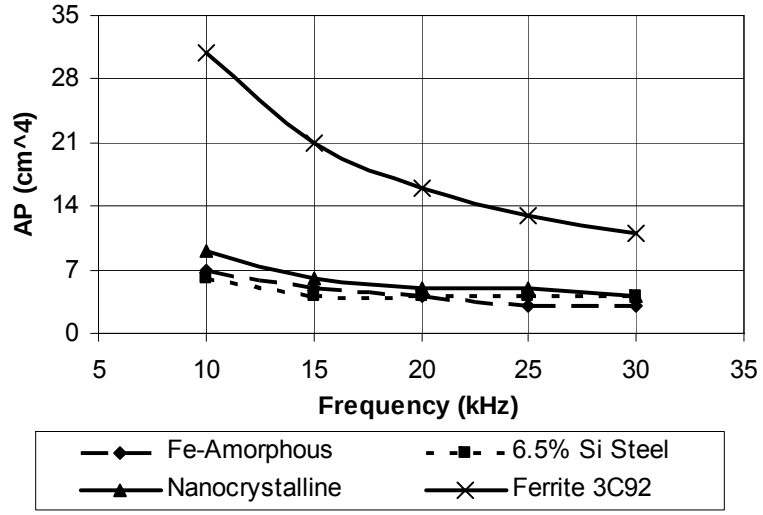

Figure 3.41: Inductor area product vs. frequency for 70 % ripple (1 kW).

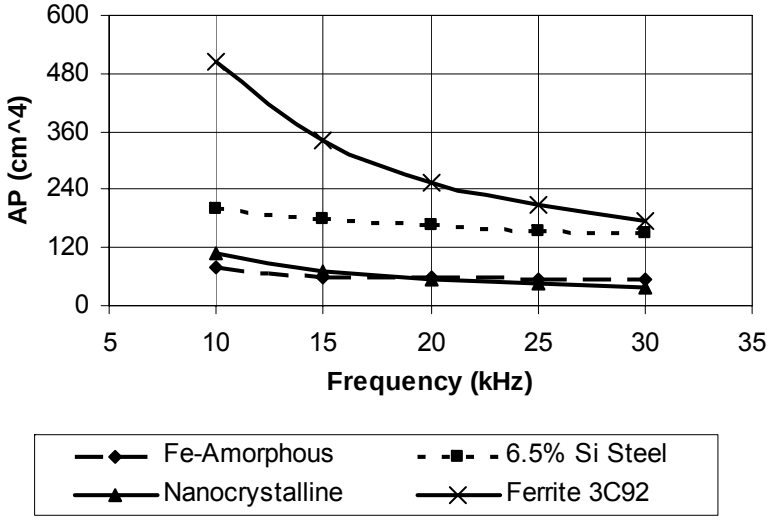

Figure 3.42: Inductor area product vs. frequency for 30 % ripple (10 kW).

L (μH)	**f (kHz)**	**Fe-Amorphous AP (cm^4)**	**6.5 % Si Steel AP (cm^4)**	**Nanocrystalline AP (cm^4)**	**3C92 AP (cm^4)**
667	10	**79**	199	**107**	**506**
444	15	60	178	**72**	**341**
333	20	58	165	55	**256**
267	25	56	155	45	**207**
222	30	55	148	37	**173**

Table 3.19: Inductor area product vs. frequency for 30 % ripple (10 kW).

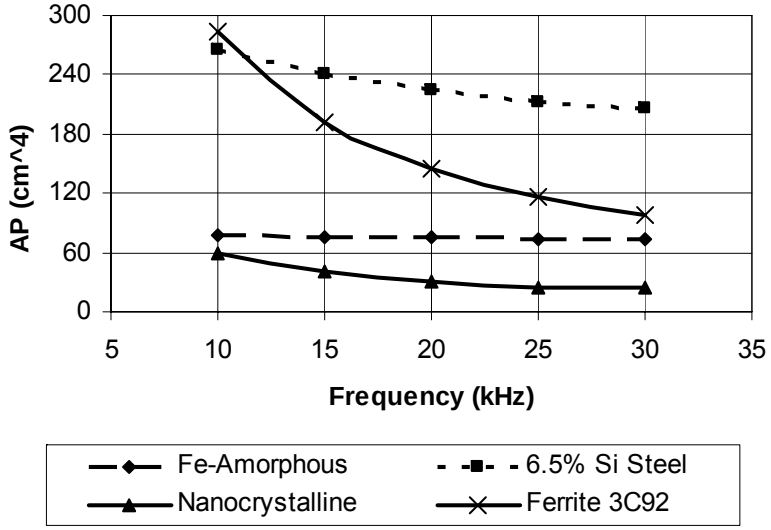

Figure 3.43: Inductor area product vs. frequency for 70 % ripple (10 kW).

L (μH)	**f (kHz)**	**Fe-Amorphous AP (cm^4)**	**6.5 % Si Steel AP (cm^4)**	**Nanocrystalline AP (cm^4)**	**3C92 AP (cm^4)**
286	10	78	266	59	**284**
190	15	76	240	40	**191**
143	20	75	224	31	**145**
114	25	74	213	**25**	**117**
95	30	74	206	**25**	**98**

Table 3.20: Inductor area product vs. frequency for 70 % ripple (10 kW).

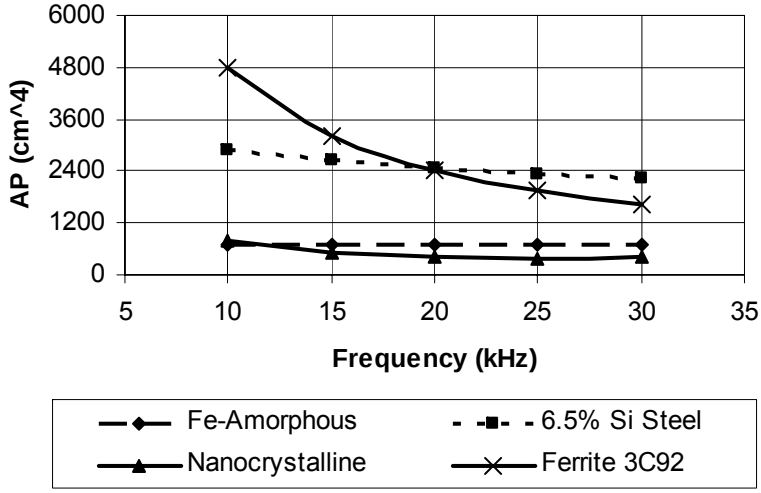

Figure 3.44: Inductor area product vs. frequency for 30 % ripple (40 kW).

L (μH)	**f (kHz)**	**Fe-Amorphous AP (cm^4)**	**6.5 % Si Steel AP (cm^4)**	**Nanocrystalline AP (cm^4)**	**3C92 AP (cm^4)**
167	10	685	2890	783	**4806**
111	15	681	2651	530	**3228**
83.3	20	679	2480	406	**2425**
66.7	25	678	2346	378	**1945**
55.6	30	677	2237	**432**	**1622**

Table 3.21: Inductor area product vs. frequency for 30 % ripple (40 kW).

L (μH)	**f (kHz)**	**Fe-Amorphous AP (cm^4)**	**6.5 % Si Steel AP (cm^4)**	**Nanocrystalline AP (cm^4)**	**3C92 AP (cm^4)**
71.4	10	988	4242	443	**2769**
47.6	15	988	3788	**395**	**1855**
35.7	20	984	3473	**494**	**1394**
28.6	25	978	3238	**592**	**1114**
23.8	30	972	3056	**689**	**940**

Table 3.22: Inductor area product vs. frequency for 70 % ripple (40 kW).

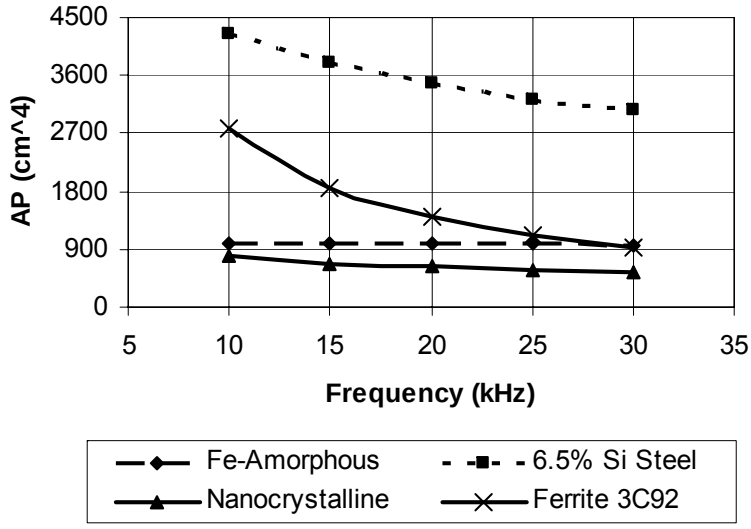

Figure 3.45: Inductor area product vs. frequency for 70 % ripple (40 kW).

3.8 Summary

Iron-based amorphous metal and 6.5 % silicon steel are competitive materials for high-power-density inductors in the low-to-medium-frequency range and lead to a low cost and low weight/volume solution for high-power dc-dc converters. In this chapter, the practical effects of frequency, ripple, load-current, airgap fringing, and thermal configuration are investigated for these materials. A 2.5 kW converter is built to verify the optimum material selection and thermal configuration over the frequency range and ripple ratio of interest. Experimental, analytical and simulation results are presented.

Inductor size can increase in both these laminated materials due to increased airgap fringing losses. Distributing the airgap is demonstrated to reduce the inductor losses and size but has practical limitations for iron-based amorphous metal cores. The effects of the manufacturing process are shown to degrade the iron-based amorphous metal core loss. The experimental results also suggest that gap loss is not a significant consideration in these experiments. The predicted

losses by the equation in [11, 49] are significantly higher than the experimental results suggest.

Conduction cooling, rather than natural convection, can result in the highest power density inductor. The cooling for these laminated materials is very dependent on the direction of the lamination and the component mounting. Experimental results are produced showing the effects of lamination direction on the cooling path. A significant temperature reduction is observed compared to the natural convection cooling experimental results for the same test conditions. A novel conduction cooling design algorithm is developed in the next Chapter.

Chapter 4

Conduction Cooling Design Algorithm for High-Power Inductors

In this chapter, a conduction cooled inductor design algorithm is developed. The algorithm is developed for foil-wound inductors with gapped CC-cores in the low to medium frequency range. The algorithm considers the following factors: winding skin and layer effects; distance from airgap to minimize copper fringing loss, airgap length to reduce core and copper fringing losses, creepage and clearance, separate cooling paths for the core and the copper. The mass of the inductor is minimized in the design algorithm. The conduction cooled inductor algorithm is used to analyze the variation of inductor weights with frequency for a constant inductance value. Conduction cooling, rather than natural convection, is shown to reduce the weight of the inductor. The weight of the 6.5 % silicon steel inductor is reduced by around a factor of ten compared to natural-convection cooling due to the high thermal conductivity of the material. Finally, the algorithm is used to develop high-power custom inductors.

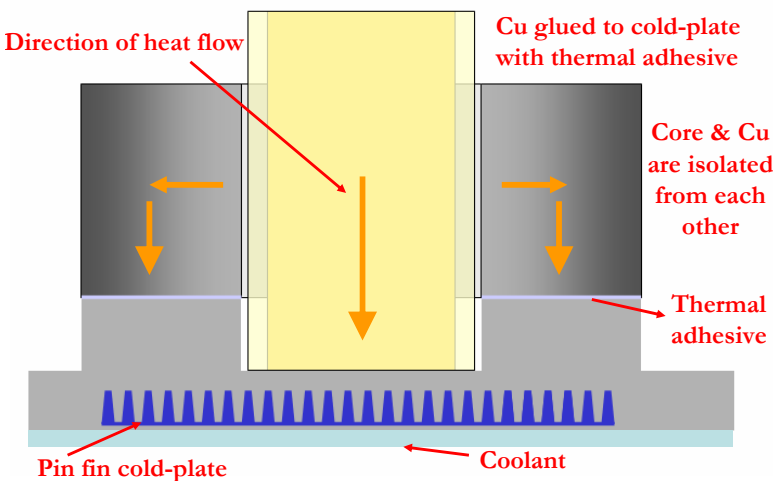

Figure 4.1: Inductor core and copper thermal structure.

4.1 Introduction

It is well established that conduction cooling, rather than natural convection, can result in the highest power density inductor as illustrated in Table 3.7 and [41, 60]. A further increase in power density is achieved by operating the inductor materials at their specified temperature ratings. As the copper can operate at the higher temperature of 180 °C compared to the core at 150 °C, additional advantage can be achieved by ensuring that the heat rise due to the copper loss does not affect the core. The core can operate at its own temperature rating if the heat can be removed from it without using the copper as its heatsink. As the copper operates at a higher temperature it will only lead to an increase in the core temperature limiting the total design to the temperature rating of the core. (If copper acts as a heatsink and reaches 150 °C then the core will only get hotter if the copper gets hotter). This can be done by ensuring there is a gap between the core and the copper and that individual heat paths are provided for the core and the copper. This is achieved by mounting the iron-based amorphous metal magnetic core horizontally as shown in Fig. 4.1.

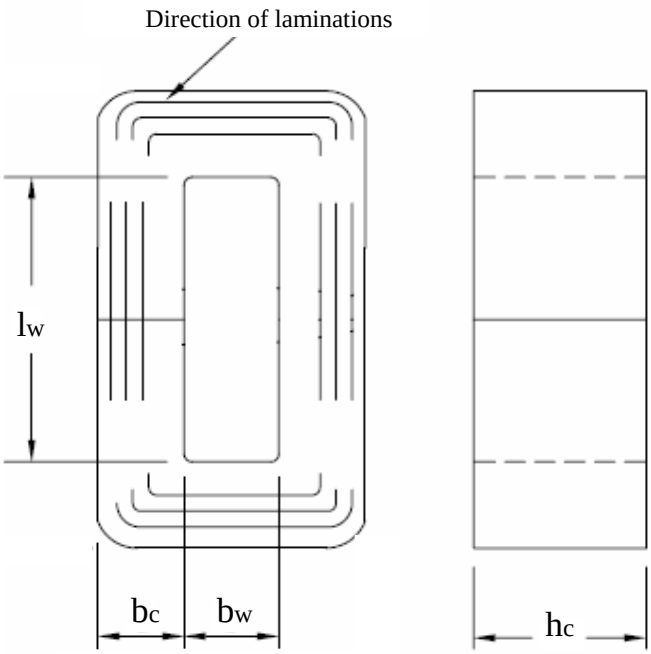

Figure 4.2: Drawing of Metglas core.

Fig. 4.2 shows a schematic drawing of an iron-based amorphous metal magnetic core. A structure needs to be designed where by the heat generated within the core can be removed. The desired goal is to reduce the temperature rise of the core by providing the lowest possible thermal resistance path to the cold plate. This is achieved by mounting the core horizontally and reducing the lamination height, h_c, as shown in Fig. 4.2. Decreasing the lamination height also helps to reduce the mass of the inductor core. As the hot copper is surrounding the window length the only way to remove the heat from the core is through its end sections. The best possible way to remove this heat is by using a highly conductive heatsink attached to the end sections of the core as illustrated in Fig 4.1 and Section 3.5. The increase in the length of the thermal path due to the height of the heatsink must be compensated by the thermal conductivity of the heatsink material, otherwise the heat will not transfer out of the core.

As the copper loss increases with increased power density the thermal path from the copper hotspot is critical. Reducing this path is the key component in removing the heat. Mounting the copper windings directly to the cold plate will minimize the length of the thermal path for the copper, as shown in Fig. 4.1.

The conduction cooling inductor design algorithm and flowchart is presented in Section 4.2. The design algorithm is then used in Section 4.4 to generate custom inductors for a 40 kW design point.

4.2 Conduction Cooling Inductor Design Algorithm and Flowchart

In this section, a customized conduction-cooling inductor-design algorithm is presented for the development of high-power custom-made inductors. This algorithm is different to the natural-convection-cooling algorithm in the way that the airgap length is controlled to minimize the ac copper losses due to the airgap. Experimental results in Sections 3.2.2 and 3.6.2 illustrate the significance of the fringing flux on the ac copper losses in the windings. The gap loss equation in [11, 49, 40] is also neglected as it over-estimates the core loss as previously shown in Sections 3.2.2 and 3.6.2. The initial core dimensions are also input in this algorithm, unlike the natural convection-cooling algorithm where the core ratios are initially input. The mass of the inductor is optimized in the design algorithm. In order to focus the task and simplify the algorithm, the following assumptions are made:

(i) conduction cooling;

(ii) foil winding;

(iii) gapped CC core set;

(iv) a boost converter topology;

(v) a linear B-H curve.

For simplicity, the algorithm considers gapped CC cores only. However, the algorithm can also be modified to consider EE gapped core sets and the various ungapped options [41].

The algorithm factors in the following design considerations:

(i) winding skin and layer effects;

(ii) distance from airgap to minimize copper fringing loss;

(iii) airgap length to reduce copper fringing loss;

(iv) core loss;

(v) creepage and clearance;

(vii) individual heat paths for the core and the copper.

Fig. 4.3 shows the flow chart for a foil-winding configuration in a conduction-cooling environment. The algorithm takes the various electrical, magnetic and thermal inputs and generates a core size based on the core dimensions initially specified by the designer. The core dimensions are modified later in the algorithm to ensure the minimum mass for the inductor is achieved. Once the core area is determined, the number of turns is calculated. The airgap length for energy storage is then calculated and adjusted for fringing flux. The energy stored in the core and the airgap is determined as is the core loss. The winding is located a distance away from the airgap to reduce copper fringing loss. A clearance is also provided between the core and the winding due to high voltage creepage. The foil insulation thickness is specified and the window area available for the winding

is calculated. The dc copper loss is then determined. The current harmonics are considered and the ac copper loss effects are calculated. The winding and inductor dimensions, mass and volume are calculated. Individual heat paths are provided for the core and the copper and the temperature rise of both the core and the copper are determined. The inductor mass is optimized by adjusting the core dimensions iteratively using the solver in EXCEL, unlike the algorithm in Chapter 2 that iterates the core and power loss ratios and optimizes the size of the inductor for area product.

The boxes in the area product flow chart are lettered to explain the design procedure. The various boxes are described as follows.

(A) In this section, the nominal electrical specifications for a continuous mode boost converter are input: low-voltage input, V_I, high-voltage output, V_O, output power, P_O, efficiency, η, switching frequency, f, and the ratio of the peak-to-peak inductor current to the dc current, r. The maximum flux density, B_{max} and core fill factor, k_{core}, are set. B_{max} is a derated value of the saturation flux density, B_{sat}, of the material (typically 80%). The material core loss indices, m,n, k, core density, ρ_{core}, and the permeability of free space, μ_0, are also input.

(B) Using the electrical specifications for a boost converter input in (A), the following electrical outputs are determined: dc input current, I_I, peak-to-peak inductor current, ΔI_{pk-pk}, duty ratio, d, dc output current, I_O, boost inductance, L, inductor peak current, I_{pk}, and inductor rms current I_{rms}. The peak-to-peak flux density, ΔB_{pk-pk}, is also calculated.

$$I_I = \frac{P_O}{\eta \cdot V_I} \ , \qquad \Delta I_{pk-pk} = r I_I \ , \qquad I_O = \frac{P_O}{V_O} \tag{4.1}$$

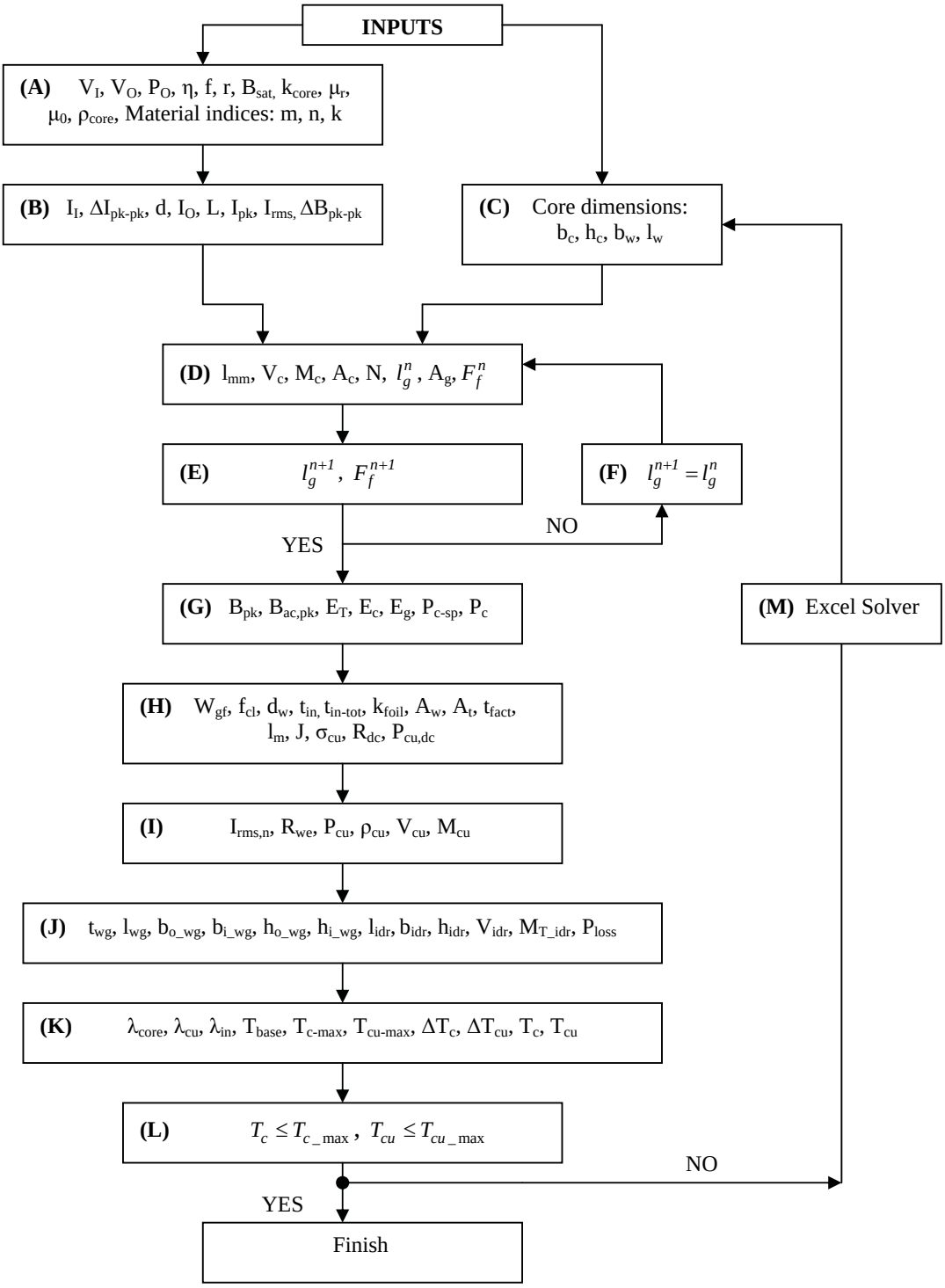

Figure 4.3: Conduction cooling inductor flow chart.

$$d = 1 - \frac{V_I}{V_O} \ , \quad I_{pk} = I_I + \frac{\Delta I_{pk-pk}}{2} \ , \quad L = \frac{V_I d}{f \Delta I_{pk-pk}} \tag{4.2}$$

$$I_{rms} = \sqrt{I_I^2 + \left(\frac{\Delta I_{pk-pk}}{\sqrt{12}} \right)^2} \ , \quad \Delta B_{pk-pk} = \frac{\Delta I_{pk-pk} B_{max}}{I_{pk}} \tag{4.3}$$

(C) The core breadth, b_c, core height, h_c, window breadth, b_w, and window length, l_w, are set. Note that later in the algorithm **(M)** these dimensions are modified to optimize the mass of the inductor. Fig. 4.2 illustrates these core dimensions.

(D) The mean magnetic path length, l_{mm}, core volume, V_c, and core mass, M_c, are calculated next. The core area, A_c, number of turns, N, airgap length, l_g^n, airgap area, A_g, and fringing factor, F_f^n are also determined. The relative permeability of the material, μ_r, is estimated and input to the design algorithm.

$$l_{mm} = 2(2b_c + b_w + l_w) \ , \quad V_c = b_c h_c l_{mm} \ , \quad M_c = V_c k_{core} \rho_{core} \tag{4.4}$$

$$A_c = b_c h_c \ , \quad N = \frac{V_I d}{\Delta B_{pk-pk} A_c k_{core}} \ , \tag{4.5}$$

$$l_g^n = \frac{\mu_0 A_c k_{core} N^2}{L} - \frac{l_{mm}}{\mu_r} \ , \quad A_g = b_c h_c \tag{4.6}$$

$$F_f^n = 1 + \frac{l_g^n}{\sqrt{A_g}} \log \frac{2(l_w + l_g^n)}{l_g^n} \tag{4.7}$$

(E) The revised airgap length, l_g^{n+1}, is the adjusted airgap length, l_g^n, and accounts for the fringing in the airgap [11]. The new fringing factor, F_f^{n+1} is

also calculated.

$$l_g^{n+1} = \frac{\mu_0 A_c k_{core} N^2 F_f^n}{L} - \frac{l_{mm}}{\mu_r} \tag{4.8}$$

$$F_f^{n+1} = 1 + \frac{l_g^{n+1}}{\sqrt{A_g}} \log \frac{2(l_w + l_g^{n+1})}{l_g^{n+1}} \tag{4.9}$$

(F) Since the fringing factor, F_f, is a function of the airgap length, l_g, $F_f = F_f(l_g)$, the airgap length is iteratively adjusted until the revised airgap length, l_g^{n+1}, is equal to the previous airgap length, l_g^n. This iterative step ensures that all of the fringing in the airgap is considered.

(G) The peak flux density, B_{pk}, and the peak ac flux swing, $B_{ac,pk}$, are now calculated.

$$B_{pk} = \frac{L I_{pk}}{N A_c k_{core}} , \qquad B_{ac,pk} = \frac{L \Delta I_{pk-pk}}{2 N A_c k_{core}} \tag{4.10}$$

The total energy stored in the inductor, E_T, the energy stored in the core, E_c, and the total air-gap energy, E_g can now be calculated, in addition to the core-specific power loss, P_{c-sp}.

$$E_T = \frac{L I_{pk}^2}{2} , \qquad E_c = \frac{B_{pk}^2 V_c k_{core}}{2 \mu_r \mu_0} , \qquad E_g = E_T - E_c \tag{4.11}$$

The equation for core-specific power loss, P_{c-sp}, describing hysteresis and eddy current losses is

$$P_{c-sp} = k\, f^m \left(\frac{\Delta B_{pk-pk}}{2} \right)^n , \qquad \left[\frac{W}{m^3} \right] \tag{4.12}$$

where k, m and n are the core specific-power loss indices. Note that this equation does not consider the gap loss equation presented in Chapter 2 as

the experimental results in Chapter 3, Sections 3.2.2 and 3.6.2 do not justify its inclusion. The actual power loss in the core, P_c, is also calculated.

$$P_c = k f^m B_{ac,pk}^n V_c k_{core} \qquad [W] \tag{4.13}$$

(H) The purpose of the winding gap factor, W_{gf}, is to push the foil away from the gap in order to reduce copper loss due to airgap fringing [46], and is defined as the number of airgap lengths that the foil is moved back from the airgap. In this algorithm, this factor is revised to 1.5 (see finite element analysis in Sections 5.3.1 and 5.3.2). The foil clearance, f_{cl}, is to ensure that there is no creepage. A distance between the two windings, d_w, is also set to ensure the windings fit comfortably inside the core window. For this study, this distance is typically set to 2 mm. These dimensions, along with the winding dimensions in **(J)**, are illustrated in Fig. 4.4. The foil insulation thickness, t_{in}, is specified, and the total insulation thickness, t_{in-tot}, is calculated. The copper fill factor, k_{foil}, winding area, A_w, area per turn, A_t, actual foil thickness, $t_{f(act)}$, mean turn length, l_m, and current density, J, are also calculated. Note that k_{foil} only considers the foil copper insulations thickness relative to the foil thickness.

$$t_{in-tot} = t_{in} N + 2 t_{in} \ , \qquad k_{foil} = 1 - \frac{t_{in-tot}}{b_w - 2 W_{gf} l_g^{n+1} - d_w} \tag{4.14}$$

$$A_w = (b_w - 2 W_{gf} l_g^{n+1} - d_w)(l_w + \frac{l_g^{n+1}}{2} - 2 f_{cl}) \ , \qquad A_t = \frac{A_w k_{foil}}{N} \tag{4.15}$$

$$t_{f(act)} = \frac{A_t}{l_w + \frac{l_g^{n+1}}{2} - 2 f_{cl}} \ , \qquad l_m = 2(h_c + b_c + 4 W_{gf} l_g^{n+1} + \frac{N\, t_{f(act)}}{k_{foil}}) \tag{4.16}$$

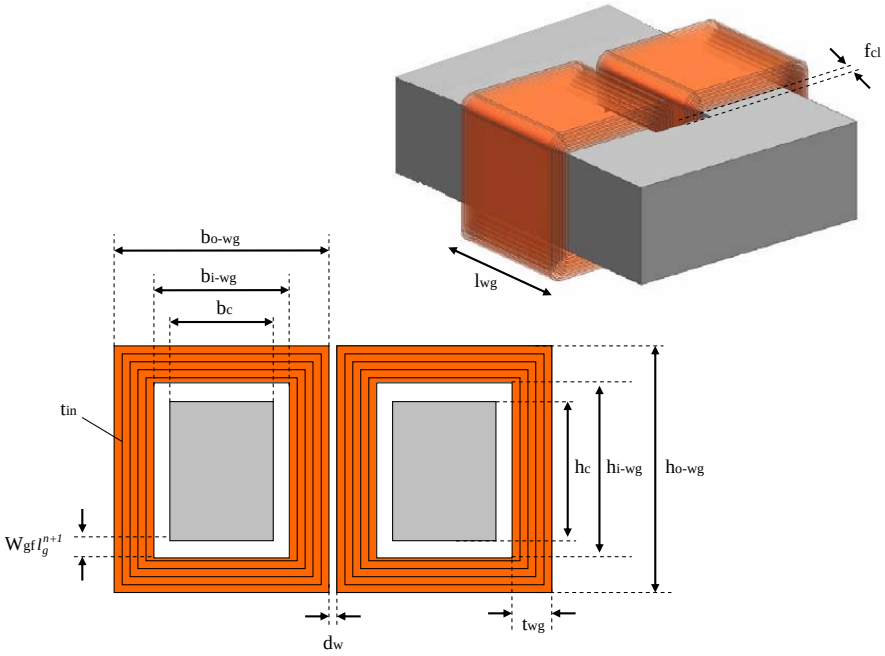

Figure 4.4: Inductor core and winding dimensions.

The current density, J, and the copper resistivity, σ_{cu}, are calculated next. The copper resistivity is calculated at the average operating temperature of the copper, $T_{cu,avg}$. The dc resistance, R_{dc}, and dc copper loss, $P_{cu,dc}$, are also calculated.

$$J = \frac{I_I}{A_t} \ , \quad \sigma_{cu} = \sigma_{cu,20^\circ C}(1 + 0.004(T_{cu,avg} - 20)) \tag{4.17}$$

$$R_{dc} = \frac{N\sigma_{cu} l_m}{A_t} \ , \quad P_{cu,dc} = R_{dc} I_I^2 \tag{4.18}$$

(I) The revised inductor rms current, $I_{rms,n}$, considers the current harmonics, I_n, and is derived in Appendix A, as is the effective winding resistance, R_{we}. Dowell's method is used to calculate the skin and layer effects.

$$I_{rms,n} = \sqrt{I_0^2 + I_1^2 + I_2^2 + ... + I_n^2} \tag{4.19}$$

$$R_{we} = \frac{R_{w0}\left(I_0^2 + I_1^2 Fr_1 + I_2^2 Fr_2 + ... + I_n^2 Fr_n\right)}{I_{rms,n}^2} \tag{4.20}$$

The total copper loss, P_{cu}, and copper loss per volume, P_{cu-sp}, can now be calculated. The copper volume, V_{cu}, and the mass of the copper, M_{cu}, are also calculated.

$$P_{cu} = R_{we} I_{rms,n}^2 \ , \quad V_{cu} = A_t l_m \ , \quad M_{cu} = V_{cu}\rho_{cu} \ , \quad P_{cu-sp} = \frac{P_{cu}}{V_{cu}} \tag{4.21}$$

where ρ_{cu} is the copper density.

(J) The winding dimensions, illustrated in Fig. 4.4, are calculated next. The winding thickness, t_{wg}, and the length of the winding, l_{wg}, are calculated first. The outer and inner breadths of the winding, b_{o-wg} and b_{i-wg} respectively, are calculated as are the outer and inner heights of the winding, h_{o-wg} and h_{i-wg} respectively.

$$t_{wg} = \frac{h_c - 2W_{gf} l_g^{n+1} - d_w}{2} \ , \quad l_{wg} = l_w + \frac{l_g^{n+1}}{2} + 2f_{cl} \tag{4.22}$$

$$b_{o-wg} = 2t_{wg} + 2W_{gf} l_g^{n+1} + b_c \ , \quad b_{i-wg} = 2W_{gf} l_g^{n+1} + b_c \tag{4.23}$$

$$h_{o-wg} = 2t_{wg} + 2W_{gf} l_g^{n+1} + h_c \ , \quad h_{i-wg} = 2W_{gf} l_g^{n+1} + h_c \tag{4.24}$$

The inductor length, l_{idr}, breadth, b_{idr}, height, h_{idr}, volume, V_{idr} and mass, M_{idr}, are calculated. The total power loss in the inductor, P_{loss}, is also calculated.

$$l_{idr} = 2b_c + l_w + \frac{l_g^{n+1}}{2} \ , \quad b_{idr} = 2b_c + b_w + 2t_{wg} + 2W_{gf} l_g^{n+1} \tag{4.25}$$

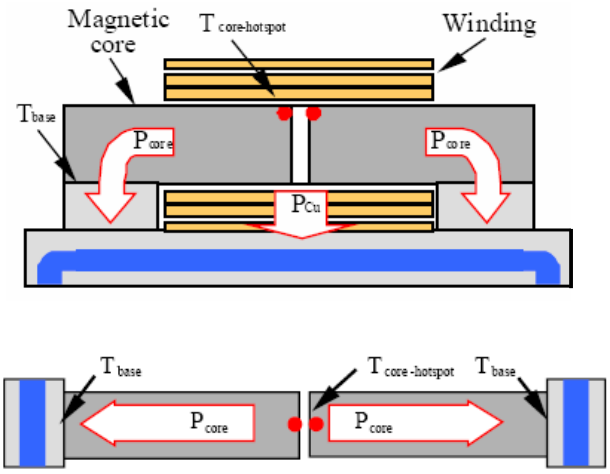

Figure 4.5: Inductor cooling 2-D model (above) and its equivalent 1-D model (below).

$$h_{idr} = h_{o-wg} \ , \qquad V_{idr} = l_{idr} b_{idr} h_{idr} \tag{4.26}$$

$$M_{idr} = M_c + M_{cu} \ , \qquad P_{loss} = P_c + P_{cu} \tag{4.27}$$

(K) The thermal conductivity of the core, λ_c, the thermal conductivity of the copper, λ_{cu}, and the thermal conductivity of the insulation at the base plate, λ_{in}, are input. The cold-plate cooling relies on conductive heat transfer as shown in Fig. 4.5. The heat path for the core and winding are assumed to be separate. The 2D heat transfer problem can be simplified by reduction to a 1D model. For simplicity, the core is assumed to be placed on the cold-plate such that the coldplate makes contact with both sides of the core as shown in Fig. 4.5.

The winding is modeled as an equivalent straight bar with a length equal to the average heat path from the winding hotspot to the cold-plate as shown

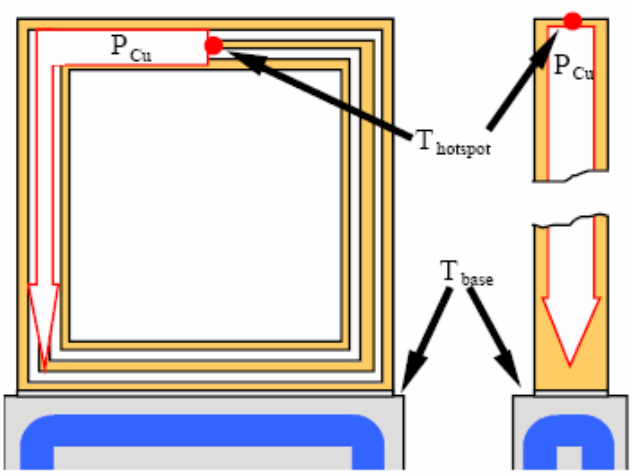

Figure 4.6: Winding cooling 2-D model and its 1-D equivalent.

in Fig. 4.6. The total power loss generated in the copper, P_{cu}, is transferred through the insulation layer, with thermal conductivity, λ_{in}, between the winding and the cold-plate.

The temperature rise of the core, ΔT_c, and the temperature rise of the copper, ΔT_{cu}, are now calculated. The base plate temperature, T_{base}, is a design specification and is dependent on the cooling system of the converter. In this algorithm, T_{base} is typically set to 70 °C. The maximum temperature of the core, T_{c-max}, and the maximum temperature of the copper, T_{cu-max}, are also calculated.

$$\Delta T_c = \frac{P_{c-sp}}{2\lambda_c}\left(\frac{l_w}{2} + b_c\right)^2 \tag{4.28}$$

$$\Delta T_{cu} = \frac{P_{cu-sp}\left(\frac{b_{i-wg}}{2} + h_{o-wg}\right)^2}{2\lambda_{cu}} + \frac{P_{cu-sp}}{\lambda_{in}}\left(\frac{b_{i-wg}}{2} + h_{o-wg}\right)t_{in} \tag{4.29}$$

$$T_{c-max} = T_{base} + \Delta T_c\ , \qquad T_{cu-max} = T_{base} + \Delta T_{cu} \tag{4.30}$$

(L) The temperature rise of the core and the copper are now considered. The core dimensions, b_c, h_c, b_w and l_w are adjusted in **(M)** if the temperature rise of the core, ΔT_c, and the temperature rise of the copper, ΔT_{cu}, exceed the maximum temperature of the core, T_{c-max}, and the maximum temperature of the copper, T_{cu-max}.

(M) The EXCEL solver optimizes the total mass of the inductor, M_{idr}, by adjusting the core dimensions, b_c, h_c, b_w and l_w. Limits are set for the peak flux density, B_{pk}, length of airgap, l_g^{n+1}, efficiency, η, maximum temperature of the core, T_{c-max}, and maximum temperature of the copper, T_{cu-max}. The length of airgap, l_g^{n+1}, is limited to reduce the fringing core and copper losses. This limit is dependent on the number of gaps in the inductor core and is typically set to 4 mm (2 mm per leg) for a single cut core.

4.3 Constant Inductance, Variable Frequency Analysis

In this section we investigate the variation of inductor weights with frequency for a constant inductance value for both conduction and natural-convection cooling. The conduction cooled design algorithm is easily modified to include natural-convection cooling [41]. The design algorithm is used to analyze inductor designs for a 40 kW converter with an inductance of 50 μH. Iron-based amorphous metal and 6.5 % silicon steel described in Table 2.1 are analyzed for the same converter specifications with input voltage, $V_I = 200$ V and output voltage, $V_O = 400$ V. The switching frequency, f, is swept from 10 to 30 kHz in steps of 5 kHz. The ripple ratio, r, decreases from a maximum of 1 at 10 kHz to a minimum of 0.333 at 30 kHz.

The inductor specifications are: core fill factor, k_{core}, is selected from Table 2.1, maximum flux density, B_{max}, is de-rated by 85 % of the saturation flux density, B_{sat}, winding gap factor, $W_{gf} = 1.5$, number of gaps, $N_g = 2$, foil clearance, $f_{cl} = 4$ mm, distance between windings, $d_w = 2$ mm, and foil insulation thickness, $t_{in} = 0.1$ mm. The limit on the length of the airgap per leg, $l_{g/leg} = 1$ mm. The ambient temperature, T_{amb}, and the temperature of the cold plate, $T_{cold,plate}$, are set at 70 °C. The maximum temperature rise, ΔT_{max}, allowed for each material is dependent on the continuous operating temperature of the material shown in Table 2.1, e.g. $\Delta T_{max} = 80$ °C for iron-based amorphous material (150 °C minus 70 °C).

Fig. 4.7 plots the inductor weight vs. frequency for the above inputs. The weight of the inductor decreases with increasing frequency for a given material temperature rise. As the frequency is increased the peak-to-peak ripple current, ΔI_{pk-pk}, and the peak-to-peak magnetic flux swing, ΔB_{pk-pk} are reduced.

Conduction cooling, rather than natural convection, is shown to reduce the weight of the inductor. The weight of the 6.5 % silicon steel inductor is reduced by around a factor of ten compared to natural-convection cooling due to the high thermal conductivity of the material. Iron-based amorphous metal and 6.5 % silicon steel are competitive materials over the frequency range of interest.

4.4 High-Power Custom Inductor Design

The inductor algorithm in Section 4.2 is now used to derive the dimensions of two inductors for a 40 kW boost converter. The converter specifications are: $I_I = 200$ A, $V_I = 200$ V, $V_O = 400$ V, $f = 16$ kHz and $r = 0.695$. The inductors are designed with the iron-based amorphous metal material as the thermal orientation is optimum for this application as discussed in Sections 3.5 and 4.1. The core loss

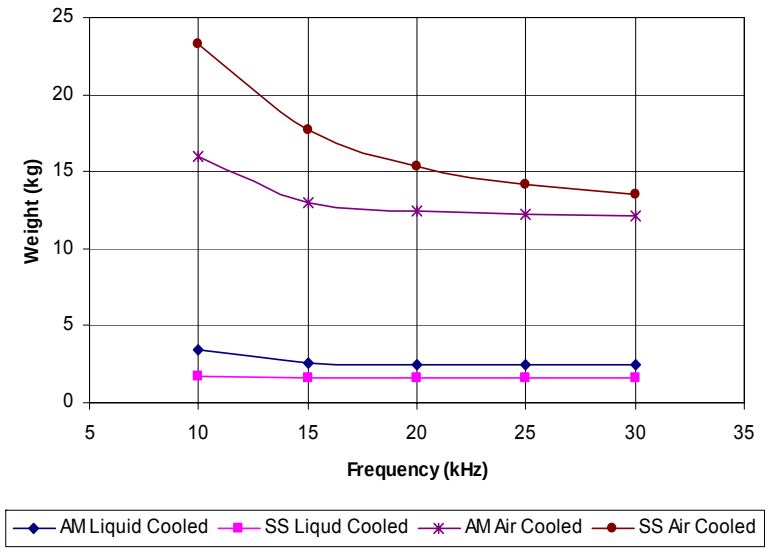

Figure 4.7: Inductor weight vs. frequency for constant inductance (40 kW).

of the iron-based amorphous metal is also lower than that of the 6.5 % silicon steel material as illustrated in Section 3.6.1.

The inductor specifications are: $k_{core} = 0.83$, B_{max} is derated by 85 % of $B_{sat} = 1.56$ T, $W_{gf} = 1.5$, and $f_{cl} = 4$ mm. The base plate temperature is set at $T_{base} = 70$ °C. The maximum temperature of the copper is set at $T_{cu,max} = 150$ °C and the maximum temperature of the core is set at $T_{c,max} = 130$ °C.

A foil winding is selected for the two designs due to the high peak-to-peak inductor current, ΔI_{pk-pk}, of 139 A. Finite element simulations in Section 5.4 show that helical windings have excessive ac losses due to the high ripple current associated with this converter. A foil winding is selected over a litz winding as it is more suitable for high volume production and has a lower cost. The litz winding is more expensive than a foil winding due to the construction costs of the litz winding and the manufacturing of the litz winding terminations.

L	$\mathbf{N}_{leg}$	$\mathbf{l}_{g/leg}$	$\mathbf{k}_{cu}$	$\mathbf{b}_c$	$\mathbf{b}_w$	$\mathbf{h}_c$	$\mathbf{l}_w$	**AP**	$\mathbf{M}_c$	$\mathbf{M}_{idr}$
μH	series	mm		mm	mm	mm	mm	cm^4	kg	kg
45	6	2.0	0.34	26	15	35	38	52	1.039	1.299

Table 4.1: Design 1 boost inductor characteristics.

4.4.1 Design 1

The inductor algorithm is used to derive a custom core that allows a maximum airgap of 4 mm (2 mm per leg). A single-cut core is used in this design and eliminates the additional cost of cutting the core for the boost inductor.

Fig. 4.2 and Table 4.1 illustrate the core dimensions for Design 1. The core has the following characteristics: core breadth, $b_c = 26$ mm, core height, $h_c = 35$ mm, window breadth, $b_w = 15$ mm, and window length, $l_w = 38$ mm. The core area, $A_c = 746$ mm^2, mean magnetic path length, $l_m = 220$ mm, number of turns, $N = 12$, total length of airgap, $lg = 4$ mm, flux swing, ΔB_{pk-pk} =0.68 T and the core mass, $M_c = 1.039$ Kg. The copper windings are constructed with a foil thickness, $t_{fact} = 0.5$ mm, and the mass of the copper, $M_{cu} = 0.26$ Kg. The copper losses in the windings are calculated in Appendix B, Section B.0.8. The temperature hotspot, located on the top of the copper winding, $T_{cu} = 142$ °C and is calculated using the conduction-cooling inductor algorithm.

Table 4.2 compares inductor designs in this chapter with a baseline automotive inductor analyzed in Section 5.2. The hotspot temperature of the copper, T_{cu}, in Table 4.2 for this design is 131 °C as calculated using finite element analysis in Section 5.3.1. Good correlation is achieved between the temperatures calculated using the inductor algorithm (142 °C) and finite element analysis (131 °C). A reduction in core and copper mass by a factor of two is achieved with this design compared to that of the baseline automotive inductor. However, as the size and weight decrease, the inductor power loss and temperature rise increase. Experimental results are presented for Design 1 in Section 5.5.

Core Name	Power	Winding Type	$\mathbf{P}_{loss}$	$\mathbf{T}_{cu,alg}$	$\mathbf{T}_{cu,FEA}$	$\mathbf{T}_{core,alg}$	$\mathbf{T}_{core,FEA}$	$\mathbf{M}_{idr}$
	(kW)		**(W)**	**(°C)**	**(°C)**	**(°C)**	**(°C)**	**(kg)**
Automotive	40	Litz	172	110	110	1.66	1.44	3.1
Design 1	40	0.5 mm foil	275	142	131	120	136	1.299
Design 2	40	0.5 mm foil	332	150	151	107	112	0.999

Table 4.2: Summary of designed inductors.

4.4.2 Design 2

Design 2 is an aggressive design aiming to reduce the total weight of the core and copper of the baseline inductor by a factor of three. The inductor algorithm is used to derive a custom core that allows a maximum airgap of 8 mm (4 mm per leg). This design has a large airgap and a multi-cut core is required. The increase in cost per extra cut with the iron-based amorphous material is significant but the overall weight and volume is significantly reduced as the amount of material required is more than 3 times less. Again, a foil winding is used to reduce the cost of the inductor in high volume.

Fig. 4.8 and Table 4.3 illustrate the core dimensions for Design 2. The core has the following characteristics: core breadth, $b_c = 25$ mm, core height, $h_c = 20$ mm, window breadth, $b_w = 20$ mm, window length, $l_w = 36$ mm, and distance between gaps, $k = 12$ mm. The core area, $A_c = 415$ mm^2, mean magnetic path length, $l_m = 220$ mm, number of turns, $N = 22$, length of airgap per leg, $lg = 4$ mm, flux swing, ΔB_{pk-pk} =0.68 T and the core mass, $M_c = 0.592$ Kg. The copper windings are constructed with a foil thickness, $t_{fact} = 0.5$ mm, and the mass of the copper, $M_{cu} = 0.407$ Kg. The copper losses in the windings are calculated in Appendix B, Section B.0.9. The hotspot temperature, located on the top of the copper winding, $T_{cu} = 150$ °C and is calculated using the conduction-cooling inductor algorithm.

Table 4.2 compares this design with a baseline automotive inductor analyzed

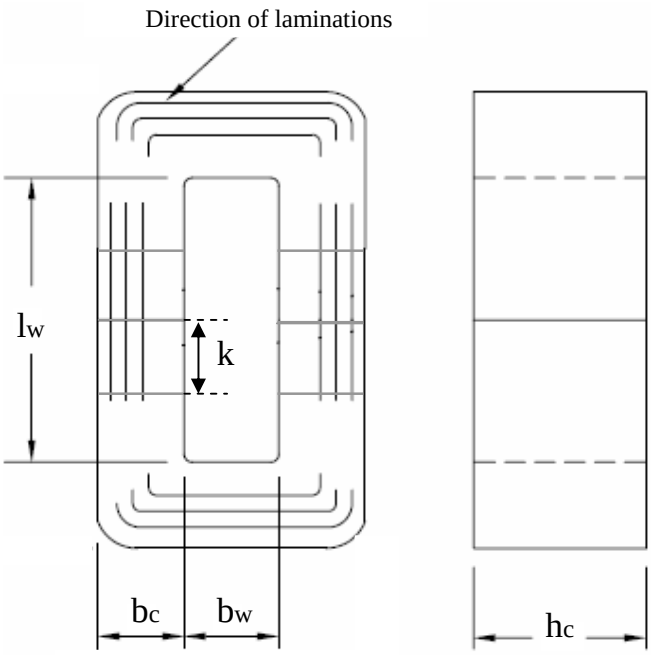

Figure 4.8: Drawing of Metglas core: Design 2.

L	$\mathbf{N}_{leg}$	$\mathbf{l}_{g/leg}$	$\mathbf{k}_{cu}$	$\mathbf{b}_c$	$\mathbf{b}_w$	$\mathbf{h}_c$	$\mathbf{l}_w$	**AP**	$\mathbf{M}_c$	$\mathbf{M}_{idr}$
μH	series	mm		mm	mm	mm	mm	cm^4	kg	kg
45	11	4.0	0.49	25	20	20	36	36	0.592	0.999

Table 4.3: Design 2 boost inductor characteristics.

in Section 5.2. The temperature of the copper, T_{cu}, in Table 4.2 for this design is 151 °C as calculated using finite element analysis in Section 5.3.2. Excellent correlation is achieved between the temperatures calculated using the inductor algorithm (150 °C) and finite element analysis (151 °C). Experimental results are presented for Design 2 in Section 5.5.

It was noted by the manufacturer of the iron-based amorphous metal core, Metglas [13], that the minimum length of a core segment for a multigap design should not be less than 20 mm due to delamination of the core. There is a degradation of core loss when the iron-based amorphous metal core is cut as illustrated in Section 3.2.1 and [51]. The 6.5 % silicon steel material does not suffer from delamination of the core and can be cut down to a segment length of 10 mm. The 6.5 % silicon steel material is a better option when small segment lenghts are required and could be used in conjuction with the end sections of the iron-based amorphous metal core to make a hybrid inductor.

4.5 Summary

In this chapter, a conduction cooling inductor design algorithm is developed. The algorithm is developed for foil-wound inductors with gapped CC-cores in the low to medium frequency range. The algorithm considers the following factors: winding skin and layer effects; distance from airgap to minimize copper fringing loss, airgap length to reduce core and copper fringing losses, creepage and clearance, separate cooling paths for the core and the copper. The mass of the inductor is optimized in the design algorithm.

Conduction cooling, rather than natural convection, is shown to reduce the weight of the inductor. The weight of the 6.5 % silicon steel inductor is reduced by around a factor of ten compared to natural-convection cooling due to the high

thermal conductivity of the material. Iron-based amorphous metal and 6.5 % silicon steel are competitive materials over the frequency range of interest. Iron-based amorphous metal and 6.5 % silicon steel have lower weights when compared to nanocrystalline and ferrite when conduction cooling is used. The algorithm is also used to develop high-power custom inductors. Finite element analysis is carried out on the new designs in Chapter 5.

It was noted by the manufacturer of the iron-based amorphous metal core, Metglas, that the minimum length of a core segment for a multigap design should not be less than 20 mm due to delamination of the core. There is a degradation of core loss when the iron-based amorphous metal core is cut. The 6.5 % silicon steel material does not suffer from delamination of the core and can be cut down to a segment length of 10 mm. The 6.5 % silicon steel material is a better option when small segment lenghts are required and could be used in conjuction with the end sections of the iron-based amorphous metal core to make a hybrid inductor.

Chapter 5

High-Power Boost Inductor Analysis and Design

This chapter first details the analysis of two high-power boost inductors currently used in the automotive industry. The Toyota Prius THSII boost inductor is analyzed in Section 5.1 and a 40 kW automotive boost inductor is analyzed in Section 5.2. Next, the 40 kW inductors designed in Sections 4.4.1 and 4.4.2 are optimized further and compared to the 40 kW automotive inductor in Section 5.2. Detailed finite element analysis of these designs is presented in Section 5.3. In Section 5.4, a helical winding configuration similar to that used in the Toyota Prius THSII boost inductor is investigated for use with the inductor cores designed in Sections 4.4.1 and 4.4.2. Designs 1 and 2 with the 0.5 mm foil windings are tested in a 32.4 kW single phase boost converter in Section 5.5.

5.1 Toyota Prius THSII Boost Inductor

Fig. 5.1 shows the electrical schematic of the Toyota Prius THSII boost converter. The nominal input power, P_{in}, is 21 kW. The input voltage, V_{in}, of 201 V is boosted up to a maximum of 500 V. The switching frequency, f_{sw}, of the converter is 10 kHz. The converter has a 425 μH inductor. The large output capacitance of

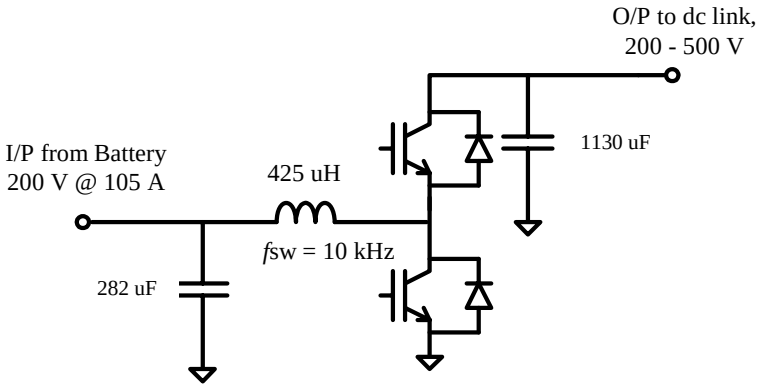

Figure 5.1: Electrical schematic of the Prius THSII boost converter

1130 μF represents the traction system inverter bus capacitance. This capacitance is larger than would be necessary for the boost converter alone and is mostly sized based on the inverter bus currents.

The Prius converter operates at 10 kHz, a relatively low frequency. This low frequency switching results in high efficiency as the switching losses of the converter become dominant at higher frequencies. The inductor uses 6.5 % silicon steel of type 10JNHF600 from JFE as the magnetic core and a copper helical winding set from Togo Incorporated [61]. The silicon steel material has a lower magnetostriction of 0.1 p.p.m [62] compared to that of the amorphous metal with a value of 27 p.p.m. [63]. As the boost converter switches with a frequency in the audible range ($<$ 16 kHz) the silicon steel material has an advantage over the amorphous metal regarding audible noise. Conducted and radiated EMI are also less significant at lower frequency operation.

5.1.1 THSII Boost Inductor Characteristics

Figs. 5.2 to 5.4 show pictures of the Prius THSII boost inductor. These pictures were provided to the university for investigation. This inductor is encapsulated

L	$\mathbf{N}_{leg}$	$\mathbf{l}_{g/leg}$	$\mathbf{k}_{cu}$	$\mathbf{b}_c$	$\mathbf{b}_w$	$\mathbf{h}_c$	$\mathbf{l}_w$	**AP**	$\mathbf{M}_c$	$\mathbf{M}_{idr}$	$\mathbf{V}_{idr}$
μH	parallel	mm		mm	mm	mm	mm	cm^4	Kg	Kg	cm^3
435	28	1.12	0.44	20	20	50	50	100	1.45	2.4	576

Table 5.1: Prius THSII boost inductor characteristics.

and potted and is fabricated using parallel windings on a laminated core. The inductor is cut with a saw at the midpoint to reveal two helical windings around each leg of the laminated core. Fig. 5.3 shows a top view of the inductor with 14 turns of the winding still remaining on each leg after the part was cut in two. After depotting in a hot bath of N-Dimethyl formamide, (DMF) the copper windings are pulled off the core. The copper windings are composed of a rectangular wire (approx. 6mm by 1.3 mm) and are located approximately 3 mm away from the airgap. Two ceramic spacers (20 mm x 50 mm x 1.12 mm) are also revealed as seen in Fig. 5.4. The core breadth, b_c, and core height, h_c, are 20 mm and 50 mm respectively. The airgap length per leg, $l_{g/leg}$, is 1.12 mm and the windings are located approximately 3 mm away from the airgaps. The window length, l_w, and window breadth, b_w are 50 mm and 20 mm respectively. The inductor core is mounted vertically which is the optimum thermal path for the 6.5 % silicon steel material as previously illustrated in Fig.3.28. Table 5.1 illustrates the inductor characteristics. Fig. 5.5 shows a full inductor core and a set of windings.

The winding appears to be a good low cost simple approach. Clearly, TMC has optimized the approach for manufacturing as there is no deformation of the enamel when the copper is wound around the inductor core corners. A detailed loss and thermal analysis is carried out on the component in the following section.

5.1.2 THSII Boost Inductor Analysis

The inductor loss and temperature rise are analyzed in this section. The system currents are previously derived in Section 1.4.3. The core loss, P_c, is calculated

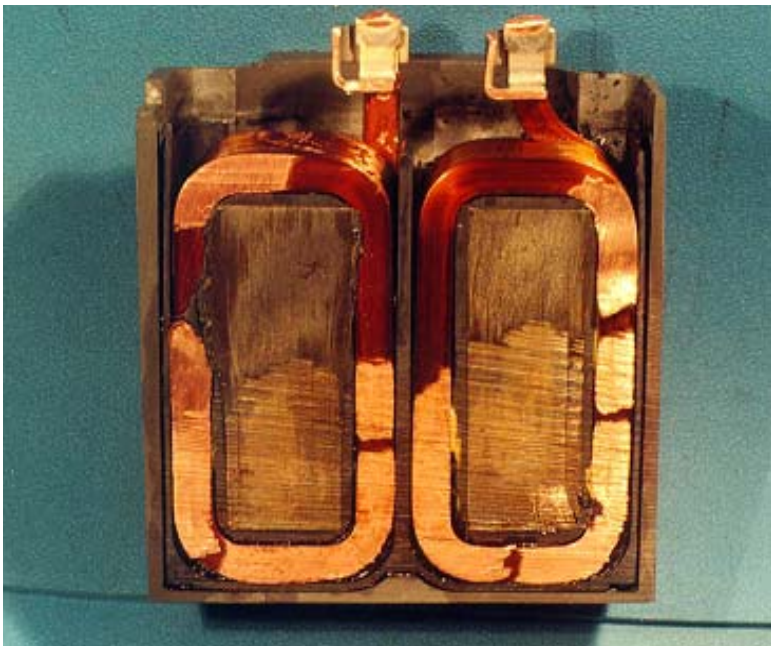

Figure 5.2: Picture of TMC Prius THSII boost inductor.

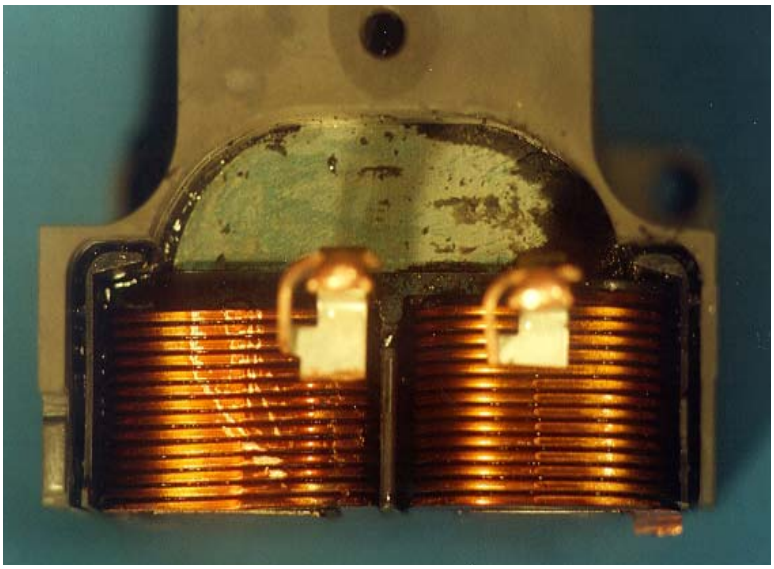

Figure 5.3: Picture of TMC Prius THSII boost inductor (topview).

Figure 5.4: Picture of Prius THSII boost inductor with ceramic spacers.

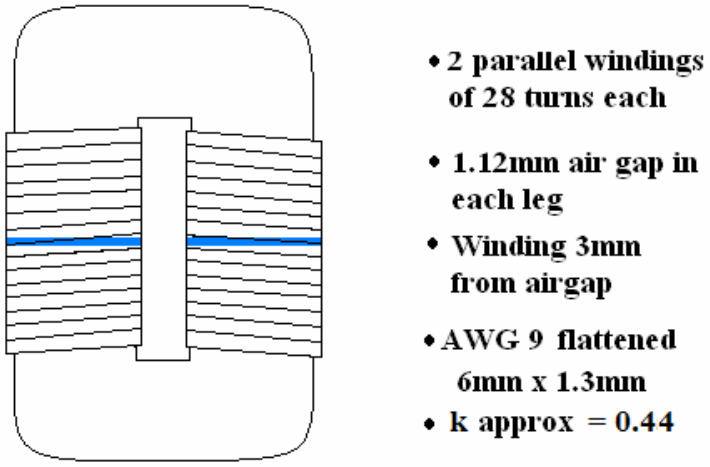

Figure 5.5: Drawing of Prius THSII inductor core and windings (not to scale).

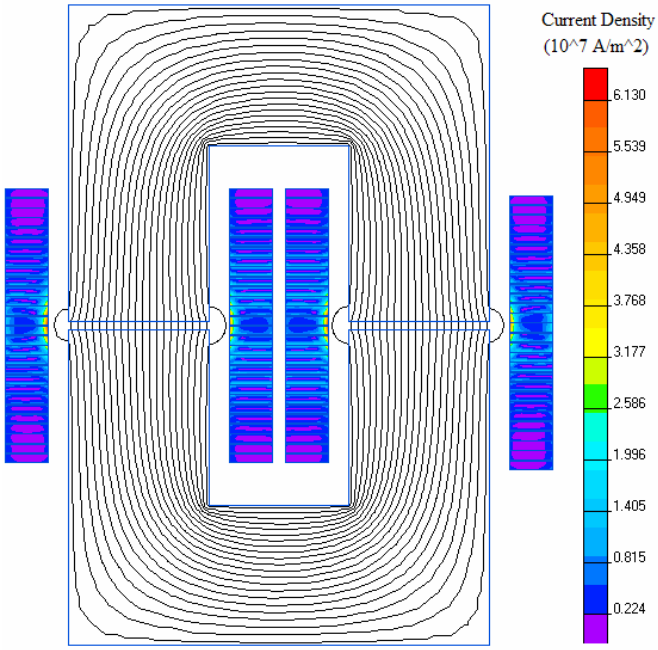

Figure 5.6: AC loss simulation of Prius THSII inductor.

first using the core loss indices in Table 2.1.

$$B_{ac,pk} = \frac{L\Delta I_{pk-pk}}{2NA_c k_{core}} = 0.24\ T \tag{5.1}$$

$$P_c = kf^m B_{ac,pk}^n M_c = 62.4\ W \tag{5.2}$$

The dc copper loss, $P_{cu,dc}$, is calculated next for the two windings.

$$P_{cu,dc} = \frac{2\sigma_{cu} l_m N}{A_{cu}} (I_{dc})^2 = 89.3\ W \tag{5.3}$$

The ac copper loss, $P_{cu,ac}$, is 87.1 W, as calculated using finite element simulation. Fig. 5.6 shows an ac loss finite element simulation of the Prius inductor. The total loss, P_{loss}, for the Prius THSII boost inductor is calculated below.

$$P_{loss} = P_c + P_{cu,dc} + P_{cu,ac} = 238.8\ W \tag{5.4}$$

The temperature rise of the inductor is calculated using the above losses in a finite element thermal model. Fig. 5.7 shows a finite element thermal simulation

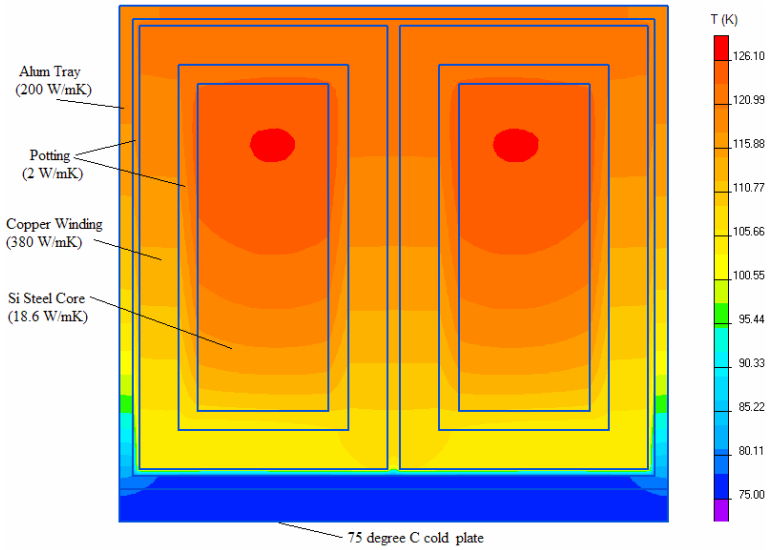

Figure 5.7: Thermal simulation of Prius THSII inductor.

of the Prius inductor with a 2 mm thick aluminum tray. The aluminum has a thermal conductivity, λ_{al}, of 200 W/mK. The thermal conductivity of the core, λ_{core}, is 18.6 W/mK and is measured along the lamination. The core is mounted vertically and the copper windings with a thermal conductivity, λ_{cu}, of 380 W/mK act as thermal heatsinks for the inductor core. The potting material is assumed low cost with a thermal conductivity of 2 W/mK. The temperature hotspot of the inductor, T_{core}, is located near the top of the core and is simulated at 126 °C on a 75 °C cold plate.

5.2 Automotive Boost Inductor

Fig. 5.8 shows the electrical schematic of a 3-phase high power interleaved automotive boost converter. The input power per phase is 40 kW, giving a total input power, P_{in}, of 120 kW. The input voltage, V_{in}, of 200 V is boosted up to a maximum of 400 V. The switching frequency, f_{sw}, of the converter is 16 kHz. Each

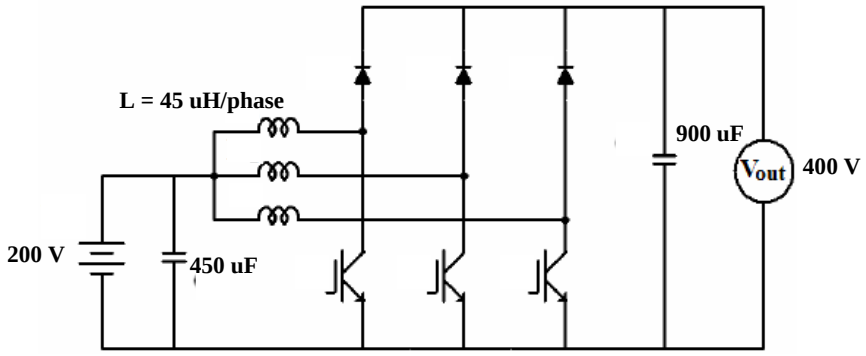

Figure 5.8: Electrical schematic of 3-phase high power interleaved boost converter

phase has a 45 μH inductor and the converter input and output capacitances are 450 μF and 900 μF respectively.

The boost inductor in this converter uses the iron-based amorphous metal of material type 2605SA1 from Metglas [63]. As shown in Chapter 3, Section 3.2.1, the iron-based amorphous metal material has a lower core loss than that of the 6.5 % silicon steel. However, as discussed in Section 3.5, the higher thermal conductivity of the 6.5 % silicon steel makes it competitive with the iron-based amorphous metal. The cost of the iron-based amorphous metal material tends also to be lower than that of the 10JNHF600 material from JFE. A litz winding structure is used in this inductor. The switching frequency of the converter is also higher than the Prius THSII boost converter because of the audible noise issues with the iron-based amorphous metal at frequencies lower than 16 kHz.

5.2.1 Automotive Boost Inductor Characteristics

Fig. 5.9 shows a picture of the 45 μH automotive boost inductor under investigation. The inductor is potted in a soft potting material and enclosed in an aluminum tray. The core is isolated from the aluminum tray using Kapton tape. Two parallel litz windings of 12 turns each are used. The litz windings have two

L	$\mathbf{N}_{leg}$	$\mathbf{l}_{g/leg}$	$\mathbf{k}_{cu}$	$\mathbf{b}_c$	$\mathbf{b}_w$	$\mathbf{h}_c$	$\mathbf{l}_w$	**AP**	$\mathbf{M}_c$	$\mathbf{M}_{idr}$	$\mathbf{V}_{idr}$
μH	parallel	mm		mm	mm	mm	mm	cm^4	Kg	Kg	cm^3
45	12	2.0	0.3	30	26	30	60	145	1.46	3.62	713

Table 5.2: Automotive boost inductor characteristics.

layers of 6 turns each and each turn is constructed with two square litz wires. The number of strands per wire is 1295, each with a diameter of 0.089 mm (AWG 39). Fig. 5.10 illustrates the windings and the core. The core cross-sectional area, A_c, core breadth, b_c, core height, h_c, window length, l_w, and the window breadth, b_w, are 900 mm^2, 30 mm, 30 mm, 60 mm and 26 mm, respectively. The airgap length per leg, $l_{g/leg}$, is 2 mm and the windings are located 2.5 mm away from the airgap. The inductor core is mounted vertically which is not optimum for this material as the thermal conductivity against the lamination is just 0.5 W/mK at the core end sections. The length of the thermal path for the core is also at a maximum for a vertical mounting configuration. Table 5.2 lists the parameters of the automotive boost inductor characteristics.

The litz winding structure can be expensive compared to the simpler helical winding structure used in the Prius inductor. Termination of the fine litz wire, a high-cost potting material and the large material quantities leads to a high cost design. The weights of the core, M_c, and the copper, M_{cu}, are 1.46 kg and 1.66 kg, respectively. The total weight of the potted inductor, M_{idr}, is 3.62 kg. A detailed loss and thermal analysis is carried out on the component in the following section.

5.2.2 Automotive Boost Inductor Analysis

The inductor loss and temperature rise are analysed in this section. The inductor specifications above are identical to those previously described in Section 4.4. The

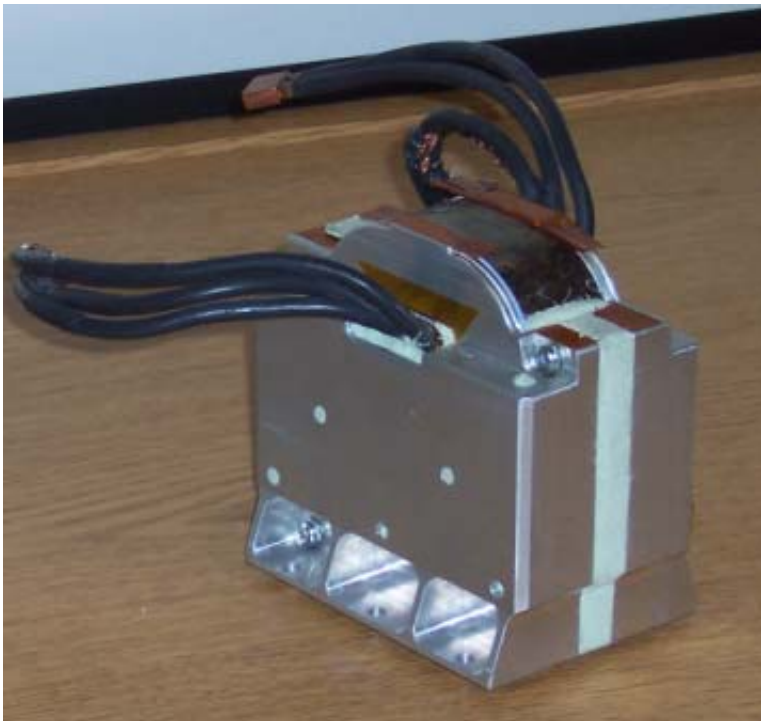

Figure 5.9: Automotive boost inductor.

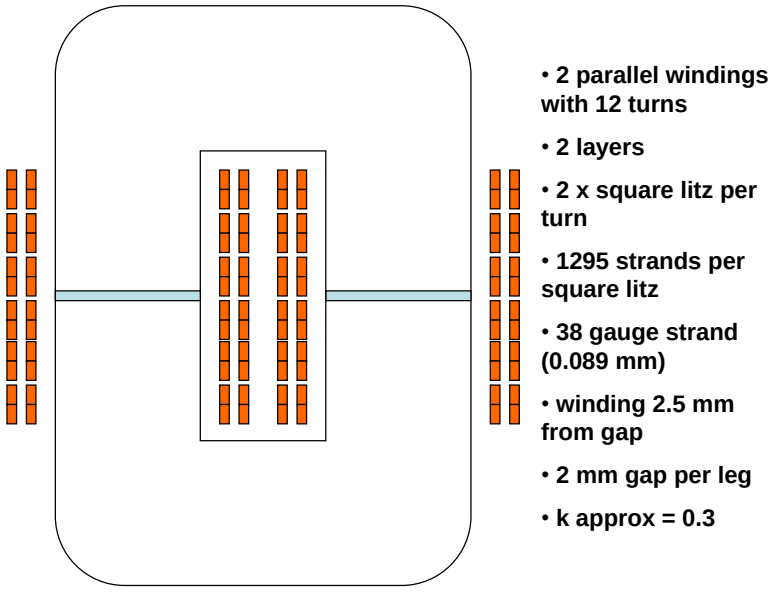

Figure 5.10: Drawing of automotive boost inductor core and windings.

core loss, P_c, is calculated first using the core loss indices in Table 2.1.

$$B_{ac,pk} = \frac{L\Delta I_{pk-pk}}{2NA_c k_{core}} = 0.34\ T \tag{5.5}$$

$$P_c = kf^m B_{ac,pk}^n M_c = 125.4\ W \tag{5.6}$$

The dc copper loss, $P_{cu,dc}$, is calculated next for the two windings.

$$P_{cu,dc} = \frac{2\sigma_{cu} l_m N}{A_{cu}} (I_{dc})^2 = 47\ W \tag{5.7}$$

The ac copper loss, $P_{cu,ac}$, is assumed negligible for the litz winding construction. The total loss, P_{loss}, for the automotive boost inductor is calculated below.

$$P_{loss} = P_c + P_{cu,dc} = 172.4\ W \tag{5.8}$$

The experimental temperature hotspot of the automotive inductor, T_{core}, is 110 °C on a 75 °C cold plate and was measured in a 40 kW single-phase boost converter in Mainz Kastel, Germany. This shows that the automotive inductor is conservatively designed and has significant margin as the maximum operating temperature of the iron-based amorphous material is 150 °C.

5.3 Boost Inductor Design

The inductors designed in Sections 4.4.1 and 4.4.2 are now optimized further using finite element analysis to minimize the size, volume and associated costs.

5.3.1 Design 1

Design 1 in Section 4.4.1 is designed with a target of reducing the total weight of the core and the copper by a factor of 2 compared to the automotive inductor analyzed in Section 5.2. The inductor algorithm in Section 4.2 is used to derive

a custom core that allows a maximum airgap of 4 mm (2 mm per leg). A single cut core is used in this design and this removes the extra cost of cutting the core for the boost inductor. It also reduces the impact of higher core loss due to the cutting of the iron-based amorphous metal core material, as illustrated in 3.2.1 and [51]. A foil winding structure is also used to reduce the cost when compared to the litz winding used in the automotive inductor in Section 5.2.

Design 1: Core Analysis

The peak-peak flux density, ΔB_{pk-pk}, from the algorithm in Section 4.2 is 0.68 T and the total core loss, P_c, is 89 W at a frequency, f, of 16 kHz. Fig. 5.11 shows a finite element thermal simulation of Design 1. The total core loss, P_c, is used to calculate the temperature hotspot of the core, T_{core}, in the finite element simulation. The thermal conductivity of the core material is 10 W/mK along the lamination and 0.5 W/mK against the lamination. The end sections of the core are fixed to a 200 W/mK aluminum heatsink and the base plate temperature is 65 °C. As shown by the simulation, the core hotspot, T_{core}, is 136 °C and is below the maximum operating temperature of 150 °C for the core.

Design 1: Winding Analysis

Foil is chosen for this application due to the high peak-peak ripple current, ΔI_{pk-pk}, of 139 A. A thin foil helps to reduce the ac copper losses, $P_{cu,ac}$, due to fringing flux, skin and proximity effects. A disadvantage of using a foil winding is the difficulty in removing the heat from the inner layers. To remove this heat a very thin layer of insulation between layers is required. If air gets between the layers the heat will not be removed due to the low thermal conductivity of air (0.026 W/mK). For this reason the foil is sourced from CMC Klebetechnik Gmbh

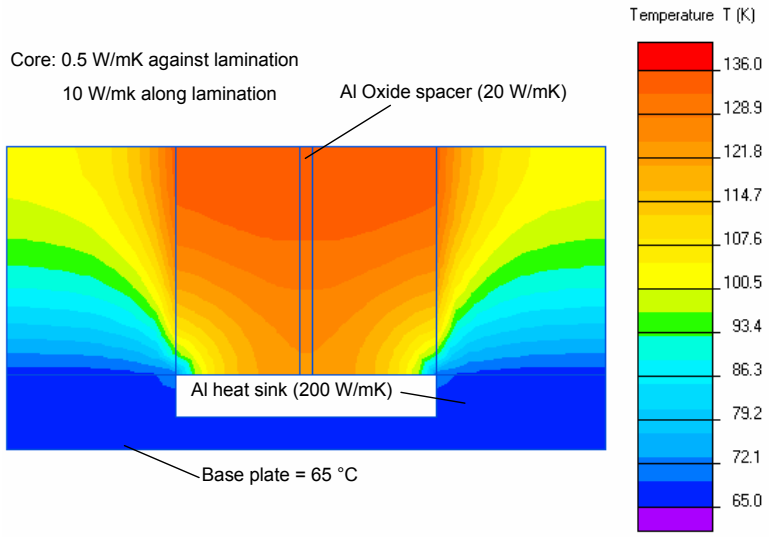

Figure 5.11: Thermal simulation of the core used in Design 1.

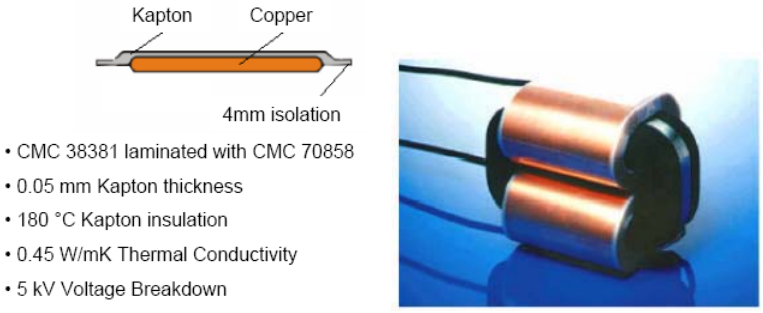

Figure 5.12: Properties of CMC foil.

[64]. CMC provides self-bonding single-layer Kapton-insulated foil. The special Kapton is rated for 180 °C and is coated with thermal adhesive. When the foil is heated for the first time the thermal adhesive on the Kapton between the layers reacts to bond both layers. The thermal conductivity of the special Kapton is 0.45 W/mK and the thickness between each layer is just 0.05 mm. Fig. 5.12 illustrates the foil properties.

The foil windings require 4 mm isolation at the top and bottom ends of the window due to the high voltage operation of the inductor. This reduces the actual

Distance from gap	0.3 mm foil (W)			0.4 mm foil (W)			0.5 mm foil (W)		
	$\mathbf{P}_{cu,ac}$	$\mathbf{P}_{cu,dc}$	$\mathbf{P}_{cu}$	$\mathbf{P}_{cu,ac}$	$\mathbf{P}_{cu,dc}$	$\mathbf{P}_{cu}$	$\mathbf{P}_{cu,ac}$	$\mathbf{P}_{cu,dc}$	$\mathbf{P}_{cu}$
1	131	200	331	130	150	280	131	120	251
2	77	210	287	77	158	235	79	126	205
3	50	220	270	51	165	216	54	132	186

Table 5.3: Copper loss versus distance from gap and foil thickness.

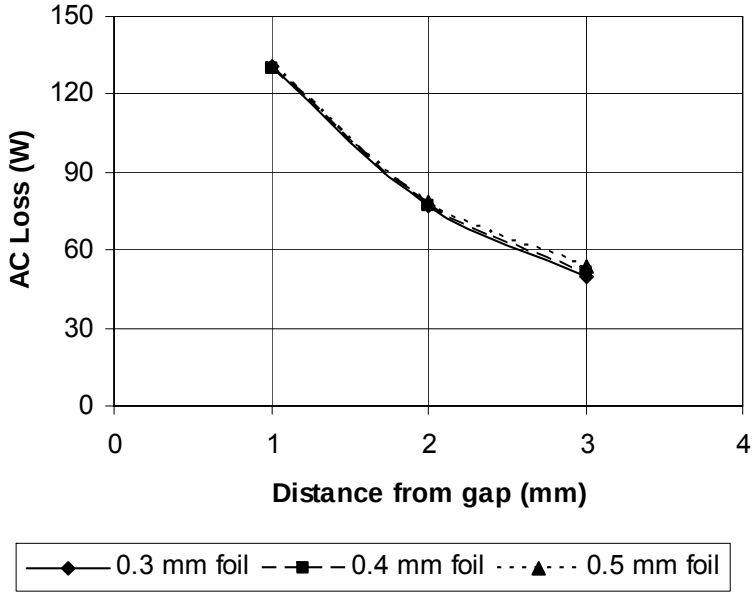

Figure 5.13: AC copper loss versus distance from gap and foil thickness (FEA Analysis).

copper length in the window to 32 mm, (40 mm - 8 mm). Two foil windings with 6 turns each are connected in series to give a total of 12 turns for the inductor. Three foil thicknesses of 0.3 mm, 0.4 mm and 0.5 mm are simulated for both ac losses and heat transfer. The skin depth, δ, at 16 kHz is 0.64 mm. The ac copper losses, $P_{cu,ac}$, from the finite element simulations for the 0.3 mm, 0.4 mm and the 0.5 mm foil windings at distances of 1 mm, 2 mm and 3 mm away from the airgap are shown in Table 5.3. These results are also illustrated in Fig. 5.13.

The three foil thicknesses have similar ac copper losses, $P_{cu,ac}$, for distances of 1 mm, 2 mm and 3 mm away from the airgap. The ac copper losses decrease

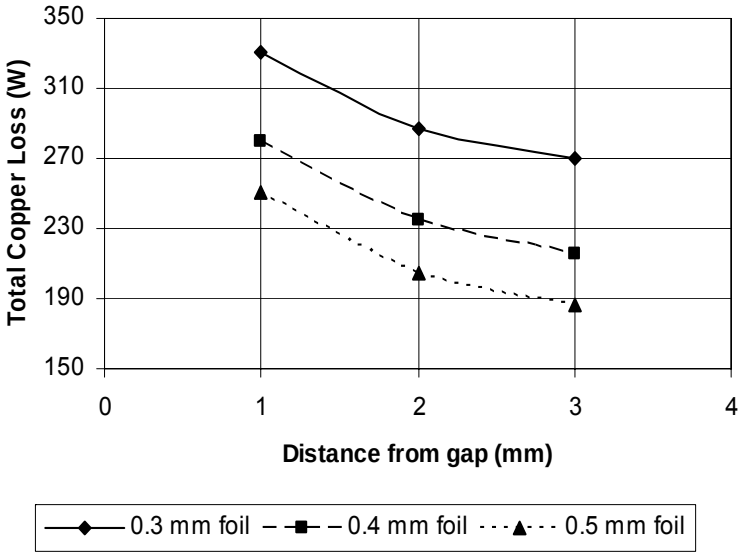

Figure 5.14: Total copper loss versus distance from gap and foil thickness.

significantly when each foil is moved away from the airgap. However, as the distance away from the airgap increases so does the mean turn length of the windings. This increases the dc copper loss, $P_{cu,dc}$, of the windings. The dc copper loss, $P_{cu,dc}$, of each foil is calculated in the conduction-cooling inductor algorithm and the mathematical results are also tabulated in Table 5.3. Here a significant advantage can be seen with the thicker 0.5 mm foil due to the wider cross-sectional area of the copper winding. The total copper loss, P_{cu}, for each of the windings at distances of 1 mm, 2 mm and 3 mm away from the airgap are tabulated in Table 5.3. Fig. 5.14 illustrates the total copper loss versus distance from the airgap for each of the foil thicknesses.

Finite element thermal simulations are carried out on each foil in order to estimate the copper hotspot temperatures, T_{cu}, of the windings. Table 5.4 shows the simulation results for the copper hotspot temperature of each foil as the foil is moved away from the airgap. The total copper loss, P_{cu}, in each foil is that shown in Table 5.3, i.e. 186 W for the 0.5 mm foil located 3 mm away from

Distance from gap	0.3 mm Foil	0.4 mm Foil	0.5 mm Foil
1	228 °C	184 °C	162 °C
2	201 °C	161 °C	141 °C
3	187 °C	150 °C	131 °C

Table 5.4: Copper hotspot versus distance from gap and foil thickness (FEA Analysis).

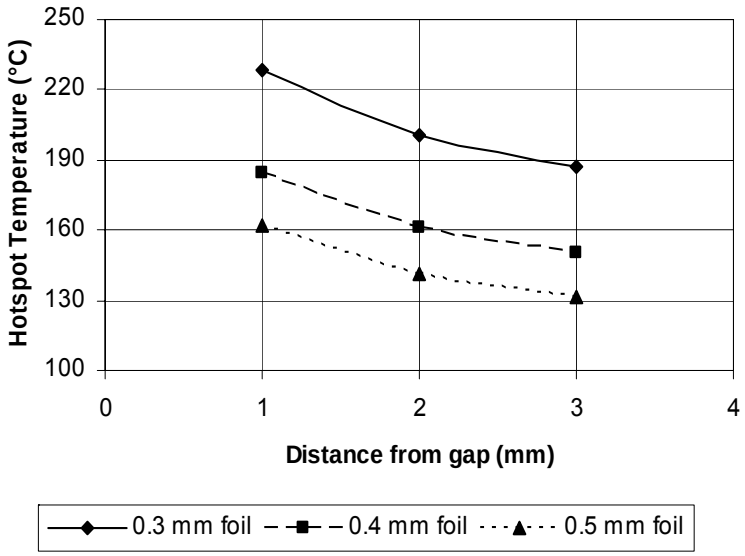

Figure 5.15: Copper hotspot versus distance from gap and foil thickness (FEA Analysis).

the airgap, has a copper hotspot temperature of 131 °C. Fig. 5.15 illustrates the copper hotspot temperature, T_{cu}, for each foil thickness as the foil is moved away from the airgap.

Fig. 5.15 shows that the design with the 0.3 mm foil overheats even at a distance of 3 mm away from the airgap due to dc copper losses. However, the inductor does not overheat if the 0.5 mm foil is used or if the 0.4 mm foil, located at a distance of 2 mm or more away from the airgap, is used. The theoretical weight of the 0.5 mm foil is 0.260 kg and that of the 0.4 mm foil is 0.208 kg. The foil windings are much lighter than the previous automotive inductor litz winding

which weighs 1.66 kg. These inductor designs are summarized in Table 5.7.

Design 1: Aluminum Winding Analysis

Previous study has shown that aluminum may replace copper in high-frequency magnetic designs [65]. The cost of aluminum is lower than it might appear from the cost per unit mass when the much lower density of aluminum is also considered. The disadvantage of higher resistivity becomes less important when high-frequency effects are also considered [65].

In this section Design 1 is analyzed with a 0.9 mm thick aluminum winding for both ac losses and thermal performance. A thicker 0.9 mm aluminum foil is selected as the electrical resistivity of aluminum is higher than the electrical resistivity of copper ($\sigma_{Al} = 4.81\ \Omega/\text{m}$, $\sigma_{cu} = 2.58\ \Omega/\text{m}$, both calculated at 150 °C). The 0.9 mm thick aluminum winding fits within the core window and leaves a 1.5 mm airgap between the core and winding as shown in Fig. 5.16. The winding ac losses, $P_{Al,ac}$, calculated from the finite element simulation are 143 W. The dc aluminum losses, $P_{Al,dc}$, are 107 W. The thermal hotspot of the aluminum winding is estimated at 163 °C as shown in Fig. 5.17. The weight of the aluminum winding is 0.137 kg and the total weight of Design 1 with the aluminum winding is 1.176 kg. The total weight of the inductor is competitive with the previous copper winding designs but the total loss of the aluminum inductor, P_{loss}, of 339 W is higher. The lower thermal conductivity of aluminum (200 W/mK) also results in a higher operating temperature of 163 °C. The aluminum winding inductor is summarized and compared to the copper winding inductors in Table 5.7.

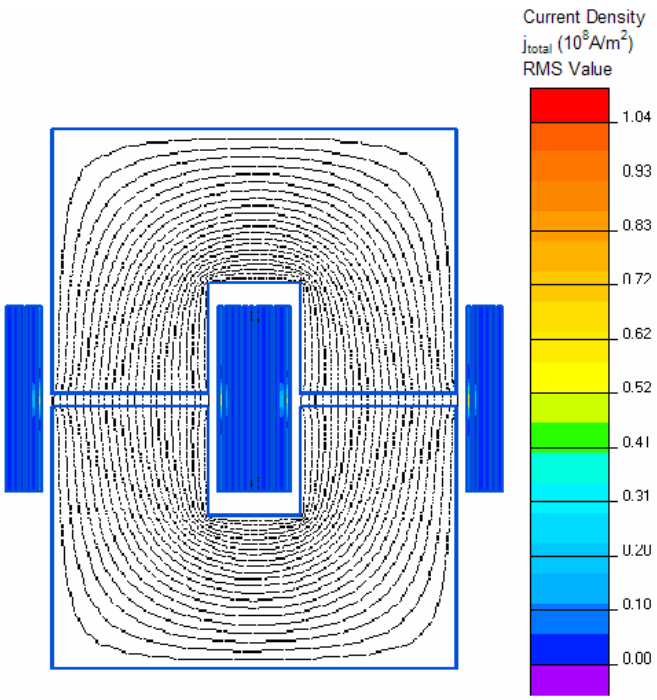

Figure 5.16: FEA of Al winding located 1.5 mm from the airgap.

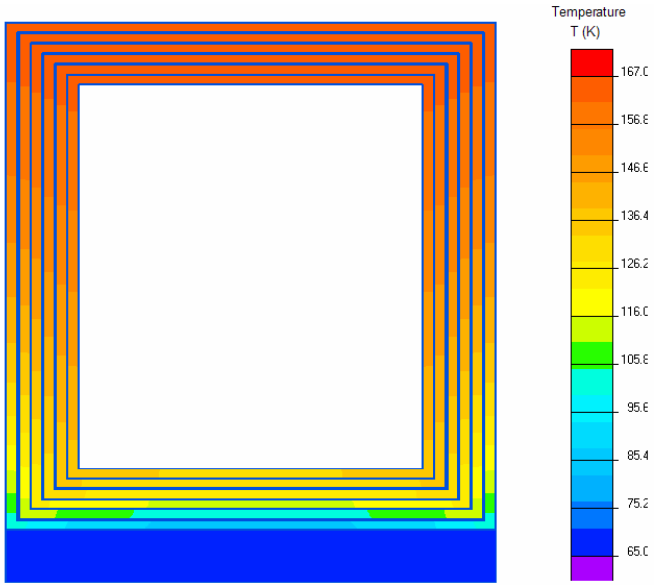

Figure 5.17: Thermal simulation of Al winding located 1.5 mm from the airgap.

5.3.2 Design 2

Design 2 in Section 4.4.2 is designed with a target of reducing the total weight of the core and the copper by a factor of 3 compared to the automotive inductor analyzed in Section 5.2. The inductor algorithm in Section 4.2 is used to derive a custom core that allows a maximum airgap of 8 mm (4 mm per leg). This design has a large airgap and a multicut core is required. The increase in cost per extra cut with the iron-based amorphous metal is significant, and as discussed in Section 3.2.1 the core loss is increased. However, the overall weight and volume is significantly reduced as the amount of material required is more than 3 times less. A less expensive foil winding structure is also used to reduce the cost when compared to the litz winding used in the automotive inductor in Section 5.2.

Design 2: Core Analysis

The inductor core for Design 2 is analyzed using 2D finite element analysis. The finite element model analyzes a 2-cut-per-leg structure as this is the worst case design for the multicut core (ac copper losses due to fringing are reduced as the distributed airgaps get closer together). The peak-to-peak flux density, ΔB_{pk-pk}, from the algorithm in Section 4.2 is 0.68 T and the total core loss, P_c, is reduced to 49.1 W due to the reduced core volume. Fig. 5.18 shows a finite element thermal simulation of Design 2. The total core loss, P_c, is used to calculate the hotspot temperature of the core, T_{core}, in the finite element simulation. The thermal conductivity of the core material is 10 W/mK along the lamination and 0.5 W/mK against the lamination. The end sections of the core are fixed to a 200 W/mK aluminum heatsink and the base plate temperature is 65 °C. As shown by the simulation, the core hotspot, T_{core}, is 112 °C and is below the maximum operating temperature of 150 °C for the core.

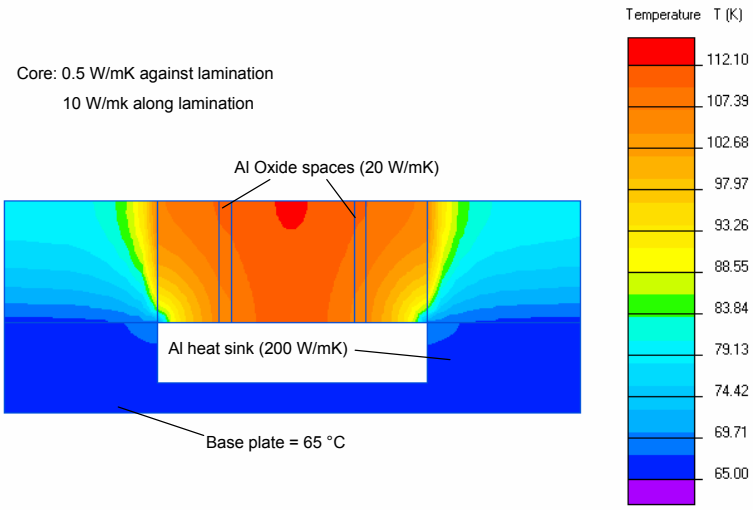

Figure 5.18: Thermal simulation of the core used in Design 2 (FEA Analysis).

Distance from gap	**0.3 mm foil (W)**			**0.4 mm foil (W)**			**0.5 mm foil (W)**		
	$\mathbf{P}_{cu,ac}$	$\mathbf{P}_{cu,dc}$	$\mathbf{P}_{cu}$	$\mathbf{P}_{cu,ac}$	$\mathbf{P}_{cu,dc}$	$\mathbf{P}_{cu}$	$\mathbf{P}_{cu,ac}$	$\mathbf{P}_{cu,dc}$	$\mathbf{P}_{cu}$
1	150	318	468	156	238	394	170	191	361
2	79	336	415	88	252	340	102	202	304
3	45	354	399	55	266	321	77	213	283

Table 5.5: Copper loss versus distance from gap and foil thickness.

Design 2: Winding Analysis

Again, the foil winding is sourced from CMC Klebetechnik Gmbh [64]. Two foil windings with 11 turns each are connected in series to give a total of 22 turns for the inductor. Three foil thicknesses of, 0.3 mm, 0.4 mm and 0.5 mm are simulated for both ac losses and heat transfer. Fig. 5.19 shows an ac loss finite element simulation of the 0.3 mm foil winding located 3 mm away from the airgap. The results of finite element simulations for 0.3 mm, 0.4 mm and 0.5 mm foil windings at distances of 1 mm, 2 mm and 3 mm away from the airgap are shown in Table 5.5. These results are also illustrated in Fig. 5.20.

As expected the 0.5 mm thick foil has the worst ac copper loss, $P_{cu,ac}$, at a distance of 1 mm from the gap. As the foil thickness decreases the ac copper

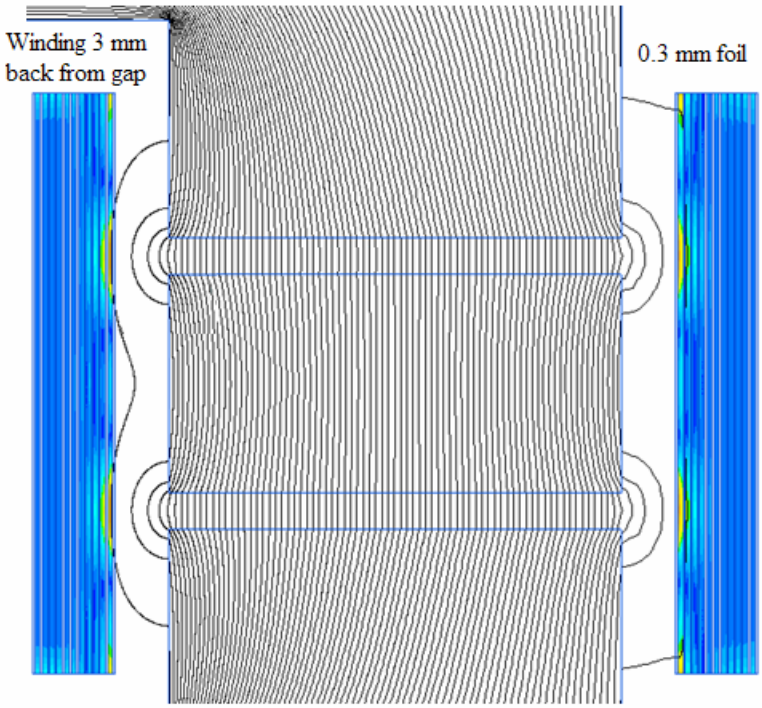

Figure 5.19: FEA of 0.3 mm foil winding located 3 mm back from airgap.

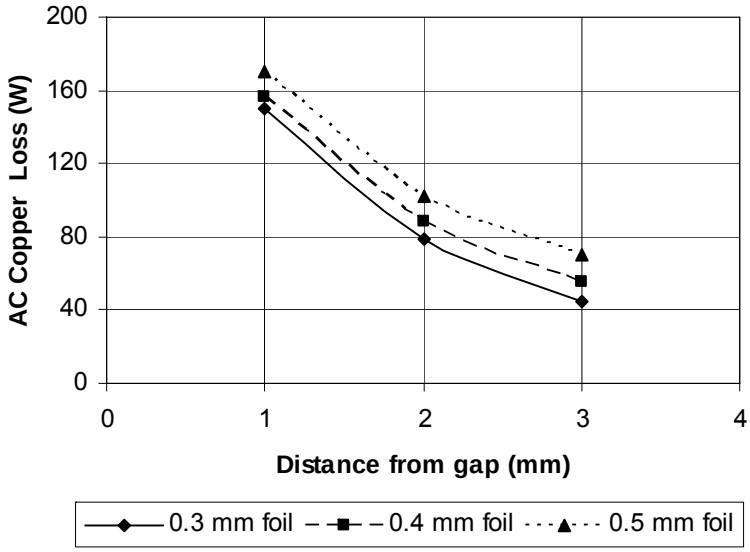

Figure 5.20: AC copper loss versus distance from gap and foil thickness (FEA Analysis).

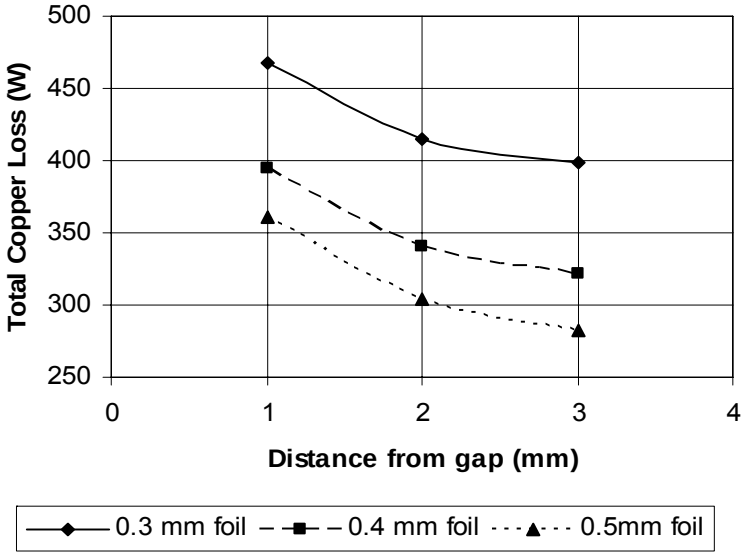

Figure 5.21: Total copper loss versus distance from gap and foil thickness.

loss is reduced. The loss is also reduced more significantly by moving each foil away from the airgap. The 0.3 mm foil located at a distance of 3 mm away from the gap has the lowest ac copper loss. Again, the dc copper loss, $P_{cu,dc}$, of each foil is calculated in the conduction-cooling inductor algorithm and the mathematical results are also tabulated in Table 5.5. A significant advantage can be seen with the thicker 0.5 mm foil due to the wider cross-sectional area of the copper winding. The total copper loss, P_{cu}, for each of the windings at distances of 1 mm, 2 mm and 3 mm away from the gap are also tabulated in Table 5.5. Fig. 5.21 illustrates the total copper loss, P_{cu}, versus distance from the airgap for each of the foil thicknesses for Design 2.

Fig. 5.22 shows a finite element thermal simulation of the 0.5 mm thick foil winding located 2 mm away from the airgap. The foil winding is mounted directly to the cold plate and has a maximum temperature of 162 °C. Table 5.6 shows the copper hotspot temperature of each foil, T_{cu}, as the foil is moved away from the airgap. The total copper loss, P_{cu}, in each foil is that shown in Table 5.5,

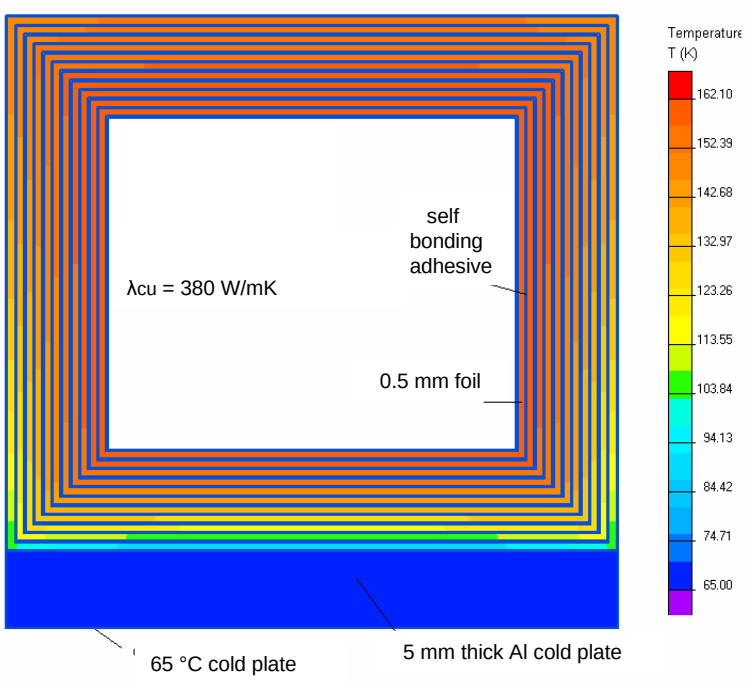

Figure 5.22: Copper hotspot of 0.5 mm foil located 2 mm away from the airgap (FEA Analysis).

i.e. 304 W for the 0.5 mm foil located 2 mm away from the airgap, has a copper hotspot temperature, T_{cu}, of 162 °C. Fig. 5.23 illustrates the copper hotspot temperature for each foil thickness, T_{cu}, as the foil is moved away from the airgap.

Fig. 5.23 shows that Design 2 with the 0.3 mm foil overheats even at a distance of 3 mm away from the airgap due to dc copper losses. However, the inductor does not overheat if the 0.4 mm and 0.5 mm foils are located at distances of

Distance from gap	**0.3 mm Foil**	**0.4 mm Foil**	**0.5 mm Foil**
1	241 °C	203 °C	186 °C
2	213 °C	178 °C	162 °C
3	200 °C	166 °C	151 °C

Table 5.6: Copper hotspot versus distance from gap and foil thickness (FEA Analysis).

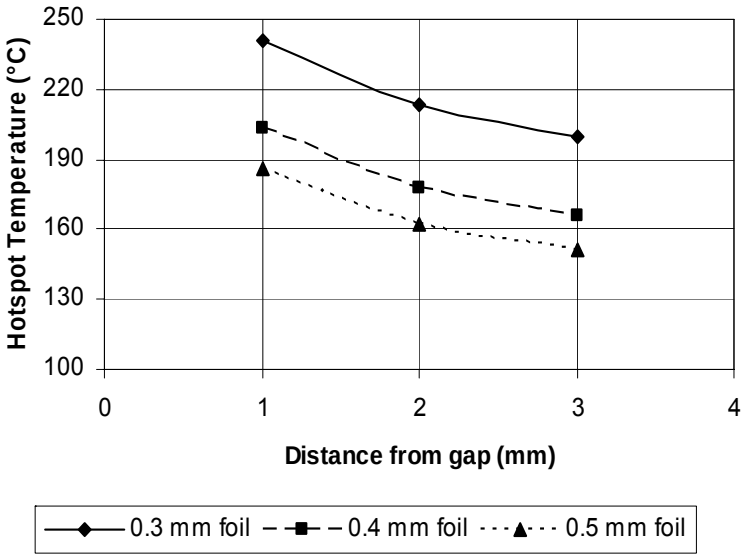

Figure 5.23: Copper hotspot versus distance from gap and foil thickness (FEA Analysis).

2 mm or more away from the airgap. The theoretical weight of the 0.5 mm foil for Design 2 is 0.407 kg and that of the 0.4 mm foil is 0.326 kg. These inductor designs are summarized in Table 5.7.

5.4 Helical Windings

A helical winding similar to the winding used in the Toytoa Prius THSII inductor is investigated in this section for use with the cores designed in Sections 4.4.1 and 4.4.2. The helical windings are optimized to minimise the copper losses. An aluminum tray and low cost potting material are assumed.

5.4.1 Design 1 with Helical Windings

Figs 5.13 and 5.20 illustrate that the ac copper losses, $P_{cu,ac}$, are minimised by moving the windings away from the airgap. The helical windings are kept 3 mm

away from the airgap for this design. The 4 mm isolation distances from the copper to the core at the top and bottom ends of the window are still required. This leaves a total remaining window length and breadth of 32 mm and 9 mm respectively. Two parallel windings with 12 turns each are placed around each core leg. The rectangular helical winding has a diameter of 4.25 mm and a thickness of 2.5 mm. This design gives the largest possible cross-sectional area for the windings taking insulation of the windings (0.2 mm) into consideration. The calculated dc copper loss, $P_{cu,dc}$, is 92 W.

A finite element simulation is carried out to determine the ac copper loss, $P_{cu,ac}$. Fig. 5.24 illustrates a finite element simulation for the helical winding on the inductor core from Design 1. The ac copper loss, $P_{cu,ac}$, calculated from the simulation is 140 W. The total core loss, P_c, for the core from Design 1 is 89 W giving a total loss, P_{loss}, of 321 W. These losses are used in a finite element thermal simulation to calculate the hotspot temperature of the helical winding inductor. Fig. 5.25 shows the finite element thermal simulation of the helical windings with the inductor core from Design 1. An aluminum tray similar to that from the Prius inductor is used to improve thermal performance. The thickness of the aluminum tray is 2 mm. A low cost potting material (2 W/mK) is also assumed. The temperature hotspot, T_{core}, is 156 ° C on a 65 ° C cold plate and is located at the top of the core. This shows that the core from Design 1 overheats when a helical winding is used. The weight of the copper also increases to 0.345 kg compared to the 0.26 kg with the 0.5 mm foil. This inductor is summarized in Table 5.7.

- Helical Winding to fit Design 1
- 2 parallel windings of 12 turns each
- Dimensions: 4.25mm x 2.5mm
- DC copper Loss = 92 W
- AC copper Loss (FEA) = 140
- Total core Loss = 89 W
- Total Loss = 321 W
- Winding 3mm back from gap
- 139 A pk-pk
- Copper weight = approx. 0.345 Kg (excluding terminations)

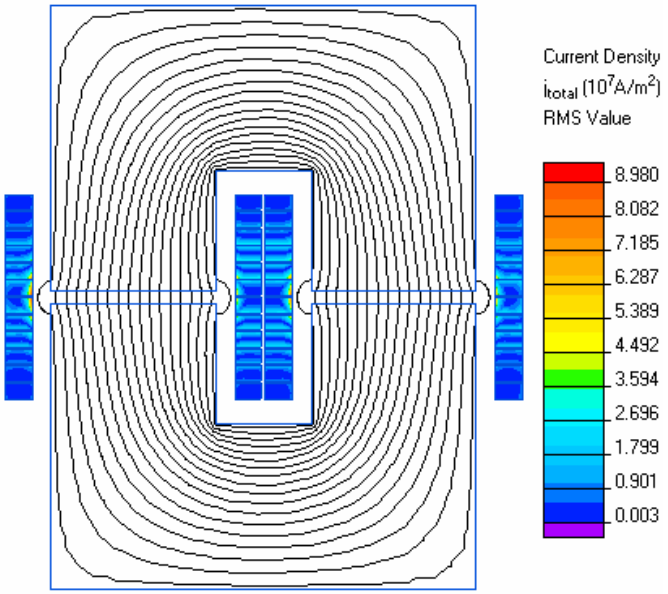

Figure 5.24: AC loss of helical winding on Design 1.

- Helical Winding to fit Design 1
- 200 Adc, 139 Apk-pk
- Dimensions: 4.25mm x 2.5mm
- DC copper Loss = 92 W
- AC copper Loss (FEA) = 140
- Total core Loss = 89 W
- Total Loss = 321 W
- Winding 3mm back from gap
- 2mm Alum tray all around inductor
- Potting: 2 W/mK
- 0.5 mm potting between core-tray and between tray-cold plate
- 65 °C Cold plate
- Copper weight = approx. 0.345 Kg (excluding terminations)

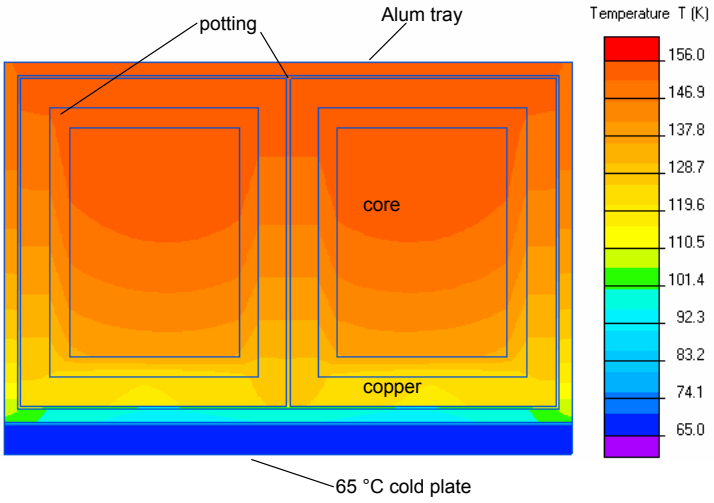

Figure 5.25: Thermal simulation of helical winding on Design 1.

5.4.2 Design 2 with Helical Windings

The inductor core from Design 2 is similarly designed with a set of helical windings. Two parallel windings with 22 turns each are placed around each core leg. The helical windings have a diameter of 6.5 mm and a thickness of 1.3 mm. The calculated dc copper loss, $P_{cu,dc}$, is 170 W. Again, a finite element simulation determines an ac copper loss, $P_{cu,ac}$, of 107 W. The total core loss, P_c, for the core from Design 2 is 49 W giving a total loss, P_{loss}, of 326 W. The temperature hotspot of the core, T_{core}, is 146 ° C. This shows that Design 2 with a helical winding operates close to the maximum allowed temperature of the core material. The weight of the copper also increases slightly to 0.43 kg compared to the 0.407 kg with the 0.5 mm foil.

Table 5.7 summarizes the weights, losses and temperatures of the new designs and compares them to the Prius THSII and automotive inductors analyzed in Sections 5.1 and 5.2 respectively. The inductors in the table do not include the inductor trays or potting material. The lightest possible inductor is Design 2 with the 0.4 mm foil and has a theoretical weight, M_{idr}, of 0.918 kg. However, in the interest of adequate derating, Design 1 with the 0.5 mm foil is the most suitable inductor for this application. Designs 1 and 2 with the 0.5 mm foil windings are initially tested in Section 5.5. Design 1 with the 0.5 mm foil windings is developed and optimized in Chapter 6, Section 6.3.4, for high-volume production and is tested in a 3-phase high-power interleaved boost converter.

5.5 Experimental Results

Designs 1 and 2 with the 0.5 mm foil windings are now tested in a single phase boost converter with the following specifications: frequency, f = 16 kHz, input

Core Name	**Power**	**Winding Type**	$\mathbf{P}_{loss}$	$\mathbf{T}_{cu}$	$\mathbf{T}_{core}$	$\mathbf{M}_{cu}$	$\mathbf{M}_{core}$	$\mathbf{M}_{idr}$
	(kW)		**(W)**	**(°C)**	**(°C)**	**(kg)**	**(kg)**	**(kg)**
Prius THSII	21	Helical	239	123	126	0.65	1.45	2.1
Automotive	40	Litz	172	110	110	1.66	1.44	3.1
Design 1	40	0.5 mm foil	275	131	136	0.26	1.039	1.299
Design 1	40	0.4 mm foil	305	150	136	0.208	1.039	1.247
Design 1 (Al)	40	0.9 mm foil	339	163	136	0.137	1.039	1.176
Design 1	40	Helical	321	148	150	0.208	1.039	1.247
Design 2	40	0.5 mm foil	332	151	112	0.407	0.592	0.999
Design 2	40	0.4 mm foil	370	166	112	0.326	0.592	0.918
Design 2	40	Helical	326	144	146	0.43	0.592	1.022

Table 5.7: Summary of analyzed and designed inductors.

voltage, $V_{in} = 180$ V, output voltage, $V_o = 360$ V, input current, $I_{in} = 180$ A. 6.5 % silicon steel cores with the same dimensions as Designs 1 and 2 above are also manufactured and tested for experimental comparison. Note that the 6.5 % silicon steel inductors are still mounted horizontally and that this is not the optimum thermal configuration for these inductors.

Figs. 5.26 and 5.27 show the core and copper temperature rises above the cold plate for Designs 1 and 2 with both the iron-based amorphous metal and the 6.5 % silicon steel cores. Table 5.8 presents the temperature hotspots of the inductors on a 70 °C cold plate. The 6.5 % silicon steel core is 59 °C higher than the iron-based amorphous metal core for Design 1 and 49 °C higher for Design 2. The heat flows with the lamination for the iron-based amorphous metal core and against the lamination for the 6.5 % silicon steel core. The heat generated due to the core power loss has to flow through the core to the cold plate as the inductor cores and copper are isolated from each other as illustrated in Fig. 4.1. The silicon steel core sees a significant thermal resistance against the lamination.

Note that in the above tests the inductor cores and windings are clamped to the cold plate introducing a minor experimental error. In Chapter 6 Design 1 is

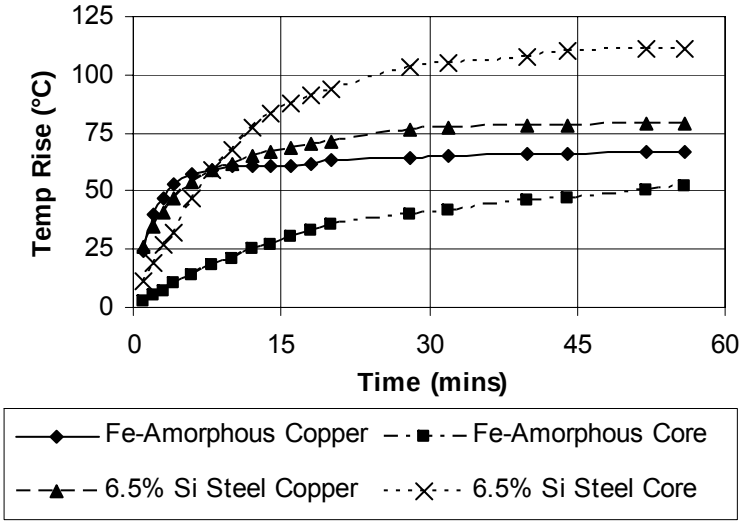

Figure 5.26: Fe-amorphous metal vs 6.5 % silicon steel (Design 1).

Material type	**Core design**	**Power (kW)**	$\mathbf{T}_{cu,FEA}$ **(°C)**	$\mathbf{T}_{cu,expt}$ **(°C)**	$\mathbf{T}_{core,FEA}$ **(°C)**	$\mathbf{T}_{core,expt}$ **(°C)**
Fe-Amorphous	Design 1	32.4	131*	137	136*	122
6.5% Si Steel	Design 1	32.4		149		181
Fe-Amorphous	Design 2	32.4	151*	162	112*	99
6.5% Si Steel	Design 2	32.4		159		148

*FEA simulation results for 40 kW (200 A) design point vs. 32.4 kW (180 A) test points.

Table 5.8: Summary of core and copper temperatures for Designs 1 and 2.

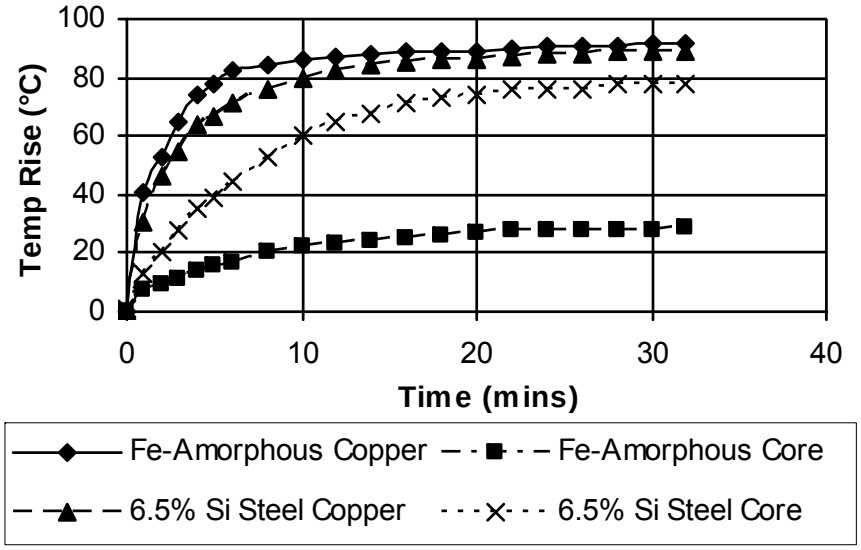

Figure 5.27: Fe-amorphous metal vs 6.5 % silicon steel (Design 2).

more rigorously tested in a fully potted aluminum inductor tray. The inductors are also tested at a lower power level of 32.4 kW compared to 40 kW as there was a change in the specifications after the inductor design phase. The core temperature operates below the predicted value while the copper temperature operates above. The thermal path for the copper is difficult to control due to the foil layers and the thermal interface between the copper and the cold plate.

5.6 Summary

This chapter first details the analysis of two high-power boost inductors currently used in the automotive industry. The 21 kW Toyota Prius THSII boost inductor uses a 6.5 % silicon steel of type 10JNHF600 as the magnetic core and a copper helical winding set. The hotspot temperature of the Prius inductor, T_{core}, is located near the top of the core and is measured at 126 °C on a 75 °C cold plate. The 40 kW automotive boost inductor uses an iron-based amorphous

metal of type 2605SA1 as the magnetic core and a litz winding set. The hotspot temperature of the automotive inductor, T_{core}, is 126 °C on a 75 °C cold plate.

Next, the 40 kW inductors designed in Sections 4.4.1 and 4.4.2 are optimized further using finite element analysis. It is shown that the ac copper losses, $P_{cu,ac}$, are significantly reduced by moving the windings away from the airgap. Several foil wound inductors are optimized and summarized in Table 5.7. The windings are designed with a self-bonding single-layer Kapton-insulated foil supplied by CMC Klebetechnik Gmbh [64]. The weights of the new designs are significantly reduced compared to the automotive inductor of the same power level of 40 kW.

In Section 5.4, a helical winding configuration similar to that used in the Toyota Prius THSII boost inductor is investigated for use with the inductor cores designed in Sections 4.4.1 and 4.4.2. The ac copper losses, $P_{cu,ac}$, are excessive for the 40 kW design point and the inductor cores operate very close to the upper limit of the core material. Finally, Designs 1 and 2 with the 0.5 mm foil windings are tested in a 32.4 kW single phase boost converter and Design 1 with the 0.5 mm foil is the most suitable inductor for the specified design point. This inductor design is developed and optimized in Chapter 6, Section 6.3.4, for high-volume production and is tested in a 3-phase high-power interleaved boost converter.

Chapter 6

3-Phase High-Power Interleaved Boost Converter

This chapter presents the design and construction of a three-phase high-power interleaved boost converter. The converter was built and part-load tested in Mainz Kastel, Germany, and full-load tested in Torrance, California in 2007. Detailed experimental results are presented on this system, which is used as a test bed for Inductor Design 1 as described in Sections 4.4.1 and 5.3.1.

6.1 Introduction

The earlier chapters have described the design of several high-power density, boost inductors. A three-phase 97.2 kW, interleaved boost converter is designed, constructed and tested for use as a test bed for Inductor Design 1 that is developed in Sections 4.4.1 and 5.3.1. This chapter documents some key practical aspects of the system and the final test results. Design 1 is tested and this system demonstrates that this inductor design operates below its maximum temperature limit at full continuous power. Section 6.2 presents the boost converter specifications and requirements. Section 6.3 presents the power stage of the converter. Section 6.4 describes the control structure and the design of the control interface

board. Section 6.5 presents the experimental results for the inductors at full continuous power.

6.2 97.2 kW Boost Converter System and Specifications

The key specifications of the boost converter are as follows:

- Nominal operation: input voltage, $V_I = 180$ V, output voltage, $V_O = 360$ V, input current, $I_I = 540$ A and switching frequency, $f = 16$ kHz.
- Multi-phase design to distribute current in a three-phase module, reduce inductor size and maintain a low effective capacitor current ripple by phase shifting 120 ° [2].
- 45 μH inductance per phase with a peak-to-peak ripple current, $\Delta I_{pk-pk} = 125$ A.
- 97 % drive cycle efficiency target, peak efficiency > 97 %.
- Uni-directional boost converter topology as discussed in Section 1.4.3.
- Input voltage variation, $V_I = 90$ V to 270 V, output voltage variation, $V_O = 270$ V to 420 V.
- Coolant temperature = 70 °C.
- Primary operation: Fuel cell current control, output voltage control.
- Texas Instruments (TI) F2808 processor is selected as a low-cost high-performance DSP specialized in controlling multi-phase converters [66].

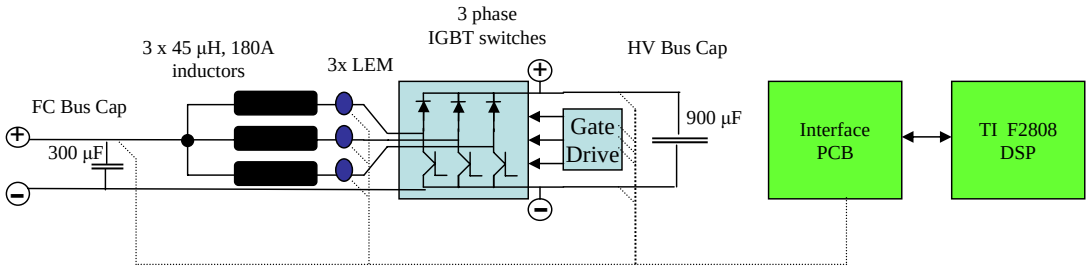

Figure 6.1: 3-phase interleaved boost converter.

Fig. 6.1 shows a schematic diagram of the 3-phase interleaved boost converter. The boost converter power stage consists of the input fuel cell bus capacitance of 300 μF, three high-power inductors, three IGBT/diode modules, the adaptor and gate drive boards from Semikron and the high-voltage-bus capacitance of 900 μF. The interface PCB serves as a signal interface from the TI F2802 evaluation board to the Semikron drivers and LEM sensors. It also provides signal conditioning, over-voltage and over-current protection. The currents in this converter are derived in Section 1.4.3.

6.3 Boost Converter Power Stage

The boost converter power stage consists of the input fuel cell bus capacitance of 300 μF, three high-power inductors, three IGBT/diode modules, the adaptor and gate drive boards from Semikron and the high-voltage-bus capacitance of 900 μF.

6.3.1 Input and Output Capacitance

The FFVE6K0157K capacitor is selected from AVX and is rated at 600 V_{dc}, 150 μF and 110 A_{rms} [67]. The FFV capacitor is a film capacitor designed for dc filtering and has a maximum operating temperature of 105 °C. The FFV capacitor

Module: SEMiX	$P_{cond,IGBT}$ (W)	$P_{sw,IGBT}$ (W)	$P_{cond,D}$ (W)	$P_{sw,D}$ (W)	P_{tot} (W)	$T_{j,IGBT}$ (°C)	$T_{j,D}$ (°C)
302GB066HDs	213	254	136	64	667	168	148
402GB066HDs	180	260	123	62	625	145	133
603GB066HDs	147	379	123	49	698	125	98

Table 6.1: IGBT modules losses and junction temperatures

has a very low level of stray inductance and can withstand large surge voltages, very high rms current ratings and long lifetimes. The input capacitance of 300 μF consists of two 150 μF capacitors connected in parallel. The output capacitance of 900 μF consists of six 150 μF capacitors connected in parallel.

6.3.2 Semiconductors

Three semiconductor modules from Semikron (SEMiX 302GB066HDs, SEMiX 402GB066HDs and SEMiX 603GB066HDs) are compared for use in the high-power converter. The modules specifications are detailed in [68, 69, 70].

The IGBT conduction loss, $P_{cond,IGBT}$, IGBT switching loss, $P_{sw,IGBT}$, diode conduction loss, $P_{cond,D}$, diodes witching loss, $P_{sw,D}$, total loss of the module, P_{tot}, IGBT junction temperature, $T_{j,IGBT}$ and diode junction temperature, $T_{j,D}$, are calculated for the nominal operating conditions of the converter and tabulated in Table 6.1. The higher current module, SEMiX 603GB066HDs, is selected and provides adequate derating of the IGBT and diode junction temperatures. This module also offers higher reliability when compared to the lower current modules, SEMiX 302GB066HDs and SEMiX 402GB066HDs.

6.3.3 Gate Drive

The gate drive module is also sourced from Semikron and consists of two parts, the gate drive board, SKYPER 32PRO, and the gate drive adapter board, 3s SKYPER

Figure 6.2: SKYPER 32 PRO with adapter board on top of SEMiX module.

32PRO. The gate drive board and the gate drive adapter board are detailed in [71, 72]. The SKYPER 32 PRO is a half bridge driver and the 3s SKYPER 32PRO is an evaluation board for the Semikron module SEMiX 603GB066HDs. The gate drive adapter board acts as an interface between the SEMiX 603GB066HDs module and the gate drive board and is mounted on top of the module as shown in Fig. 6.2. The benefits of the gate drive module are listed below and the practical implementation of the module is detailed in Appendix D.

- Integrated potential free power supply for secondary side.
- Short pulse suppression.
- Under-voltage protection on primary and secondary side.
- Dynamic short circuit protection.
- Soft turn off.
- Over-temperature trip level.
- Adaptable gate resistors.
- Dc bus voltage up to 1200 V.

All the PWM signals and the bias power supplies for the adapter board are supplied by the control interface board designed in Section 6.4.3. The IGBT fault monitoring signals are also sent to the control interface board from the adapter board if dynamic short circuit or temperature faults are detected.

6.3.4 High-Power Boost Inductor

Several high-power density inductors are designed in Chapter 5 and Design 1 with the 0.5 mm foil is the most suitable inductor for this application as shown in Tables 5.7 and 5.8. The experimental hotspot temperature of the copper, T_{cu}= 137 °C and is located on the inner layer of the copper winding. The inductor core has an experimental hotspot temperature, T_{core} = 122 °C and is located on the top of the core as illustrated in Fig. 5.11. This inductor is now developed and optimized for high volume production.

The inductor is potted in an aluminum tray to increase the mechanical strength of the inductor. The aluminum tray also helps to remove the heat from the inductor and relaxes the requirements for the thermal interface between the copper windings and the cold plate. Fig. 6.3 shows a picture of the aluminum tray developed for this inductor. When a potting material is used some of the heat can transfer between the core and the copper due to the thermal conductivity of the potting material. Design 1 with both 0.5 mm foil windings and 0.6 mm foil windings are manufactured as the inductor with the 0.5 mm foil windings operates close to the maximum operating temperature of 150 °C of the core material. A 0.6 mm foil winding reduces the dc copper losses , $P_{cu,dc}$, of the windings by 20 % and also improves the thermal performance of the windings by 20 %. Fig. 6.4 shows a 3D finite element simulation of the potted inductor with the 0.5 mm foil windings. The temperature hotspot is 125°C and is located on the top layer of

Figure 6.3: Picture of inductor tray for Design 1.

Phase	**Design 1**	$\mathbf{P}_{loss}$ **(W)**	$\boldsymbol{T}_{core,FEA}$ **°(C)**	$\boldsymbol{T}_{core,expt}$ **°(C)**	$\boldsymbol{T}_{cu,FEA}$ **°(C)**	$\boldsymbol{T}_{cu,expt}$ **°(C)**	$\mathbf{M}_{idr}$ **(kg)**
1	0.6 mm foil	229	116	128	116	130	2.003
2	0.5 mm foil	250	125	139	125	147	1.940
3	0.5 mm foil	250	125	138	125	141	1.945

Table 6.2: Inductor temperatures and weights.

the copper winding. The total loss of Design 1 with the 0.5 mm foil windings is reduced to 250 W when the lower input voltage and current specifications of 180 V and 180 A respectively are used compared to the input voltage and current specifications of 200 V and 200 A used in Section 5.3.1. The total loss of Design 1 reduces further with the 0.6 mm foil windings to 229 W. The increase in copper thickness increases the weight of this inductor by 0.06 kg. Table 6.2 in Section 6.5.1 compares the total losses, P_{loss}, weights, M_{idr}, and estimated and experimental temperatures of the core, T_{core}, and the copper, T_{cu}, for the 0.5 mm and 0.6 mm foil wound inductors.

- **250 Watts Total Dissipation**
- **$\lambda_{potting}$ = 2.16 W/m C (low cost)**
- **5.3 gpm (20 lpm) EG/H2O @ 70 °C Inlet**
- **1 °C coolant temp rise included**

- **Inductor hotspot on copper = 125 °C**

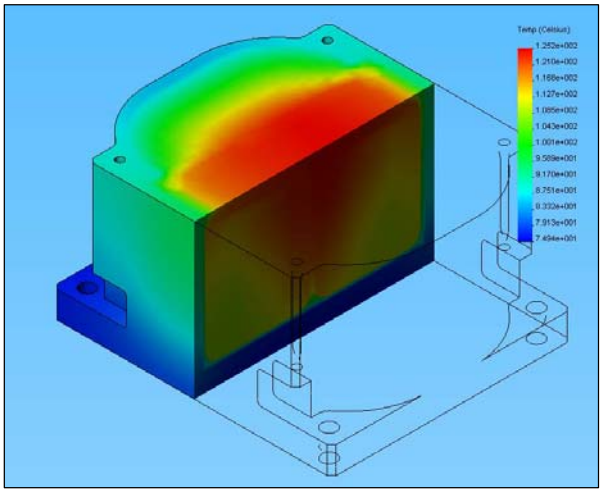

Figure 6.4: Thermal simulation of potted inductor.

High-Power Boost Inductor Assembly

The foil is manufactured by CMC Klebetechnik Gmbh [64] and then shipped to Block Transformatoren-Elektronik Gmbh [73]. A high tension winding machine developed specifically for the windings is used to manufacture the high quality windings. The windings and inductor core are then assembled in an aluminum tray using arctic silver thermal adhesive [74]. A thin layer of the thermal adhesive is used to ensure that there is no air between the thermal interfaces of the core and the copper to the cold plate. The arctic silver thermal adhesive has a thermal conductivity of 7 W/mK. The assembly is then shipped to Schunk GmbH [75] where the foil windings are connected in series using an ultrasonic welding machine. The ultrasonic weld of the series connection does not create any extra weight and there is no increase in termination heating. The assembly is then shipped back to Block Transformatoren-Elektronik Gmbh and fully potted with a low-cost epoxy supplied by Epoxies, Etc... [76]. The thermal conductivity of the epoxy is 2.16 W/mK. Fig. 6.5 illustrates the reductions in weight and volume of Design 1 compared to the automotive inductor analyzed in Section 5.2.

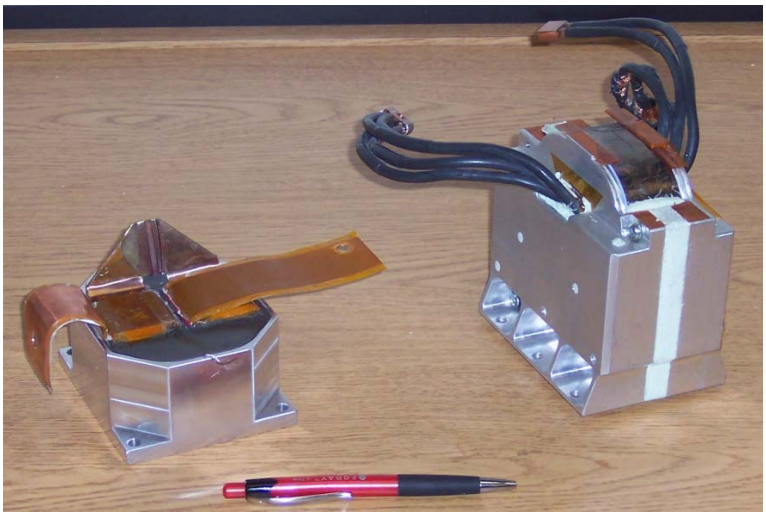

Figure 6.5: 1.9 kg, Design 1 (left) vs. 3.62 kg, automotive inductor (right).

6.4 System Control

The boost converter has the following primary control requirements:

- Proportional + integral current control loop for each PWM phase.
- Proportional + integral output voltage control loop.

6.4.1 Control Structure

The boost converter in the fuel cell vehicle operates in either average current mode control or output voltage mode control. Fig. 6.6 shows an overview of the boost converter control structure. The output voltage of the 3-phase boost converter is held constant and the current is dependent on the load. The high voltage bus is sensed and compared to a voltage setpoint, *HV_setpoint_CAN*, on the CAN bus. The error signal goes through a PI controller in software. As the load demands more current the input current of the inductor is sensed and compared to the current required by the load, *I_req*. The error signal goes through a PI controller

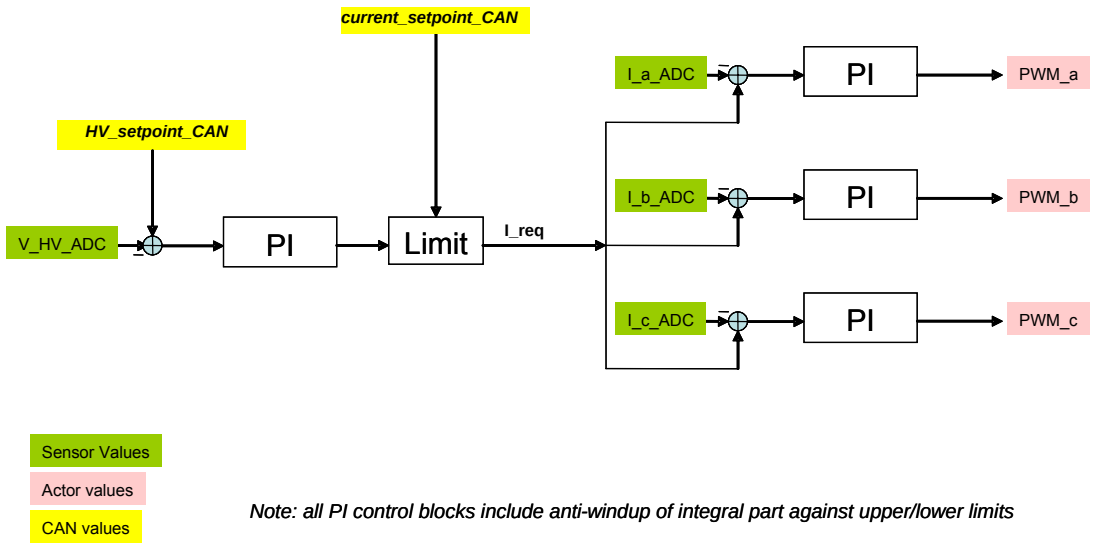

Figure 6.6: Overview of control structure.

in software and the pwm signals are generated for the boost switches. The current required by the load, *I_req*, is limited to the current setpoint on the CAN bus, *current_setpoint_CAN*, if the required current exceeds the current setpoint.

Fig. 6.7 shows the detailed control structure. A state-machine in the main loop of the software program ensures that all faults are cleared and that the boost converter is safe before enabling current to the system. This is seen in Fig. 6.7 as *boost_run*. The voltage control loop receives a voltage command and produces a limited current command. It also does anti-integral-windup [77], limiting and soft starting of the boost converter. The current control loop receives as input a current command and produces a regulated PWM signal for each phase. The current control loop also has anti-integral-windup and PWM limiting for each phase. This control structure is implemented on the TI F2808 Ezdsp and further details are discussed in Appendix D.

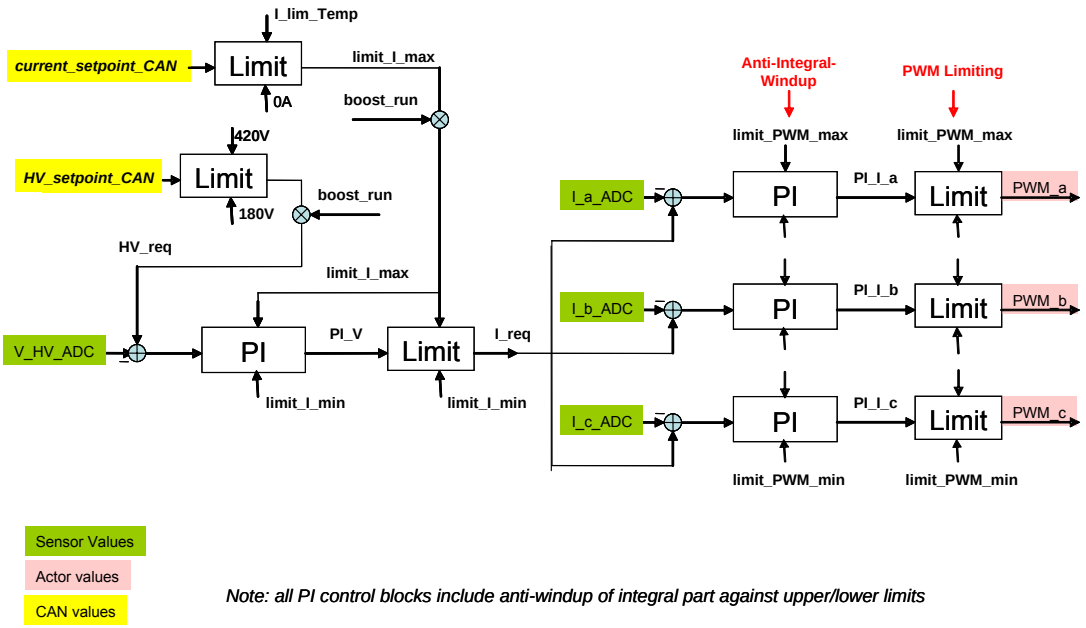

Figure 6.7: Detailed control structure.

6.4.2 Analog-Digital Conversion (ADC) and Timing Requirements

Fig. 6.8 shows the analog-digital conversion (ADC) requirements for the boost converter. The delay plus sample time should not exceed 100 ns. This will ensure that an accurate error is calculated on the correct sequence and that no CPU time is lost in algorithms that correct for time delays.

Fig. 6.9 illustrates the timing for the three individual phases. At the start of the yellow bar an interrupt is serviced. During the yellow bar the analogue sample is taken and converted to a digital value by the ADC. The digital value in the microprocessor is used in the control algorithm in the red section. The control algorithm is completed and the new PWM value is updated before the interrupt for phase B is serviced. There is no operation during the green bar. Further details of the control algorithm are discussed in Appendix D.

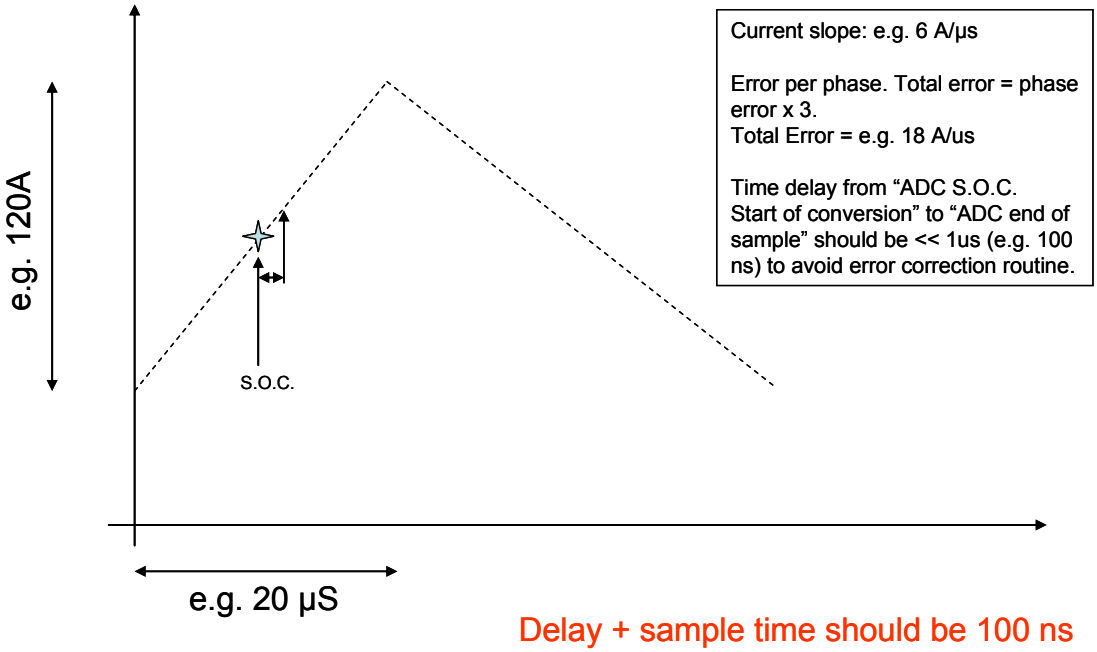

Figure 6.8: PWM sampling in the middle of each PWM on state.

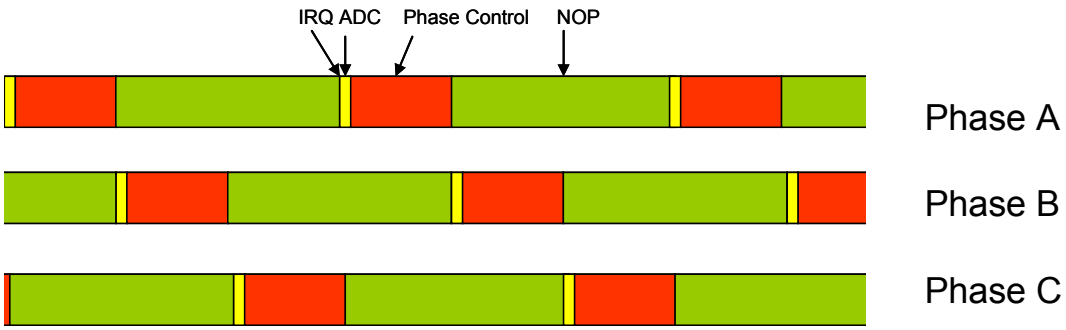

Figure 6.9: Control timing requirements.

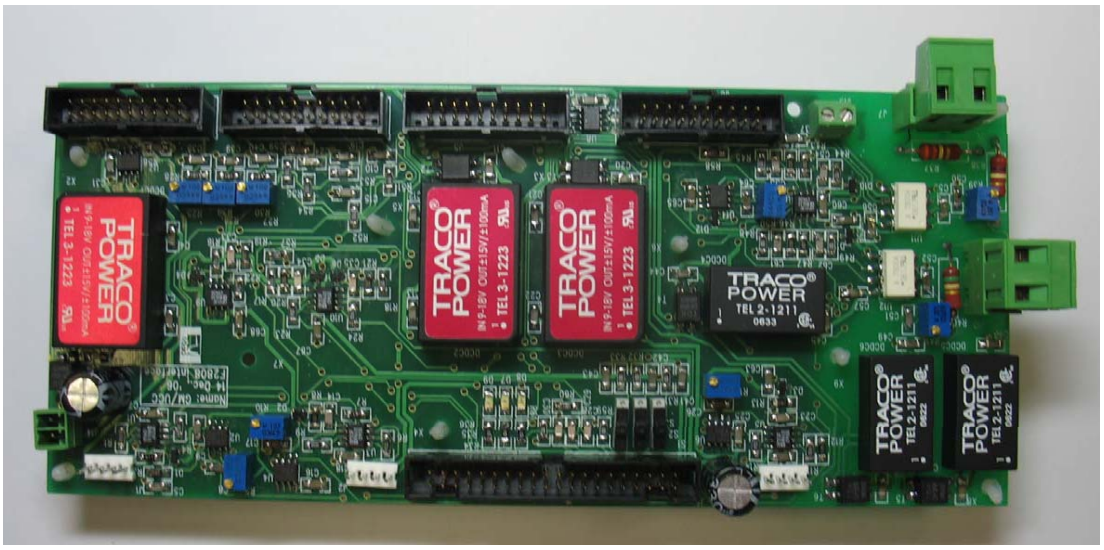

Figure 6.10: Picture of control interface board.

6.4.3 Control Interface Board

The control interface board acts as an interface between the TI F2808 Ezdsp and the gate drive adapter boards for each phase. All the PWM signals and the bias power supplies for the gate drive adapter boards are generated by the control interface board. The control interface board also has the following secondary controls:

- Output over-voltage detection.
- Phase over-current protection.
- Inductor / IGBT temperature monitoring.
- Hardware fault monitoring (IGBT, bias supplies).

Fig. 6.10 shows a picture of the control interface board. Design details of the control interface board are presented in Appendix D.

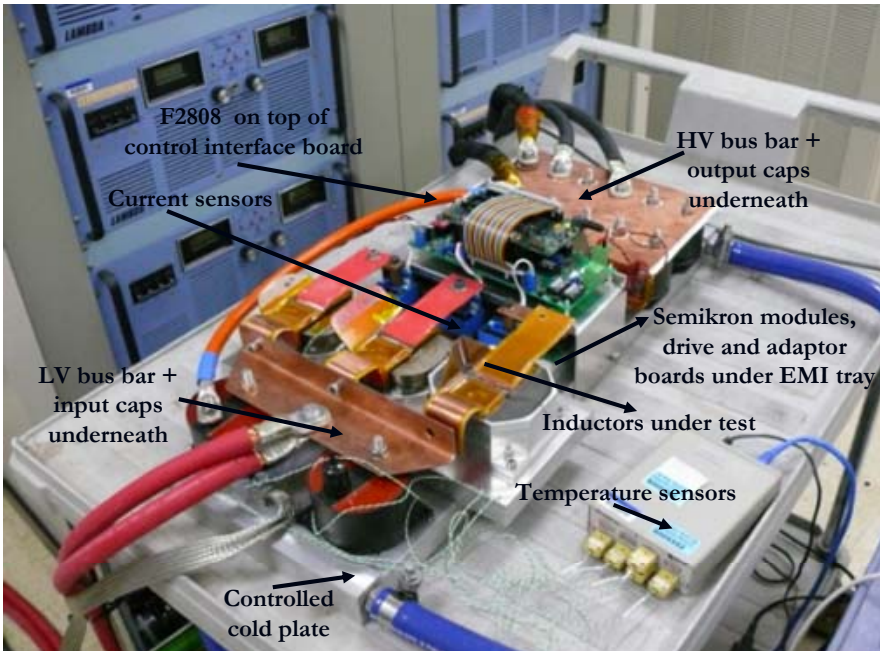

Figure 6.11: 3-phase 97.2 kW interleaved boost converter.

6.5 Experimental Results

The potted inductors are tested in the 3-phase high-power interleaved boost converter. The converter specifications are: input voltage, $V_I = 180$ V, output voltage, $V_O = 360$ V, input current, $I_I = 540$ A (180 A per phase) and the switching frequency, $f = 16$ kHz. Design 1 with the 0.6 mm foil windings is used in phase 1 and Design 1 with the 0.5 mm foil windings is used in phases 2 and 3. Fig. 6.12 shows the input and output voltage waveforms. Fig. 6.13 shows the pole voltages and the inductor currents for phases 1 and 2. The inductor currents in phases 1 and 2 are 120 ° out of phase.

6.5.1 Thermal Results

Experimental thermal results for the potted inductors are presented next. The system runs at full continuous power for 60 minutes and the temperatures of both

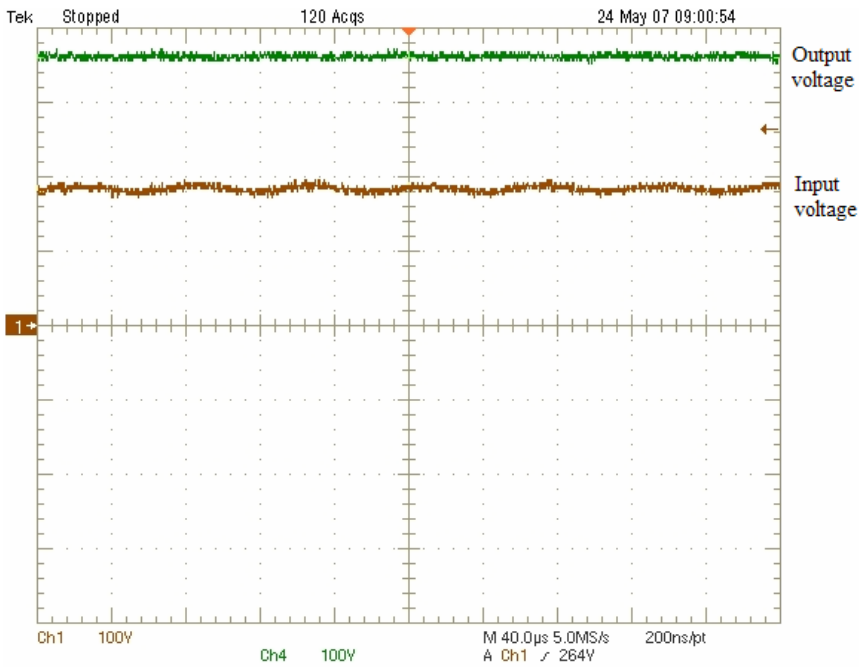

Figure 6.12: The boost converter input and output voltage waveforms.

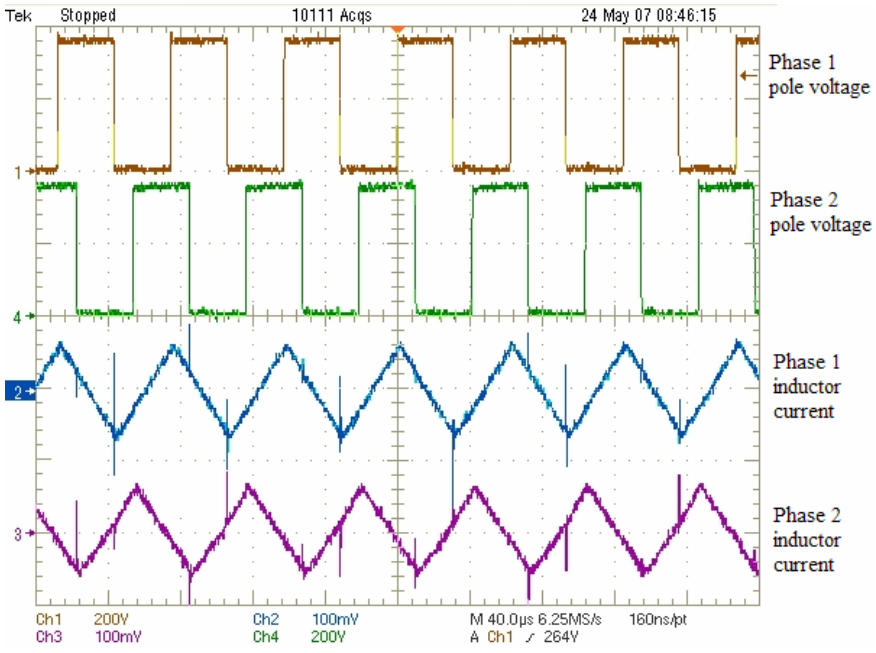

Figure 6.13: Phase 1 and phase 2 pole voltage and inductor current waveforms.

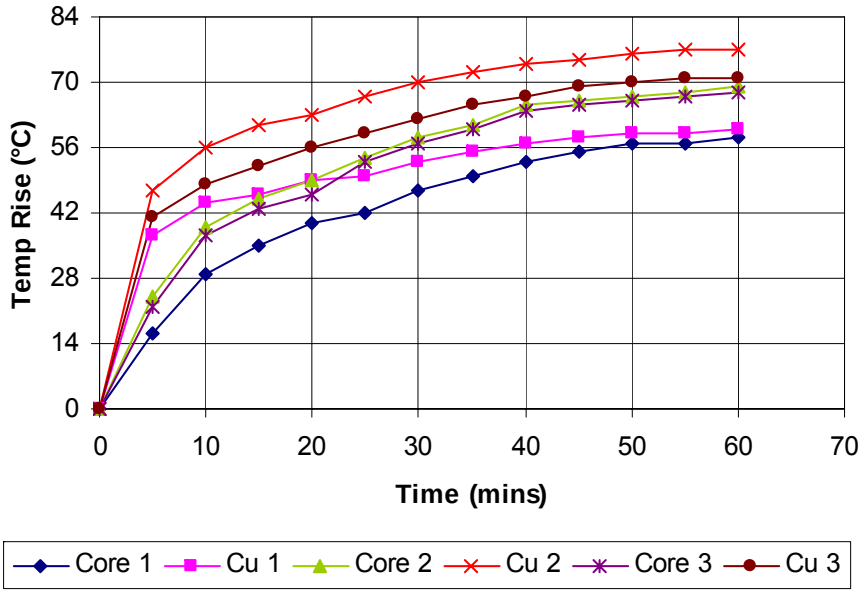

Figure 6.14: Inductor experimental thermal results.

the core, T_{core}, and the copper, T_{cu}, in all three phases are monitored. Fig. 6.14 shows the temperature rise above a 70 °C cold plate for the core and the copper in each phase. The inductor in phase 1 has 0.6 mm foil windings and performs better than the inductors in phases 2 and 3 with 0.5 mm foil windings.

Table 6.3 shows the final experimental temperature hotspots of the cores, $T_{core,expt}$, and the copper windings, $T_{cu,expt}$, on a 70 °C cold plate. Table 6.3 also shows the theoretical losses, P_{loss}, and experimental weights, M_{idr}, of the inductors. Design 1 with the 0.6 mm foil windings is slightly heavier than Design 1 with the 0.5 mm foil windings in phases 2 and 3. However, the 0.6 mm foil has better thermal performance due to the lower dc copper losses. Design 1 with both the 0.5 mm and 0.6 mm foil windings operate below the rated temperatures of the copper (180 °C) and the core (150 °C).

Phase	Design 1	$\mathbf{P}_{loss}$ (W)	$\boldsymbol{T}_{core,FEA}$ °(C)	$\boldsymbol{T}_{core,expt}$ °(C)	$\boldsymbol{T}_{cu,FEA}$ °(C)	$\boldsymbol{T}_{cu,expt}$ °(C)	$\mathbf{M}_{idr}$ (kg)
1	0.6 mm foil	229	116	128	116	130	2.003
2	0.5 mm foil	250	125	139	125	147	1.940
3	0.5 mm foil	250	125	138	125	141	1.945

Table 6.3: Inductor temperatures and weights.

6.5.2 System Efficiency

The experimental efficiency, η, of the boost converter is also measured. The input voltage and current, V_{in} and I_{in}, are measured at 180 V and 543.3 A respectively. The output voltage and current, V_{out} and I_{out}, are measured at 360 V and 264.3 A respectively.

$$\eta = \frac{P_{out}}{P_{in}} * 100 = \frac{V_{out}I_{out}}{V_{in}I_{in}} * 100 = 97.3\ \% \tag{6.1}$$

6.6 Summary

In this Chapter, a three-phase 97.2 kW interleaved boost converter is designed, constructed and tested for use as a test bed for Design 1. This chapter documents some key aspects of the system build and the final test results. Design 1 is developed and optimized for high volume production and it is shown that Design 1 with the 0.6 mm foil windings has better thermal performance than Design 1 with the 0.5 mm foil windings. The system verifies that the optimized inductors perform below the maximum operating temperatures of the materials at full continuous power. The inductor experimental weights of 2.003 kg and 1.940 kg for Design 1 with 0.6 mm foil windings and Design 1 with 0.5 mm foil windings respectively, are significantly lower than the automotive inductor analysed in Section 5.2 with an experimental weight of 3.62 kg. The experimental efficiency of the boost converter is measured at 97.3 % and meets the converter specification.

Chapter 7

Conclusions and Future Work

This final chapter summarizes the overall thesis and identifies some areas for future work.

7.1 Thesis Summary

This thesis has focused on the analysis of magnetic materials and the design of high-current inductors in low-to-medium frequency dc-dc converters.

Chapter 1 identifies the published methods of comparing magnetic materials and identifies the limitations of these methods in comparing the materials of interest over a wide range of frequency and ripple ratio. In Chapter 2 a novel area-product EXCEL-based program is developed for comparison of the various materials over a wide range of frequency and ripple. The program factors in gap loss and foil layer effects, and generates a custom core for the various converter inputs. The algorithm is fully automated and theoretical results are shown for various design points. The correct choice of magnetic material can significantly reduce the size of the inductor in the low-to-medium frequency range. As expected, inductor size and loss decrease for increased frequency. However, inductor size and loss can increase due to increased airgap effects. The ferrite material becomes

competitive at high ripple ratios and high frequencies and can be considered in high-ripple converters.

Iron-based amorphous metal and 6.5 % silicon steel are competitive materials for high-power-density inductors in the low-to-medium-frequency range and lead to a low cost and low weight/volume solution for high-power dc-dc converters. In Chapter 3, the practical effects of frequency, current ripple, load-current, air-gap fringing, and thermal configuration are investigated for these materials. A 2.5 kW converter is built to verify the optimum material selection and thermal configuration over the frequency range and ripple ratio of interest. Inductor size can increase in both these laminated materials due to increased airgap fringing losses. Distributing the airgap is demonstrated to reduce the inductor losses and size but has practical limitations for iron-based amorphous metal cores. The effects of the manufacturing process are shown to degrade the iron-based amorphous metal multi-cut core loss. The experimental results also suggest that gap loss is not a significant consideration in these experiments. The losses predicted by the equation in [11, 49] are significantly higher than the experimental results suggest. Iron-based amorphous metal has better preformance than 6.5 % silicon steel when a single-cut core and natural-convection-cooling are used.

Conduction cooling, rather than natural convection, can result in the highest power density inductor. The cooling for these laminated materials is very dependent on the direction of the lamination and the component mounting. Experimental results are produced showing the effects of lamination direction on the cooling path. A significant temperature reduction is observed compared to the natural-convection-cooling experimental results for the same test conditions. Iron-based amorphous metal and 6.5% silicon steel are competitive materials when conduction cooling, rather than convection, is used.

It was noted by the manufacturer of the iron-based amorphous metal core,

Metglas, that the minimum length of a core segment for a multi-gap design should not be less than 20 mm due to de-lamination of the core. There is also a degradation of core loss when the iron-based amorphous metal core is cut. The 6.5 % silicon steel material does not suffer from de-lamination of the core and can be cut down to a core segment length of 10 mm. The 6.5 % silicon steel material is a better option when small core segment lenghts are required and could be used in conjuction with the end sections of the iron-based amorphous metal core to make a hybrid inductor.

In Chapter 4, a conduction cooling inductor design algorithm is developed. The algorithm is developed for foil-wound inductors with gapped CC-cores in the low to medium frequency range. The algorithm considers the following factors: winding skin and layer effects; distance from airgap to minimize copper fringing loss, airgap length to reduce copper fringing losses, creepage and clearance, separate cooling paths for the core and the copper. The mass of the inductor is optimized and the algorithm is used to compare iron-based amorphous metal, 6.5 % silicon steel and ferrite 3C92 over a range of frequencies and ripple ratios. Again, conduction cooling, rather than natural convection, is shown to reduce the size and weight of the inductor. The weight of the 6.5 % silicon steel inductor is reduced by around a factor of ten compared to natural-convection cooling due to the high thermal conductivity of the material. The conduction cooling algorithm is used to develop two high-power custom inductors for use in a single-phase, 40 kW boost converter.

Chapter 5 details the analysis of two high-power boost inductors currently used in the automotive industry. The 21 kW Toyota Prius THSII boost inductor uses a 6.5 % silicon steel of type 10JNHF600 as the magnetic core and a copper helical winding set. The 40 kW automotive boost inductor uses an iron-based amorphous metal of type 2605SA1 as the magnetic core and a litz winding set.

Core Name	**Power**	**Winding Type**	$\mathbf{P}_{loss}$	$\mathbf{T}_{cu}$	$\mathbf{T}_{core}$	$\mathbf{M}_{cu}$	$\mathbf{M}_{core}$	$\mathbf{M}_{idr}$
	(kW)		**(W)**	**(°C)**	**(°C)**	**(kg)**	**(kg)**	**(kg)**
Prius THSII	21	Helical	239	123	126	0.65	1.45	2.1
Automotive	40	Litz	172	110	110	1.66	1.44	3.1
Design 1	40	0.5 mm foil	275	131	136	0.26	1.039	1.299
Design 1	40	0.4 mm foil	305	150	136	0.208	1.039	1.247
Design 1 (Al)	40	0.9 mm foil	339	163	136	0.46	1.039	1.499
Design 1	40	Helical	321	148	150	0.208	1.039	1.247
Design 2	40	0.5 mm foil	332	151	112	0.407	0.592	0.999
Design 2	40	0.4 mm foil	370	166	112	0.326	0.592	0.918
Design 2	40	Helical	326	144	146	0.43	0.592	1.022

Table 7.1: Summary of analyzed and designed inductors.

Next, the 40 kW inductors designed in Chapter 4 are optimized further using finite element analysis. It is shown that the ac copper losses are significantly reduced by moving the windings away from the airgap. Several inductors are optimized and summarized in Table 7.1. The foil wound inductors are designed with a self-bonding single-layer Kapton-insulated foil supplied by CMC Klebetechnik Gmbh [64]. The weights of the new designs are significantly reduced compared to the automotive inductor of the same power level of 40 kW.

In Chapter 6, a three-phase 97.2 kW interleaved boost converter is designed, constructed and tested for use as a test bed for Design 1. Design 1 is developed and optimized for high volume production. The system verifies that the optimized inductors perform below the maximum operating temperatures of the materials at full continuous power. Table 7.2 illustrates the temperatures, losses and experimental weights of the potted inductors. The inductor experimental weights of 2.003 kg and 1.940 kg for Design 1 with 0.6 mm foil windings and Design 1 with 0.5 mm foil windings respectively, are significantly lower than the automotive inductor analyzed in Chapter 5 with an experimental weight of 3.62 kg. Fig. 7.1 illustrates the reductions in weight and volume.

Phase	**Design 1**	$\mathbf{P}_{loss}$ **(W)**	$\boldsymbol{T}_{core,FEA}$ **°(C)**	$\boldsymbol{T}_{core,expt}$ **°(C)**	$\boldsymbol{T}_{cu,FEA}$ **°(C)**	$\boldsymbol{T}_{cu,expt}$ **°(C)**	$\mathbf{M}_{idr}$ **(kg)**
1	0.6 mm foil	229	116	128	116	130	2.003
2	0.5 mm foil	250	125	139	125	147	1.940
3	0.5 mm foil	250	125	138	125	141	1.945

Table 7.2: Inductor temperatures and weights.

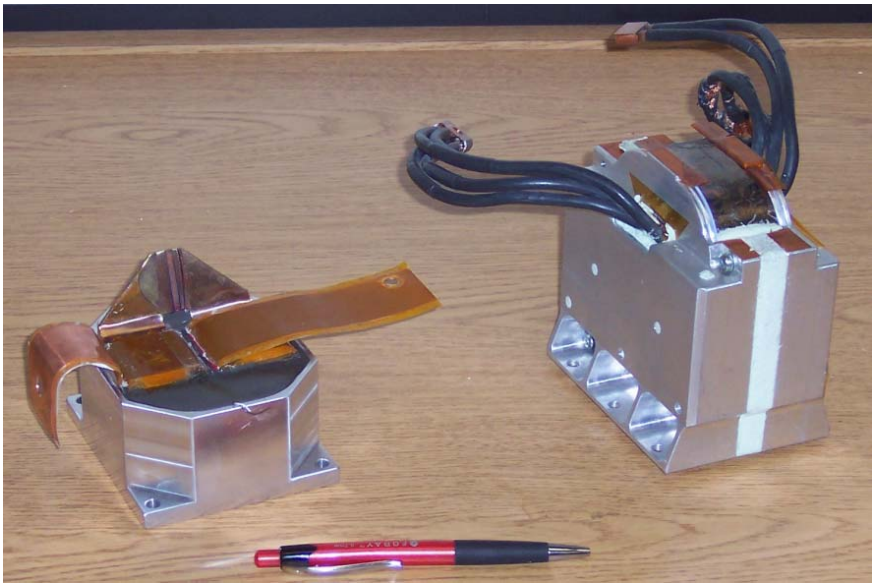

Figure 7.1: Design 1, foil wound inductor and earlier automotive inductor.

7.2 Future work

Future work on the project may be divided into a number of areas all of which represent work outside the scope of the present thesis.

- Consideration of gapless materials in high-power, low-to-medium frequency dc-dc converters.

- Expansion of the design algorithm to include material analysis at higher frequencies (100 kHz). This work is under way and initial results will be presented in IEEE EPE 2008.

- Verification of the gap core loss equation described in [11, 49]. The experimental results have suggested that these losses are insignificant compared to the predictions. Further work is required to quantify the effects of the fringing flux on the gap core loss in order to update and modify the earlier work by Reuben Lee.

- Analysis and design of a hybrid inductor consisting of 6.5 % silicon steel core legs and iron-based amorphous metal core end-sections. As previously discussed this may result in the minimum size inductor. Fig. 7.2 illustrates the proposed hybrid inductor core. A 15 % reduction in weight is envisaged with this design compared to Design 1 in Chapter 6.

- Design and experimental investigation of a three-phase integrated 6.5 % silicon steel inductor. The silicon steel due to the manufacturability of the core segments makes this material most suitable for designing as an integrated magnetic component. Fig. 7.3 and Fig. 7.4 show a 3-phase integrated 6.5 % silicon steel inductor. A 30 % reduction in weight is envisaged for this concept compared to three individual inductors of Design 1.

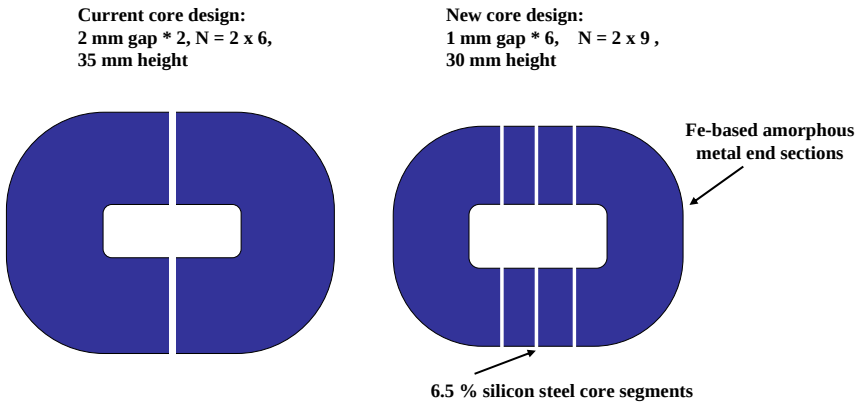

Figure 7.2: Core size reduction using a hybrid core.

- Expansion of the design algorithms to consider materials for high-frequency, high-power transformers. This work can be extended for transformer and coupled-inductor design.

- Expansion of the design algorithms and the associated experimental testing to quantify the effects of material saturation on the core loss.

- Expansion of the design algorithms to consider mathematical approximations for the copper fringing losses [12, 47, 78].

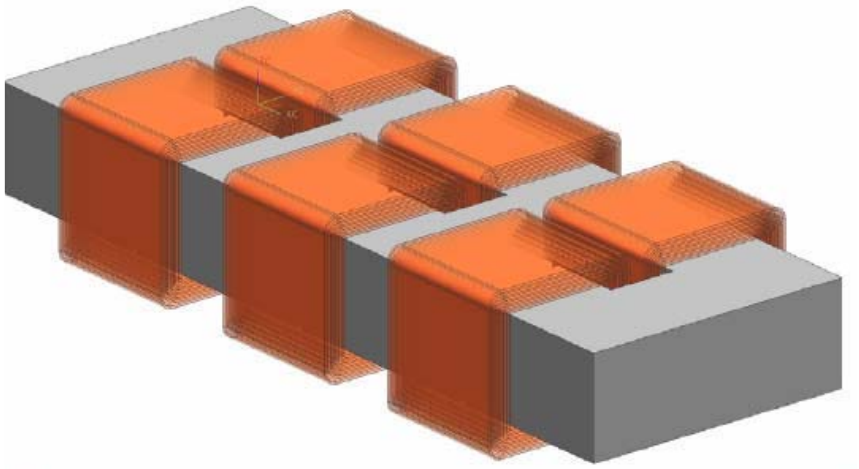

Figure 7.3: Potential 3-phase integrated silicon steel inductor (3D).

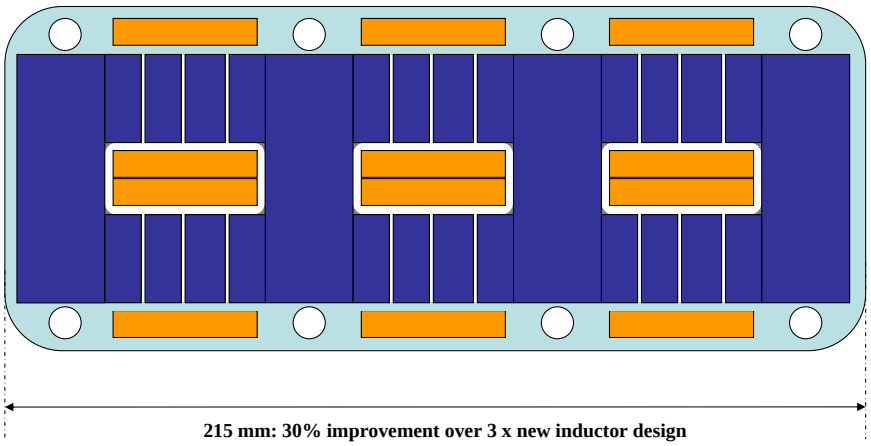

Figure 7.4: Potential 3-phase integrated silicon steel inductor.

Bibliography

[1] B. Eckardt, "High power buck-boost dc-dc converter for automotive power train applications," in *Power Electronics Intelligent Motion Conference, PCIM Europe*, 2005, pp. 287–293.

[2] B. Eckardt and M. Marz, "A 100 kW automotive power-train dc-dc converter with 25 kW/dm^3 by using SiC," in *Power Electronics Intelligent Motion Conference, PCIM Europe*, 2006, pp. 185–190.

[3] K. Rajashekara, "Hybrid and Fuel Cell Systems for Transportation," http://ieee.get.bme.hu/uploads/meetings/Budapest_paper-Raja.pdf.

[4] D. P. Urciuoli and C. W. Tipton, "Development of a 90 kW bi-directional DC-DC converter for power dense applications," in *IEEE Applied Power Electronics Conference*, 2006.

[5] R. M. Schupbach and J. C. Balda, "Comparing DC-DC converters for power management in hybrid electric vehicles," in *IEEE Electric Machines and Drives Conference*, 2003, pp. 1369–1374.

[6] ——, "35 KW ultracapacitor unit for power management of hybrid electric vehicles: bidirectional DC-DC converter design," in *IEEE Power Electronics Specialists Conference*, 2004, pp. 2157–2163.

[7] B. J. Masserant, E. W. Beans, and T. A. Stuart, "A study of volume versus frequency for soft switching IGBT converters," *IEEE Transactions on Aerospace and Electronic Systems*, vol. 31, no. 1, pp. 280–287, Jan. 1995.

[8] J. Czogalla, J. Li, and C. R. Sullivan, "Automotive application of multiphase coupled-inductor DC-DC converter," in *IEEE Industry Applications Conference*, 2003, pp. 1524–1529.

[9] R. A. Jensen and C. R. Sullivan, "Optimal core dimensional ratios for minimizing winding loss in high-frequency gapped-inductor windings," in *IEEE Applied Power Electronics Conference*, 2003, pp. 1164–1169.

[10] M. Gerber, J. A. Ferreira, I. W. Hofsajer, and N. Seliger, "A very high density, heatsink mounted inductor for automotive applications," in *IEEE Industry Applications Conference*, 2002, pp. 948–954.

[11] C. W. T. McLyman, *Transformer and Inductor Design Handbook*, 2nd ed. New York: Marcel Dekker, Inc., 1988.

[12] A. van den Bossche and V. C. Valchev, *Inductors and Transformers for Power Electronics*, 1st ed. Boca Raton, Florida: CRC Press, Taylor & Francis Group, 2005.

[13] www.metlgas.com.

[14] www.hitachi-metals.co.jp.

[15] www.ferroxcube.com.

[16] www.jfe.co.jp.

[17] www.mag-inc.com.

[18] www.vacuumschmelze.de.

[19] B. J. Lyons, J. G. Hayes, and M. G. Egan, "Magnetic material comparisons for high-current inductors in low-medium frequency DC-DC converters," in *IEEE Applied Power Electronics Conference*, 2007.

[20] S. Gottesfeld, C. F. Keller, S. Mller-Holst, and A. Redondo, "Fuel Cells Green Power," http://www.scied.science.doe.gov/nmsb/hydrogen/Guide\%20to\%20Fuel\%20Cells.pdf.

[21] F. C. Moore, "Average global temperatures," http://www.earth-policy.org/Indicators/Temp/2008.htm.

[22] http://www.opec.org/home/basket.aspx.

[23] "Toyota Hybrid System THS II Hybrid Synergy Drive," http://www.toyota.co.jp/en/tech/environment/ths2/SpecialReports_12.pdf.

[24] K. Hamada, "Evolution of Hybrid Vehicle Electric System and its Support Technologies," http://www.apec-conf.org/2007/images/stories/free_downloads/APEC2007/3.1\%20(version\%201.1).pdf.

[25] S. Matsumoto, "Advancement of hybrid vehicle technology," in *Power Electronics and Applications Conference*, 2005.

[26] A. O. AG, *Fuel Cell Technology, Energy for the Mobility of Tomorrow*. 65423, Russelsheim, Germany: Adam Opel AG, Public Affairs, 2004.

[27] A.J.Appleby and F. Foulkes, *Fuel Cell Handbook*. Van Nostrand Reinhold, NY: Kluwer Academic Publishers, 1989.

[28] S. Srinivasan and R. Mosdale, "Fuel cells for the 21st century progress, challenges and prognosis," in *Fifth International on Advances in Electrochemical Science and Technology Conference*, 1996.

[29] J. Norbeck and J. Heffel, "Hydrogen fuel for surface transportation," *SAE Technical Paper Series, Society of Automotive Engineers*, 1996.

[30] C. Kukkonen and M. Shelf, "Hydrogen as an alternative automobile fuel: 1993 update," *SAE Technical Paper Series, Society of Automotive Engineers*, 1994.

[31] K. Rajashekara, "Propulsion system strategies for fuel cell vehicles," *SAE Technical Paper Series, Society of Automotive Engineers*, 2000.

[32] H.-S. Choi and B. H. Cho, "Novel zero-current-switching (ZCS) PWM switch cell minimizing additional conduction loss," *IEEE Transactions on Power Electronics*, vol. 49, no. 1, pp. 165–172, Feb. 2002.

[33] M. Rylko, M. G. Egan, J. G. Hayes, and D. Power, "A soft-switched bi-directional DC-DC converter," in *IEEE Power Electronics and Applications Conference*, 2007, pp. 1–10.

[34] J. Li, A. Stratakos, A. Schultz, and C. R. Sullivan, "Using coupled inductors to enhance transient performance of multi-phase buck converters," in *IEEE Applied Power Electronics Conference*, 2004, pp. 1289–1293.

[35] P.-L. Wong, P. Xu, P. Yang, and F. C. Lee, "Performance improvements of interleaving VRMs with coupling inductors," *IEEE Transactions on Power Electronics*, vol. 16, no. 4, pp. 499–507, Jul. 2001.

[36] X. Huang, X. Wang, T. Nergaard, J.-S. Lai, X. Xu, and L. Zhu, "Parasitic ringing and design issues of digitally controlled high power interleaved boost converters," *IEEE Transactions on Power Electronics*, vol. 19, no. 5, pp. 1341–1352, Sep. 2004.

[37] F. Caricchi, F. Crescimbini, F. G. Capponi, and L. Solero, "Study of bidirectional buck-boost converter topologies for application in electrical vehicle motor drives," in *IEEE Applied Power Electronics Conference*, 1998, pp. 287–293.

[38] M. Shen, A. Joseph, J. Wang, F. Z. Peng, and D. J. Adams, "Comparison of traditional inverters and Z-source inverter for fuel cell vehicles," *IEEE Transactions on Power Electronics*, vol. 22, no. 4, pp. 1453–1463, Jul. 2007.

[39] M. Shen, A. Joseph, Y. Huang, F. Z. Peng, and Z. Qian, "Design and development of a 50 kW Z-source inverter for fuel cell vehicles," in *IEEE Power Electronics and Motion Control Conference*, 2006, pp. 1–5.

[40] B. J. Lyons, J. G. Hayes, and M. G. Egan, "Design algorithm for high-current gapped foil-wound inductors in low-to-medium frequency DC-DC converters," in *IEEE Power Electronics Specialists Conference*, 2007, pp. 1760–1766.

[41] M. Rylko, B. J. Lyons, J. G. Hayes, and M. G. Egan, "Magnetic material comparisons for high-current gapped and gapless foil inductors in high frequency DC-DC converters," in *IEEE Power Electronics Specialists Conference*, Poznan, Poland, Sep. 1–3, 2008.

[42] T. E. Salem, D. P. Urciuoli, V. Lubomirsky, and G. K. Ovrebo, "Design Considerations for High Power Inductors in DC-DC Converters," in *IEEE Applied Power Electronics Conference*, 2007, pp. 1258–1263.

[43] R. W. Erickson, *Fundamental of Power Electronics*, 5th ed. 101 Philip Drive, Assinippi Park, Norwell, Massachusetts, 02061, USA: Kluwer Academic Publishers.

[44] W. G. Hurley, "Optimizing core and winding design in high frequency transformers," in *IEEE Power Electronics Congress*, 1996, pp. 2–13.

[45] R. Lee, *Electronic Transformers and Circuits*, 2nd ed. New York: John Wiley & Sons, Inc., 1955.

[46] R. Severns, "Additional losses in high frequency magnetics due to non ideal field distributions," in *IEEE Applied Power Electronics Conference*, 1992, pp. 333–338.

[47] X. Nan and C. R. Sullivan, "An improved calculation of proximity-effect loss in high-frequency windings of round conductors," in *IEEE Power Electronics Specialist Conference*, 2003, pp. 853–860.

[48] P. Dowell, "Effects of eddy currents in transformer windings," in *Proceedings of the IEEE*, August 1966.

[49] R. Lee and D. Stephens, "Influence of core gap in design of current-limiting transformers," *IEEE Transactions on Magnetics*, vol. 9, no. 3, pp. 408–410, Sep. 1973.

[50] S.-G. Yoon, J.-M. Lee, J.-H. Park, I.-K. Lee, and B. H. Cho, "A frequency controlled bidirectional synchronous rectifier converter for HEV using supercapacitor," in *IEEE Power Electronics Specialists Conference*, 2004, pp. 135–140.

[51] N. Misao, N. Hironori, and Y. Tsunehiro, "High Silicon Steel Sheets Realizing Excellent High Frequency Reactor Performance," http://www.jfe-steel.co.jp/en/research/report/006/pdf/006-04.pdf.

[52] J. Hu and C. R. Sullivan, "Ac resistance of planar power inductors and the quasidistributed gap technique," *IEEE Transactions on Power Electronics*, vol. 16, no. 4, pp. 558–567, Jul. 2001.

[53] W. K. Mo, D. K. W. Cheng, and Y. S. Lee, "Simple approximations of the DC flux influence on the core loss power electronic ferrites and their use in design of magnetic components," *IEEE Transactions on Industrial Electronics*, vol. 44, no. 6, pp. 788–799, Dec. 1997.

[54] M. S. Lancarotte, C. Goldemberg, and A. A. J. Penteado, "Estimation of FeSi core losses under PWM or DC bias ripple voltage excitations," *IEEE Transaction on Energy Conversion*, vol. 20, no. 2, pp. 367–372, Jun. 2005.

[55] T. Shimizu, K. Mishima, K. Wada, and K. Ishii, "Mitigation of inductor loss based on minor-loop hysteresis characteristics," in *Telecommunications Energy Conference*, 2003, pp. 834–839.

[56] www.metlgas.com/design/dcr.asp.

[57] www.amtmagnetics.com.

[58] M. Gerber, J. A. Ferreira, I. W. Hofsajer, and N. Seliger, "A high-density heat-sink-mounted inductor for automotive applications," *IEEE Transactions on Industrial Applications*, vol. 40, no. 4, pp. 1031–1038, Jul./Aug. 2004.

[59] www.mininglife.com.

[60] B. J. Lyons, J. G. Hayes, and M. G. Egan, "Experimental investigation of iron-based amorphous metal and 6.5% silicon steel for high-current inductors in low-medium frequency DC-DC converters," in *IEEE Industry Applications Conference*, 2007, pp. 1781–1786.

[61] "Quality Spring/Togo Incorporated," http://www.qsti.com.

[62] "JFE Super Core (Electrical steel sheets for high-frequency applications)," http://www.jfe-steel.co.jp/en/products/electrical/catalog/f1e-002.pdf.

[63] "High Frequency Distributed Gap Inductor Cores Technical Bulletin," http://metglas.com/downloads/powerlite.pdf.

[64] "CMC Klebetechnik Gmbh, der Beschichtungspezialist, Robert-Bosch-Strae 8, D-67227, Frankenthal, Germany," http://Info@cmc-klebetechnik.de.

[65] C. R. Sullivan, "Aluminum windings and other strategies for high-frequency magnetics design in an era of high copper and energy costs," in *IEEE Applied Power Electronics Conference*, Feb. 2007, pp. 78–84.

[66] "TMS320f2809, F2808, F2806, F2802, F2801, C2802, C2801, and F2801x DSPs (Rev. I)," http://www.ti.com/lit/gpn/tms320f2808.

[67] "Medium Power Film Capacitors," http://www.avxcorp.com/docs/Catalogs/ffve-ffvi.pdf.

[68] "SEMiX 302GB066HDs," http://www.semikron.com/internet/webcms/online/asim/066er/27158012_DS.pdf.

[69] "SEMix 402GB066HDs," http://www.semikron.com/internet/webcms/online/asim/066er/27158022_DS.pdf.

[70] "SEMiX 603GB066HDs," http://www.semikron.com/internet/webcms/online/asim/066er/27168012_DS.pdf.

[71] "Evaluation Board 3s SKYPER 32 PRO," http://www.semikron.com/internet/webcms/online/pdf/Board_3s_SKYPER_32PRO_rev02.pdf.

[72] "SKYPER 32 PRO Revision," http://www.semikron.com/internet/webcms/online/pdf/SKYPER_32PRO_rev03.pdf.

[73] "Block Transformatoren-Elektronik Gmbh & Co. KG," http://www.block-trafo.de.

[74] "Arctic Silver Incorporated, 2230 W. Sunnyside Ave. Suite 6 Visalia, CA, 93277, USA," http://www.arcticsilver.com.

[75] "Schunk Gmbh & Co. KG, Spann-und Greiftechnik, Bahnhofstr. 106 - 134, 74348 Lauffen/Neckar, Germany," http://www.schunk.com.

[76] "Epoxies, Etc..., 21 Starline Way, Cranston, RI, 02921, USA," http://www.epoxies.com/.

[77] K. M. Passino and N. Quijano, "Proportional-Integral-Derivative Control with Derivative Filtering and Integral Anti-Windup for a DC Servo," http://www.ece.osu.edu/~passino/lab3prelab.pdf.

[78] W. A. Roshen, "Fringing Field Formulas and Winding Loss Due to an Air Gap," *IEEE Transactions on Magnetics*, vol. 43, no. 8, pp. 3387–3394, Aug. 2007.

[79] "Modules Explanations SEMiX," http://www.semikron.com/internet/webcms/objects/a_part/A02_det_eng.pdf.

[80] "Current Transducer HAS 50..600-S," http://www.lem.com.cn/news/news/admin/upload/photo/2006110163337has50_600s_e.pdf.

[81] "DC/DC Converters TEL 3 Series, 3 Watt," http://doc.chipfind.ru/traco/tel3.htm.

[82] "Low Noise, Low Drift Single-Supply Operational Amplifiers," http://www.farnell.com/datasheets/38868.pdf.

[83] "High-Speed, Low-Power, 3V/5V, Rail-to-Rail, Single-Supply Comparators," http://www.farnell.com/datasheets/58609.pdf.

[84] "High CMR Isolation Amplifiers," http://www.datasheetcatalog.com/datasheets_pdf/H/C/P/L/HCPL7800.shtml.

[85] "DC/DC Converters TEL 2 Series, 2 Watt," http://doc.chipfind.ru/traco/tel2.htm.

[86] "Dual 4-A Peak High Speed Low-Side Power MOSFET Drivers," http://focus.ti.com/lit/ds/symlink/ucc37324.pdf.

Appendix A

Converter Active and Passive Component Stresses

The following section derives the rms, average and peak currents of the components in a boost converter operating in continuous conduction mode. The voltage transfer function of the boost converter is derived first.

A.0.1 Boost Converter Voltage Transfer Function

Fig. A.1 shows the circuit waveforms for a boost converter. For simplicity, the devices are assumed ideal and the voltage drops across the devices are also neglected. The input and output currents are easily calculated.

$$I_{in} = I_{dc} = \frac{P_{out}}{V_{in}} \tag{A.1}$$

$$I_{out} = \frac{P_{out}}{V_{out}} \tag{A.2}$$

For steady state operation the average voltage across the inductor is zero as shown in Fig. A.1. Hence, by equating the positive (A) and negative (B) volt-second areas the voltage transfer function and duty cycle can be calculated. During the on-time,

$$\Delta I_{L,pk-pk} = I_{max} - I_{min} = \frac{V_{in}}{L} D T_s \tag{A.3}$$

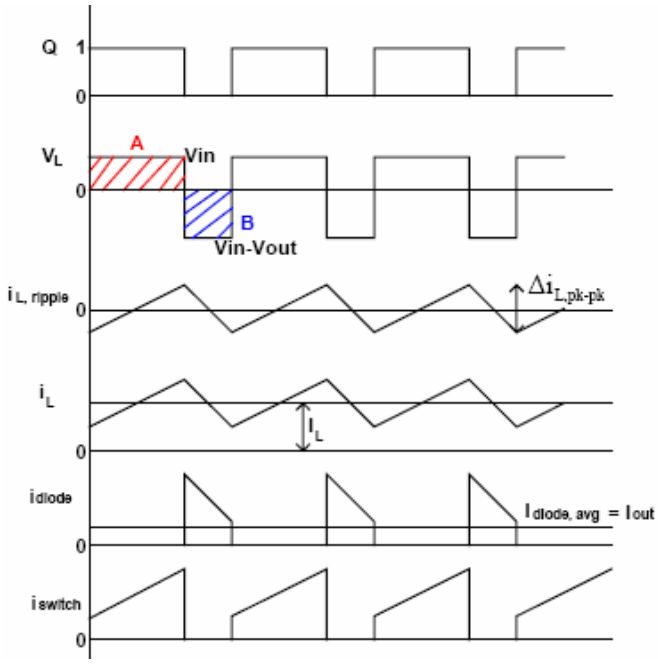

Figure A.1: Boost converter circuit waveforms.

During the off-time,

$$\Delta I_{L,pk-pk} = I_{max} - I_{min} = \frac{V_{out} - V_{in}}{L}(1 - D)T_s \tag{A.4}$$

The voltage transfer function, $\frac{V_{out}}{V_{in}}$, and the duty cycle, D, can be solved by equating the on and off times of the circuit.

$$\frac{V_{in}}{L}DT_s = \frac{V_{out} - V_{in}}{L}(1 - D)T_s \tag{A.5}$$

Thus, the voltage ratio is given by

$$\frac{V_{out}}{V_{in}} = \frac{1}{1 - D} \tag{A.6}$$

and the duty ratio is given by

$$D = \frac{1 - V_{in}}{V_{out}} \tag{A.7}$$

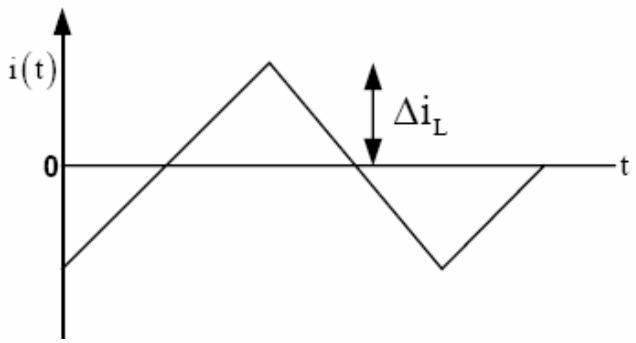

Figure A.2: Capacitor triangular current waveform.

A.0.2 Inductor and Input Capacitor Current Stresses

The inductor peak-to-peak ripple current, $\Delta I_{L,pk-pk}$, consists of linear segments rising when the voltage across the inductor, V_L, is positive and falling when V_L is negative. The inductor peak-to-peak ripple current, $\Delta I_{L,pk-pk}$, can be calculated using either A or B in Fig. A.1. Using A,

$$\Delta I_{L,pk-pk} = \frac{V_{in}}{L} D T_s = \frac{V_{in} D}{L f_s} \tag{A.8}$$

From equation A.8, an inductance value can be calculated for a desired ripple current. The average inductor current, $I_{L,avg}$, is equal to the input current, I_{in}.

$$I_{L,avg} = I_{in} = \frac{P_{out}}{V_{in}} = \frac{V_{out} I_{out}}{V_{in}} \tag{A.9}$$

Using equation A.6, the average inductor current, $I_{L,avg}$, can be represented as a function of the output current, I_{out}, and the duty cycle, D.

$$I_{L,avg} = I_{in} = \frac{I_{out}}{1 - D} \tag{A.10}$$

The input capacitor rms current, $I_{Cin,rms}$, is equal to the rms current of a triangular waveform with no dc component [43]. Fig. A.2 shows the capacitor triangular waveform.

$$I_{Cin,rms} = \frac{\Delta I_{L,pk-pk}}{2\sqrt{3}} = \frac{\Delta I_{L,pk-pk}}{\sqrt{12}} \tag{A.11}$$

The inductor rms current, $I_{L,rms}$, is calculated using the input current, I_{in}, and the input capacitor rms current, $I_{Cin,rms}$.

$$I_{L,rms} = \sqrt{I_{in}^2 + I_{Cin,rms}^2} \tag{A.12}$$

The inductor current ripple ratio, r_L, is defined as the ratio of the peak-to-peak inductor current, $I_{L,pk-pk}$, to the input current, I_{in}.

$$r_L = \frac{\Delta I_{L,pk-pk}}{I_{in}} \tag{A.13}$$

Using equation A.10, the peak-to-peak inductor current, $I_{L,pk-pk}$, can be represented as a function of the output current, I_o, the duty cycle, D, and the inductor current ripple ratio, r_L. The peak-to-peak inductor current, $I_{L,pk-pk}$, is also equal to the input capacitor peak-to-peak current, $I_{Cin,pk-pk}$.

$$\Delta I_{L,pk-pk} = I_{Cin,pk-pk} = \frac{r_L I_o}{1-D} \tag{A.14}$$

The input capacitor rms current, $I_{Cin,rms}$, and the inductor rms current, $I_{L,rms}$, can also be represented as a function of the output current, I_o, the duty cycle, D, and the inductor current ripple ratio, r_L.

$$I_{Cin,rms} = \frac{I_o r_L}{(1-D)\sqrt{12}} \tag{A.15}$$

$$\begin{aligned} I_{L,rms} &= \sqrt{I_{in}^2 + I_{Cin,rms}^2} \\ &= \sqrt{\left(\frac{I_o}{1-D}\right)^2 + \left(\frac{I_o r_L}{(1-D)\sqrt{12}}\right)^2} \\ &= \frac{I_o}{1-D}\sqrt{1 + \frac{r_L^2}{12}} \end{aligned} \tag{A.16}$$

A.0.3 Switch and Diode Current Stresses

The average switch current, $I_{sw,avg}$, the switch rms current, $I_{sw,rms}$, the average diode current, $I_{d,avg}$ and the diode rms current, $I_{d,rms}$, are calculated next using

the inductor rms current, $I_{L,rms}$, and are represented as a function of the output current, I_o, the duty cycle, D, and the inductor current ripple ratio, r_L.

$$\begin{aligned} I_{sw,avg} &= DI_{L,rms} \\ &= \frac{DI_o}{1-D}\sqrt{1+\frac{r_L^2}{12}} \end{aligned} \tag{A.17}$$

$$\begin{aligned} I_{sw,rms} &= \sqrt{D}I_{L,rms} \\ &= \frac{\sqrt{D}I_o}{1-D}\sqrt{1+\frac{r_L^2}{12}} \end{aligned} \tag{A.18}$$

$$\begin{aligned} I_{d,avg} &= (1-D)I_{L,rms} \\ &= \frac{(1-D)I_o}{1-D}\sqrt{1+\frac{r_L^2}{12}} \\ &= I_o\sqrt{1+\frac{r_L^2}{12}} \end{aligned} \tag{A.19}$$

$$\begin{aligned} I_{d,rms} &= \sqrt{(1-D)}I_{L,rms} \\ &= \frac{\sqrt{(1-D)}I_o}{1-D}\sqrt{1+\frac{r_L^2}{12}} \\ &= \frac{I_o}{\sqrt{1-D}}\sqrt{1+\frac{r_L^2}{12}} \end{aligned} \tag{A.20}$$

A.0.4 Output Capacitor Current Stress

The output capacitor rms current, $I_{Cout,rms}$, is calculated using the diode rms current, $I_{d,rms}$, and the output current, I_o, and is represented as a function of the output current, I_o, the duty cycle, D, and the inductor current ripple ratio, r_L.

$$\begin{aligned} I_{Cout,rms} &= \sqrt{I_{d,rms}^2 - I_o^2} \\ &= \sqrt{\frac{I_o^2}{(1-D)}\left(1+\frac{r_L^2}{12}\right) - I_o^2} \\ &= I_o\sqrt{\frac{D+\frac{r_L^2}{12}}{1-D}} \end{aligned} \tag{A.21}$$

The peak-to-peak current in the output capacitor, $I_{Cout,pk-pk}$, is equal to the peak current in the inductor, $I_{L,pk}$. This current is also equal to the peak current in the switch, $I_{sw,pk}$, and the peak current in the diode, $I_{d,pk}$.

$$\begin{aligned} I_{Cout,pk-pk} &= I_{L,pk} \\ &= I_{in} + \frac{\Delta I_{L,pk-pk}}{2} \\ &= I_{in} + \frac{I_{in} r_L}{2} \\ &= I_{in}\left(1 + \frac{r_L}{2}\right) \\ &= \frac{I_{out}}{(1-D)}\left(1 + \frac{r_L}{2}\right) \end{aligned} \tag{A.22}$$

Appendix B

Fourier Analysis of a Triangular Waveform

The following discussion is required for Chapter 4 and is used to calculate the ac loss effects at a 40 kW inductor design point.

B.0.5 Fourier Background

A French mathematician Joesph Fourier (1768 – 1830) derived a series known as a Fourier series, which is used to express a function, *f(x)*, as an infinite number of sine and cosine functions.

$$f(x) = a_0 + \sum_{n=1}^{\infty} (a_n \cos nx + b_n \sin nx) \tag{B.1}$$

where *f (x)* is the function in question, a_0 is the dc component, a_n is the amplitude of each cosine wave and b_n is the amplitude of each sine wave. Expanding (B.1) gives

$$f(x) = a_0 + a_1 \cos x + a_2 \cos 2x + a_3 \cos 3x.....$$

$$+b_1 \sin x + b_2 \sin 2x + b_3 \sin 3x.....$$

Assuming that the fourier series converges and has a continuous function, *f(x)*, as its sum on the interval [-π, π], then coefficients for $a_{0,}$, a_n and b_n in terms of

f(x) can be derived.

$$f(x) = a_0 + \sum_{n=1}^{\infty} (a_n \cos nx + b_n \sin nx) \ , \quad -\pi \leq x \leq \pi \tag{B.2}$$

The coefficients can be derived by integrating both sides of equation (B.2), assuming it is permissible to integrate the series term by term.

$$\int_{-\pi}^{\pi} f(x)\, dx = \int_{-\pi}^{\pi} a_0 dx + \int_{-\pi}^{\pi} \sum_{n=1}^{\infty} (a_n \cos nx + b_n \sin nx)\, dx$$

$$\int_{-\pi}^{\pi} f(x)\, dx = 2\pi a_0 + \sum_{n=1}^{\infty} a_n \int_{-\pi}^{\pi} \cos nx dx + \sum_{n=1}^{\infty} b_n \int_{-\pi}^{\pi} \sin nx dx$$

But,

$$\int_{-\pi}^{\pi} \cos nx dx = \frac{1}{n} \sin nx \Big]_{-\pi}^{\pi} = \frac{1}{n} [\sin n\pi - \sin(-n\pi)] = 0 \tag{B.3}$$

because n is an integer. Similarly, $\int_{-\pi}^{\pi} \sin nx dx = 0$, so

$$\int_{-\pi}^{\pi} f(x)\, dx = 2\pi a_0$$

Solving for a_0 gives

$$a_0 = \frac{1}{2\pi} \int_{-\pi}^{\pi} f(x)\, dx \tag{B.4}$$

To determine a_n for $n \geq 1$, equation (B.2) must be multiplied by $\cos mx$ (where m is an integer and $m \geq 1$) and integrated term by term from $-\pi$ to π.

$$\int_{-\pi}^{\pi} f(x) \cos mx dx = \int_{-\pi}^{\pi} \left[a_0 + \sum_{n=1}^{\infty} (a_n \cos nx + b_n \sin nx) \right] \cos mx dx$$

$$\begin{aligned} \int_{-\pi}^{\pi} f(x) \cos mx dx &= a_0 \int_{-\pi}^{\pi} \cos mx dx + \sum_{n=1}^{\infty} a_n \int_{-\pi}^{\pi} \cos nx \cos mx dx \\ &+ \sum_{n=1}^{\infty} b_n \int_{-\pi}^{\pi} \sin nx \cos mx dx \end{aligned} \tag{B.5}$$

From (B.3) above it is seen that the first integral is 0. Using trigonometric identities it can be shown that

$$\int_{-\pi}^{\pi} \sin nx \cos mx dx = 0 \ , \qquad for\ all\ n, m \tag{B.6}$$

$$\int_{-\pi}^{\pi} \cos nx \cos mx dx = 0 \ , \qquad for\ all\ n \neq m \tag{B.7}$$

$$\int_{-\pi}^{\pi} \cos nx \cos mx dx = \pi \ , \qquad for\ all\ n = m \tag{B.8}$$

So the only non-zero term in (B.5) is $a_m \pi$ giving

$$\int_{-\pi}^{\pi} f(x) \cos mx dx = a_m \pi \tag{B.9}$$

Solving for a_m, and then replacing m by n gives

$$a_n = \frac{1}{\pi} \int_{-\pi}^{\pi} f(x) \cos nx dx \ , \qquad for\ all\ n \tag{B.10}$$

Similarly if we multiply both sides of equation (B.2) by $\sin mx$ and integrate from $-\pi$ to π,

$$b_n = \frac{1}{\pi} \int_{-\pi}^{\pi} f(x) \sin nx dx \ , \qquad for\ all\ n \tag{B.11}$$

It can now be defined that if *f(x)* is a piecewise continuous function on $[-\pi, \pi]$ then the Fourier series of *f(x)* is the series

$$f(x) = a_0 + \sum_{n=1}^{\infty} (a_n \cos nx + b_n \sin nx) \ , \qquad -\pi \leq x \leq \pi$$

where the coefficients a_0, a_n and b_n in this series are defined by

$$a_0 = \frac{1}{2\pi} \int_{-\pi}^{\pi} f(x) dx \ , \quad a_n = \frac{1}{\pi} \int_{-\pi}^{\pi} f(x) \cos nx dx \ , \quad b_n = \frac{1}{\pi} \int_{-\pi}^{\pi} f(x) \sin nx dx$$

and are called the Fourier coefficients of *f(x)*.

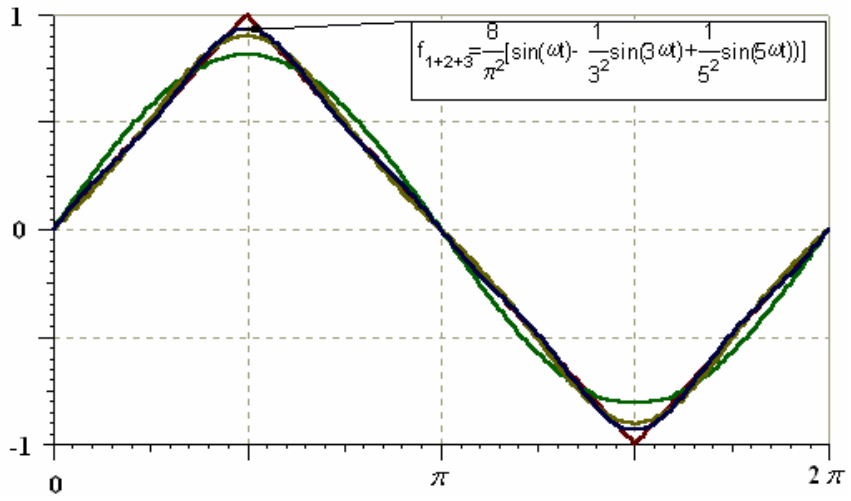

Figure B.1: Normalized triangular waveform for Fourier analysis.

In order to calculate an accurate power loss in a winding it is necessary to calculate the harmonic content of the current going through the winding. Using Fourier series it is possible to calculate the magnitude and frequencies of all the sine waves that make up the waveform. At maximum power (a duty cycle of 0.5) the inductor current waveform is triangular. Therefore, if the harmonic content of a triangular waveform can be determined then the maximum ac power loss in the inductor windings can be calculated. Fig. B.1 shows a normalized triangular waveform for the Fourier analysis.

First the function for the triangle, $f_{tri}(x)$, must be derived by breaking the function up into three distinct parts. Consider part *(a)*, $f_{tri}(x)$ over the interval $-\pi \leq x \leq \frac{-\pi}{2}$. Taking the two points that describe part *(a)*, $(-\pi,\ 0)$, $(\frac{-\pi}{2},$ *-1)*. The equation of the line is $f_{tri}(x) = ax + b$

$$0 = a(-\pi) + b\,, \quad b = a\pi$$

$$-1 = a\left(-\frac{\pi}{2}\right) + b$$

$$-1 = a\left(-\frac{\pi}{2}\right) + a\pi$$

$$b = -2$$

$$f_{tri}(x) = -\frac{2x}{\pi} - 2\,, \qquad if \quad -\pi \leq x \leq \frac{-\pi}{2} \tag{B.12}$$

Similarly for part *(b)*, $f_{tri}(x)$ over the interval $-\frac{\pi}{2} \leq x \leq \frac{\pi}{2}$ gives

$$f_{tri}(x) = \frac{2x}{\pi}\,, \qquad if \quad -\frac{\pi}{2} \leq x \leq \frac{\pi}{2} \tag{B.13}$$

And for part *(c)*, $f_{tri}(x)$ over the interval $\frac{\pi}{2} \leq x \leq \pi$ gives

$$f_{tri}(x) = 2 - \frac{2x}{\pi}\,, \qquad if \quad \frac{\pi}{2} \leq x \leq \pi \tag{B.14}$$

When calculating the Fourier series of a waveform the process is a lot easier by taking advantage of the symmetry of sine and cosine waves on the left and right sides of the y axis. A function, *g(x)*, is said to be odd if *g(-x) = -g(x)*. Hence, a waveform is odd when the waveform on the right side of the y-axis, after being mapped back over the y-axis results in an inverted version of the waveform on the left side of the y-axis. Also for odd functions, the left and right side contributions to the cosine coefficients exactly cancel leaving the value of a_n at zero. Likewise, the contributions of the left and right sides to the sine coefficients are exactly equal so calculating one side and doubling it can save work. Hence equations (B.10) and (B.11) in the Fourier series are

$$a_n = 0$$

$$b_n = \frac{2}{\pi}\int_0^{\frac{\pi}{2}} \frac{2x}{\pi}\sin(nx)\,dx + \frac{2}{\pi}\int_{\frac{\pi}{2}}^{\pi}\left(2 - \frac{2x}{\pi}\right)\sin(nx)\,dx \tag{B.15}$$

To proceed from here the integral of *xsin(nx)* must be known. The rule for integration by parts is

$$\int udv = uv - \int vdu$$

Let $\begin{array}{ll} u = x & dv = \sin(nx)\,dx \\ du = dx & v = -\frac{1}{n}\cos(nx) \end{array}$

$$\int x\sin(nx)\,dx = -\frac{x}{n}\cos(nx) - \int -\frac{1}{n}\cos(nx)\,dx$$

$$\int x\sin(nx)\,dx = -\frac{x}{n}\cos(nx) + \int \frac{1}{n}\cos(nx)\,dx \tag{B.16}$$

But

$$\int \frac{1}{n}\cos(nx)\,dx = \frac{1}{n}\left[\frac{1}{n}\sin(nx)\right] = \frac{1}{n^2}\sin(nx) \tag{B.17}$$

Substituting (B.17) into (B.16) gives

$$\int x\sin(nx)\,dx = \frac{1}{n^2}\sin(nx) - \frac{x}{n}\cos(nx) \tag{B.18}$$

Using the solution of (B.18) in (B.15) gives

$$\begin{aligned} b_n &= \frac{4}{\pi^2}\left(\frac{\sin(nx)}{n^2} - \frac{xcox(nx)}{n}\right)\Bigg]_0^{\frac{\pi}{2}} \\ &+ \frac{4}{\pi}\left[\left(\frac{-\cos(nx)}{n}\right) - \frac{1}{\pi}\left(\frac{\sin(nx)}{n^2} - \frac{xcox(nx)}{n}\right)\right]_{\frac{\pi}{2}}^{\pi} \end{aligned} \tag{B.19}$$

Plugging in the values at the endpoints gives

$$\begin{aligned} b_n = {} & \tfrac{4}{\pi^2}\left(\tfrac{\sin\left(\frac{n\pi}{2}\right)}{n^2} - \tfrac{\frac{\pi}{2}\cos\left(\frac{n\pi}{2}\right)}{n} - \tfrac{\sin(0)}{n^2} + \tfrac{0\cos(0)}{n}\right) + \\ & \tfrac{4}{\pi}\left[\begin{array}{l} \tfrac{-\cos(n\pi)}{n} - \tfrac{1}{\pi}\left(\tfrac{\sin(n\pi)}{n^2} - \tfrac{\pi\cos(n\pi)}{n}\right) - \tfrac{-\cos\left(\frac{n\pi}{2}\right)}{n} + \\ \tfrac{1}{\pi}\left(\tfrac{\sin\left(\frac{n\pi}{2}\right)}{n^2} - \tfrac{\frac{\pi}{2}\cos\left(\frac{n\pi}{2}\right)}{n}\right) \end{array}\right] \end{aligned} \tag{B.20}$$

Referring to the terms as one through ten above, terms one and nine add together, terms two and ten add up to cancel term eight, terms three and four are zero, term five and seven cancel and term six is zero because the $\sin(n\pi)$ function is zero for all multiples of π. So equation (B.20) reduces to

$$b_n = \frac{8\sin\left(\frac{n\pi}{2}\right)}{\pi^2 n^2} \tag{B.21}$$

The $\sin\left(\frac{n\pi}{2}\right)$factor repeats a series *1, 0, -1, 0,* in a loop and so equation (B.21) could be represented as

$$b_n = \frac{8}{\pi^2}\left(1, 0, -1, 0, 1, 0, -1, 0, 1, ...\right) \; for \; n = 1 \rightarrow \infty \tag{B.22}$$

The normalised triangle waveform represented as a Fourier series is then

$$f_{tri}(x) = \frac{8}{\pi^2}\left(\sin(x) - \frac{\sin(3x)}{9} + \frac{\sin(5x)}{25} - \frac{\sin(7x)}{49} + \frac{\sin(9x)}{81} - .....\right) \tag{B.23}$$

This Fourier series can be represented as

$$f_{tri}(x) = \frac{8}{\pi^2}\sum_{n=1,3,5..}^{\infty} \frac{(-1)^{\frac{n-1}{2}}}{n^2}\sin\left(\frac{n\pi x}{L}\right) \tag{B.24}$$

where period $T = 2\pi = 2L$ and x is the distance of the peak of the sine wave from the origin.

B.0.6 Harmonic Currents for 40 kW Inductor Design Point

At the 40 kW inductor design point in Chapter 4 the frequency of operation is, *f = 16 kHz.* Therefore the period, *T, = 2L = 62.5 μs.* As the duty cycle is 0.5 at maximum power the inductor peak current occurs at *x = 15.625 μs.* Substituting these values into equation (B.24) above yields the following results for the first five odd harmonics.

$$n = 1\,; \quad \frac{8}{\pi^2}\left[\frac{(-1)^0}{1}\sin\left(\frac{\pi 15.625e^{-6}}{31.25e^{-6}}\right)\right] = \frac{8}{\pi^2}(1) = 0.811$$

$$n = 3\,; \quad \frac{8}{\pi^2}\left[\frac{(-1)^1}{9}\sin\left(\frac{3\pi 15.625e^{-6}}{31.25e^{-6}}\right)\right] = \frac{8}{\pi^2}(0.1111) = 0.09$$

Harmonic Number	Frequency(kHz)	Peak amplitude (A)	Rms Amplitude(A)
n = 1	16	(0.811)(69.5) = 56.37	$56.37/\sqrt{2}$= 39.9
n = 3	48	(0.09)(69.5) = 6.255	$6.255/\sqrt{2}$= 4.42
n = 5	80	(0.033)(69.5) = 2.252	$2.252/\sqrt{2}$= 1.59
n = 7	112	(0.016)(69.5) = 1.127	$1.127/\sqrt{2}$= 0.80
n = 9	144	(0.009)(69.5) = 0.676	$0.676/\sqrt{2}$= 0.48

Table B.1: Harmonic currents in Design 1.

$$n = 5\ ; \quad \frac{8}{\pi^2}\left[\frac{(-1)^2}{25}\sin\left(\frac{5\pi 15.625e^{-6}}{31.25e^{-6}}\right)\right] = \frac{8}{\pi^2}(0.04) = 0.0324$$

$$n = 7\ ; \quad \frac{8}{\pi^2}\left[\frac{(-1)^3}{49}\sin\left(\frac{7\pi 15.625e^{-6}}{31.25e^{-6}}\right)\right] = \frac{8}{\pi^2}(0.02) = 0.01621$$

$$n = 9\ ; \quad \frac{8}{\pi^2}\left[\frac{(-1)^4}{81}\sin\left(\frac{9\pi 15.625e^{-6}}{31.25e^{-6}}\right)\right] = \frac{8}{\pi^2}(0.012) = 0.0097$$

It can be seen from the first five odd harmonics that the harmonic content is quite small in the triangular waveform and decays quickly. The peak amplitude of the current and the frequency at which it occurs is calculated in Table B.1.

B.0.7 Expansion of Dowell's Equations

In 1966 P.L. Dowell made major advances with simplifying assumptions that allowed inductor winding proximity and skin effects to be calculated. Dowell's assumptions are detailed below:

1. Winding layers are taken as conductive foils or ribbons;
2. Flux is everywhere uniform and axial between winding layers;
3. Layer thickness is much less than the radius of curvature;
4. All windings have the same breadth;

5. All layers in a winding portion have the same thickness;

A summary of Dowell's equations is presented below for sinusoidal currents. This analysis will be extended later to include non-sinusoidal currents. F_r is defined as the ratio of the ac winding resistance to the dc winding resistance,

$$F_r = \frac{R_w}{R_{w0}} \tag{B.25}$$

For an integral number of layers, all the same thickness,

$$F_r = M' + \frac{(m^2 - 1)}{3} D' \tag{B.26}$$

where m is the number of layers, and M' and D' are defined as

$$M' = x\frac{\sinh(2x) + \sin(2x)}{\cosh(x) + \cos(x)} = x\frac{e^{2x} - e^{-2x} + 2\sin(2x)}{e^{2x} + e^{-2x} - 2\cos(2x)} \tag{B.27}$$

$$D' = 2x\frac{\sinh(x) - \sin(x)}{\cosh(x) + \cos(x)} = 2x\frac{e^{x} - e^{-x} - 2\sin(x)}{e^{x} + e^{-x} - 2\cos(2x)} \tag{B.28}$$

where x is defined as

$$x = \frac{t_{fact}}{skin\ depth}\sqrt{\alpha} = \frac{t_{fact}}{\delta}\sqrt{\alpha} \tag{B.29}$$

The porosity factor, α, is used in these modified Dowell equations because the length of the foil does not occupy the full length of the window [12].

These equations can now be expanded to calculate winding losses with non-sinusoidal currents. Complex repetitive waveforms contain a number of frequency components at integer multiples of the fundamental frequency. The multiples are known as harmonics and the waveform may also contain a dc component, which can be considered a "zero"th order harmonic. In a conductor carrying a complex current waveform with multiple frequencies, the loss at each frequency is independent of the loss at other frequencies. This means that Dowell's equations

can be used to calculate the loss at each frequency individually. All that is required is to know the harmonic amplitudes of the current waveform (derived above), and to realize that 'F_r' is different for each frequency, as the relative layer thickness, $\frac{h}{\delta}$, is different for each. In order to calculate the power loss an effective winding resistance, R_{we}, needs to be calculated.

$$P_{cu} = I_0^2 R_{w0} + I_1^2 R_{w1} + I_2^2 R_{w2} + ... + I_n^2 R_{wn} \tag{B.30}$$

where I_n is the rms current at harmonic frequency 'n' ($n = 0$ at dc), R_{wn} is the resistance at harmonic frequency 'n', and P_{cu} is the total copper loss in the windings.

$$F_{rn} = \frac{R_{wn}}{R_{w0}} \tag{B.31}$$

where F_{rn} equals F_r at harmonic frequency 'n'. As F_{rn} can be calculated for each harmonic frequency using Dowell's equations, R_{wn} can be calculated at each frequency. The power loss in the winding, P_{cu}, is then

$$P_{cu} = R_{w0} \left(I_0^2 + I_1^2 F_{r1} + I_2^2 F_{r2} + ... + I_n^2 F_{rn} \right) \tag{B.32}$$

The effective winding resistance, R_{we}, is

$$R_{we} = \frac{P_{cu}}{I_{rms}^2} \tag{B.33}$$

where I_{rms} is the total rms current in the winding and

$$I_{rms}^2 = I_0^2 + I_1^2 + I_2^2 + ... + I_n^2 \tag{B.34}$$

Hence,

$$R_{we} = \frac{R_{w0} \left(I_0^2 + I_1^2 F_{r1} + I_2^2 F_{r2} + ... + I_n^2 F_{rn} \right)}{I_{rms}^2} \tag{B.35}$$

Harmonic Number	Frequency(kHz)	F_{rn}	$R_{wn}(\Omega)$	I_n	P_{cu}
n = 0	DC component	1	3.313e-3	200	132.52
n = 1	16,000	2.55	8.44e-3	39.86	13.42
n = 3	48,000	13.39	0.044	4.42	0.866
n = 5	80,000	29.17	0.097	1.59	0.244
n = 7	112,000	44.47	0.147	0.80	0.094
n = 9	144,000	57.16	0.189	0.48	0.044

Table B.2: AC Loss calculations for Design 1.

Using the equations above the values of F_{rn}, R_{wn}, and P_{cu} can be calculated at each frequency for both the inductors designed in Chapter 4.

B.0.8 AC Loss Analysis for Design 1

Design 1 has 12 turns and 6 layers per winding. The results are tabulated in Table B.2. The inductor rms current, I_{rms}, is

$$I_{rms} = \sqrt{(200^2 + 39.86^2 + 4.42^2 + 1.59^2 + 0.8^2 + 0.48^2)} = 203.98\ A \qquad \text{(B.36)}$$

The effective winding resistance, R_{we}, is

$$R_{we} = 0.00356\ \Omega \qquad \text{(B.37)}$$

This gives a total copper loss, P_{cu}, for design 1,

$$P_{cu} = 0.00356 \times 203.98^2 = 148.12\ W \qquad \text{(B.38)}$$

B.0.9 AC Loss Analysis for Design 2

Design 2 has 22 turns and 11 layers and the results are tabulated in Table B.3. The inductor rms current, I_{rms}, is

$$I_{rms} = \sqrt{(200^2 + 39.86^2 + 4.42^2 + 1.59^2 + 0.8^2 + 0.48^2)} = 203.98\ A \qquad \text{(B.39)}$$

Harmonic Number	Frequency(kHz)	F_{rn}	$R_{wn}(\Omega)$	I_n	P_{cu}
n = 0	DC component	1	5.315e-3	200	212.6
n = 1	16,000	6.23	0.0331	39.86	52.06
n = 3	48,000	42.80	0.227	4.42	4.44
n = 5	80,000	96.00	0.51	1.59	1.29
n = 7	112,000	147.59	0.788	0.80	0.50
n = 9	144,000	190.3	1.011	0.48	0.23

Table B.3: AC Loss calculations for Design 2.

The effective winding resistance, R_{we}, is

$$R_{we} = 0.0065\ \Omega \tag{B.40}$$

This gives a total copper loss, P_{cu}, for design 2,

$$P_{cu} = 0.0065 \times 203.98^2 = 270.47\ W \tag{B.41}$$

Appendix C

Experimental Analysis

The following appendix presents further B-H loops and inductor current and voltage waveforms for Section 3.2.3 and the tabulated experimental results for Chapter 3.

C.0.10 B-H loops and inductor current and voltage waveforms for Section 3.2.3

1. Fig.C.1: λ-I loop for 10JNHF600 at 10 kHz, 0 mm gap
2. Fig.C.2: Inductor waveforms for 10JNHF600 at 10 kHz, 0 mm gap
3. Fig.C.3: λ-I loop for 10JNHF600 at 20 kHz, 0 mm gap
4. Fig.C.4: Inductor waveforms for 10JNHF600 at 20 kHz, 0 mm gap
5. Fig.C.5: λ-I loop for 10JNHF600 at 20 kHz, 1 mm gap
6. Fig.C.6: Inductor waveforms for 10JNHF600 at 20 kHz, 1 mm gap

C.0.11 Experimental Tables for Chapter 3

1. Table C.1: Experimental results for Fig. 3.4.
2. Table C.2: Experimental results for Fig. 3.5.

3. Table C.3: Experimental results for Fig. 3.6.
4. Table C.4: Experimental results for Fig. 3.8.
5. Table C.5: Experimental results for Fig. 3.25.
6. Table C.6: Experimental results for Fig. 3.4
7. Table C.7: Experimental results for Fig. 3.31.
8. Table C.8: Experimental results for Fig. 3.26.
9. Table C.9: Experimental results for Fig. 3.32.
10. Table C.10: Experimental results for Fig. 3.33.

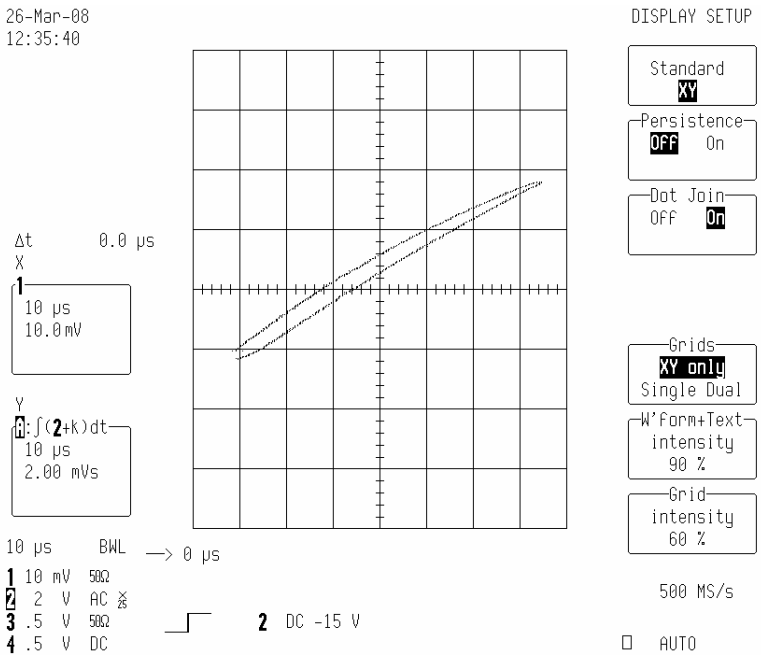

Figure C.1: λ-I loop for 10JNHF600 at 10 kHz, 0 mm gap.

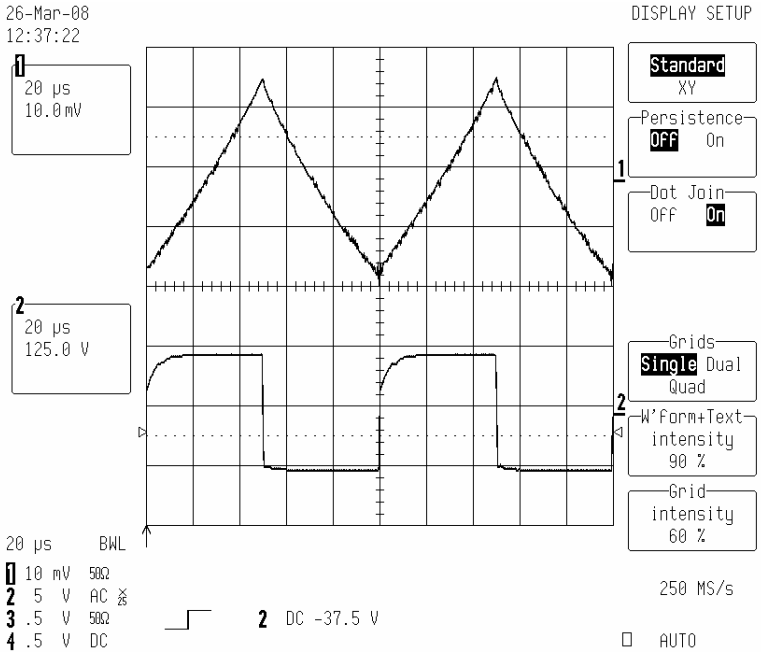

Figure C.2: Inductor waveforms for 10JNHF600 at 10 kHz, 0 mm gap.

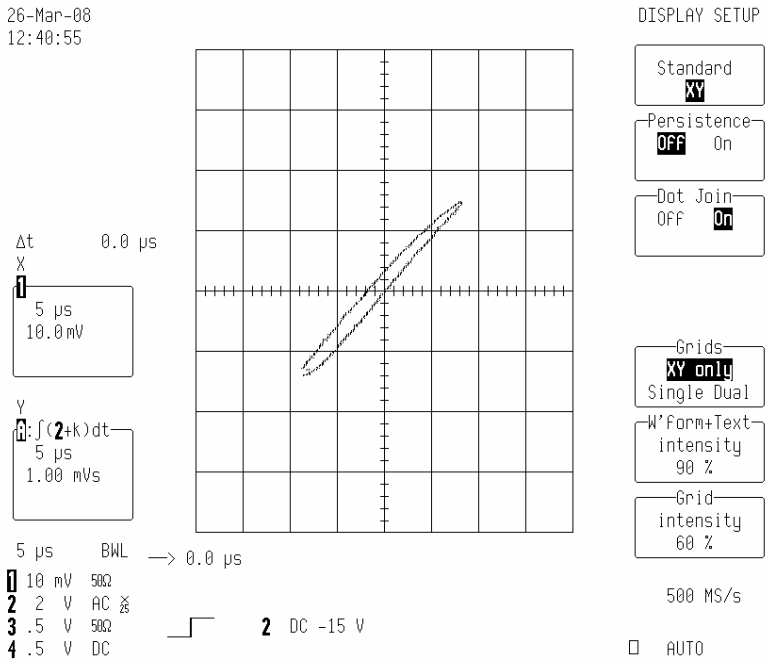

Figure C.3: λ-I loop for 10JNHF600 at 20 kHz, 0 mm gap.

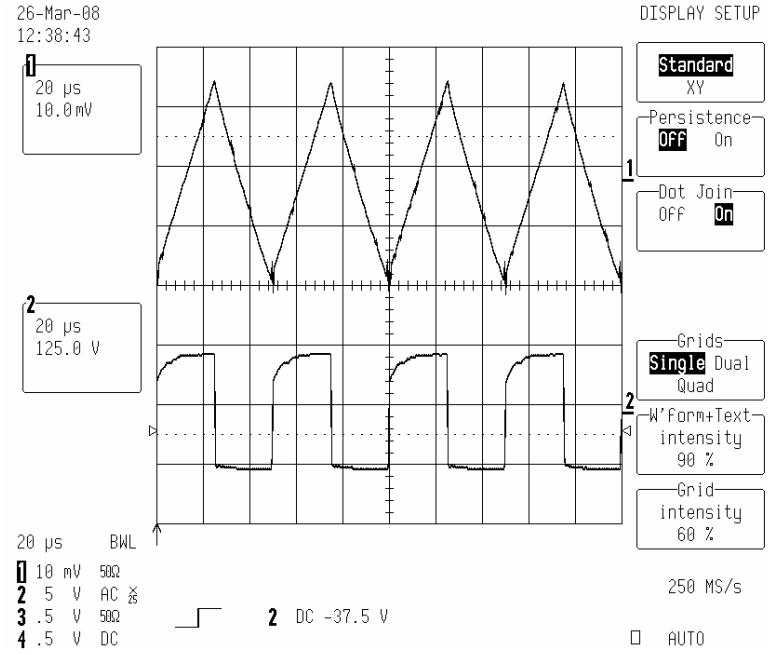

Figure C.4: Inductor waveforms for 10JNHF600 at 20 kHz, 0 mm gap.

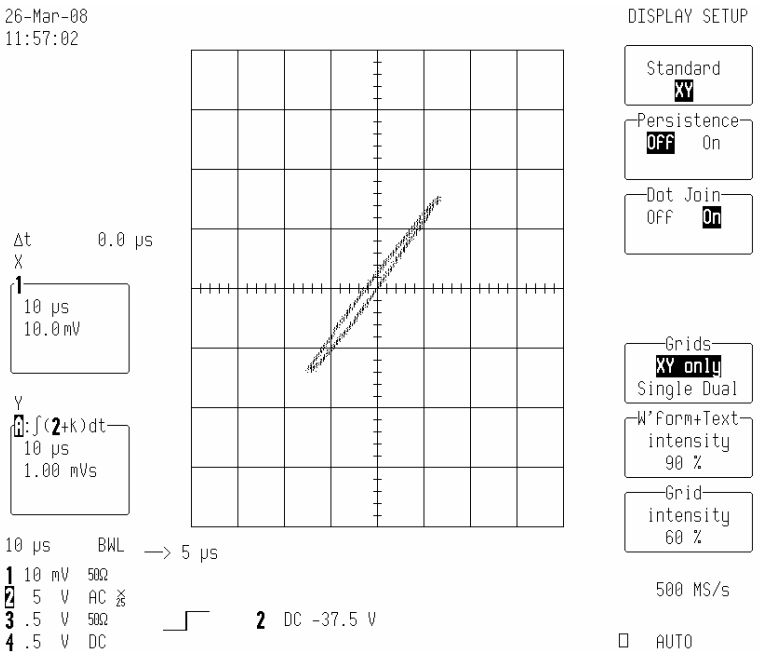

Figure C.5: λ-I for 10JNHF600 at 20 kHz, 1 mm gap.

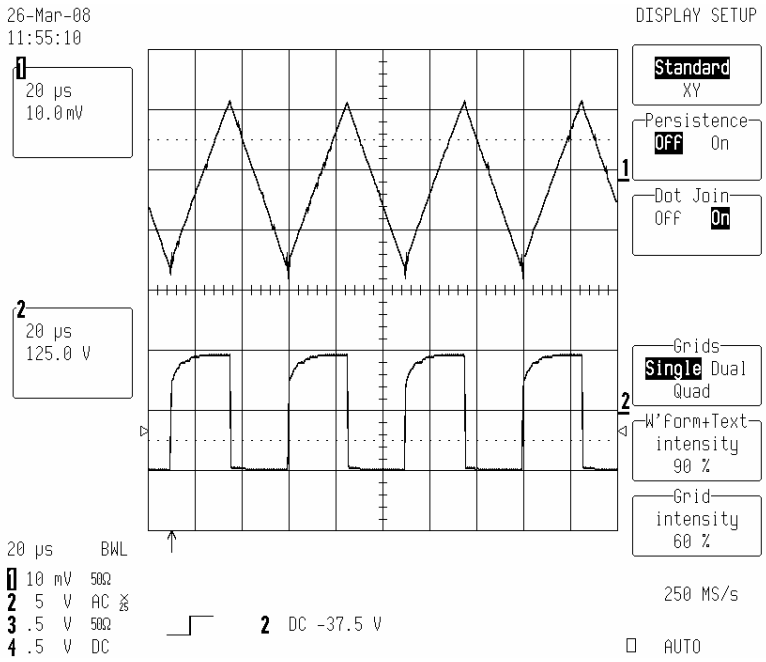

Figure C.6: Inductor waveforms for 10JNHF600 at 20 kHz, 1 mm gap.

Material	**f** (kHz)	$\mathbf{V}_{in}$ (V)	$\mathbf{V}_{o}$ (V)	$\mathbf{I}_{in}$ (A)	$\mathbf{I}_{o}$ (A)	$\mathbf{P}_{in}$ (W)	$\mathbf{P}_{out}$ (W)	η %	ΔI_{pk-pk} (A)	$\mathbf{I}_{max}$ (A)	**L** (μH)	ΔT_{core} (°C)	ΔT_{cu} (°C)
2605SA1	15	125.61	253.3	19.59	9.333	2.452	2.363	96.37	34.5	36	120.77	113	76
2605SA1	20	125.54	254.6	19.79	9.381	2.483	2.389	96.21	26	31.8	120.19	100	65
2605SA1	25	124.63	254.9	20.11	9.385	2.505	2.392	95.49	21.2	30.2	117.9	89	58
2605SA1	30	123.47	254.5	20.31	9.376	2.507	2.386	95.17	17.6	29.4	118.4	80	52
10JNHF600	15	126.31	254.6	19.66	9.371	2.484	2.385	96.01	32.4	35.6	129.9	114	83
10JNHF600	20	125.32	254.1	19.81	9.359	2.481	2.379	95.89	25.2	32	124.33	102	76
10JNHF600	25	124.9	255.2	20.14	9.395	2.513	2.401	95.54	20.4	29.6	122.45	94	68
10JNHF600	30	122.37	251.9	20.19	9.286	2.469	2.341	94.82	16.4	28.0	124.4	87	62

Table C.1: Experimental results for Fig. 3.4.

Material	**f** (kHz)	$\mathbf{V}_{in}$ (V)	$\mathbf{V}_{o}$ (V)	$\mathbf{I}_{in}$ (A)	$\mathbf{I}_{o}$ (A)	$\mathbf{P}_{in}$ (W)	$\mathbf{P}_{out}$ (W)	η %	ΔI_{pk-pk} (A)	$\mathbf{I}_{max}$ (A)	**L** (μH)	ΔT_{core} (°C)	ΔT_{cu} (°C)
2605SA1	30	125.82	254.3	20.13	9.429	2.512	2.398	95.46	18	29.2	115.57	83	54
2605SA1	30	124.24	253.4	20.02	9.36	2.486	2.364	95.09	17.8	29.0	116.3	82	56
2605SA1	30	123.47	254.5	20.31	9.376	2.507	2.386	95.17	17.6	29.4	118.4	80	52
10JNHF600	30	123.01	252.1	20.01	9.234	2.461	2.328	94.59	16.4	27.8	125.01	84	63
10JNHF600	30	123.18	252.1	20.03	9.285	2.475	2.341	94.66	16.6	28.0	123.67	85	63
10JNHF600	30	122.37	251.9	20.19	9.286	2.469	2.341	94.82	16.4	28.0	124.4	87	62

Table C.2: Experimental results for Fig. 3.5.

Material	$\mathbf{l}_g$ (mm)	$\mathbf{V}_{in}$ (V)	$\mathbf{V}_o$ (V)	$\mathbf{I}_{in}$ (A)	$\mathbf{I}_o$ (A)	$\mathbf{P}_{in}$ (W)	$\mathbf{P}_{out}$ (W)	η %	ΔI_{pk-pk} (A)	$\mathbf{I}_{max}$ (A)	$\mathbf{L}$ (μH)	μ_r	ΔT_{core} (°C)	ΔT_{cu} (°C)
2605SA1	0.3	123.80	254.7	20.33	9.365	2.51	2.382	94.9	9.6	25.4	214.9	319.3	77	47
2605SA1	0.625	123.24	253.3	20.25	9.351	2.501	2.368	94.68	12.8	27.2	160.47	372.5	71	50
2605SA1	1	123.47	254.5	20.31	9.376	2.507	2.386	95.17	17.6	29.4	118.4	360.3	80	52
2605SA1	2	124.19	254.2	20.33	9.357	2.526	2.372	93.9	28	35.2	73.92	355.8	88	63
2605SA1	3	123.68	252.7	20.26	9.312	2.511	2.360	93.98	37.2	37.2	55.41	320.5	98	73
10JNHF600	0.3	123.6	253.8	20.36	9.333	2.515	2.363	93.96	11.2	22.6	183.93	228.8	105	79
10JNHF600	0.625	123.59	253.9	20.36	9.362	2.516	2.376	94.44	14.4	27.6	143.04	259.4	79	59
10JNHF600	1	122.37	251.9	20.19	9.286	2.469	2.341	94.82	16.4	28.0	124.4	399.5	87	62
10JNHF600	2	123.88	252.6	20.34	9.334	2.515	2.370	94.23	27.6	33.6	74.82	351.5	89	70
10JNHF600	3	124.02	254.8	20.38	9.356	2.524	2.371	93.94	37.2	40.0	55.57	301.3	101	84

Table C.3: Experimental results for Fig. 3.6.

Material	$\mathbf{l_g}$**/leg** (mm)	$\mathbf{V}_{in}$ (V)	$\mathbf{V}_o$ (V)	$\mathbf{I}_{in}$ (A)	$\mathbf{I}_o$ (A)	$\mathbf{P}_{in}$ (W)	$\mathbf{P}_{out}$ (W)	η %	ΔI_{pk-pk} (A)	$\mathbf{I}_{max}$ (A)	**L** (μH)	μ_r	ΔT_{core} (°C)	ΔT_{cu} (°C)
2605SA1	0	121.49	249.4	20.36	9.246	2.473	2.306	93.25	23.2	34.4	87.28	76.1	166	105
2605SA1	0	120.87	249.7	15.492	6.99	1.872	1.746	93.27	15.6	24.0	129.13	112.6	136	87
2605SA1	0	119.42	248.6	10.438	4.653	1.246	1.156	92.82	8.2	15.0	242.72	211.6	102	64
10JNHF600	0	122.07	251.5	20.43	9.29	2.492	2.337	93.78	11.6	24.4	175.38	141.0	128	100
10JNHF600	0	120.07	248.7	15.52	6.971	1.863	1.733	93.02	10.0	20.4	200.11	160.9	112	88
10JNHF600	0	119.68	249.1	10.564	4.66	1.262	1.160	91.92	7.8	14.2	255.73	205.2	97	76
2605SA1	1	123.47	254.5	20.31	9.376	2.507	2.386	95.17	17.6	29.4	118.4	360.3	80	52
2605SA1	1	121.31	251.2	15.28	7.097	1.855	1.758	94.77	16.0	23.6	126.36	461.8	72	47
2605SA1	1	120.78	250.7	10.35	4.673	1.249	1.171	93.75	16.0	18.0	125.81	453.5	70	45
10JNHF600	1	122.37	251.9	20.19	9.286	2.469	2.341	94.82	16.4	28.0	124.4	399.5	87	62
10JNHF600	1	121.19	250.4	15.32	6.99	1.858	1.751	94.24	16.8	25.6	120.28	351.5	81	54
10JNHF600	1	120.40	249.5	10.368	4.655	1.247	1.163	93.26	16.8	19.2	119.44	342.7	79	53

Table C.4: Experimental results for Fig. 3.8.

Material	**No. of airgaps**	$\mathbf{V}_{in}$ (V)	$\mathbf{V}_{o}$ (V)	$\mathbf{I}_{in}$ (A)	$\mathbf{I}_{o}$ (A)	$\mathbf{P}_{in}$ (W)	$\mathbf{P}_{out}$ (W)	η %	ΔI_{pk-pk} (A)	$\mathbf{I}_{max}$ (A)	$\mathbf{L}$ (μH)	ΔT_{core} (°C)	ΔT_{cu} (°C)
2605SA1	1	123.37	252.7	20.27	9.311	2.502	2.355	94.13	38.8	38.8	52.99	91	80
2605SA1	2	123.65	253.3	20.26	9.32	2.508	2.362	94.18	40.4	40.4	50.97	81	70
2605SA1	3	124.07	254.0	20.26	9.343	2.511	2.371	94.43	40.4	40.4	51.18	76	63
10JNHF600	1	123.09	252.1	20.26	9.296	2.495	2.345	93.98	38.8	38.8	52.87	90	78
10JNHF600	2	123.48	252.8	20.26	9.307	2.495	2.353	94.31	38.8	38.8	53.04	84	70
10JNHF600	3	123.76	253.3	20.22	9.292	2.501	2.353	94.08	40.0	40.0	51.56	83	60

Table C.5: Experimental results for Fig. 3.25.

Material	**f** (kHz)	$\mathbf{V}_{in}$ (V)	$\mathbf{V}_{o}$ (V)	$\mathbf{I}_{in}$ (A)	$\mathbf{I}_{o}$ (A)	$\mathbf{P}_{in}$ (W)	$\mathbf{P}_{out}$ (W)	η %	ΔI_{pk-pk} (A)	$\mathbf{I}_{max}$ (A)	**L** (μH)	ΔT_{core} (°C)	ΔT_{cu} (°C)
10JNHF600	30	123.85	254.1	20.22	9.382	2.505	2.385	95.21	38.5	39.0	53.61	84	65
10JNHF600	30	124.21	254.8	20.27	9.401	2.525	2.393	94.77	39.0	39.5	53.08	90	70

Table C.6: Experimental results for Section 3.4 illustrating the shielding effect of the winding.

Material	**f** (kHz)	$\mathbf{V}_{in}$ (V)	$\mathbf{V}_{o}$ (V)	$\mathbf{I}_{in}$ (A)	$\mathbf{I}_{o}$ (A)	$\mathbf{P}_{in}$ (W)	$\mathbf{P}_{out}$ (W)	η %	ΔI_{pk-pk} (A)	$\mathbf{I}_{max}$ (A)	**L** (μH)	ΔT_{core} (°C)	ΔT_{cu} (°C)
2605SA1	16	180.2	360.0	180.2	87.3	32.472	31.428	97.32	125	242.7	45.05	29	92
10JNHF600	16	182.3	360	180.0	88.0	32.814	31.680	97.08	125	242.5	45.58	78	89

Table C.7: Experimental results for Fig. 3.26.

Material	**Heat flow direction**	$\mathbf{V}_{in}$ (V)	$\mathbf{V}_{o}$ (V)	$\mathbf{I}_{in}$ (A)	$\mathbf{I}_{o}$ (A)	$\mathbf{P}_{in}$ (W)	$\mathbf{P}_{out}$ (W)	η %	ΔI_{pk-pk} (A)	$\mathbf{I}_{max}$ (A)	$\mathbf{L}$ (μH)	ΔT_{core} (°C)
2605SA1	x	123.62	253.6	20.29	9.342	2.514	2.369	94.23	38.6	37.2	61.32	38
2605SA1	y	123.55	253.4	20.28	9.336	2.507	2.367	94.42	33.6	36.8	61.29	31.5
2605SA1	xy	123.24	252.6	20.30	9.308	2.50	2.351	94.04	33.2	35.6	61.87	29
10JNHF600	x	123.24	252.4	20.3	9.315	2.502	2.353	94.05	36.8	38.4	55.82	21
10JNHF600	y	123.19	252.4	20.3	9.317	2.502	2.354	94.09	36.0	38.0	57.03	42
10JNHF600	xy	123.16	252.7	20.3	9.318	2.501	2.354	94.12	34.8	37.6	58.99	16.2

Table C.8: Experimental results for Fig. 3.31.

Material	**f** (kHz)	$\mathbf{V}_{in}$ (V)	$\mathbf{V}_{o}$ (V)	$\mathbf{I}_{in}$ (A)	$\mathbf{I}_{o}$ (A)	$\mathbf{P}_{in}$ (W)	$\mathbf{P}_{out}$ (W)	η %	ΔI_{pk-pk} (A)	$\mathbf{I}_{max}$ (A)	**L** (μH)	ΔT_{core} (°C)	ΔT_{cu} (°C)
2605SA1	15	63.44	126.4	19.59	9.425	1.243	1.192	95.88	38.8	38.8	54.46	64	49
2605SA1	20	63.4	127.2	19.82	9.47	1.258	1.204	95.7	28.4	34.4	55.73	55	42
2605SA1	25	64.6	130.23	20.43	9.68	1.319	1.259	95.45	24	32.8	53.3	50	37.5
2605SA1	30	63.74	128.83	20.45	9.586	1.303	1.235	94.78	20	30.8	52.5	45	35
10JNHF600	15	126.31	254.6	19.66	9.371	2.484	2.385	96.01	32.4	35.6	129.9	114	83
10JNHF600	20	125.32	254.1	19.81	9.359	2.481	2.379	95.89	25.2	32	124.33	102	76
10JNHF600	25	124.9	255.2	20.14	9.395	2.513	2.401	95.54	20.4	29.6	122.45	94	68
10JNHF600	30	122.37	251.9	20.19	9.286	2.469	2.341	94.82	16.4	28.0	124.4	87	62

Table C.9: Experimental results for Fig. 3.32.

Material	$\mathbf{l}_g$ (mm)	$\mathbf{V}_{in}$ (V)	$\mathbf{V}_o$ (V)	$\mathbf{I}_{in}$ (A)	$\mathbf{I}_o$ (A)	$\mathbf{P}_{in}$ (W)	$\mathbf{P}_{out}$ (W)	η %	ΔI_{pk-pk} (A)	$\mathbf{I}_{max}$ (A)	$\mathbf{L}$ (μH)	ΔT_{core} (°C)	ΔT_{cu} (°C)
2605SA1	1	63.74	128.83	20.45	9.586	1.303	1.235	94.78	20	30.8	52.5	45	35
2605SA1	2	62.88	127.35	20.41	9.507	1.284	1.211	94.31	29.2	35.6	35.96	50	46
2605SA1	3	62.6	126.5	20.41	9.43	1.276	1.221	95.6	40	40	26.25	63	65
10JNHF600	1	122.37	251.9	20.19	9.286	2.469	2.341	94.82	16.4	28.0	124.4	87	62
10JNHF600	2	123.88	252.6	20.34	9.334	2.515	2.370	94.23	27.6	33.6	74.82	89	70
10JNHF600	3	124.02	254.8	20.38	9.356	2.524	2.371	93.94	37.2	40.0	55.57	101	84

Table C.10: Experimental results for Fig. 3.33.

Appendix D

High-Power Boost Converter Analysis

In this appendix, the gate drive, control structure and software, and control interface board are discussed further for Chapter 6.

D.1 Gate Drive

The gate drive module is also sourced from Semikron and consists of two parts, the gate drive board, SKYPER 32PRO, and the gate drive adapter board, 3s SKYPER 32PRO. The gate drive board and the gate drive adapter board are detailed in [71, 72]. The SKYPER 32 PRO is a half bridge driver and the 3s SKYPER 32PRO is an evaluation board for the Semikron module SEMiX 603GB066HDs. The gate drive adapter board acts as an interface between the SEMiX 603GB066HDs module and the gate drive board and is mounted on top of the module as shown in Fig. D.1.

The practical implementation of the gate drive board is detailed next. The dynamic short circuit protection is achieved by monitoring the collector-emitter voltage [72]. The following resistors and capacitors are assembled to the adaptor board before operation for this function:

Figure D.1: SKYPER 32 PRO with adapter board on top of SEMiX module.

$$R_{ce} \text{ (resistors R162, R262)} = 11\ \Omega$$
$$C_{ce} \text{ (capacitors C150, C250)} = 200\ \text{pF}$$
$$R_{vce} \text{ (R150, R250)} = 0\ \Omega$$

In the case of a short circuit the IGBT can be turned off at a lower speed reducing the voltage spike above the collector emitter of the IGBT by reducing the di/dt value. In short circuit conditions the IGBT's peak current increases and must fall to zero in a longer time than at normal operation. The soft turn-off time can be adjusted by the connection of an external resistor $R_{Goff(SC)}$ (R160, R161 parallel connected and R260, R261 parallel connected) [72]. This function is disabled by shorting the above resistors [71]. In the 97.2 kW system the interface board senses over-currents on each phase and shuts down the system if there is a fault. The soft turn-off resistors = 0 Ω in this system.

The temperature of the SEMiX module case can also be monitored [79]. The driver module will stop all signals to the SEMiX module if the SEMiX case exceeds 85 °C by setting resistor R172 = 730 Ω.

The turn-on and turn-off speeds of the IGBT's are controlled by the gate resistors and must also be assembled to the adaptor board before operation. The gate resistors are set as follows:

$$R_{Gon(TOP)} \text{ (R151, R152, R153, parallel connected)} = 3\ \Omega$$

$R_{Gon(BOT)}$ (R251, R252, R253, parallel connected) = 3 Ω

$R_{Goff(TOP)}$ (R154, R155, R156, parallel connected) = 3 Ω

$R_{Goff(BOT)}$ (R254, R255, R256, parallel connected) = 3 Ω

The gate drive adaptor board does not need any further modifications. All PWM signals and bias power supplies to the adaptor board are supplied by the control interface board. IGBT fault monitoring signals are also sent to the control interface board from the adaptor board if dynamic short circuit or temperature faults are detected.

D.2 Control Structure and Software

The boost converter in the fuel cell vehicle operates in either average current mode control or output voltage mode control. The converter is tested experimentally using average current mode control and the gain for the PI current loops is calculated below.

Fig. D.2 shows the inductor current for an increase in demand in current. When the converter is operating in average current mode control the average inductor current is sensed and compared to a setpoint. If the current setpoint increases the PI controller in the current control loop will compensate for the error between the setpoint and the sensed inductor current. The proportional and integral gains of the PI current loop controller are calculated below. Both gains were experimentally tuned using the Ziegler-Nichols tuning method.

$$\frac{\Delta I}{\Delta t} = \frac{V_{in}}{L} = \frac{180\ V}{45\ \mu H} = 4\ \frac{MA}{s} \tag{D.1}$$

Consider a change in the current setpoint, ΔI, of 1 A for a switching frequency, f_{sw}, of 16 kHz. The percentage change in duty cycle for a change in the current setpoint is calculated.

$$\frac{1\ A}{4\frac{MA}{s}} = 0.25\ \mu\ s \tag{D.2}$$

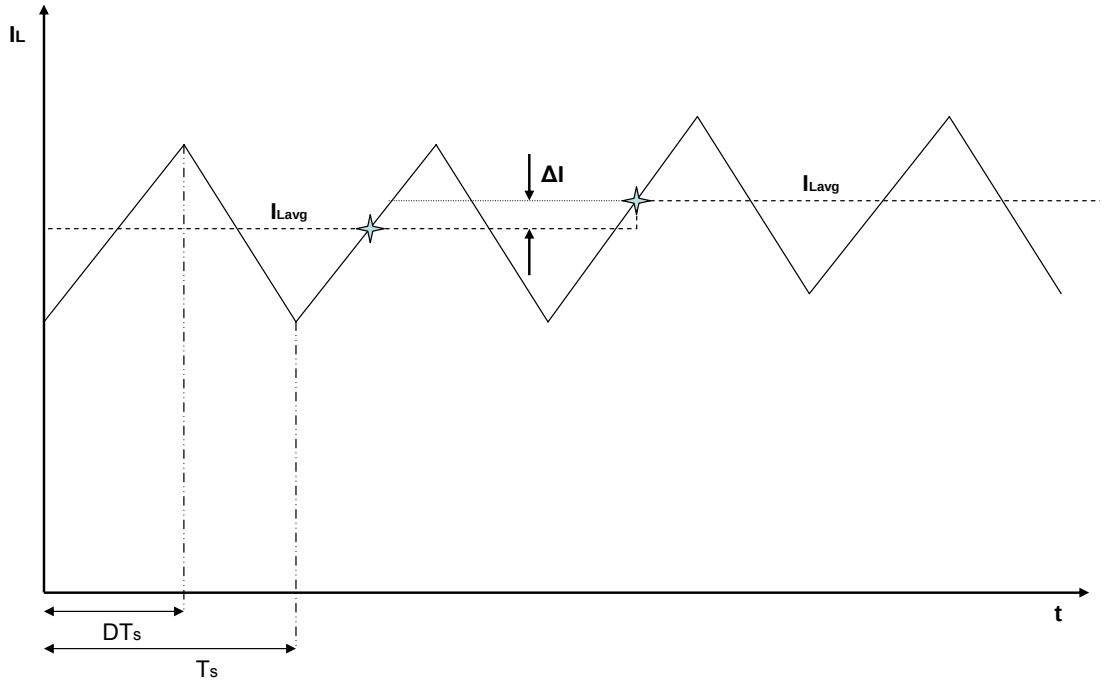

Figure D.2: Tracking of inductor current.

$$\frac{0.25\ \mu\ s}{T} = \frac{0.25\ \mu\ s}{62.5\ \mu\ s} = 0.4\% \tag{D.3}$$

A switching frequency of 16 kHz represents 3125 clock cycles in the F2808 Ezdsp. For a change in the current setpoint, ΔI, of 1 A the number of clock cycles must be changed by 0.4 %. The value of the proportional gain, k_P_I, of the PI current loop controller is calculated.

$$k\_P\_I = 0.004 * 3125 = 12.5 \tag{D.4}$$

The integral gain, k_I_I, is initially set to 1.25 ($\frac{k\_P\_I}{10}$). Both the proportional and integral gains are tuned experimentally to ensure that the system does not oscillate and that the transient response is acceptable.

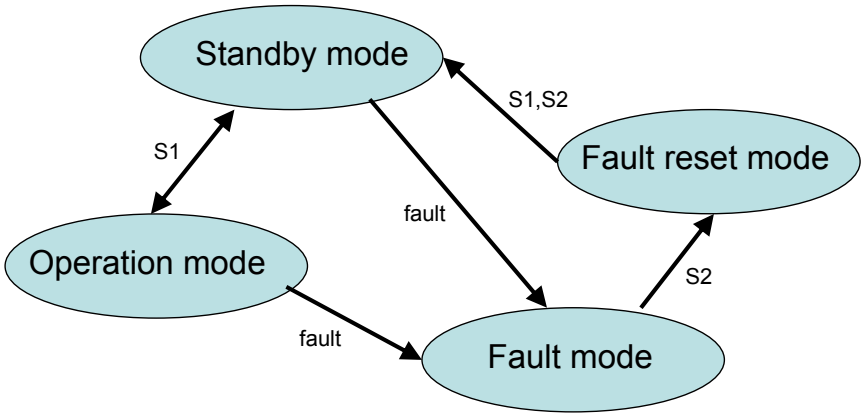

Figure D.3: Boost converter statemachine.

D.2.1 Software Control Algorithm

The following section describes the software algorithm for the output voltage and the current in phase 1 of the boost converter. A statemachine in the main loop of the program checks the system for faults before enabling current to the converter. The statemachine is described first.

Boost Converter Statemachine

Fig. D.3 illustrates the boost converter statemachine. If the system is in standby mode and the switch, *S1*, is enabled then the statemachine will switch to operation mode. When the statemachine is in operation mode the input current is enabled. In all other states the current is disabled. If the statemachine is in standby mode and a fault is detected then the statemachine will switch to fault mode. Similary, if the statemachine is in operation mode and a fault is detected the statemachine will switch to fault mode. The following psuedo code is implemented.

```
if  ((state==standby_mode) & (S1))
{ statetime = 0;
state = operation_mode;
```

```
}
if  (state == operation_mode)
current_enable = true;
else
current_enable = false;
if  ((state==standby_mode) & (fault_standby))
{ statetime = 0;
state = fault_mode;
}
if  ((state==operation_mode) & (fault_operation))
{ statetime = 0;
state = fault_mode;
}
```

If the statemachine is in operation mode and the switch, *S1*, is turned off then the statemachine will revert back to standby mode. If the statemachine is in fault mode and switch, *S2*, is turned on then the statemachine will switch to fault reset mode. All faults are cleared when the statemachine is in fault reset mode. If the statemachine is in fault reset mode and the switchs, *S1* and *S2*, are switched off then the statemachine will switch to standby mode.

```
if  ((state==operation_mode) & (!S1))
{ statetime = 0;
state = standby_mode;
}
if  ((state==fault_mode) & (S2))
{ statetime = 0;
state = fault_reset_mode;
```

```
fault_reset_tripzone();
}
if ((state==fault_reset_mode) & (!S1) & (!S2))
{ statetime = 0;
state = standby_mode;
}
```

Boost Converter Control Algorithm

The boost converter control algorithm is described next. When the interrupt service routine for phase 1 is first serviced the digital value of the output voltage, *V_HV_ADC*, is calculated by multiplying the converted analogue voltage signal from the voltage sensor by the gain *ADC_2_HV*. This is the lumped gain of the voltage sensor and the gain of the high voltage processing circuit on the control interface board. The digital value of the current in phase 1, *I_a_ADC*, is calculated similarly using *ADC_2_Iphase*, where *ADC_2_Iphase* is the lumped gain of the current sensor and the gain of the current processing circuit on the control interface board. The following psuedo code is implemented on the F2808 Ezdsp.

```
V_HV_ADC = AdcRegs.ADCRESULT0*ADC_2_HV;
I_a_ADC = AdcRegs.ADCRESULT1*ADC_2_Iphase;
```

The output voltage regulation of the boost converter is detailed first. The maximum limits for the current, *limit_I_max*, and the required voltage, *HV_req*, are set in software as *current_setpoint_CAN* and *HV_setpoint_CAN* respectively. The boost converter is only allowed to operate if *boost_run* holds true. Soft starting of the system is required to ensure that this condtion is met.

```
limit_I_max = current_setpoint_CAN;
if (!boost_run) limit_I_max = -1;  // softstart
```

```
HV_req = HV_setpoint_CAN;
if (!boost_run)  HV_req = -1;  // softstart
```

The error voltage, *error_V*, is the difference between the sensed output voltage, *V_HV_ADC* and the required output voltage, *HV_req*. The proportional gain, *k_P_V*, and the integral gain, *k_I_V*, are input. The proportional part, *proportional_V*, and the integral part, *integral_V* of the output of the voltage loop, *PI_V*, are calculated by multiplying the proportional and integral gains by the error voltage.

```
error_V = (HV_req - V_HV_ADC);
proportional_V = k_P_V * error_V;
integral_V += k_I_V * error_V;
```

Anti-integral-windup of the voltage loop integrator is also implemented by limiting the integral part of the controller to the maximum and minimum currents limits. The output of the voltage loop, *PI_V*, is also limited to the maximum and minimum current limits.

```
if (integral_V < limit_I_max)  integral_V = limit_I_max;
if (integral_V < limit_I_min)  integral_V = limit_I_min;
PI_V = proportional_V + integral_V;
if (PI_V > limit_I_max)  PI_V = limit_I_max; // limiting
if (PI_V < limit_I_min)  PI_V = limit_I_min; // limiting
```

A regulated PWM signal for phase one is now calculated using the output of the voltage loop, *PI_V*. The required current, *I_req*, is equal to the output of the voltage loop. Once again, the boost converter is only allowed to operate if *boost_run* holds true. Soft starting of the system ensures that this condtion is met.

```
I_req = PI_V;
if (!boost_run)  I_req =-1;  // softstart
```

The error current, *error_I*, is the difference between the sensed inductor current in phase one, *I_a_ADC* and the required current, *I_req*. The proportional gain, *k_P_I*, and the integral gain, *k_I_I*, are calculated in the above section. The proportional part, *proportional_I*, and the integral part for phase one, *integral_I_1* of the output of the current loop, *PI_I_a*, are calculated by multiplying the proportional and integral gains by the error current.

```
error_I = (I_req - I_a_ADC);
proportional_I = k_P_I * error_I;
integral_I_1 += k_I_I * error_I;
```

Anti-integral-windup of the current loop integrator for phase one is also implemented by limiting the integral part of the controller to the maximum or minimum PWM limits. The output of the current loop for phase one, *PI_I_a*, is also limited to the maximum or minimum PWM limits. The PWM register for phase one is then updated with the new value for the PWM signal. Similar algorithms for phase two and phase three currents are also implemented on the TI F2808 Ezdsp.

```
if (integral_I_1 > limit_PWM_max)  integral_I_1 = limit_PWM_max;
if (integral_I_1 > limit_PWM_min)  integral_I_1 = limit_PWM_min;
PI_I_a = proportional_I + integral_I_1;
if (PI_I_a > limit_PWM_max)   PI_I_a = limit_PWM_max; // limiting
if (PI_I_a > limit_PWM_min)   PI_I_a = limit_PWM_min; // limiting
EPwm1Regs.CMPA.half.CMPA = PI_I_a;
```

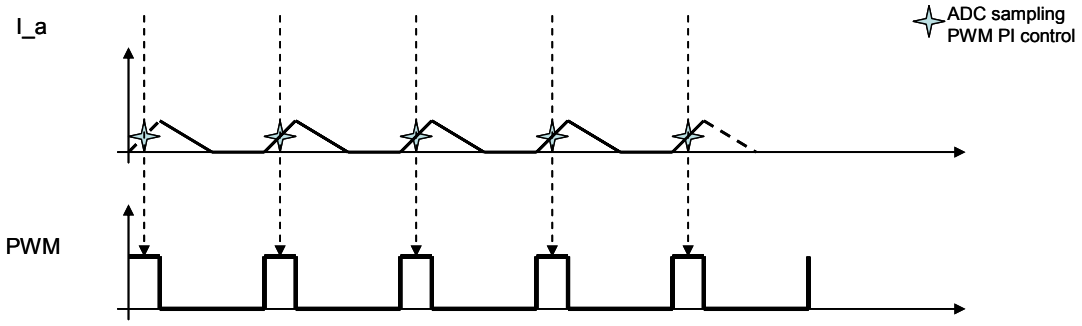

Figure D.4: PWM sampling in the middle of each PWM on state.

Continuous versus discontinuous conduction

The control algorithm needs to be modified if the system enters discontinuous conduction mode. Fig. D.4 shows a diagram of symmetric PWM with sampling in the middle of each PWM on state. This yields the correct average current in continuous conduction mode (CCM) but the values are too high in discontinuous conduction mode (DCM). The error in discontinuous conduction can be modeled and compensated by software. Correction function pseudo code:

```
if (I_a_ADC > I_CCM_limit)
I_a_ADC = I_a_ADC // Yes: CCM
else
I_a_ADC = I_a_ADC^2 / I_CCM_limit; // No: DCM
```

D.3 Control Interface Board

The control interface board acts as an interface between the TI F2808 Ezdsp and the gate drive adapter boards for each phase. Details of the design of the control interface board are now presented.

Fig. D.5 shows the electrical schematic for the bias supply for the LEM current sensor [80], the signal conditioning circuit and the over-current protection circuit

for phase 1. The TEL-3 traco power supply [81] on the left side of this schematic provides the bias supply for the current sensor, op-amps [82] and comparator [83] for phase 1. The signal, *J1-C*, from the current sensor for phase 1 goes through a filter, a resistor divider stage and a buffer stage before the signal, *J9-2*, is processed by the microcontroller. A comparator signal, *J8-37*, is sent to the microcontroller and is used to shut down the boost converter system if an over-current is detected on phase 1. Similar electrical schematics for phases 2 and 3 are shown in Fig. D.6 and Fig. D.7 respectively.

Fig. D.8 shows the electrical schematic for the 5 V bias supplies for the input and output voltage sensors [84], the 5 V bias supply for the TI F2808 ezdsp, the input and output voltage signal conditioning circuits and the output over-voltage protection circuit. The 5 V bias supplies are generated from the TEL-2 tracos [85]. The input and output voltage buses, *J7-2* and *J10-2*, initially go through voltage resistor dividers before reaching each of their respective voltage sensors. The voltage sensors provide the required isolation and the differential gain stages provide the buffered signals, *J9-13* and *J9-16*, for the mircocontroller. A comparator signal, *J9-14*, is also sent to the microcontroller and is used to shut down the boost converter in the event of an over-voltage on the output voltage bus.

Fig. D.9 shows the electrical schematic for the level shift and the Semikron fault monitoring circuits. The TI F2808 ezdsp supplies a 3.3 V PWM signal for each phase to the control interface board. A level shift driver [86] changes the 3.3 V signals, *J8-9*, *J8-11* and *J8-13*, to 15 V signals, *J4-16*, *J5-16* and *J6-16*, as required by the Semikron adapter boards.

Fig. D.9 also shows the fault detection circuits. If IGBT faults are detected by the Semikron adapter boards the signals, *J4-9*, *J5-9* and *J6-9*, are sent to the control interface board. These signals go through voltage divider networks and buffer circuits before the signals, *J8-23*, *J8-24* and *J8-25*, are sent to the F2808

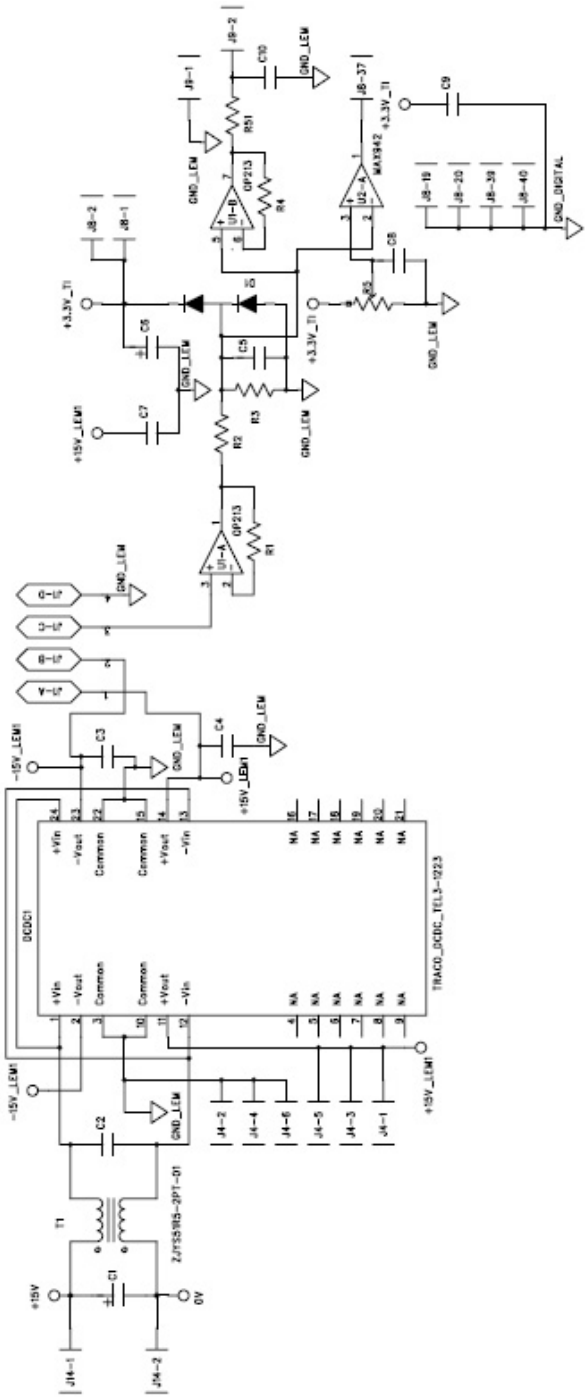

Figure D.5: Electrical schematic of phase 1 current sense network.

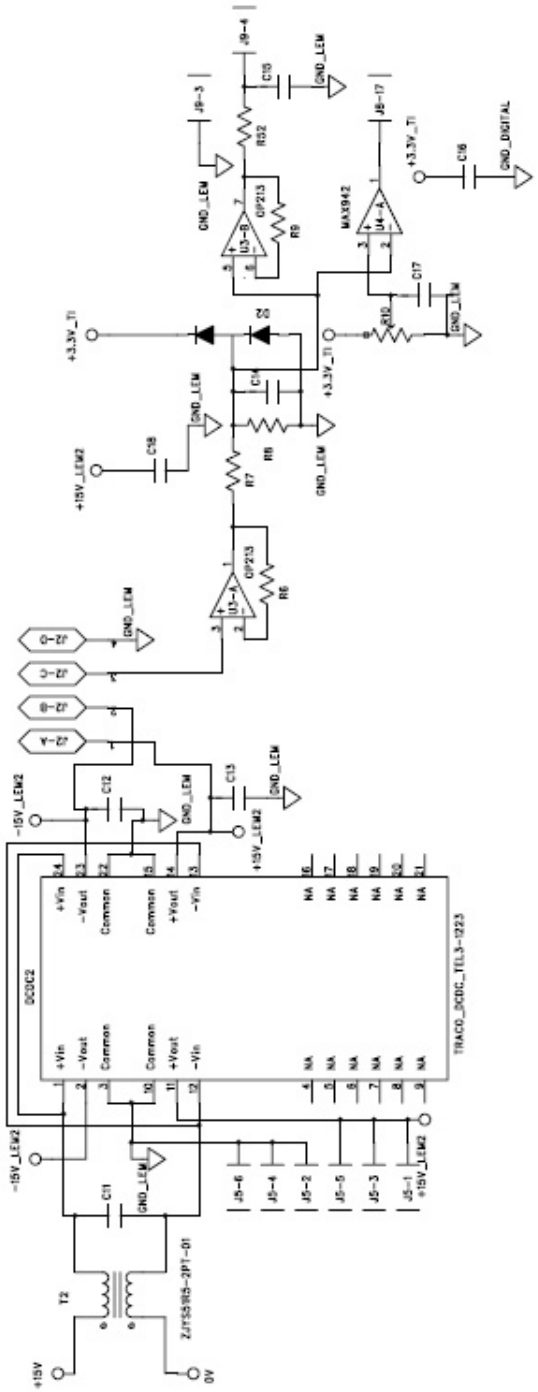

Figure D.6: Electrical schematic of phase 2 current sense network.

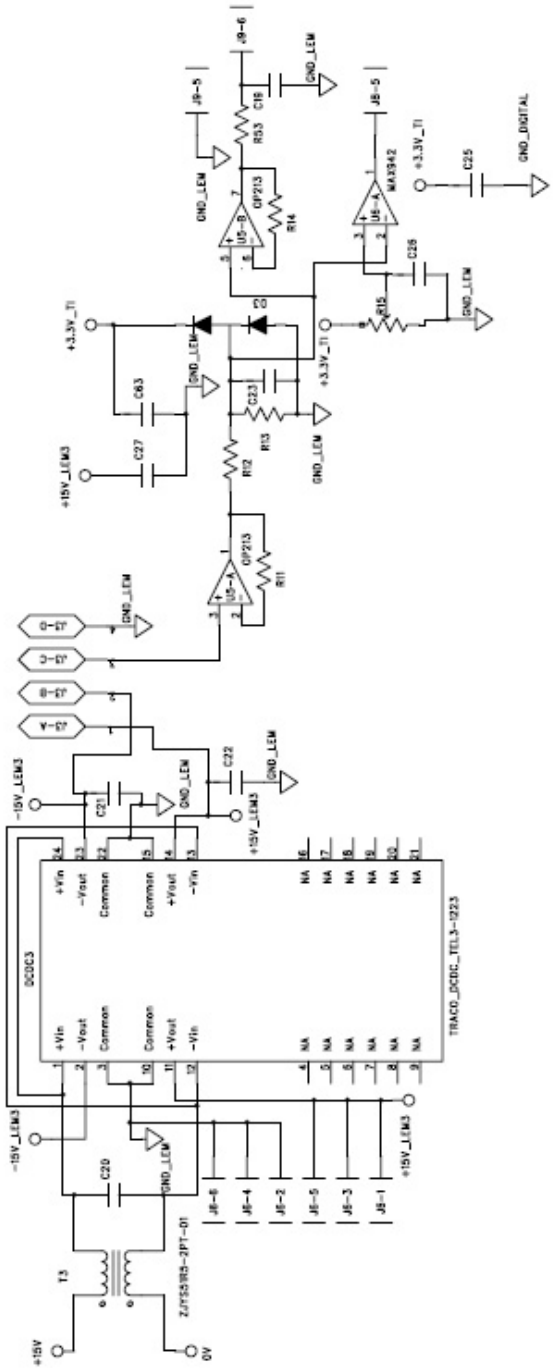

Figure D.7: Electrical schematic of phase 3 current sense network.

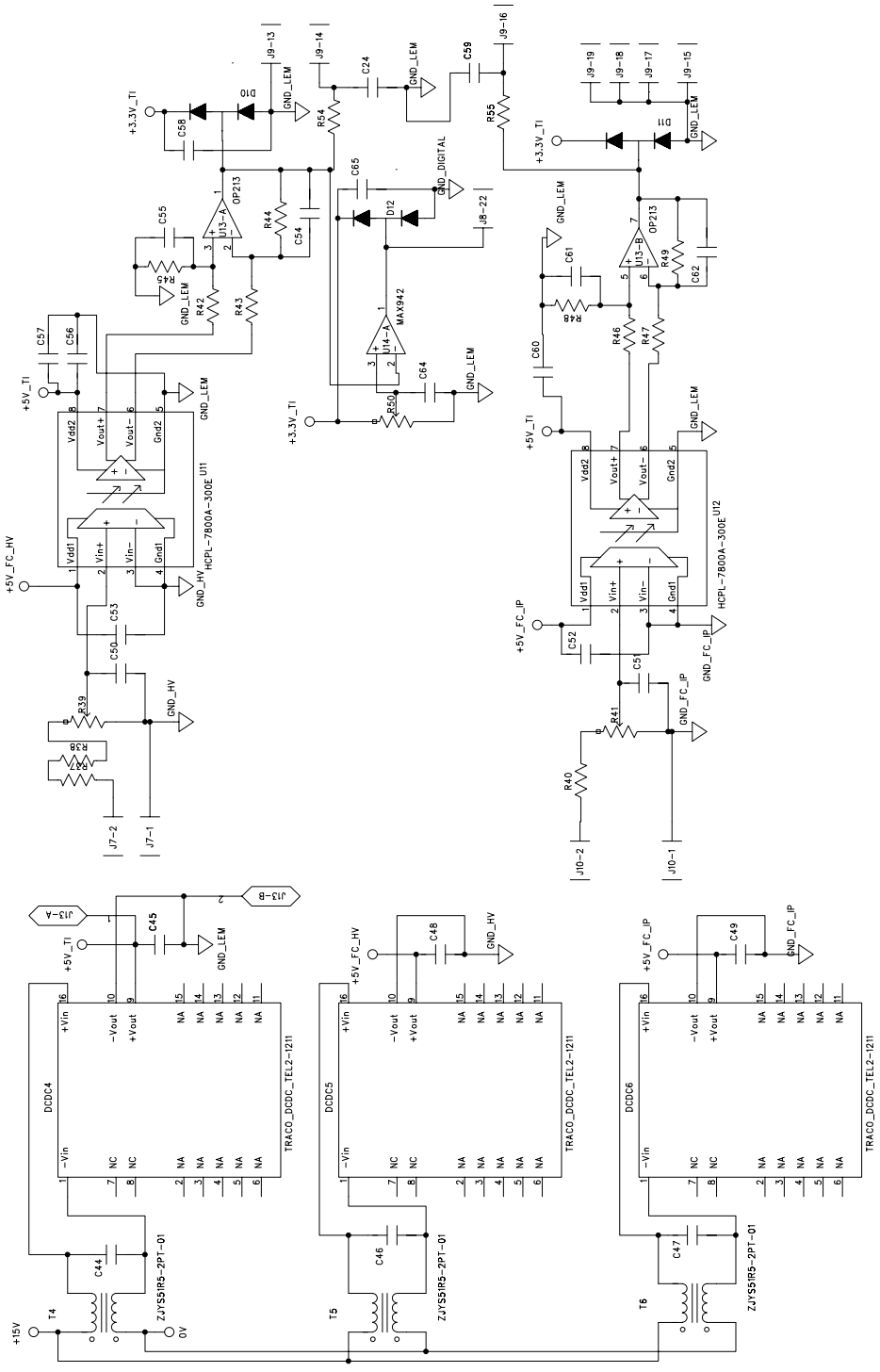

Figure D.8: Electrical schematic of voltage sense network.

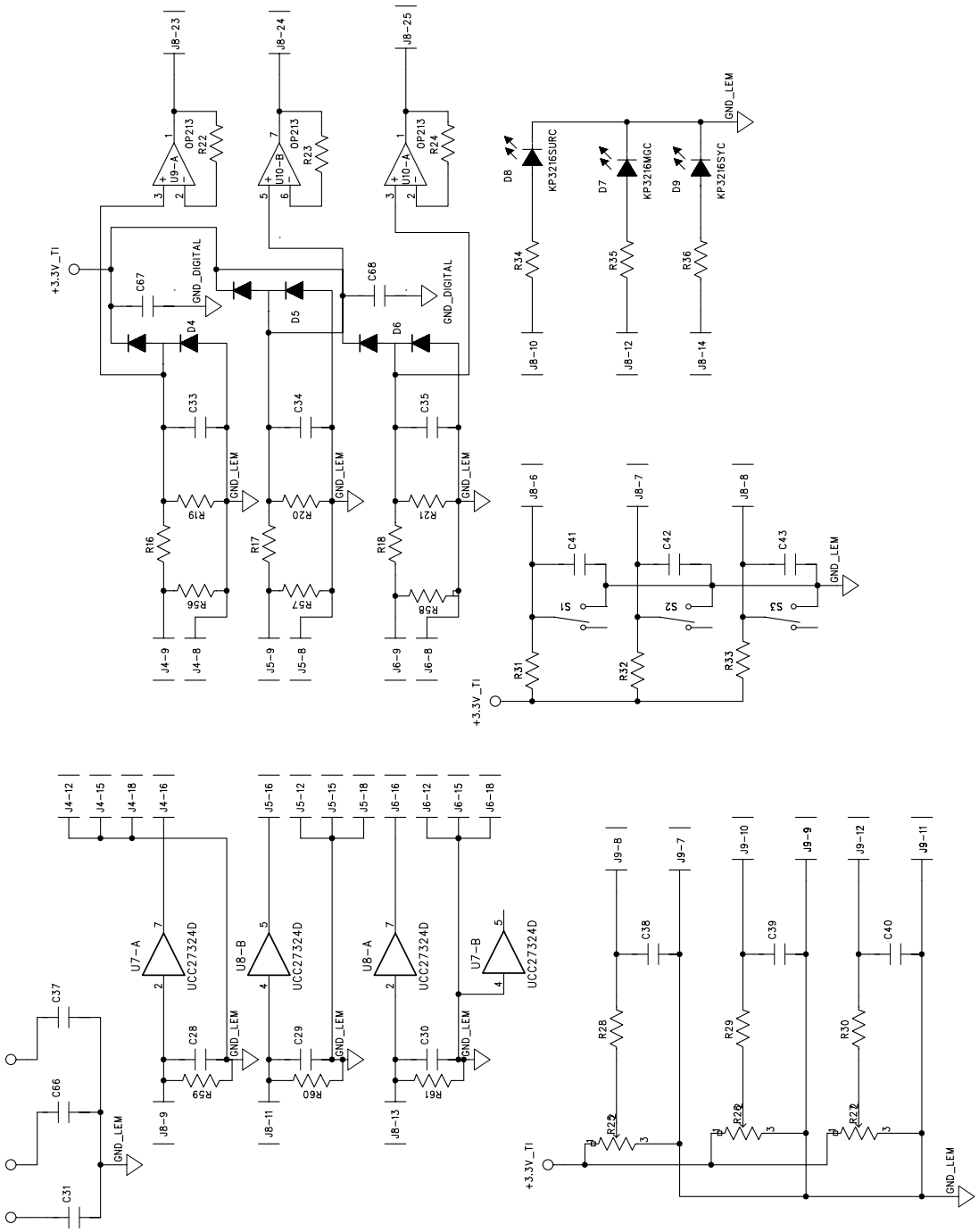

Figure D.9: Electrical schematic of control interface components.

ezdsp for evaluation.

Fig. D.9 also shows switches, LED's and potentiometers. Switch, *S1*, is used to turn on and off the boost converter. Switch, *S2*, is used to clear a fault and to reset the state machine to standby mode in the software program. Switch, *S3*, is used to select either open or closed loop control. LED, *D8*, indicates if the system is in operation mode. LED, *D7*, indicates if the system is in fault mode, and LED, *D9*, indicates if the system is in standby mode. The potentiometers can be used to set voltage and current setpoints.